

ANNUAL REPORT 2011

INSTITUTE OF ION BEAM PHYSICS
AND MATERIALS RESEARCH

hzdr

 **HELMHOLTZ**
ZENTRUM DRESDEN
ROSSENDORF

Wissenschaftlich-Technische Berichte
HZDR-014

Annual Report 2011

**Institute of Ion Beam Physics
and Materials Research**

Editors

A. L. Cordeiro, J. Fassbender,
V. Heera, M. Helm

HZDR

 **HELMHOLTZ**
ZENTRUM DRESDEN
ROSSENDORF

Cover Picture

Illustration of coupled spin vortices in magnetic multilayer disks and their possible circulation configurations. The different states were directly imaged by magnetic scanning transmission X-ray microscopy (right panels). Depending on the interlayer material and thickness, the circulation states are either predetermined or bistable.

For further information see:

S. Wintz et al., Appl. Phys. Lett. **98**, 232511 (2011),
reprinted at pp. 30 – 33 of this Annual Report.

Print edition: ISSN 2191-8708

Electronic edition: ISSN 2191-8716

The electronic edition is published under Creative Commons License (CC BY-NC-ND):

Qucosa: <http://fzd.qucosa.de/startseite/>

Published by Helmholtz-Zentrum Dresden-Rossendorf e.V.

This report is also available at <http://www.hzdr.de/FWI>

Helmholtz-Zentrum Dresden-Rossendorf e.V.

Institute of Ion Beam Physics and Materials Research

P.O. Box 51 01 19

01314 Dresden

Germany

Directors

Phone

Fax

Email

Prof. Dr. M. Helm

+ 49 (351) 260 2260

+ 49 (351) 260 3285

m.helm@hzdr.de

Prof. Dr. J. Fassbender

+ 49 (351) 260 3096

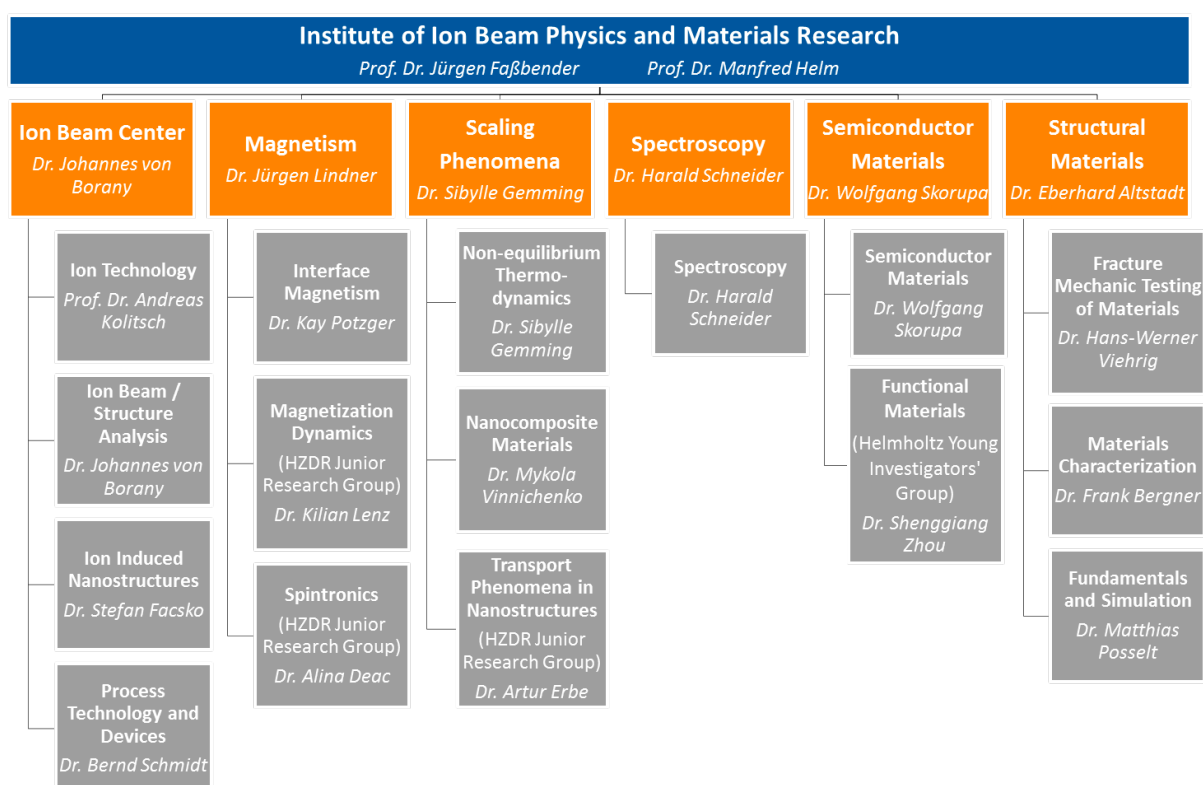
+ 49 (351) 260 3285

j.fassbender@hzdr.de

<http://www.hzdr.de/FWI>

Preface by the directors

The first year of membership of the Helmholtz-Zentrum Dresden-Rossendorf (HZDR) in the Helmholtz Association of German Research Centers (HGF) was a year of many changes also for the Institute of Ion Beam Physics and Materials Research (IIM). The transition period, however, is not yet over, since the full integration of the Center into the HGF will only be completed in the next period of the so-called program-oriented funding (POF). This funding scheme addresses the six core research fields identified by the Helmholtz Association (Energy; Earth and Environment; Health; Key Technologies; Structure of Matter; Aeronautics, Space and Transport) to deal with the grand challenges faced by society, science and industry. Since the Institute has strong contributions to both core fields “Key Technologies” and “Structure of Matter”, intense discussions were held amongst the leading scientists of the Institute, across the Institutes of the HZDR, and finally with leading scientists of other Helmholtz centers, to determine the most appropriate classification of the Institute’s research. At the end we decided to establish ourselves in **Structure of Matter**, the core field in which most of the large-scale photon, neutron and ion facilities in Germany are located. As a consequence, the Ion Beam Center (IBC) of the Institute submitted an application to become a HGF recognized large-scale facility, providing more than 50% of its available beam time to external users. This application perfectly reflects the development of the IBC over more than a decade as a European Union funded infrastructure in the framework of the projects “Center for Application of Ion Beams in Materials Research (AIM)” (1998-2000, 2000-2003, 2006-2010) and subsequently as the coordinator of the integrated infrastructure initiative (I3) “Support of Public and Industrial Research using Ion Beam Technology (SPIRIT)” (2009-2013). Another part of the Institute’s activities is dedicated to exploit the infrared/THz free-electron laser at the 40 MeV superconducting electron accelerator ELBE for condensed matter research. This facility is also open to external users and funded by the European Union.



Two major organizational changes were implemented during 2011. First, in October 2011 the spin-off company HZDR Innovation GmbH (www.hzdr-innovation.de) was founded. The company uses the Institute's infrastructure and provides ion irradiation and implantation services as well as clean room processing to industrial customers. Secondly, as a consequence of the Institute's integration within the HGF programs and the application of the IBC as a HGF large-scale facility, the divisions of the institute were re-structured. These structural changes became effective on January 1st, 2012. The main goal was to unite all employees involved in ion beam technology under the umbrella of the IBC, thus providing a better match to the HGF funding scheme for user facilities. To this end the division "Structural Materials" (formerly part of the Institute of Safety Research) led by Dr. Eberhard Altstadt was integrated into the Institute, and the accelerator mass spectrometry/resource analytics activities led by Dr. Silke Merchel were transferred to the Helmholtz Institute Freiberg for Resource Technology. Concerning the latter, we target at a strong collaboration between both Institutes, namely by using ion beam analysis in the field of mineral and metalliferous raw materials.

Concerning third-party funding we successfully started to receive funding from the HGF "Initiative and Networking Fund" granted by the president of the Helmholtz Association. Dr. Shengqiang Zhou, working on "Ion beam processed functional materials for spintronics and photovoltaics", established the first HGF Young Researcher Group of the HZDR. In addition, the Virtual Institute "Memory effects in resistive ion-beam modified oxides" led by Dr. Sibylle Gemming has started its operation. In this Virtual Institute the HZDR expertise is combined with those from the Forschungszentrum Jülich, TU Dresden, TUBA Freiberg, FSU Jena, ETH Zürich and UC San Diego. More recently, the Helmholtz-Russia Joint Research Group "Defects in magnetic TiO₂" led by Dr. Kay Potzger was established. After last year's big success with grant applications to the Deutsche Forschungsgemeinschaft (DFG), we are very proud to have started just as successfully with applications to HGF funding. We should also mention that contracts with industry continue to play a major role in the Institute's funding landscape, reflecting the broad spectrum of research carried out at our institute: from very basic to relevant applied research.

Last but not least, 2011 was a year in which we continued to do very good science. Eleven selected publications out of 158 published by our researchers in the fields of semiconductor physics, magnetism and materials science using ion beams are reproduced in this Annual Report. In addition, our scientists delivered 43 invited conference talks, and a total of 23 young researchers working at IIM graduated with a BSc, diploma or a PhD in 2011. The outstanding thesis of Dr. Norbert Martin in the area of nanomagnetism was recently selected for the HZDR Doktorandenpreis 2012 and we take the opportunity to congratulate him for this success. We also congratulate Prof. Dr. Jeffrey McCord, former head of the division of "Nanomagnetism", who left the Institute in 2011 to accept a W2-Heisenberg Professorship on "Nanoscale Materials – Magnetic Domains" at the Faculty of Engineering of Kiel University. His successor, Dr. Jürgen Lindner, took over the responsibility for the division "Magnetism" in March 2012.

Finally we would like to cordially thank all partners, friends, and organizations, who supported our progress in 2011. Special thanks are due to the Executive Board of the Helmholtz-Zentrum Dresden-Rossendorf, the Minister of Science and Arts of the Free State of Saxony, and the Minister of Education and Research of the Federal Government of Germany. Numerous partners from universities, industry and research institutes around the world have strongly contributed, and continue to play a crucial role in the further development of the Institute. Last but not least, the directors would like to thank all IIM staff for their efforts and excellent contributions in 2011.



Prof. Manfred Helm



Prof. Jürgen Fassbender

Contents

Selected Publications

Copyright remarks	9
n-InAs Nanopyramids fully integrated into silicon	11
S. Prucnal, S. Facsko, C. Baumgart, H. Schmidt, M.O. Liedke, L. Rebohle, A. Shalimov, H. Reuther, A. Kanjilal, A. Mücklich, M. Helm, J. Zuk, and W. Skorupa	
Carrier relaxation in epitaxial graphene photoexcited near the Dirac point	16
S. Winnerl, M. Orlita, P. Plochocka, P. Kossacki, M. Potemski, T. Winzer, E. Malic, A. Knorr, M. Sprinkle, C. Berger, W. A. de Heer, H. Schneider, and M. Helm	
Coherent control of a THz intersubband polarization in a voltage controlled single quantum well	21
M. Wagner, M. Helm, M. S. Sherwin, and D. Stehr	
Photoluminescence dynamics in GaAs/AlGaAs quantum wells under pulsed intersubband excitation	24
S. Zybll, H. Schneider, S. Winnerl, M. Wagner, K. Köhler, and M. Helm	
Acceptor deactivation in individual silicon nanowires: From thick to ultrathin	27
X. Ou, N. Geyer, R. Kögler, P. Werner, and W. Skorupa	
Direct observation of antiferromagnetically oriented spin vortex states in magnetic multilayer elements	30
S. Wintz, T. Strache, M. Körner, M. Fritzsche, D. Markó, I. Mönch, R. Mattheis, J. Raabe, C. Quitmann, J. McCord, A. Erbe, and J. Fassbender	
Reduced leakage current in BiFeO₃ thin films with rectifying contacts	34
Y. Shuai, S. Zhou, S. Streit, H. Reuther, D. Bürger, S. Slesazeck, T. Mikolajick, M. Helm, and H. Schmidt	
Rise and fall of defect induced ferromagnetism in SiC single crystals	37
L. Li, S. Prucnal, S. D. Yao, K. Potzger, W. Anwand, A. Wagner, and S. Zhou	
Frequency dependence of spin relaxation in periodic systems	40
I. Barsukov, F. M. Fömer, R. Meckenstock, K. Lenz, J. Lindner, S. Hemken to Krax, A. Banholzer, M. Körner, J. Grebing, J. Fassbender, M. Farle	
Spatial manipulation of magnetic damping in ferromagnetic-antiferromagnetic films by ion irradiation	44
J. McCord, T. Strache, I. Mönch, R. Mattheis, J. Fassbender	
Microstructure analysis at the interface of Er decorated Ge nanocrystals in SiO₂	48
A. Kanjilal, S. Gemming, L. Rebohle, A. Muecklich, T. Gemming, M. Voelskow, W. Skorupa, and M. Helm	

Statistics

Publications and patents	55
Books and chapters	55
Publications in journals	55
Patents	66
Concluded scientific degrees	67
PhD theses	67
Diploma theses	67
BSc theses	68
Appointments and honors	69
Participation in conferences and lectures / talks	70
Invited conference talks	70
Conference talks	73
Posters	80
Lectures / talks	87
Workshop, colloquia and seminars	90
Organization of workshops	90
Colloquia	90
Seminar series	91
Seminars	91
Exchange of researchers	96
SPIRIT visitors	96
FEL visitors	97
ROBL-MRH visitors	99
Other guests	100
Laboratory visits	101
Projects	104
Experimental equipment	109
User facilities and services	114
SPIRIT	114
Free Electron Laser FELBE	115
ROBL	116
Services	117
Organization chart	118
List of personnel	119

A man in a brown sweater and yellow gloves is working on a large, perforated metal component of a machine. The component is circular and has many small holes. The background is a bright, industrial setting with other machinery.

Selected Publications

Copyright remarks

The following journal articles are reprinted with kind permission from

S. Prucnal, S. Facsko, C. Baumgart, H. Schmidt, M.O. Liedke, L. Rebohle, A. Shalimov, H. Reuther, A. Kanjilal, A. Mücklich, M. Helm, J. Zuk, and W. Skorupa
n-InAs Nanopyramids fully integrated into silicon
Nano Letters, Vol. **11**, Issue 7, pp. 2814–2818
© 2011, American Chemical Society
DOI: 10.1021/nl201178d

S. Winnerl, M. Orlita, P. Plochocka, P. Kossacki, M. Potemski, T. Winzer, E. Malic, A. Knorr, M. Sprinkle, C. Berger, W. A. de Heer, H. Schneider, and M. Helm
Carrier relaxation in epitaxial graphene photoexcited near the Dirac point
Physical Review Letters, Vol. **107**, Issue 23, Art.-No. 237401
© 2011, The American Physical Society
DOI: 10.1103/PhysRevLett.107.237401

M. Wagner, M. Helm, M. S. Sherwin, and D. Stehr
Coherent control of a THz intersubband polarization in a voltage controlled single quantum well
Applied Physical Letters, Vol. **99**, Issue 13, Art.-No. 131109
© 2011, American Institute of Physics
DOI: 10.1063/1.3644988

S. Zybell, H. Schneider, S. Winnerl, M. Wagner, K. Köhler, and M. Helm
Photoluminescence dynamics in GaAs/AlGaAs quantum wells under pulsed intersubband excitation
Applied Physical Letters, Vol. **99**, Issue 4, Art.-No. 041103
© 2011, American Institute of Physics
DOI: 10.1063/1.3615298

X. Ou, N. Geyer, R. Kögler, P. Werner, and W. Skorupa
Acceptor deactivation in individual silicon nanowires: From thick to ultrathin
Applied Physical Letters, Vol. **98**, Issue 25, Art.-No. 253103
© 2011, American Institute of Physics
DOI: 10.1063/1.3602924

S. Wintz, T. Strache, M. Körner, M. Fritzsche, D. Markó, I. Mönch, R. Mattheis, J. Raabe, C. Quitmann, J. McCord, A. Erbe, and J. Fassbender
Direct observation of antiferromagnetically oriented spin vortex states in magnetic multilayer elements
Applied Physical Letters, Vol. **98**, Issue 23, Art.-No. 232511
© 2011, American Institute of Physics
DOI: 10.1063/1.3597297

Y. Shuai, S. Zhou, S. Streit, H. Reuther, D. Bürger, S. Slesazeck, T. Mikolajick, M. Helm, and H. Schmidt
Reduced leakage current in BiFeO₃ thin films with rectifying contacts
Applied Physical Letters, Vol. **98**, Issue 23, Art.-No. 232901
© 2011, American Institute of Physics
DOI: 10.1063/1.3597794

L. Li, S. Prucnal, S. D. Yao, K. Potzger, W. Anwand, A. Wagner, and S. Zhou
Rise and fall of defect induced ferromagnetism in SiC single crystals
Applied Physical Letters, Vol. **98**, Issue 22, Art.-No. 222508
© 2011, American Institute of Physics
DOI: 10.1063/1.3597629

I. Barsukov, F. M. Fömer, R. Meckenstock, K. Lenz, J. Lindner, S. Hemken to Krax, A. Banholzer, M. Körner, J. Grebing, J. Fassbender, M. Farle
Frequency dependence of spin relaxation in periodic systems
Physical Review B, Vol. **84**, Issue 14, Art.-No. 140410(R)
© 2011, The American Physical Society
DOI: 10.1103/PhysRevB.84.140410

J. McCord, T. Strache, I. Mönch, R. Mattheis, J. Fassbender
Spatial manipulation of magnetic damping in ferromagnetic-antiferromagnetic films by ion irradiation
Physical Review B, Vol. **83**, Issue 22, Art.-No. 224407
© 2011, The American Physical Society.
DOI: 10.1103/PhysRevB.83.224407

A. Kanjilal, S. Gemming, L. Rebohle, A. Muecklich, T. Gemming, M. Voelskow, W. Skorupa, and M. Helm
Microstructure analysis at the interface of Er decorated Ge nanocrystals in SiO₂
Physical Review B, Vol. **83**, Issue 11, Art.-No. 113302
© 2011, The American Physical Society
DOI: 10.1103/PhysRevB.83.113302

n-InAs Nanopyramids Fully Integrated into Silicon

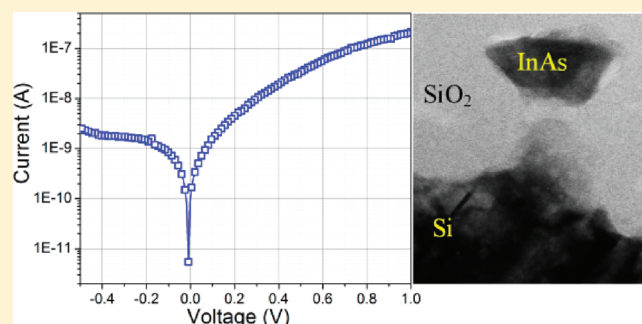
Slawomir Prucnal,^{*,†,‡} Stefan Facsko,[†] Christine Baumgart,[†] Heidemarie Schmidt,[†] Maciej Oskar Liedke,[†] Lars Rebohle,[†] Artem Shalimov,[†] Helfried Reuther,[†] Alope Kanjilal,[†] Arndt Mücklich,[†] Manfred Helm,[†] Jerzy Zuk,[‡] and Wolfgang Skorupa[†]

[†]Institute of Ion Beam Physics and Materials Research, Helmholtz-Zentrum Dresden-Rossendorf, P.O. Box 510119, 01314 Dresden, Germany

[‡]Maria Curie-Skłodowska University, Pl. M. Curie-Skłodowskiej 1, 20-035 Lublin, Poland

ABSTRACT: InAs with an extremely high electron mobility (up to 40 000 cm²/V s) seems to be the most suitable candidate for better electronic devices performance. Here we present a synthesis of inverted crystalline InAs nanopyramids (NPs) in silicon using a combined hot ion implantation and millisecond flash lamp annealing techniques. Conventional selective etching was used to form the InAs/Si heterojunction. The current–voltage measurement confirms the heterojunction diode formation with the ideality factor of $\eta = 4.6$. Kelvin probe force microscopy measurements indicate a type-II band alignment of n-type InAs NPs on p-type silicon. The main advantage of our method is its integration with large-scale silicon technology, which also allows applying it for Si-based electronic devices.

KEYWORDS: Heterojunction, flash lamp annealing, InAs, heteronanowires, silicon



The downscaling and stressor technology of Si-based devices is extending the performance of the silicon channel to its limits. The replacement of standard SiO₂ gate dielectric by high-*k* materials helps to follow the Moore's law for the next few years. For further enhancement of the device speed the integration of III–V compound semiconductors with silicon is unavoidable. The InAs nanostructure combined with the silicon platform seems to be the most promising for tunnel field effect transistors (TFET) operating at low voltage (<0.5 V) with silicon as the drain channel and InAs as the source. A promising approach toward this is the direct growth of such quantum structures on silica or crystalline silicon. Experiments indicate that quantum dots (QDs) can have several shapes depending on the manufacturing method, such as disk, ellipsoid, conical, pyramid, and tetrahedron or an island-like shape, which has strong influence on their optical and electrical properties.^{1–5} Among the most investigated three-dimensional (3D) islands are self-assembled pyramidally shaped InAs, Ge and SiGe nanostructures on silicon grown by the Stranski–Krastanov (S–K) mode which is characterized by the formation of gradually relaxing 3D islands over a fully strained initially two-dimensional wetting layer.^{5–8} The evolution of islands during deposition results from a competition between the relaxation of misfit strain and the increase of the surface energy. Another option is the direct growth of III–V nanowires on silicon.^{9–11} Recently, Björk et al. have demonstrated Si–InAs heterojunctions consisting of n-type InAs nanowires grown in oxide mask openings on p-type Si with a current density as high as 100 kA/cm² at 0.5 V reverse bias.¹⁰ A novel approach to integrate III–V semiconductors with silicon was

proposed by Ko and co-workers.¹² They modify the epitaxial lift-off method to transfer an ultrathin InAs layer onto a Si/SiO₂ substrate in order to fabricate FETs. Such a device shows a peak transconductance of about 1.6 m S μm^{−1} at a drain–source voltage of 0.5 V, with an on/off current ratio of greater than 10 000.¹² This technique is very promising and can probably be used for different types of semiconductors but is still limited to small areas.

In this paper we propose an alternative to the epitaxy method to integrate the III–V compound semiconductors with silicon technology. The formation of inverted pyramidally shaped InAs quantum structures in silicon was done by sequential ion implantation and millisecond range flash lamp annealing. The size of InAs pyramids is in the range of 40–80 nm depending on the annealing conditions. Subsequently the InAs/Si nanocolumns were formed by standard selective wet chemical etching. As proved by Kelvin probe force microscopy (KPFM) measurements, the InAs nanostructure is a strongly degenerated n-type semiconductor with a Fermi level lying high in conduction band (CB), which allows a good ohmic contact formation with various kinds of metals. The current–voltage (*I*–*V*) characteristics made by variable-temperature atomic force/scanning tunneling microscope (VT-AFM/STM) confirms the InAs/Si heterojunction diode formation.

Received: April 8, 2011

Revised: May 19, 2011

Published: June 06, 2011

Single crystalline p-type (100) silicon wafers with a resistivity in the range of 1–20 Ω cm covered by a 100 nm thick thermally grown oxide layer were implanted sequentially with As and In ions at a depth of \sim 120 nm from the sample surface. Initially, the 170 keV As⁺ ions were implanted with a dose of 3.2×10^{16} ion/cm². The implantation was performed at 500 °C in order to initiate the clustering process of arsenic during ion implantation. Subsequently the samples were implanted by 240 keV In⁺ ions with a dose of 3×10^{16} ion/cm² at room temperature. The expected In and As ion concentration is in the range of 5×10^{21} cm⁻³ in p-Si. The distribution of the implanted ions was calculated by the SRIM 2007 code and experimentally confirmed by Rutherford backscattering spectrometry (RBS). The RBS spectra were collected with a collimated 1.7 MeV He⁺ beam at a backscattering angle of 170°. After the implantation the samples were annealed at different temperatures and times in order to estimate the most suitable annealing conditions for InAs NP formation. Three different annealing techniques were employed: furnace annealing in the temperature range from 700 to 900 °C for 30 min, rapid thermal annealing (RTA) in the same temperature range but with annealing times of 30 and 60 s, and flash lamp annealing (FLA) with 600 or 700 °C preheating for 1–5 min and an annealing temperature during FLA ranging from 900 up to 1300 °C for 20 ms. In all cases the samples were annealed in argon ambient. The InAs/Si nanocolumns were formed by selective wet chemical etching. In a first step the SiO₂ layer was removed with a HF:H₂O solution. Next 30% KOH was used to etch selectively silicon. The selective etching was performed at room temperature with an etching rate of about 20 nm/min.

The optical properties were investigated by μ -Raman spectroscopy. The μ -Raman spectra were recorded at room temperature in backscattering geometry in the range of 150–600 cm⁻¹ using a 532 nm Nd:YAG laser. High-resolution transmission electron microscopy (HRTEM), high-angle annular dark-field scanning TEM (HAADF-STEM), and energy dispersive X-ray spectroscopy (EDS) were performed in cross-sectional geometry by means of an FEI Titan 80–300 STEM operating at 300 keV. Lattice parameters and dimension of the InAs nanoparticles were determined at room temperature by means of synchrotron radiation X-ray diffraction (SRXRD) at the BM20 (ROBL) beamline of the European Synchrotron Radiation Facility (ESRF). Longitudinal $2\theta/\omega$ scans were performed in coplanar geometry using a parallel monochromatic beam with a wavelength $\lambda = 1.54056$ Å. The element distribution on the etched samples was measured by μ -Auger spectroscopy with a lateral resolution of about 15 nm. The KPFM and VT-AFM/STM (Omicron NanoTechnology) were used to determine the electrical properties of the InAs/Si heterostructures. For the I – V measurements, the conductive diamond coating n⁺-Si cantilever tip was used. The surface morphology after each preparation step was characterized by means of atomic force microscopy (AFM).

Many types of semiconductor nanocrystals have been successfully synthesized in different hosts by ion implantation techniques and subsequent annealing. The main problem which appears during long-term annealing is the wide size distribution of the nanoparticles and the strong broadening of the depth profile of the doped elements due to diffusion.^{13,14} Such problems may be solved by precise control of the implanted element's fluence and by millisecond range annealing. Figure 1 shows the diagram of the fabrication process for the InAs/Si heterojunction. After ion implantation, samples were annealed for 20 ms at temperatures by far exceeding the melting point of InAs. It leads

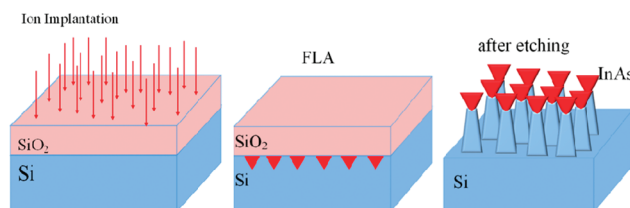


Figure 1. Schematic of the InAs/Si heterojunction formation.

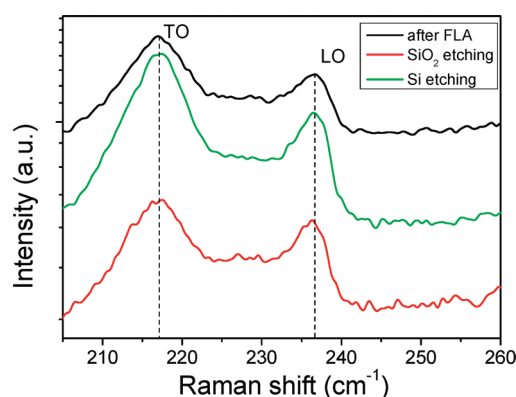


Figure 2. μ -Raman spectra of InAs nanocrystals after FLA at 1200 °C for 20 ms and subsequent SiO₂ and Si etching (KOH, 4 min), showing the InAs TO and LO phonon modes.

to formation of InAs nanostructures due to liquid-phase epitaxy. The minimum surface free energy appears generally along the [111] orientation for most of epitaxially growth III–V semiconductor nanostructure.¹⁵ As a result, the InAs NPs are formed just below the Si/SiO₂ interface with crystallographic orientation along [111] direction. After annealing the standard wet chemical etching was performed. In a first step the SiO₂ layer was removed with HF:H₂O solution. Next silicon was etched selectively with 30% KOH at room temperature with an etching rate of about 20 nm/min. Both solutions did not react with InAs. In order to remove the residual potassium from the etched surface the samples were rinsed in deionized water. The InAs NPs are used here as the etching mask, which simplifies the preparation process of InAs/Si heterostructures.

After each preparation step, the InAs/Si heterostructures were investigated by μ -Raman spectroscopy. Figure 2 shows the μ -Raman spectra obtained from samples after FLA annealing and after the two etching steps. The sample was annealed at 1200 °C for 20 ms with 600 °C preheating for 2 min. The transverse optical (TO) and longitudinal optical (LO) phonon modes of InAs at about 216.8 and 236.5 cm⁻¹, respectively, are clearly visible.¹⁶ The full width at half-maximum (fwhm) of the LO phonon mode peak decreases from 5.2 cm⁻¹ before etching to 4.5 cm⁻¹ after silicon selective etching. It is worth mentioning that the depth profile of the implanted elements has a Gaussian shape centered about 20 nm below the Si/SiO₂ interface. Small InAs nanocrystals are formed in the SiO₂ layer close to the Si/SiO₂ interface as well leading to wide size distribution of them. Phonon confinement in NCs of different size leads to broadening of the phonon mode peaks. During selective etching of oxide and silicon small InAs, NCs are removed likewise. Therefore, after a second etching step the fwhm of the LO phonon mode peak

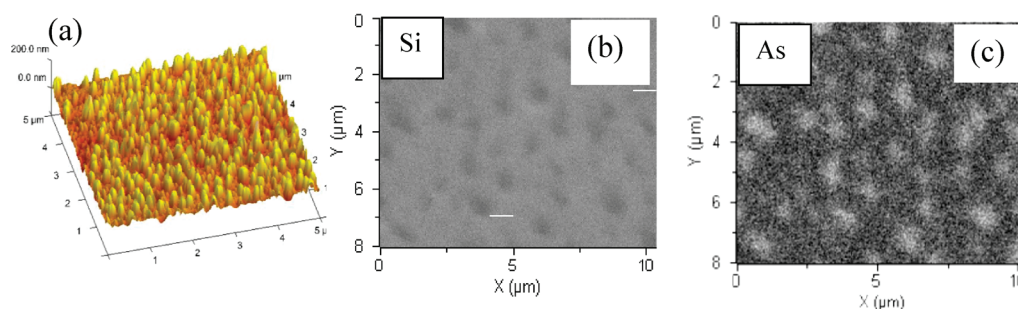


Figure 3. AFM topography (a) and Si (b) and As (c) redistribution over the sample after 7 min etched detected by μ -Auger spectroscopy.

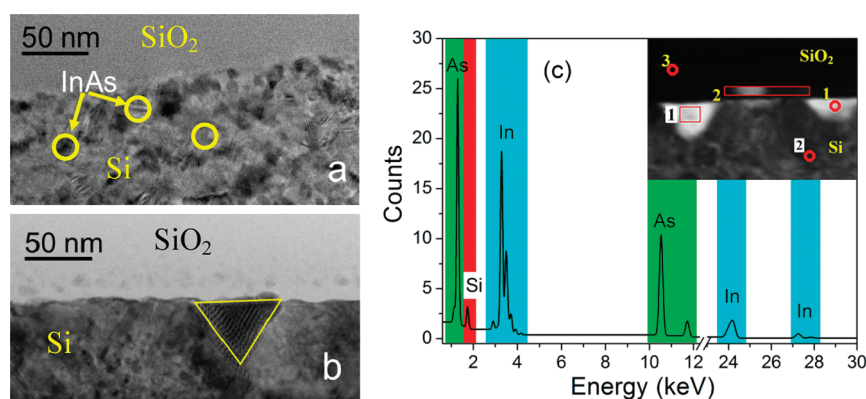


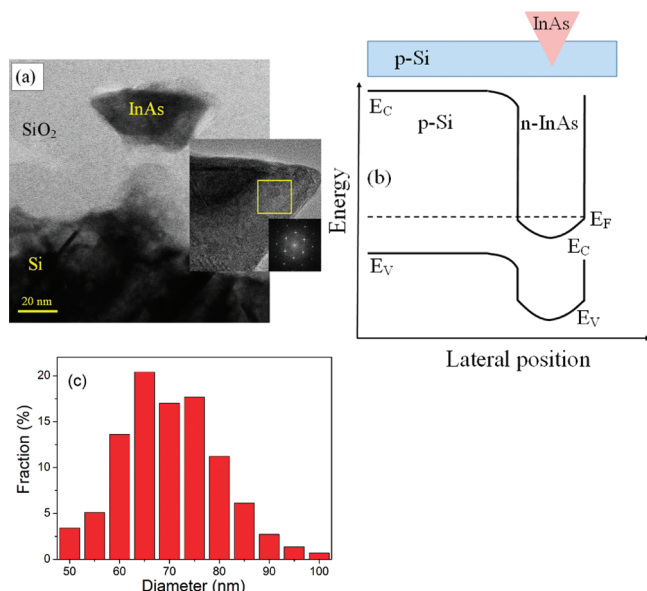
Figure 4. Bright field HRTEM micrographs of Si coimplanted by As and In followed by RTA at 850 °C for 1 min (a) and FLA at 1200 °C for 20 ms (b). A typical inverted InAs NP is indicated by a triangle, while a distribution of InAs nanodots in SiO₂ is also visible in (b); and (c) shows the EDS spectrum, which was recorded in box-1 (see inset). The inset of (c) is a HAADF-STEM image showing the formation of InAs NPs (white contrast) in Si (gray background).

decreases and leads to InAs NCs that are more homogeneous in size. The topography and element distribution on the annealed and etched samples were measured by means of AFM and μ -Auger spectroscopy, respectively. Figure 3a shows the 3D scan of the 7 min etched sample with KOH. Besides big islands which were formed due to agglomeration of a few InAs quantum dots, many columnar structures are visible. The average diameter of the single columns is 60 ± 10 nm, and the height is in the range of 120 ± 20 nm. The InAs/Si nanostructures are randomly distributed, and their height depends on the etching time. As mentioned before, the etching rate for silicon in this system was estimated to be about 20 nm/min. Figure 3b and c shows the distribution of silicon and arsenic on the sample surface after 7 min etching with KOH. Bright and dark areas correspond to a high and low concentration of the investigated element, respectively. As can be clearly seen in the regions where the arsenic concentration is high (bright spots), the signal detected from silicon was low. It correlates with the SEM scan of the investigated area and the indium distribution across the sample (not shown here). For direct confirmation of InAs crystalline nanostructures formation, cross-section TEM investigations were performed. The measurements were done at samples annealed at 850 °C for 1 min (RTA) and 1200 °C for 20 ms (FLA). Figure 4a and b shows the cross-sectional TEM images of the RTA and FLA prepared samples, respectively. The microstructural properties of the As and In implanted and annealed samples were investigated using bright-field HRTEM by keeping the electron beam along [011]-zone axis. Discernibly, the InAs

nanocrystals are formed in the silicon matrix after RTA at 850 °C for 1 min close to the SiO₂/Si interface with an average size of 15 ± 3 nm, and they are randomly oriented (see Figure 4 a). Besides self-assembled and randomly oriented small InAs NCs with an average diameter of 7 ± 2 nm, in the SiO₂ layer pyramidal shaped crystalline InAs nanostructures with a size larger than 40 nm were produced in the silicon matrix after FLA. The InAs NPs are grown vertical to the Si substrate, and they are formed between $\langle 111 \rangle$ -oriented twins. A Moiré pattern was observed in pyramidal shaped InAs. The corresponding HRTEM image confirms the formation of crystalline NPs (Figure 4 b). They are located close to the SiO₂/Si interface around 2 nm below the interface. The sample annealed at 1150 °C for 20 ms shows the NPs with an average size of 45 nm. After annealing at 1100 or 1200 °C, the average size of the InAs NPs slightly changes by about ± 5 nm (see Table 1). Moreover, the formation of partially amorphous and crystalline InAs nanodots in SiO₂ was observed when annealed at 1200 °C. This feature confirms our assumption about change of the fwhm of the TO and LO phonon mode peaks in the Raman spectra before and after etching. In parallel to HAADF-STEM, we performed the EDS measurements to understand the composition of the NPs. Samples were examined in four regions: in bulk silicon, silicon dioxide, and inside pyramids and nanodots formed in the SiO₂ layer. Figure 4c shows the EDS spectrum obtained from an InAs nanopyramid (box-1) embedded in silicon after annealing at 1200 °C for 20 ms. As can be seen, the concentration ratio between indium and arsenic inside the pyramid is almost 1:1. The same composition

Table 1. InAs lattice Parameters (a_{exp}), Nanoparticle Dimension (D) and Relative Lattice Strain (ϵ)

sample	a_{exp} (Å)	D (nm)	ϵ (%)
1100 °C	6.0518	40.2	-0.107
1150 °C	6.0542	42.5	-0.068
1200 °C	6.0554	45.2	-0.047

**Figure 5.** Bright-field HRTEM micrographs of InAs/Si heterostructures (a), schematic diagram representing band alignment in n-InAs/p-Si heterojunction (b) and histogram of the InAs NP size distribution obtained from FLA annealed sample etched for 7 min in KOH solution (c). The inset in (a) shows the magnification of the pyramid and diffraction pattern of crystalline InAs.

was also found in the case of nanodots formed in the SiO₂ layer (the rectangular box-2). Instead, in the bulk silicon and SiO₂ (circles 2 and 3) neither indium nor arsenic was found. The RBS measurements show the broadening of the In and As depth profile only after the long-term annealing. Hence, we can conclude that all observed nanostructures are composed of In and As. Moreover, synchrotron radiation X-ray diffraction was used to determine the lattice parameters and dimensions of InAs nanoparticles. Longitudinal $2\theta/\omega$ scans have been performed in coplanar geometry using a parallel monochromatic beam with a wavelength of $\lambda = 1.54056$ Å. We have found that the average size of the InAs inclusions increases from 40.2 up to 45.2 nm and grows with the annealing temperature, while the internal strain consequently decreases (preheating temperature was kept constant 600 °C for 1 min). The obtained results are in good agreement with HRTEM measurements. The relative strain of the InAs unit cell is estimated according to the relation $\epsilon = (a_{\text{exp}} - a_0)/a_0$, where a_{exp} and $a_0 = 6.0583$ Å are the experimentally obtained and the known¹⁷ lattice parameters of InAs, respectively. Lattice parameters of InAs nanopillars and their average size and relative lattice strain are given in Table 1. The decrease of the relative strain ϵ with growing annealing temperature is due to the annealing of defects and internal strain in crystalline InAs nanostructures.

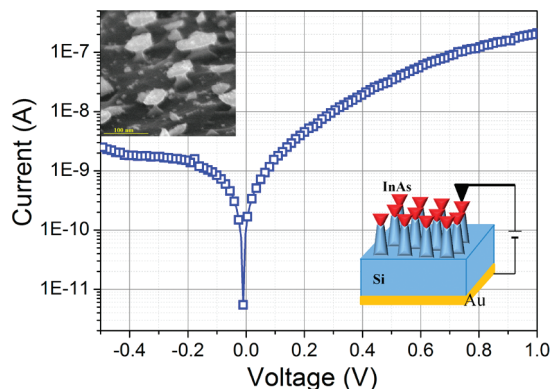
**Figure 6.** Room temperature semilogarithmic I - V characteristic of n-InAs/p-Si heterojunction. Insets show the schematic view of the I - V measurements setup (right corner) and SEM image of annealed and etched sample (left corner).

Figure 5a shows an InAs/Si nanocolumn after etching which consists of a pyramidal-shaped InAs nanocrystal placed on a crystalline silicon finger. The structure was obtained from a FLA annealed sample etched for 7 min in KOH solution. The magnification of the pyramid and diffraction pattern indicates single crystalline InAs formation. Moreover, a Moiré pattern at the InAs/Si interface is clearly visible. Such a structure is obtained only after FLA at temperatures at least 100 K higher than the melting point of bulk InAs. We assume that the InAs crystallites are formed due to liquid-phase epitaxy. Interestingly, the standard annealing techniques (RTA or FA) did not show such features, and after long-term annealing only circular InAs dots are formed. Figure 5c shows histogram of the InAs nanocrystals size distribution after selective etching. More than 85% of InAs nanocrystals are in the size range of 60–85 nm.

The conductivity type of the InAs nanostructures was investigated by means of KPFM. In order to avoid an influence of topography on the KPFM bias signal, only 20 nm of silicon was etched leaving partially open InAs NCs. Using KPFM measurements under ambient conditions, the variation of the Fermi level position with respect to the conduction band minimum E_C or to the valence band maximum E_V can be determined with a resolution of 25 meV in n- and p-type semiconductors, respectively.¹⁸ The KPFM results show that the InAs nanocrystals are n-type degenerate with type-II band alignment of InAs NP in p-Si. According to measurements the Fermi level at the position of the InAs NP lies deep inside the conduction band region of InAs. Since silicon is commonly used as n-type dopant, for InAs in our case the n-type conductivity of InAs is obtained during its formation. The measured lateral KPFM bias variation ranges between 0 mV at the edge of the InAs NP and 100 mV at the center of the NP. Under the assumption that the Fermi level is constant throughout the p-Si/InAs NP heterostructure, the conduction band E_C and valence band E_V of the InAs NP may be sketched as visible in Figure 5b. Obtained results are in good agreement with Björk et al.¹⁰ Taking into account the position of Fermi level inside of InAs nanocrystals (around 100 meV above E_C), the doping concentration is in the range of 10^{18} cm⁻³.¹⁹

The electrical characterization of the n-InAs/p-Si heterojunction was performed at room temperature by means of VT-AFM/STM. For the back ohmic contact, a 180 nm thick gold layer was sputtered on p-Si. The bias voltage was applied in reverse ($V < 0$) and forward directions ($V > 0$) between the back gold contact

and the top of the InAs nanocolumn (see inset Figure 6) via a conductive tip. Figure 6 shows room temperature current–voltage (I – V) characteristic obtained from the InAs/p-Si heterojunction. The investigated structures consist of about 60 nm in diameter InAs nanopillars on 100 nm high silicon fingers. The average p–n junction area between the InAs NP and the silicon finger is in the range of 700 nm². The measured current–voltage curves showed typical diode behavior. When the positive bias voltage is applied to the Au bottom electrode ($V > 0$ in Figure 6), the current increases exponentially up to 300 nA, which is the maximum measurable current value in our system. The measured I – V data correspond to the I – V characteristics of heterojunction diode with the ideality factor $\eta = 4.6$. The high value of the ideality factor can be related to defects at the heterojunction resulting in recombination centers and Poole–Frenkel conduction.²⁰ The inset in the left top corner of Figure 6 shows a SEM image of the FLA and the etched sample used for I – V measurements. The InAs NPs placed on silicon fingers are clearly visible as bright spots.

In summary, InAs nanopillars on Si fingers were formed by ion implantation, flash lamp annealing, and wet chemical etching, leading to an InAs/Si heterojunction. It is shown that III–V semiconductors can be fully integrated into the silicon technology. The presented experiments prove the high-quality InAs nanocrystal formation in silicon. Measurements demonstrate that the n-type InAs NP are degenerate with a type-II band alignment of InAs-Si system. The I – V characteristics confirm the InAs/p-Si heterojunction diode formation. Here we have used InAs as the active material, but other compound semiconductors could be explored in the future using the same preparation method.

■ AUTHOR INFORMATION

Corresponding Author

*E-mail: s.prucnal@hzdr.de.

■ ACKNOWLEDGMENT

Authors thank the Rossendorf Implantation Group for ion implantation and H. Felsmann, G. Schnabel, and I. Skorupa for their careful semiconductor preparation work.

■ REFERENCES

- (1) Li, Y.; Voskoboynikov, O.; Lee, C. P.; Sze, S. M.; Tretyak, O. *J. Appl. Phys.* **2001**, *90*, 6416.
- (2) Tablero, C. J. *Appl. Phys.* **2009**, *106*, 074306.
- (3) Prucnal, S.; Turek, M.; Drozdziel, A.; Pyszniak, K.; Zhou, S. Q.; Kanjilal, A.; Skorupa, W.; Zuk, J. *Appl. Phys. B: Lasers Opt.* **2010**, *101*, 315.
- (4) Kuo, D. M. T.; Chang, Y. C. *Phys. Rev. B* **2000**, *61*, 11051.
- (5) Heitz, R.; Ledentsov, N. N.; Bimberg, D.; Yu, A.; Egorov, M. V.; Maximo, V. M.; Ustinov, A.; Zhukov, E.; Alferov, Zh. I. *Appl. Phys. Lett.* **1999**, *74*, 1701.
- (6) Mo, Y.-W.; Savage, D. E.; Swartzentruber, B. S.; Lagally, M. G. *Phys. Rev. Lett.* **1990**, *65*, 1020.
- (7) Zhong, Z.; Schwinger, W.; Schaeffler, F.; Bauer, G.; Vastola, G.; Montalenti, F.; Miglio, L. *Phys. Rev. Lett.* **2007**, *98*, 176102.
- (8) Vastola, G.; Marzegalli, A.; Montalenti, F.; Miglio, L. *Mater. Sci. Eng., B* **2009**, *159–160*, 90.
- (9) Tanaka, T.; Tomioka, K.; Hara, S.; Motohisa, J.; Sano, E.; Fukui, T. *Appl. Phys. Express* **2010**, *3*, 025003.
- (10) Björk, M. T.; Schmid, H.; Bessire, C. D.; Moselund, K. E.; Ghoneim, H.; Karg, S.; Lörtcher, E.; Riel, H. *Appl. Phys. Lett.* **2010**, *97*, 163501.

(11) Tomioka, K.; Kobayashi, Y.; Motohisa, J.; Hara, S.; Fukui, T. *Nanotechnology* **2009**, *20*, 145302.

(12) Ko, H.; Takei, K.; Kapadia, R.; Chuang, S.; Fang, H.; Leu, P. W.; Ganapathi, K.; Plis, E.; Kim, H. S.; Chen, S.-Y.; Madsen, M.; Ford, A. C.; Chueh, Y.-L.; Krishna, S.; Salahuddin, S.; Javey, A. *Nature* **2010**, *468*, 286.

(13) Meldrum, A.; Boatner, L. A.; White, C. W. *Nucl. Inst. Meth. Phys. Res. B* **2001**, *178*, 7.

(14) Komarov, F.; Vlasukova, L.; Wesch, W.; Kamarou, A.; Milchanin, O.; Grachnyi, S.; Mudryi, A.; Ivaniukovich, A. *Nuc. Instr. Meth. Phys. Res. B* **2008**, *266*, 3557.

(15) Braun, W.; Kaganer, V.; Trampert, A.; Schönherr, H.; Gong, Q.; Notzel, R.; Daweritz, L.; Ploog, K. *J. Cryst. Growth* **2001**, *227*, 51.

(16) Ladanov, M. Y.; Milekhin, A. G.; Toropov, A. I.; Bakarov, A. K.; Gutakovskii, A. K.; Tenne, D. A.; Schulze, S.; Zahn, D. R. T. *J. Exp. Theor. Phys.* **2005**, *101*, 554.

(17) *Handbook Series on Semiconductor Parameters*; Levinstein, M.; Rumyantsev, S.; Shur, M., Eds.; World Scientific: Singapore, 1996; Vol. 2.

(18) Baumgart, C.; Helm, M.; Schmidt, H. *Phys. Rev. B* **2009**, *80*, 085305.

(19) Astromskas, G.; Storm, K.; Karlström, O.; Caroff, P.; Borgström, M.; Wernersson, L.-E. *J. Appl. Phys.* **2010**, *108*, 054306.

(20) Brötzmann, M.; Vetter, U.; Hofsäss, H. *J. Appl. Phys.* **2009**, *106*, 063704.

Carrier Relaxation in Epitaxial Graphene Photoexcited Near the Dirac Point

S. Winnerl,^{1,*} M. Orlita,^{2,5} P. Plochocka,² P. Kossacki,² M. Potemski,² T. Winzer,³ E. Malic,³ A. Knorr,³ M. Sprinkle,⁴ C. Berger,⁴ W. A. de Heer,⁴ H. Schneider,¹ and M. Helm¹

¹Helmholtz-Zentrum Dresden-Rossendorf, P.O. Box 510119, 01314 Dresden, Germany

²Grenoble High Magnetic Field Laboratory, CNRS-UJF-UPS-INSA F-38042 Grenoble Cedex 09, France

³Technische Universität Berlin, Hardenbergstraße 36 10623 Berlin, Germany

⁴Georgia Institute of Technology, Atlanta, Georgia 30332, USA

⁵Faculty of Mathematics and Physics, Charles University, Ke Karlovu 5, 121 16 Praha 2, Czech Republic

(Received 19 April 2011; published 28 November 2011)

We study the carrier dynamics in epitaxially grown graphene in the range of photon energies from 10 to 250 meV. The experiments complemented by microscopic modeling reveal that the carrier relaxation is significantly slowed down as the photon energy is tuned to values below the optical-phonon frequency; however, owing to the presence of hot carriers, optical-phonon emission is still the predominant relaxation process. For photon energies about twice the value of the Fermi energy, a transition from pump-induced transmission to pump-induced absorption occurs due to the interplay of interband and intraband processes.

DOI: [10.1103/PhysRevLett.107.237401](https://doi.org/10.1103/PhysRevLett.107.237401)

PACS numbers: 78.47.jd, 63.22.Rc, 78.66.Qn, 78.67.Wj

Graphene, consisting of a single atomic layer of carbon atoms in a hexagonal lattice, exhibits a unique band structure with zero energy gap and linear energy dispersion, the so-called Dirac cone. The band structure gives rise to several remarkable properties, some of which are highly attractive for novel optoelectronic and photonic devices [1]. Of key importance is the dynamics of electronic relaxation, in particular, due to the interaction with the phonon system. During the last years many insights into the relaxation dynamics have been obtained from single-color [2–5] and two-color [6–10] pump-probe experiments. Thermalization of the nonequilibrium electron distribution via electron-electron scattering on a sub-100 fs time scale and efficient scattering via optical phonons on a 100 fs time scale—few ps time scales have been identified. Common to previous pump-probe experiments is an excitation energy of ~ 1.5 eV, i.e., high above the Dirac point. Also most graphene photonic applications demonstrated so far involve near-infrared or visible light [11,12]. The nature of graphene as a gapless material with constant absorption in the range, where the band structure is well described by Dirac cones, suggests expanding the studies into the mid-infrared and terahertz range. In particular, it is crucial to obtain thorough insights into the relaxation dynamics in the range of the optical-phonon energy and below, i.e., close to the Dirac point, where Coulomb as well as optical and acoustic phonon processes can be significant and where both interband and intraband processes are relevant. Here graphene serves as a model system to understand the relevance of electron-electron and electron-phonon interaction for both intraband and interband relaxation in materials with small or vanishing energy gaps.

In this Letter, we study the carrier dynamics close to the Dirac point by varying the excitation energy E by more than an order of magnitude (245–10 meV). An

optical-phonon bottleneck is observed in the range $E = 245\text{--}30$ meV, with decay times increasing from sub-ps to several hundred ps. Microscopic calculations based on the density matrix formalism explain these time constants by optical-phonon scattering and additionally reveal contributions due to Coulomb- and acoustic phonon-induced processes. For $E < 30$ meV, a striking and unexpected sign reversal of the pump-probe signal is found. The involved processes are understood by a simple model based on the dynamic conductivity including *intra-* and *interband* absorption.

We study multilayer graphene containing ~ 70 layers grown by thermal decomposition on the carbon terminated surface of 4H-SiC [13]. It has been shown that such samples behave graphenelike rather than graphitic due to rotational stacking of layers which preserves the electronic symmetry of a single graphene layer [14]. The graphenelike nature of our samples has been verified by Raman spectroscopy [15] and magneto-spectroscopy [16,17]. In contrast to a recent two-color experiment on similar samples, where parts of the signal could be selectively attributed to the few highly doped graphene layers at the interface [8], our single-color study with much lower excitation energies investigates the relaxation dynamics in the large number of almost intrinsic graphene layers on top of the interface layers. Since our photon energies are below twice the value of the Fermi energy of the interface layers, no interband transitions in these layers are excited. The free-electron laser FELBE serves as a source for tunable picosecond pulses of infrared radiation [18]. FELBE operates in a wavelength range from 4 to 280 μm (photon energy $E = 310\text{--}4$ meV) with a repetition rate of 13 MHz. In the experiments (performed at $E = 245, 72, 51, 30, 20, 18, 14,$ and 8 meV [19]) the pump beam was mechanically chopped, the polarization of the probe beam was rotated by

90° with respect to the pump beam and a polarization analyzer was placed in front of the detector in order to minimize scattered pump radiation. Mercury-cadmium-telluride detectors optimized for the respective wavelength were used for the three highest photon energies. For the lower photon energies a liquid He cooled extrinsic Ge:Ga detector was employed.

In Fig. 1(a), the pump-induced transmission change obtained for different photon energies down to 30 meV is shown. The lattice temperature was 10 K. The different rise times correspond to different durations of the FELBE pulses (see Table I). The secondary peaks observed in the signals for the two highest photon energies are artifacts due to a second pump pulse which is caused by internal reflections in beam line windows used for the respective wavelengths. To extract relaxation times the experimental data were fitted taking into account a Gaussian excitation pulse and a bi-exponential decay. The resulting time constants are summarized in Table I: For $E = 245$ meV, we observe a fast (0.5 ps) and a slower (5.2 ps) relaxation time. The observation of two time scales is consistent with previous results obtained in experimental studies in the near infrared showing a fast component ranging from 70 to 120 fs and a slower phonon-induced component in the range of 0.4 to 2.5 ps [2–4]. Our room temperature value $\tau_2 = 3.4 \pm 1$ ps obtained for $E = 245$ meV is only slightly longer, thus pointing to an optical-phonon related mechanism. Note

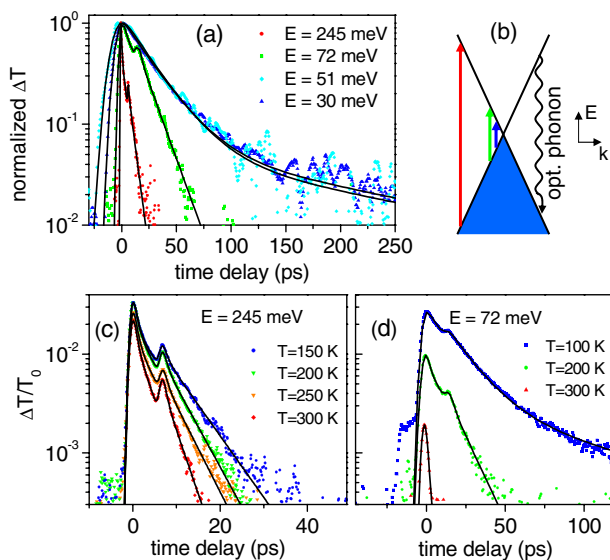


FIG. 1 (color online). Experiment: Normalized pump-induced transmission for different photon energies E (a) measured at 10 K. Illustration of the optical pumping in comparison with relaxation via optical phonons (b). The arrows indicate the applied photon energies. Temperature dependence of the pump-induced transmission for $E = 245$ meV (c) and $E = 72$ meV (d). The symbols are experimental data, the lines are fits taking into account the laser pulse duration and a bi-exponential decay.

that at this excitation energy the relaxation is due to efficient *interband* scattering on optical phonons of an energy of ~ 200 meV because direct *intra*band relaxation is strongly suppressed [cf. Figure 1(b)]. In contrast, for near-infrared excitation, *intra*band relaxation is the dominating relaxation channel. As the excitation energy is reduced to values below the optical-phonon energy, τ_2 is strongly increased to 14–25 ps. Additionally an even longer time scale of $\tau_3 = 300 \pm 50$ ps is observed, which was buried in the noise floor for $E = 245$ meV. Furthermore, we find an interesting temperature dependence: While for $E = 245$ meV both the maximum transmission change and the relaxation times depend only weakly on temperature, both quantities drop sharply with increasing temperature for $E = 72$ meV [cf. Figure 1(c) and 1(d)]. At room temperature the relaxation for $E = 72$ meV is equally fast as for $E = 245$ meV within the measurement accuracy.

To understand the involved relaxation dynamics more thoroughly, we use a microscopic theory [20] to calculate the relaxation dynamics of nonequilibrium carriers resolved in time, momentum, and angle. Within the density matrix formalism, we derive the graphene Bloch-equations [20–22] describing the momentum dependent carrier density $\rho_{\lambda k}$ (in the valence and conduction band), the microscopic polarization, and the phonon occupation number taking into account both optical and acoustic phonons at the Γ and K points. The Coulomb and the carrier-phonon interactions are considered using second order Born-Markov approximation resulting in a microscopic Boltzmann-like scattering equation with time and momentum dependent scattering rates and explicitly including Pauli blocking terms. To compare our microscopic results with the experiment, we approximate the differential transmission signal by the change of the carrier density in the optically excited state $\Delta \rho_{k_0}$ [23].

In accord with the experiment we find that the relaxation is significantly slowed down as the photon energy is reduced below the optical-phonon energy [Fig. 2(a)]. Also the calculated temperature dependence [Fig. 2(b) and 2(c)] confirms the experimental observations [Fig. 1(c) and 1(d)]. However, in contrast straight-forward expectations [24], optical phonons are still the dominant process for cooling the electronic system, even if the

TABLE I. Full width at half maximum of the FEL pulse and the decay components of the pump-probe signals measured at $T = 10$ K. For small photon energies, τ_1 is below the experimental time resolution.

E (meV)	τ_{pulse} (ps)	τ_1 (ps)	τ_2 (ps)	τ_3 (ps)
245	0.7	0.5 ± 0.1	5.2 ± 0.2	within noise
72	3	...	14.5 ± 1	300 ± 50
51	11	...	25 ± 2	300 ± 50
30	7	...	25 ± 2	300 ± 50

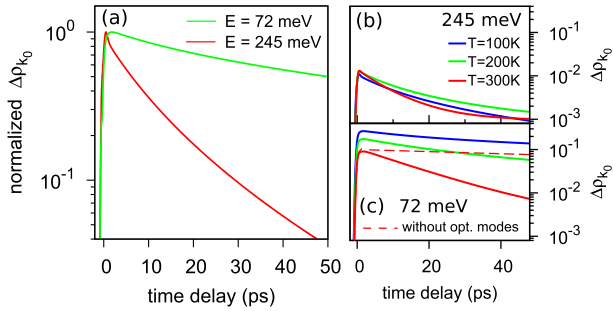


FIG. 2 (color online). Theory: Normalized change of the carrier density of optically excited states for different photon energies at 10 K (a). Temperature dependence of the relaxation dynamics at $E = 245$ meV (b) and $E = 72$ meV (c) for $T = 100, 200,$ and 300 K. The dashed line is calculated without optical-phonon modes illustrating their importance even at the low energy.

excitation energy is below the optical-phonon energy. This is illustrated in Fig. 2(c), where the curve for $T = 300$ K is also calculated with the optical-phonon contribution switched off. The reason for this is the strong carrier-carrier interaction in graphene which provides a hot carrier distribution on sub-ps time scales, allowing hot electrons to scatter efficiently with optical phonons. This is energetically possible because some fraction of the hot electrons have energies exceeding the optical-phonon energy. The scattering by acoustic phonons is slower and leads to a decay time $\tau_3 \approx 300$ ps, which is also consistent with the experiment. For $E = 245$ meV, the calculation reveals another feature seen in the experiment, namely, an initial fast time constant τ_1 . The microscopic calculation allows us to identify this contribution as Auger-type processes: the predominant impact excitation redistributes the energy of the excitation pulse to an increasing number of charge carriers leading to a fast cooling of the electronic system. Unlike the initial thermalization process, where only conduction band electrons are involved, the impact ionization transfers electrons from the valence band into the conduction band [20]. While the microscopic calculations give an excellent qualitative agreement with experimental results, the quantitative values at low temperature for τ_1 and τ_2 are by about a factor of 2 larger in the theory, which could be due to neglected non-Markov channels or scattering via defects. The experimentally observed effect of increased temperature on both the relaxation time and the maximum transmission change is stronger (especially for $E = 72$ meV) than in the calculation. One possible reason for this is the neglected momentum dependence in the electron-phonon coupling matrix elements and the phonon dispersion, which is here considered linear for acoustic phonons and constant for optical phonons. Furthermore, the role of the SiC substrate is only included via a global dielectric screening constant. The effects discussed here are expected to result in modified relaxation times

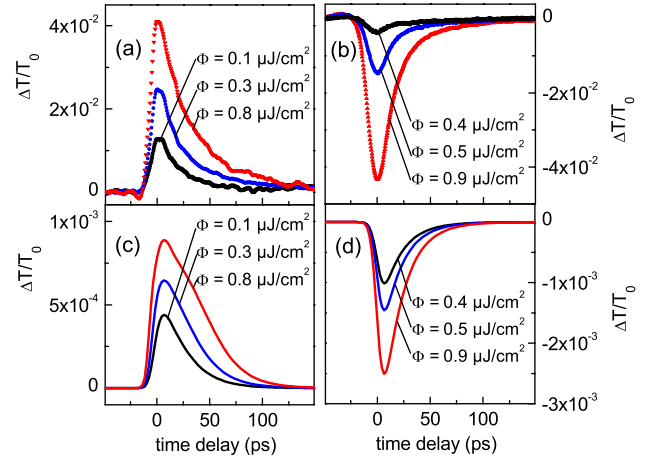


FIG. 3 (color online). Experimental pump-induced transmission change for three different fluences for the photon energy 30 meV (a) and 20 meV (b). Calculated pump-induced transmission of a single graphene layer for photon energies of 30 meV (c) and 20 meV (d) obtained with the simple model based on electron heating described in the text.

especially at elevated temperatures, where they become more prominent due to the broader thermal distribution.

Now we turn to discussing the carrier dynamics in the vicinity of $2E_f$ of the almost intrinsic graphene layers. As E is decreased from 30 to 20 meV, a striking change in the sign of the pump-probe signals is observed [Fig. 3(a) and 3(b)]. The positive pump-probe signal, i.e., pump-induced transmission, is caused by the bleaching of the interband transition (cf. right inset of Fig. 4) similar to the cases discussed above. If the photon energy becomes smaller than twice the value of the Fermi energy, this process is not possible anymore. However, the carrier distribution can be heated via free-carrier absorption. As a result, states for which interband absorption is possible get populated with electrons (or equivalently, depleted of

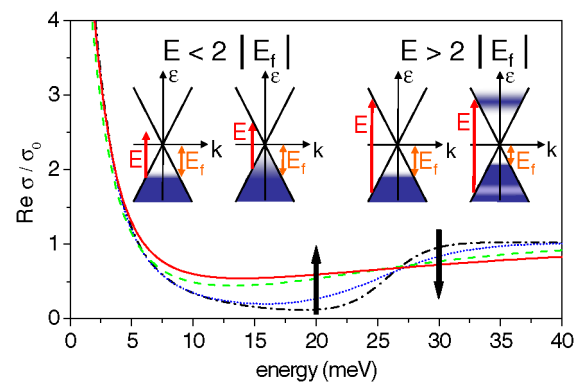


FIG. 4 (color online). The dynamic conductivity for different temperatures (black dash-dotted: 10 K, blue dotted: 20 K, green dashed: 50 K, and red solid: 100 K). The inset sketches the carrier distribution before and after the pump beam for $E < 2|E_f|$ and $E > 2|E_f|$.

holes) as indicated in the left inset of Fig. 4 [25]. Hence, pumping in this regime results in induced absorption. For a quantitative description, we consider the real part of the dynamic conductivity [10,26]

$$\begin{aligned} \text{Re}[\sigma(\omega)] = & \frac{8\sigma_0\tau k_B T_{\text{el}}}{\pi\hbar(\omega\tau + 1)} \ln[2 \cosh(-E_f/2k_B T_{\text{el}})] + \frac{\sigma_0}{2} \\ & \times \left[\tanh\left(\frac{\hbar\omega + 2E_f}{4k_B T_{\text{el}}}\right) + \tanh\left(\frac{\hbar\omega - 2E_f}{4k_B T_{\text{el}}}\right) \right]. \end{aligned} \quad (1)$$

Here $\sigma_0 = e^2/4\hbar$ is the “universal value” of the dynamic conductivity, T_{el} the carrier temperature and τ the momentum relaxation time. The first summand of Eq. (1) indicates intraband Drude absorption, the second one interband absorption. In Fig. 4 the dynamic conductivity is plotted for $E_f = -13$ meV and $\tau = 300$ fs. This value for the momentum relaxation time has been deduced from the linewidth in magneto-spectroscopy experiments [17]. Even at 10 K the Drude peak at low energies merges with the tail of the interband absorption; i.e., there is finite absorption at all energies. The arrows indicate the increase (decrease) of the absorption with increasing temperature for the photon energy 20 meV (30 meV).

For comparison with the experimental data of Fig. 3(a) and 3(b) we consider heating and relaxation of the electron distribution via the equation $dT_{\text{el}}/dt = P(t)/c_p - (T_{\text{el}} - T_{\text{latt}})/\tau_2$, where $P(t) = I(t)\text{Re}[\sigma(T_{\text{el}})]/\epsilon_0 c$ is the absorbed power per area (I , laser intensity; c , speed of light), c_p the specific heat [27], and $\tau_2 = 25$ ps a phenomenological energy relaxation time (see Table I). This simple model cannot account for the full dynamics; however, it contains the most important processes, since, at the time scales relevant here, a thermalized carrier distribution can be expected. The calculated transmission changes for a single graphene layer are plotted in Fig. 3(c) and 3(d). The model captures the experimentally observed sign reversal. The agreement with the experiment is best for $|E_f| = 13 \pm 2$ meV. From magneto-spectroscopy experiments of samples grown with the same method $|E_f| = 8$ meV has been concluded [17]. We note that the interplay of interband and intraband processes has been suggested recently to explain a change in sign of the pump-probe signal as pump fluence is varied in a UV-pump near-infrared-probe experiment [28].

In summary, we have studied the relaxation dynamics of carriers in graphene close to the Dirac point. A slowing down of relaxation has been observed for energies below the optical-phonon energy, but optical phonons still play an important role, as shown through microscopic calculations. The theoretical description of the results shows that the interplay of electron-electron and electron-phonon scattering produce new and efficient relaxation channels in situations when both intraband and interband relaxation are allowed, as they are in many narrow or vanishing gap

systems. Most remarkably, the sign of the pump-probe signal is inverted, as the photon energy is varied across the value of $2E_f$. This behavior can be understood by the interplay between inter- and intraband absorption and, besides being a fascinating behavior by itself, it allows a rather accurate determination of the Fermi energy. Furthermore the effect can be the basis of innovative THz optical switches and active filters.

We thank F. Peter, M. Mittendorff, O. Drachenko, D. Stehr, and W. Seidel for friendly collaboration. Support from the German Science Foundation DFG in the framework of the Priority Program 1459 Graphene and from GACR via Grants No. P204/10/1020 and No. GRA/10/E006 is gratefully acknowledged. The research at the free-electron laser FELBE was supported by the European Community's Seventh Framework Programme (FP7/2007-2013) under Grant agreement No. 226716. We are grateful to P. Michel and the FELBE team for their dedicated support.

*Electronic address: s.winnerl@hzdr.de

- [1] F. Bonaccorso *et al.*, *Nat. Photon.* **4**, 611 (2010).
- [2] J.M. Dawlaty *et al.*, *Appl. Phys. Lett.* **92**, 042116 (2008).
- [3] P. Plochocka *et al.*, *Phys. Rev. B* **80**, 245415 (2009).
- [4] H. Wang *et al.*, *Appl. Phys. Lett.* **96**, 081917 (2010).
- [5] M. Breusing, C. Ropers, and T. Elsaesser, *Phys. Rev. Lett.* **102**, 086809 (2009).
- [6] D. Sun *et al.*, *Phys. Rev. Lett.* **101**, 157402 (2008).
- [7] R.W. Newson *et al.*, *Opt. Express* **17**, 2326 (2009).
- [8] D. Sun *et al.*, *Phys. Rev. Lett.* **104**, 136802 (2010).
- [9] P.A. George *et al.*, *Nano Lett.* **8**, 4248 (2008).
- [10] H. Choi *et al.*, *Appl. Phys. Lett.* **94**, 172102 (2009).
- [11] F. Xia *et al.*, *Nature Nanotech.* **4**, 839 (2009).
- [12] G.C. Xing *et al.*, *Opt. Express* **18**, 4564 (2010).
- [13] C. Berger *et al.*, *J. Phys. Chem. B* **108**, 19912 (2004).
- [14] J. Hass *et al.*, *Phys. Rev. Lett.* **100**, 125504 (2008).
- [15] A.C. Ferrari *et al.*, *Phys. Rev. Lett.* **97**, 187401 (2006).
- [16] M.L. Sadowski *et al.*, *Phys. Rev. Lett.* **97**, 266405 (2006).
- [17] M. Orlita *et al.*, *Phys. Rev. Lett.* **101**, 267601 (2008).
- [18] U. Lehnert *et al.*, in *Proc. 29th International FEL Conference, Novosibirsk, Russia, 2007*, edited by B. Goldenberg, V. Eliseev, A. Zhirkova, and P. Budz (unpublished), <http://accelconf.web.cern.ch/AccelConf/f07/PAPERS/MOPPH036.PDF>.
- [19] No experiments could be performed in the range from 100 to 200 meV due to the reststrahlenband of the SiC substrate.
- [20] T. Winzer, A. Knorr, and E. Malic, *Nano Lett.* **10**, 4839 (2010).
- [21] M. Lindberg and S.W. Koch, *Phys. Rev. B* **38**, 3342 (1988).
- [22] S. Butscher *et al.*, *Appl. Phys. Lett.* **91**, 203103 (2007).

- [23] M. Breusing *et al.*, *Phys. Rev. B* **83**, 153410 (2011).
- [24] V. Ryzhii, M. Ryzhii, and T. Otsuji, *J. Appl. Phys.* **101**, 083114 (2007).
- [25] This is for *p* type doping. For *n* type, states in the conduction band get depleted of electrons. The type of doping can not be determined by our experiments and does not affect the interpretation.
- [26] S. A. Mikhailov and K. Ziegler, *Phys. Rev. Lett.* **99**, 016803 (2007).
- [27] We apply the value of 1.3×10^{-6} J/(K m²) in accordance with experimental and theoretical studies of graphite at 10 K, see T. Nihira and T. Iwata, *Phys. Rev. B* **68**, 134305 (2003).
- [28] L. M. Malard *et al.*, arXiv:1104.3104.

Coherent control of a THz intersubband polarization in a voltage controlled single quantum well

M. Wagner,^{1,a)} M. Helm,¹ M. S. Sherwin,² and D. Stehr¹

¹*Institute of Ion Beam Physics and Materials Research, Helmholtz-Zentrum Dresden-Rossendorf, P.O. Box 510119, 01314 Dresden, Germany*

²*Physics Department, University of California Santa Barbara, Santa Barbara, California 93106, USA*

(Received 28 July 2011; accepted 12 September 2011; published online 28 September 2011)

Ultrashort terahertz pulses in the far-infrared spectral region centered around 2 THz are used to coherently control an intersubband polarization in a GaAs/AlGaAs quantum well structure at low temperature. While the first pulse excites a macroscopic polarization, a second temporally delayed pulse switches the polarization off or refreshes it depending on the relative time delay. The switching is directly demonstrated in the time-domain for the few picosecond long free-induction decay of the induced polarization. Model calculations based on the optical Bloch equations agree well with the experimental data. © 2011 American Institute of Physics. [doi:10.1063/1.3644988]

In linear spectroscopy, broadband incoherent and hence intensity-sensitive techniques based on interferometers or dispersive spectrometers give access to transmission or reflection spectra. In contrast, time domain spectroscopy is sensitive to the amplitude and phase of the individual pulses. Using two consecutive phase-locked pulses, coherent optical material properties can be probed and even manipulated, i.e., coherent control with the final goal of ultrafast all-optical switching of quantum states becomes possible. To this end, the relative time delay between pump and control pulses as well as the individual pulse lengths have to be much shorter than the dephasing time. Consequently, the dynamics is strongly dependent on this relative time delay and the phase of the control pulse. For near-infrared (NIR) light pulses, different semiconductor excitations and processes have been switched coherently, such as photocurrents,¹ exciton population and polarization,^{2,3} electron-phonon scattering,⁴ or a single quantum dot excitation.⁵

A variety of material excitations such as phonons, magnons, polaritons, and intersubband transitions in quantum heterostructures lie in the few meV or terahertz (THz) spectral region. Here, coherent control has been demonstrated, for instance, for intra-donor transitions in doped silicon⁶ or directly with electric field resolution for NIR excited quantum beats in a coupled quantum well (QW).⁷ Recently, also ultrafast coherent switching of spin waves has been shown⁸ using the magnetic field of an intense THz pulse. THz intersubband transitions⁹ between confined QW states are very promising for coherent control due to their large transition matrix element, their picosecond long dephasing times, and the flexibility in the material system of the QW whose charge state can be controlled via electrical gates. Intersubband dephasing times, the involved broadening mechanisms and the polarization dynamics are important parameters for coherent THz switching and have been investigated in several studies.^{10,13–15,17,18} Eickemeyer *et al.*¹⁹ demonstrated coherent control in the time domain of an intersubband polarization in a GaAs multiple QW using $\lambda = 12.5 \mu\text{m}$

mid-infrared light pulses. In that study, the field-resolved dynamics were extracted by comparison with an undoped reference sample of the same geometry assuming that the THz beam path is identical for the sample and the reference. It has been demonstrated that the inherently phase-locked pulses in THz time domain systems represent a perfect tool for coherent control.

Here, we make use of few-cycle THz pulses to switch the THz induced polarization around 2 THz in a single, doped GaAs QW. By applying a gate voltage at a Schottky contact, the QW can be filled or depleted, directly enabling us to measure the difference in the transmitted electric field. This gives direct access to the polarization free-induction decay as electric field oscillations in the time domain.

300 fs short THz pulses are generated via optical rectification of NIR pulses in a 200 μm thin (110) oriented GaP crystal. Standard electro-optic sampling (eos) in a second 300 μm thin GaP crystal directly monitors the electric-field transients.²⁰ The NIR laser source used both for THz generation and sampling is a regenerative amplifier (Coherent: RegA) delivering 32 fs short pulses with a repetition rate of 250 kHz. The NIR beam is split into three parts: two intense parts are used for THz generation, while the smaller part is used for detection (see Fig. 1(a)). Hence, two NIR pulses with an adjustable time delay in between are incident on the same nonlinear emitter crystal resulting in two THz pulses with a fixed relative phase that comprise the pump and control pulses for the switching experiment. The NIR probe beam is led over a mechanical delay line before it is

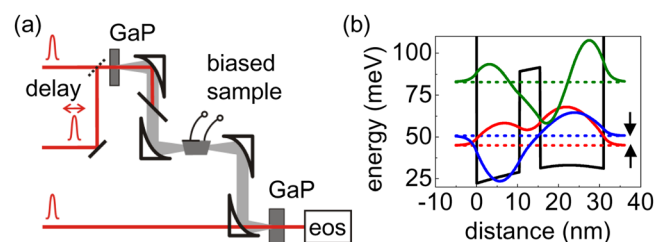


FIG. 1. (Color online) (a) Experimental setup. Two time delayed NIR pulses generate the THz pump and control pulses in GaP and are detected via eos. (b) QW band structure with the first three levels and wavefunctions.

^{a)}Author to whom correspondence should be addressed. Electronic mail: m.wagner@hzdr.de.

recombined with the THz generation path. A typical NIR pulse energy for optical rectification is $0.8 \mu\text{J}$, resulting in broadband pulses centered at the sample's intersubband resonance around 2 THz. The free-space peak electric field strength around the QW absorption line for the few-cycle THz pulses incident on the sample is estimated to be around 0.3 kV/cm , well within the linear regime where an occupation of the upper state and nonlinear behavior^{11,12} is negligible. The generated THz pulses are separated from the NIR rectification pulses by a high resistivity Si wafer and pass through the sample in the cryostat. Instead of comparing a doped sample and an undoped reference one, we extract the intersubband response directly by modulating the charge density with a gate.¹³ When the QW is charged, a THz pulse excites a coherent optical intersubband polarization between the $n = 1$ and $n = 2$ conduction band states in the QW, which are shown in Fig. 1(b) in a self-consistently calculated band diagram of the QW. The induced polarization decays subsequently as free-induction decay (FID), and THz radiation is emitted parallel to the incident beam. Applying a bias modulation at a frequency of 4.6 kHz and, thus, filling and emptying the QW periodically for lock-in detection allows for measuring the FID signal, i.e., the derivative of the induced polarization, directly in the time domain.

The sample consists of a modulation doped 31 nm wide GaAs QW structure that represents also the back contact while an Aluminum Schottky contact forms the top gate. The barriers are made of $\text{Al}_{0.33}\text{Ga}_{0.67}\text{As}$, and a 5 nm thin $\text{Al}_{0.075}\text{Ga}_{0.925}\text{As}$ layer is placed in the well. The wafer has been processed in a 70° wedged waveguide geometry with a single internal THz reflection at the semiconductor metal interface. While the Schottky contact ensures an effective overlap of QW and THz mode, the THz polarization is oriented in QW growth direction to allow for a coupling of light to the intersubband transition.⁹ The sample is mounted in a liquid-He flow cryostat which is equipped with diamond windows that guarantee broadband THz transmission at low dispersion. The experiment is performed at 10 K, and the experimental setup is purged with nitrogen gas to prevent water vapor absorption.

The intersubband transition is widely tunable from 1.65 THz to 5.5 THz for different applied biases via the quantum confined Stark effect.¹⁶ Data shown here are all taken at a voltage of -0.2 V , where the transition lies at 2 THz and where C-V measurements give a charge density of $2.2 \times 10^{11} \text{ cm}^{-2}$. Figure 2(a) illustrates the generated amplitude spectrum of the GaP emitter, spanning one octave up to 7 THz and covering the intersubband absorption that is given in Fig. 2(b). The Lorentzian shaped line has a FWHM of $\Gamma = 0.22 \text{ THz}$. It was calculated from the Fourier transforms of the difference in the transmitted electric fields, i.e., the FID signal $\Delta E(\omega)$, and the transmitted reference field $E_{\text{ref}}(\omega)$ according to $\alpha(\omega) = I_{\text{abs}}(\omega)/I_{\text{ref}}(\omega) \approx -2\text{Re}[\Delta E(\omega)/E_{\text{ref}}(\omega)]$. The imaginary part $\text{Im}[\Delta E(\omega)/E_{\text{ref}}(\omega)]$ is given in the lower panel, along with the Lorentz oscillator model fit that is in good agreement with the measurement which indicates a homogeneous broadening.

First, the pure FID signal is investigated after single THz pulse excitation in Fig. 3(a). The incident THz pulse temporally shifted²¹ is illustrated in the upper panel, while

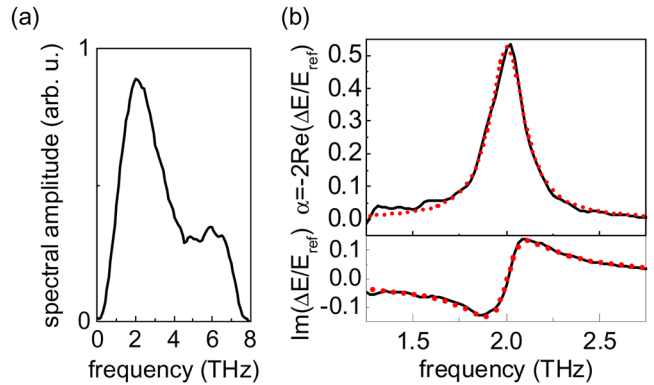


FIG. 2. (Color online) (a) Broadband GaP emission spectrum. (b) QW absorption with Lorentzian fit (dotted red line) and imaginary, i.e., reactive part of the response.

the reemitted FID oscillation as time derivative of the induced intersubband polarization is given below as solid line. After the exciting THz pulse has vanished, a long decay is observed with a decay time constant of 1.5 ps. The red dotted line is a model calculation based on the optical Bloch equations. The calculation assumes a negligible population of the excited level which is justified by the small electric peak field strength. As input field, the incident pulse without sample is taken. Dispersion that is introduced by the sample is then included in the calculation. For the single pulse FID signal, we find an excellent agreement between experiment and theory.

After the single pulse excitation, a second THz pulse is employed as a control pulse in order to modify the FID transient. The control pulse amplitude is chosen as half the amplitude of the first pump pulse. At a time delay of 1.94 ps in Fig. 3(b), we observe an identical rise of the FID signal compared to the single pulse excitation before. However, the measured transient differs from the single polarization decay beyond 3.5 ps. The control pulse now refreshes the polarization resulting in an overshoot in the FID transient before its subsequent decay. This behavior is in excellent agreement with the calculation. Note that the constructive refreshing requires a control pulse time delay of an even number of THz intersubband half-cycles.

Decreasing the time delay between pump and control pulses to 1.27 ps, i.e., an odd number of THz intersubband half-cycles, gives a polarization decay signal as shown in Fig. 3(c). Again, after an identical rise as observed before, the signal decays with a time constant of 1.5 ps. However, at a time step of 4 ps where the single pulse FID transient is still present, the second THz pulse suppresses the polarization completely. It has been switched off totally and does not recover afterwards as is confirmed by the simulation. Note that the incident pump and control pulses are sufficiently apart in time, so that the induced polarization switch off is not due to an interference of the incident fields but due to a switching of the polarization that is still radiating when the incident pulse has passed.

For any other delay in between these two extremes, the polarization is not entirely suppressed, but can be amplified. Additionally, changing the control pulse amplitude leads also to a refreshing or total suppression, respectively, of the FID, but now at different time delays.

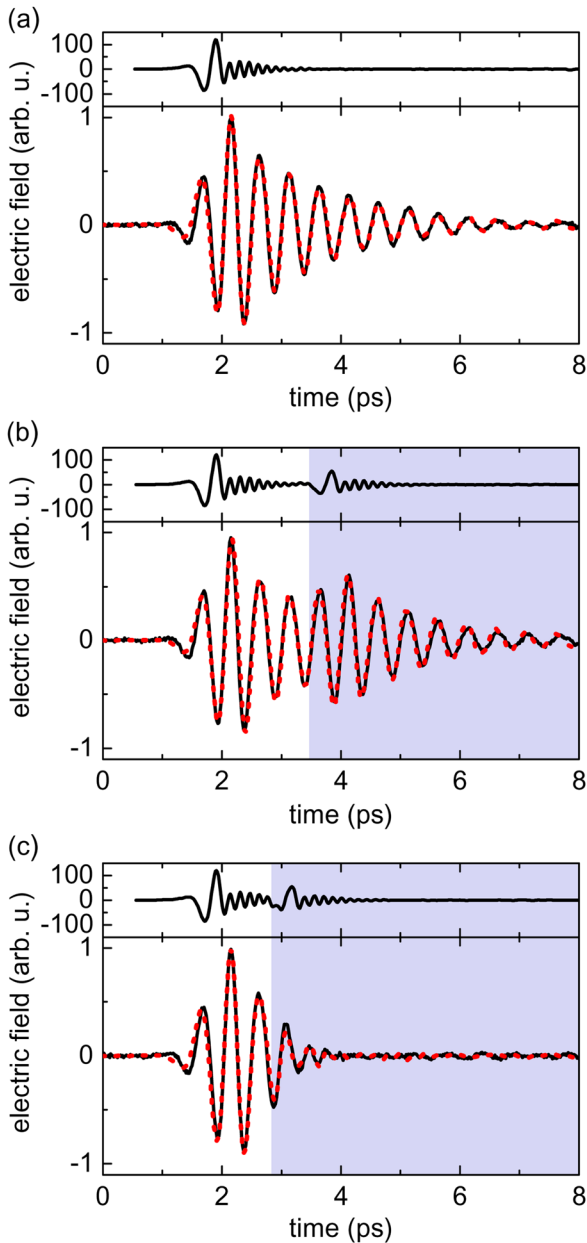


FIG. 3. (Color online) Incident THz pulse shifted in time (top panel) and induced FID (bottom panel). The red dotted line is a simulation based on the optical Bloch equations. (a) FID after a single pulse excitation. (b) Coherent refreshing of the intersubband polarization with a second THz control pulse after 1.94 ps. (c) Coherent polarization switch off for a control pulse delayed by 1.27 ps.

In conclusion, we have demonstrated coherent control of a macroscopic polarization in a single QW structure. To this end, an intersubband polarization was excited using a

THz pulse, while a second time-delayed THz pulse either switches the polarization off totally or refreshes it constructively. Both cases have been observed directly in the time-domain in the free-induction decay of the induced polarization and within a time interval where the polarization did not decay entirely, i.e., a few picoseconds. Given that only a single voltage controlled QW has been employed, the system could be attractive for future devices where all-optical coherent manipulations in the THz spectral region is necessary.

The authors thank K. Campman and A. C. Gossard for sample growth and C. Morris for processing the sample.

- ¹A. Haché, Y. Kostoulas, R. Atanasov, J. L. P. Hughes, J. E. Sipe, and H. M. van Driel, *Phys. Rev. Lett.* **78**, 306 (1997).
- ²A. P. Heberle, J. J. Baumberg, and K. Köhler, *Phys. Rev. Lett.* **75**, 2598 (1995).
- ³D. S. Yee, K. J. Yee, S. C. Hohng, D. S. Kim, T. Meier, and S. W. Koch, *Phys. Rev. Lett.* **84**, 3474 (2000).
- ⁴M. U. Wehner, M. H. Ulm, D. S. Chemla, and M. Wegener, *Phys. Rev. Lett.* **80**, 1992 (1998).
- ⁵N. H. Bonadeo, J. Erland, D. Gammon, D. Park, D. S. Katzer, and D. G. Steel, *Science* **282**, 1473 (1998).
- ⁶P. T. Greenland, S. A. Lynch, A. F. G. van der Meer, B. N. Murdin, C. R. Pidgeon, B. Redlich, N. Q. Vinh, and G. Aeppli, *Nature* **465**, 1057 (2010).
- ⁷P. C. M. Planken, I. Brener, M. C. Nuss, M. S. C. Luo, and S. L. Chuang, *Phys. Rev. B* **48**, 4903 (1993).
- ⁸T. Kampfrath, A. Sell, G. Klatt, A. Pashkin, S. Mährlein, T. Dekorsy, M. Wolf, M. Fiebig, A. Leitenstorfer, and R. Huber, *Nature Photon.* **5**, 31 (2011).
- ⁹M. Helm, in *Intersubband Transitions in Quantum Wells: Physics and Device Applications*, 1st ed., edited by H. C. Liu and F. Capasso (Academic, New York, 2000), pp. 1–99.
- ¹⁰A. Bonvalet, J. Nagle, V. Berger, A. Migus, J.-L. Martin, and M. Joffe, *Phys. Rev. Lett.* **76**, 4392 (1996).
- ¹¹C. W. Luo, K. Reimann, M. Woerner, T. Elsaesser, R. Hey, and K. H. Ploog, *Phys. Rev. Lett.* **92**, 047402 (2004).
- ¹²S. Leinß, T. Kampfrath, K. v. Volkman, M. Wolf, J. T. Steiner, M. Kira, S. W. Koch, A. Leitenstorfer, and R. Huber, *Phys. Rev. Lett.* **101**, 246401 (2008).
- ¹³J. N. Heyman, R. Kersting, and K. Unterrainer, *Appl. Phys. Lett.* **72**, 644 (1998).
- ¹⁴R. A. Kaindl, S. Lutgen, M. Woerner, T. Elsaesser, B. Nottelmann, V. M. Axt, T. Kuhn, A. Hase, and H. Künzel, *Phys. Rev. Lett.* **80**, 3575 (1998).
- ¹⁵R. Kersting, R. Bratschitsch, G. Strasser, K. Unterrainer, and J. N. Heyman, *Opt. Lett.* **25**, 272 (2000).
- ¹⁶D. A. B. Miller, D. S. Chemla, T. C. Damen, A. C. Gossard, W. Wiegmann, T. H. Wood, and C. A. Burrus, *Phys. Rev. Lett.* **53**, 2173 (1984).
- ¹⁷R. A. Kaindl, K. Reimann, M. Woerner, T. Elsaesser, R. Hey, and K. H. Ploog, *Phys. Rev. B* **63**, 161308 (2001).
- ¹⁸R. Ascazubi, O. C. Akin, T. Zaman, R. Kersting, and G. Strasser, *Appl. Phys. Lett.* **81**, 4344 (2002).
- ¹⁹F. Eickemeyer, M. Woerner, A. M. Weiner, T. Elsaesser, R. Hey, and K. H. Ploog, *Appl. Phys. Lett.* **79**, 165 (2001).
- ²⁰Q. Wu and X.-C. Zhang, *Appl. Phys. Lett.* **70**, 1784 (1997).
- ²¹The incident THz pulse was measured without cryostat. Here, it is shifted in time to overlap with the reference pulse that is transmitted through the cryostat and affected by material dispersion.

Photoluminescence dynamics in GaAs/AlGaAs quantum wells under pulsed intersubband excitation

S. Zybell,^{1,a)} H. Schneider,¹ S. Winnerl,¹ M. Wagner,¹ K. Köhler,² and M. Helm¹

¹Helmholtz-Zentrum Dresden-Rossendorf (HZDR), P.O. Box 51 01 19, 01314 Dresden, Germany

²Fraunhofer-Institut für Angewandte Festkörperphysik, 79108 Freiburg, Germany

(Received 6 April 2011; accepted 1 July 2011; published online 25 July 2011)

We investigate the time-resolved photoluminescence (PL) dynamics of an undoped GaAs/AlGaAs multiple quantum well under mid-infrared (MIR) irradiation. A time-delayed MIR laser pulse from a free-electron laser, tuned to the intersubband transition energy of the quantum well, induces temporal quenching of the PL intensity with subsequent recovery. The experimental data can be accurately described by a simple rate-equation model, which accounts for the cooling of the non-radiative states to radiative states. By performing polarization sensitive measurements, we are able to discriminate the contributions of free-carrier absorption from that of intersubband absorption, where the latter is about 50 times more efficient. © 2011 American Institute of Physics. [doi:10.1063/1.3615298]

The cooling of an electron-hole plasma and the formation of excitons after nonresonant optical excitation of a quantum well (QW) has been the topic of numerous experimental and theoretical studies, since these processes are important for applications in optoelectronics. While many aspects of carrier dynamics manifest themselves in the time evolution of the photoluminescence (PL), there are also *hidden* parameters due to the presence of dark states which do not contribute to the PL because of momentum and spin selection rules.^{1–6} A prominent signature of the presence of dark states is the long rise time (up to several hundreds of ps) of the PL at low temperatures. While early papers concluded that excitons are formed within 10–20 ps and the slow PL rise is caused by momentum relaxation,¹ later works suggested much longer exciton formation times of several 100 ps up to 1 ns.^{2–4} A related question is, up to which carrier density the excitonic picture is dominant and at which point a description as an (electrically conductive) electron-hole plasma is more appropriate.^{5,6} The discussion culminated in the question whether the presence of PL at the exciton energy is an absolute evidence for the existence of excitons.^{6–9} Another complication is the presence of multiple *dark* excitons in addition to the high-momentum ones, which include the heavy-hole exciton with parallel spins ($j = \pm 2$) and certain excited states (like the 2p-exciton). In order to shed more light into this discussion, terahertz absorption of the 1s-2p transition has been used to prove the existence of excitons.^{9,10} Another option is to excite the carriers by an additional optical pulse in order to obtain further signatures associated with the carrier redistribution. An interesting step in this direction has been the work by Amo *et al.*¹¹ who applied two time-delayed interband excitation pulses. In fact, the second pulse was observed to cause PL quenching (in spite of the generation of additional carriers), followed by PL recovery and enhanced PL emission as compared to the PL without the second pulse. In earlier publications, reporting on the suppression of time-integrated PL from undoped QWs by far-infrared radiation,^{12,13} the carrier dynamics has

been discussed based on the picture that the excited carriers in the QW relax to the low momentum states where they form excitons and recombine radiatively.

In this letter, we study the PL dynamics in undoped GaAs/AlGaAs QWs by applying an additional time-delayed mid-infrared (MIR) pulse from the free-electron laser (FEL) source FELBE at Helmholtz-Zentrum Dresden-Rossendorf, causing intraband excitation of the carriers in the QWs. The MIR pulse is tuned to the fundamental electron intersubband transition energy, such that the excitons and the electron-hole plasma are redistributed into a hot-carrier population. As the MIR pulses were much shorter (~ 2 ps) than the PL recovery time, the time-resolved PL exhibits a clear sharp dip at the arrival time of the MIR pulse. After the quench, the PL recovers to an intensity slightly higher than that for the unperturbed case. In this way, a direct analysis of the carrier dynamics is possible, since no carriers are newly injected. Furthermore, the fast quenching of the PL allows for accurate monitoring and controlling of the timing of infrared and terahertz radiation pulses from accelerator based sources with respect to near-infrared (NIR) pulses from table-top sources. This has already been applied at FELBE for finding the temporal overlap which is essential for experiments like THz-sideband generation.¹⁴ In the present work, we discuss the quenching of the PL and its subsequent recovery as a function of MIR fluence.

The measurements were performed on a multiple quantum well (MQW) sample that consists of 40 undoped GaAs wells (thickness 6 nm) separated by 15 nm thick Al_{0.35}Ga_{0.65}As barriers grown by molecular-beam epitaxy. For these parameters, there are two bound states in the conduction band. All measurements were performed at a lattice temperature of 10 K while keeping the sample in an optical cryostat. The Ti:sapphire laser pulse repetition rate was reduced to 13 MHz by an acousto-optic modulator and synchronized to the quasi-continuous pulse train of the FEL by using a commercial synchronization unit locked to the FEL clock signal. The picosecond laser pulses at a photon energy of 1.635 eV created a free carrier density of approximately $5 \times 10^{10} \text{ cm}^{-2}$ per well in the MQW structure via interband excitation. The

^{a)}Electronic mail: s.zybell@hzdr.de.

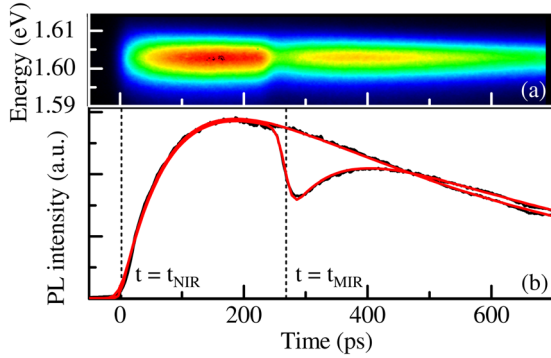


FIG. 1. (Color online) (a) A typical streak camera image under FEL irradiation. (b) Experimental and calculated PL transients showing a PL quenching dip at $t = t_{\text{MIR}}$. The curves without the dip are reference traces with the same MIR fluence ($7 \mu\text{J}/\text{cm}^2$).

delay t_{MIR} between the NIR and MIR pulses was tuned by means of mechanical delay units. The measurements were performed at a FEL wavelength of $7.2 \mu\text{m}$ (172 meV), which is resonant to the intersubband transition energy of the QWs. The resulting PL is detected by a streak camera attached to a grating spectrometer allowing for spectrally and temporally resolved measurements (see Fig. 1(a)). The PL peak is observed at 1.604 eV with a linewidth (FWHM) of 8 meV. The PL transient in presence of quenching is compared with a reference curve measured under similar conditions. To account for the lattice heating caused by the average FEL power, the reference transient was measured also under MIR irradiation but the arrival time of the MIR pulse was shifted out of the time window of the streak image. Figure 1(b) shows a typical PL transient at its spectral maximum for the reference signal and with MIR excitation with a MIR fluence of $7 \mu\text{J}/\text{cm}^2$. Here, the carrier redistribution caused by the MIR pulse induces a sharp drop of the PL intensity followed by a recovery which slightly overshoots the reference trace. The time-integrated PL, however, remains the same in this intensity regime. This implies that the PL intensity overshoot after the dip compensates the PL quench perfectly, indicating negligible carrier losses due to nonradiative channels. This observation complements earlier studies^{12,13} which were only sensitive to the time-integrated PL and thus corresponded to a different intensity regime.

In order to quantify the PL quenching and the PL recovery after the quench, we apply a model based on rate equations with two effective levels. The PL intensity is proportional to the occupation number of the radiative state $n_r(t)$ with zero momentum $k=0$ as a function of time t . The carriers recombine radiatively with a PL decay time of τ_{PL} . The dimensionless parameter $n_{\text{nr}}(t)$ denotes the occupation number of the non-radiative states, i.e., dark excitons and free carriers. This approach is based on the assumption that the PL risetime is solely determined by carrier cooling and that exciton formation, which would be described by bimolecular formation,^{3,4} does not influence the PL dynamics at the investigated time scale. We get two coupled rate equations for the dynamics of the non-radiative and radiative state occupation number $n_{\text{nr}}(t)$ and $n_r(t)$:

$$\frac{dn_{\text{nr}}}{dt} = -\frac{1}{\tau_c} n_{\text{nr}}, \quad \frac{dn_r}{dt} = -\frac{1}{\tau_{\text{PL}}} n_r + \frac{1}{\tau_c} n_{\text{nr}},$$

where τ_c is the cooling time of the carriers from the non-radiative to the radiative state. At the arrival time of the NIR pulse, defined as $t=0$, the occupation numbers of the radiative and non-radiative states are $n_r(0)=0$ and $n_{\text{nr}}(0)=1$, respectively. Thus, the solution of the rate equations in this regime I is $n_{\text{nr}}^{\text{I}}(t) = e^{-\frac{t}{\tau_c}}$ and $n_r^{\text{I}}(t) = \tau_{\text{PL}}(e^{-\frac{t}{\tau_{\text{PL}}}} - e^{-\frac{t}{\tau_c}})(\tau_{\text{PL}} - \tau_c)^{-1}$. At the arrival time of the MIR pulse $t=t_{\text{MIR}}$, the population is transferred from the radiative effective level to the nonradiative one and the rate equations are solved in this regime II with different initial conditions $n_{\text{nr}}^{\text{II}}(t_{\text{MIR}}) = n_{\text{nr}}^{\text{I}}(t_{\text{MIR}}) + qn_r^{\text{I}}(t_{\text{MIR}})$. The introduced quenching parameter q , where $0 \leq q \leq 1$, is a measure of the dip depth and shows the fraction of radiative carriers excited due to the MIR pulse. The function applied to fit the experimental data is $C n_r(t) \otimes G(\sigma, t)$, i.e. a convolution of the occupation number of the radiative state with a Gaussian $G(\sigma, t)$, which accounts for the laser pulse length and the jitter of the laser synchronization. The time resolution of our experimental setup is about 25 ps. The constant C is an amplitude scaling factor. The model fits to the experimental data very well. Best fit was achieved for all MIR fluences if the PL rise time (τ_c^{I}) was the same as the PL recovery time after the quenching (τ_c^{II}). One example is shown in Fig. 1(b), where the values of the fitted parameter are $q = 0.53$, $\tau_c = 85$ ps, $\tau_{\text{PL}} = 540$ ps, and $t_{\text{MIR}} = 270$ ps.

Several groups have reported on exciton formation times. Szczytko *et al.*^{3,4} have proposed exciton formation times of less than 10 ps in InGaAs QW for a photon density of 3×10^{11} photons/cm², leading to slightly smaller carrier densities than in our present experiment. This implies that the observed PL recovery after the PL quench in our experiment accounts for the cooling of the hot excitons rather than exciton formation. This interpretation is further supported by the observations that (1) the observed time evolution of both the PL rise and the PL recovery is in extremely good agreement with our fit functions and that (2) we could not find any evidence for an additional dynamic component which would be produced if both exciton formation and relaxation were processes with comparable time constants. We also point out that our interpretation is consistent with recent terahertz absorption studies,⁹ according to which a major part of the carriers ($\sim 40\%$) forms excitons immediately after their excitation in spite of the much slower rise of the PL. The remaining carriers form excitons at such long delays that the related signatures cannot be easily discriminated from the PL decay.

In the following section, the physical mechanism of the PL quenching is discussed. Free carrier absorption and intersubband transitions are two competing processes that take place under MIR excitation. This causes an abrupt drop of the radiative zero momentum state $k=0$ population resulting in an ultrafast quenching of the PL. Due to the selection rules,¹⁵ intersubband transitions are expected only for p-polarization while free carrier absorption is expected for both polarization directions. For polarization sensitive measurements the delayed MIR laser pulse was coupled into the sample via a polished 45° facet in order to obtain an electric field component perpendicular (p-polarization) or parallel (s-polarization) to the QW plane. A schematic of this waveguide geometry is shown in the inset of Fig. 2. The relative quenching $q(\Phi_{\text{MIR}})$ is plotted in Fig. 2 for a delay of 270 ps

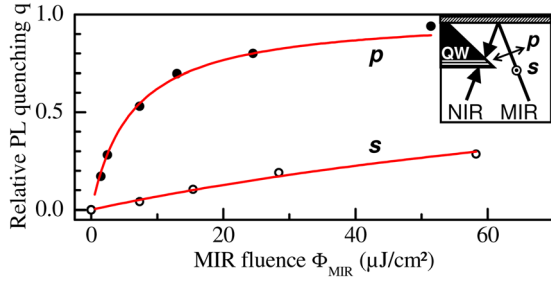


FIG. 2. (Color online) Relative PL quenching as a function of MIR fluence for p-polarized (solid dots) and s-polarized (open dots) MIR pulses. Both the plots show saturation behaviour at high MIR fluence. The lines are the fitting curves of the data points. The inset shows a schematic of the measurement geometry for coupling the p- and s-polarized MIR radiation to the 45° facet of the sample.

between the two laser pulses. It shows an initial linear increase with p- (s-)polarized MIR fluence (Φ_{MIR}) which eventually saturates at $\Phi_{\text{sat}} = 6 \mu\text{J}/\text{cm}^2$ ($140 \mu\text{J}/\text{cm}^2$) as deduced from the general saturation fit $q(\Phi_{\text{MIR}}) = (1 + \Phi_{\text{sat}}/\Phi_{\text{MIR}})^{-1}$. Taking a pulse width of 1.6 ps (Ref. 16) and reflectivity losses at the sample surface of 22% (36%) for p- (s-) polarized light, we obtain a saturation intensity of 3 MW/cm² (56 MW/cm²). Considering the geometry of the facet (only one third of the p-polarized light intensity has an electric field component perpendicular to the QW plane), we get a saturation intensity of 1 MW/cm² for the intersubband absorption, which is comparable to published values for GaAs/AlGaAs QWs.¹⁷

The carrier cooling times and the PL decay times are strongly influenced by the lattice temperature (T_L). This is attributed to the fact that for higher lattice temperatures, the increased phonon densities causes faster cooling of the excited carriers leading to smaller τ_c . The PL decay times increase with increasing temperature due to the broad distribution to high k values and the lower exciton formation efficiency. The cooling time and the PL decay time obtained from our measurements were found to depend linearly on the MIR fluence (see Fig. 3). However, the PL spectra showed negligible redshift with increased MIR intensities indicating a lattice heating effect of less than 50 K. In order to quantify this heating due to the MIR pulse, we compare the data with another set of PL measurements taken at different lattice temperatures T_L without any MIR excitation. τ_c and τ_{PL} for the maximum MIR fluence of $51 \mu\text{J}/\text{cm}^2$, corresponding to an average power of 210 mW, were found to match those for a lattice temperature of about 28 K.

In conclusion, we observed time-resolved PL quenching in undoped QWs using MIR pulses resonant to the intersubband transition energy. Fitting a rate-equation based function to the measured PL transients, we obtained the strength of the PL quenching, the PL rise time, the PL recovery time, and the PL decay time as a function of MIR fluence. Our results point to the interpretation that the rise and recovery of the PL intensity are dominated by relaxation of excitons towards radiative zero-momentum states, whereas exciton

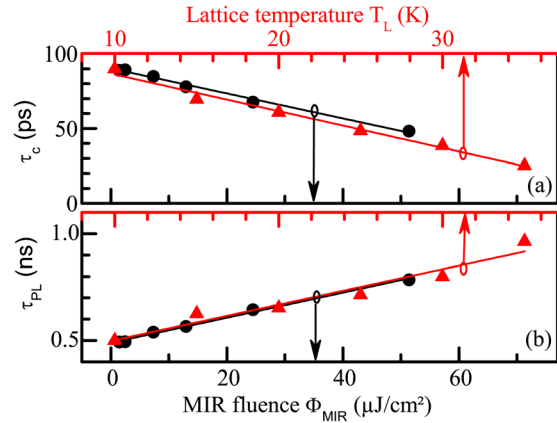


FIG. 3. (Color online) (a) Cooling time τ_c and (b) PL decay time τ_{PL} as a function of MIR fluence (dots) and lattice temperature (triangles). The lines show their corresponding linear fits. Note that both data sets start at 10 K and zero MIR fluence.

formation does not produce additional signatures. Using polarized MIR pulses, we observed PL quenching for s-polarized excitation due to free-carrier absorption. However, the saturation intensity for the PL quenching due to intersubband transition induced by p-polarized light is about 50 times smaller, validating the strictness of the polarization selection rule.¹⁸ Furthermore, we could show that the variation of the carrier cooling times and the PL decay times allows for a sensitive local probing of the temperature change induced by the MIR radiation in a range with negligible spectral shift.

We gratefully acknowledge discussions with J. Bhattacharyya, D. Stehr, and S. Chatterjee, as well as friendly cooperation with W. Seidel. We thank P. Michel and the FELBE team for their dedicated support.

- ¹T. C. Damen *et al.*, *Phys. Rev. B* **42**, 7434 (1990).
- ²R. Kumar *et al.*, *Phys. Rev. B* **54**, 4891 (1996).
- ³J. Szczytko *et al.*, *Phys. Rev. Lett.* **93**, 137401 (2004).
- ⁴J. Szczytko *et al.*, *Phys. Rev. B* **71**, 195313 (2005).
- ⁵L. Kappei, J. Szczytko, F. Moirier-Genoud, and B. Deveaud, *Phys. Rev. Lett.* **94**, 147403 (2005).
- ⁶S. Chatterjee *et al.*, *Phys. Rev. Lett.* **92**, 067402 (2004).
- ⁷I. Galbraith *et al.*, *Phys. Rev. B* **71**, 073302 (2005).
- ⁸S. W. Koch, M. Kira, G. Khitrova, H. M. Gibbs, *Nature Mater.* **5**, 523 (2006).
- ⁹R. A. Kaindl, D. Hägele, M. A. Carnahan, and D. S. Chemla, *Phys. Rev. B* **79**, 045320 (2009).
- ¹⁰R. A. Kaindl, M. A. Carnahan, D. Hägele, R. Lövenich, and D. S. Chemla, *Nature* **423**, 734 (2003).
- ¹¹A. Amo *et al.*, *Appl. Phys. Lett.* **92**, 061912 (2008).
- ¹²S. M. Quinlan *et al.*, *Phys. Rev. B* **45**, 9428 (1992).
- ¹³J. Černe *et al.*, *Phys. Rev. B* **51**, 5253 (1995).
- ¹⁴M. Wagner *et al.*, *Appl. Phys. Lett.* **94**, 241105 (2009).
- ¹⁵M. Helm, "The basic physics of intersubband transitions," in *Semiconductor and Semimetals* (Academic, San Diego, CA, 2000), Vol. **62**, pp. 1–99.
- ¹⁶H. Schneider, O. Drachenko, S. Winnerl, M. Helm, and M. Walthers, *Appl. Phys. Lett.* **89**, 133508 (2006).
- ¹⁷H. Schneider and H. C. Liu, *Quantum Well Infrared Photodetectors*, Springer Series in Optical Sciences (Springer, Berlin, Germany, 2007), Vol. **126**.
- ¹⁸H. C. Liu, M. Buchanan, and Z. R. Wasilewski, *Appl. Phys. Lett.* **72**, 1682 (1998).

Acceptor deactivation in individual silicon nanowires: From thick to ultrathin

Xin Ou,^{1,a)} Nadine Geyer,² Reinhard Kögler,¹ Peter Werner,² and Wolfgang Skorupa¹

¹*Institute of Ion Beam Physics and Materials Research, Helmholtz-Zentrum Dresden-Rossendorf (HZDR) e.V., P.O. Box 510119, 01314 Dresden, Germany*

²*Max Planck Institute of Microstructure Physics, Weinberg 2, Halle D-06120, Germany*

(Received 4 May 2011; accepted 31 May 2011; published online 21 June 2011)

We investigate the doping behavior in the ultrathin part of individual free standing spicular or conic silicon nanowires (NWs) by measuring the local resistivity of the NWs using scanning spreading resistance microscopy. The NWs are boron-doped and the doping efficiency is found to dramatically decrease as the NW diameter is below 25 nm. Our experimental results reveal the dependence of the acceptor deactivation on the diameter of the NW cross section. The deactivation mechanism is discussed by comparing the experimental data with theoretical models considering the dopant deactivation induced by carrier traps at the Si/SiO₂ interface and due to the dielectric mismatch.

© 2011 American Institute of Physics. [doi:10.1063/1.3602924]

Controlled doping of Si nanowires (NWs) is indispensable for their functionality as the promising building block for nanoelectronic devices.¹ Because of the much higher surface to volume ratio of the NW in comparison to bulk materials the surface effect plays an important role in determining the doping behavior. This leads to a strong driving force to develop a variety of techniques^{2–10} to qualify the spatial distribution of dopant atoms and their activation. Segregation and deactivation of dopants at the surface are two major effects in NW doping. Both of them were illustrated theoretically¹¹ and experimentally^{3–6,8,10} for p- and n-type dopants. The preferable NW size for the future logic application is down to diameters of sub-20 nm.¹ However, the experimental doping studies of individual NWs were mostly performed for significantly larger diameters due to the challenges in analyzing a thin single NW without averaging over a sample set. But, the electrical properties of the NWs are strongly diameter dependent and closely related to the contribution of deactivation effects.^{12,13} For NWs with small diameters of several tens of nanometers the dopant deactivation is strengthened by charge trapping due to interface states^{13–15} and by the dielectric mismatch.^{12,16} In this paper the size-dependent acceptor deactivation is demonstrated by measuring the local resistivity in individual NWs of different shape, a spicular one (NW1) with a long thin part of about 16 nm in diameter and a short NW of conic shape (NW2) nearby a thick one (NW3). The electrical characterization is performed by scanning spreading resistance microscopy (SSRM) which can give a direct visualization and quantification of the local resistivity of the NW cross section.⁵ SSRM is based on the contact mode atomic force microscope system.^{17,18} By scanning of the sharp and hard diamond-coated tip over a cross sectional specimen surface the local spreading resistance (R_s) is measured. R_s is directly related to the local resistivity (ρ) and can be converted to the local carrier concentration via a calibration procedure.^{5,17}

The NWs were fabricated by metal-assisted chemical etching an undoped (100) Si substrate with a resistivity of

6 Ω cm.¹⁹ After fabrication the Ag catalyst was removed. The topology of the investigated NWs was accidentally found among the regular (thick) NWs. Doping was performed after covering with a SiO₂ layer by four boron ion implantation steps with gradually decreasing ion energy in order to achieve a homogenous dopant concentration along the investigated NW length. The boron concentration in the NW is calculated to be 10^{18} cm⁻³ using the transport of ions in matter (TRIM) computer code.²⁰ Subsequent rapid thermal annealing was performed at 1000 °C for 30 s in air. Notice that the NW surface is slightly oxidized during annealing. The preparation of the cross section specimen for SSRM was described recently.⁵ The spatial resolution of SSRM was determined to be better than 4 nm by measuring an atomically sharp (thermally oxidized) SiO₂/Si interface and the surface roughness of the specimen was below 2 nm. To increase the resolution SSRM scans were repeated with decreased distance between neighboring data points (DNPs). DNP values defining the pixel size of the SSRM image were reduced from 1.6 nm for an overview image down to 0.2 nm for a high resolution detail image.

Figure 1 presents the scanning electron microscopy (SEM) image taken after the SSRM measurement and the corresponding SSRM images of the same cross section of NW1. The fine lines in the SEM image approximately parallel to the NW axis are tip traces caused by the SSRM prescan.²¹ The size of the NW gradually decreases from 200 to 20 nm whereas the top thin part of 350 nm in length is not perfectly uniform. It slightly varies around the average width of 16 nm. A light green area (bottom right) shows the unimplanted substrate with two orders of magnitude higher R_s value and the red area surrounding the NW corresponds to the deposited SiO₂ layer with a very high resistance (HR). The transition location between undoped and doped Si is in approximate agreement with the penetration depth of the boron ions calculated by TRIM. A detailed image of the doping effect in the thin part of the NW1 is given by Fig. 1(c) with a decreased DNP of 0.5 nm. Taking into account the doping level of 10^{18} cm⁻³ only 70 dopant atoms are in the volume of the thin NW1 piece of 350 nm in length. The lowest R_s values in this part are around 10^8 Ω , which demonstrates

^{a)} Author to whom correspondence should be addressed. Electronic mail: x.ou@hzdr.de.

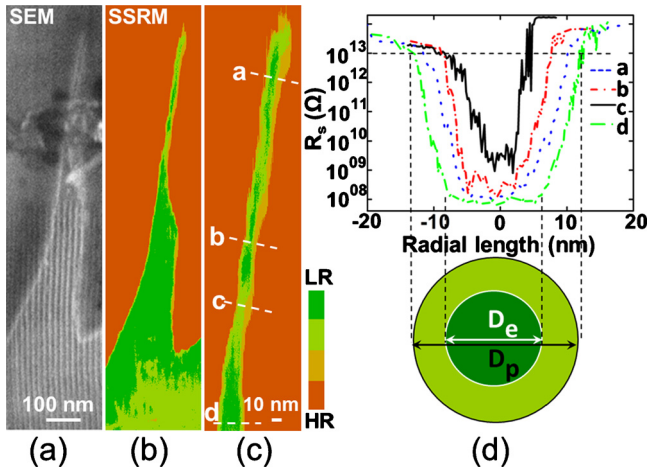


FIG. 1. (Color online) (a) SEM image of the cross section specimen of the Si NW1 (spicular) observed after the SSRM. (b) SSRM images of the same NW as shown in (a) measured with DNP=1.6 nm. (c) SSRM image (DNP=0.5 nm) of the thin part of NW1. The color scale indicates high (HR, oxide) and low (LR, boron-doped Si) resistance. (d) Four examples of R_S profiles in radial direction. These profiles are extracted from high resolution SSRM images (DNP=0.2 nm, not shown). Their positions (a, b, c, d) are indicated in (c). The scheme illustrates the determination of D_p and D_e from measured radial R_S profiles.

this part is effectively doped as compared with the unimplanted substrate of above $10^9 \Omega$ [light green area in Fig. 1(b)]. In order to quantitatively determine the diameter dependence of doping SSRM images of the cross section NW specimen were measured with the smallest DNP of 0.2 nm. Each scan was taken for a 100 nm piece along the axis of NW1. Then, radial R_S profiles across the cross sections with the different diameters were extracted from these high resolution SSRM images and only four of them are shown in Fig. 1(d), for example. As illustrated below in Fig. 1(d) the physical diameter (D_p) of the NW and the electrical effective diameter (D_e) were determined from the R_S profiles. D_p means the width between the interfaces Si/SiO₂ which are fixed at a R_S value of $10^{13} \Omega$,²² and D_e is the width of the region in the NW center with low R_S value. These two parameters describe a core-shell model of the NW comprehending an electrically conductive NW core and a carrier depleted shell. Also, the increase of R_S in the NW core with decreasing D_p [from green to black profile in Fig. 1(d)] demonstrates a decreasing ionization efficiency, i.e., the ratio of the ionized and neutral acceptors $IE = N_A^- / N_A$.

In order to confirm the strong diameter dependence of the doping, a couple of neighboring NW structures of the same sample were investigated and are shown by Fig. 2(a). The structure consists of a relatively thick piece, NW3, with a diameter around 90 nm and close aside NW2 with a conic shape. The diameter of NW2 gradually shrinks from 60 nm at its bottom to sub-10 nm at its top. Radial R_S profiles across both, NW2 and NW3, are taken for each 20 nm distance. As seen in Fig. 2(b) the average R_S values in the core of NW2 are significantly higher than in the counterpart of NW3 when $D_p < 25$ nm (at axial position of 160 nm). This finding is confirmed by the axial R_S profiles of NW2 and NW3 in Fig. 2(c). It is worth noting that the initial doping conditions are expected to be same for the same axial positions in NW2 and NW3. Therefore, the systematic trend in the differences of the R_S values can only be attributed to the diameter dependence of the acceptor deactivation.

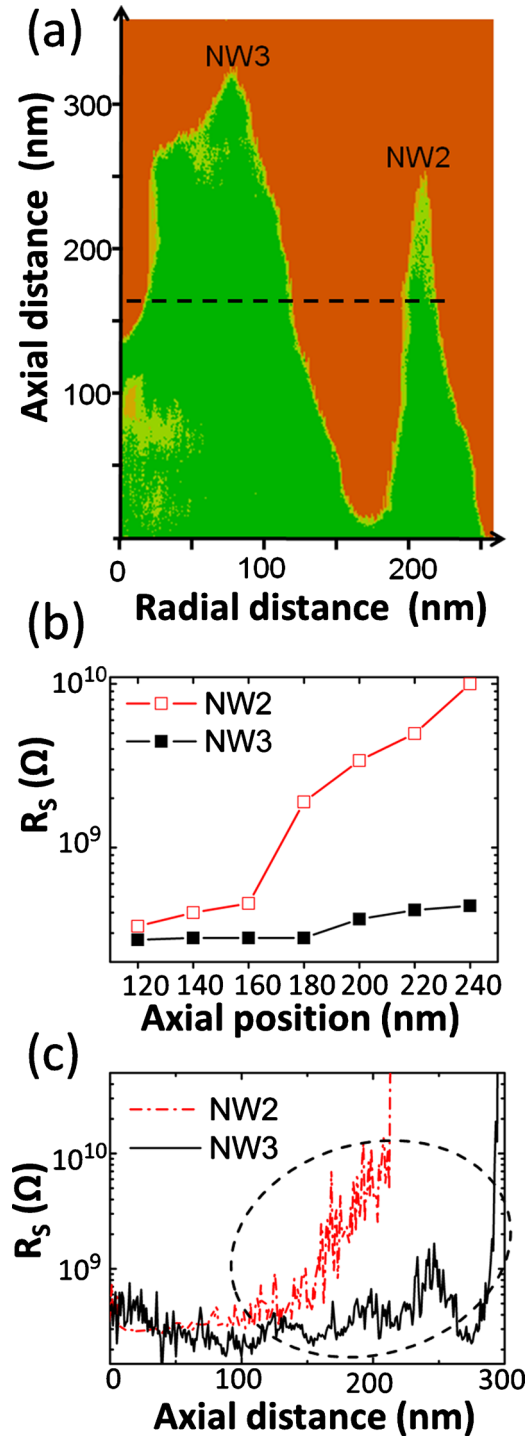


FIG. 2. (Color online) (a) SSRM image with DNP=0.98 nm of the neighboring NW2 (cone) and NW3 (thick). A dashed line marks the position of the diameter of 25 nm for NW2. The color scale corresponds to Fig. 1. (b) R_S values at different axial positions according to (a) for NW2 and NW3. The values are averaged over the D_e range of the radial R_S profiles. (c) Axial R_S profiles of NW2 and NW3 given at radial distance position in (a) of 210 nm and 80 nm, respectively.

The diameter dependence of IE is given in Fig. 3(a) for NW1. IE as a function of D_p can be extracted from the measured R_S values by assuming that acceptors in the thick part of the NW are fully activated and the acceptor mobility (μ_p) is not diameter dependent. By using the proportional relationship of R_S and ρ determined from the calibration curve and the ratio R_S/ρ taken from the thickest part of the NW, N_A^- can be converted from the scaled ρ of NW cross sections by

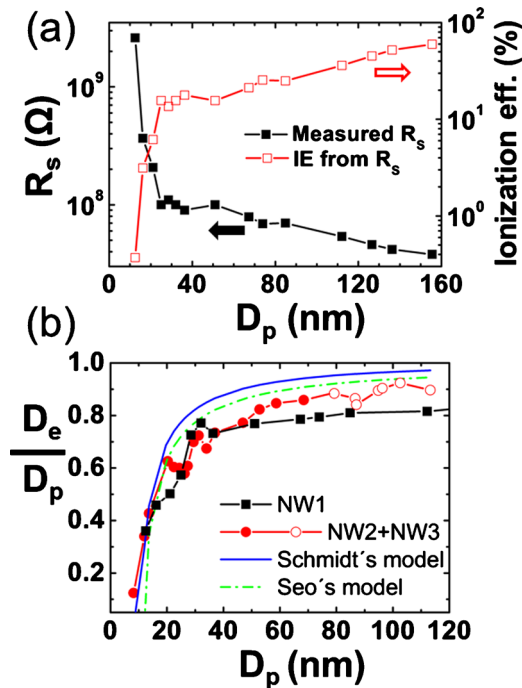


FIG. 3. (Color online) (a) R_S values of NW1 as a function of D_p averaged over the D_e range and the corresponding calculated acceptor ionization efficiency (IE). (b) The ratio D_e/D_p as a function of D_p derived from experimental radial R_S profiles. The data of NW2 and NW3 are combined to the thinner and thicker part of one curve. The blue and green lines are calculated by using Schmidt's model (Ref. 13) and Seo's model (Ref. 14), respectively. Corresponding parameters are given in the text.

applying the standard carrier concentration versus resistivity curve for silicon.^{23,24}

Both, the IE curve and the corresponding R_S data from which it is derived are shown in Fig. 3(a). This result is in agreement with Diarra *et al.*¹⁶ who calculated the diameter dependence of IE by considering the dielectric mismatch between the Si body of the NW and the surrounding SiO_2 . This effect increases the dopant ionization energy as the NW diameter decreases, and hence results in an acceptor deactivation. However, there are also other effects which may cause the additional acceptor deactivation. Positive surface charges at the Si/ SiO_2 interface create an acceptor depleted region in the NW at the surface. The thickness of this layer was calculated by Schmidt *et al.*¹³ and Seo *et al.*¹⁴ assuming a conductive NW core of diameter D_e with an activation degree of 100% and a fully depleted shell with a thickness of $(D_p - D_e)/2$. The measured D_e/D_p ratio is compared in Fig. 3(b) with calculated results obtained by those models. The best fit was achieved for surface state density $D_{it} = 1.2 \times 10^{12} \text{ cm}^{-2} \text{ eV}^{-1}$ (Schmidt's model) and for surface charge density $N_S = 6 \times 10^{11} \text{ cm}^{-2}$ (Seo's model). Our N_S value seems reasonable compared with Seo's value of 5×10^{11} to $10 \times 10^{11} \text{ cm}^{-2}$ given for a NW with oxidized surface.¹⁴

In summary, a diameter dependence of the local resistivity of the NWs is observed by SSRM measurement. The spreading resistance increases as the NW diameter decreases and this tendency is significantly enhanced as the diameter is

below 25 nm. The acceptor depletion is found at the surface as well as in the NW core. These results can be explained by an interaction of the enhanced ionization energy in the NW because of the dielectric mismatch and of the acceptor depletion at the NW surface due to interface traps. In terms of a core-shell model deactivation at the ultrathin part of the NW is characterized by the abrupt shrinking of the diameter of the electrically conductive NW core and by the decrease of its ionization efficiency.

Xin Ou and Nadine Geyer contribute equally to this work.

- ¹C. Thelander, P. Agarwal, S. Brongersma, J. Eymery, L. F. Feiner, A. Forchel, M. Scheffler, W. Riess, B. J. Ohlsson, U. Gösele, and L. Samuelson, *Mater. Today* **9**, 28 (2006).
- ²K. K. Lew, L. Pan, T. E. Bogart, S. M. Dilts, E. C. Dickey, J. M. Redwing, Y. F. Wang, M. Cabassi, T. S. Mayer, and S. W. Novak, *Appl. Phys. Lett.* **85**, 3101 (2004).
- ³P. Xie, Y. J. Hu, Y. Fang, J. J. Huang, and C. M. Lieber, *Proc. Natl. Acad. Sci. U.S.A.* **106**, 15254 (2009).
- ⁴G. Imamura, T. Kawashima, M. Fujii, C. Nishimura, T. Saitoh, and S. Hayashi, *Nano Lett.* **8**, 2620 (2008).
- ⁵X. Ou, P. D. Kanungo, R. Kögler, P. Werner, U. Gösele, W. Skorupa, and X. Wang, *Nano Lett.* **10**, 171 (2010).
- ⁶E. Koren, N. Berkovitch, and Y. Rosenwaks, *Nano Lett.* **10**, 1163 (2010).
- ⁷J. M. Stiegler, A. J. Huber, S. L. Diedenhofen, J. G. Rivas, R. E. Algra, E. P. A. M. Bakkers, and R. Hillenbrand, *Nano Lett.* **10**, 1387 (2010).
- ⁸M. I. den Hertog, H. Schmid, D. Cooper, J. L. Rouviere, T. M. Björk, H. Riel, P. Rivallin, S. Karg, and W. Riess, *Nano Lett.* **9**, 3837 (2009).
- ⁹R. A. Schlitz, D. E. Perea, J. L. Lensch-Falk, and L. J. Lauhon, *Appl. Phys. Lett.* **95**, 162101 (2009).
- ¹⁰N. Fukata, S. Ishida, S. Yokono, R. Takiguchi, J. Chen, T. Sekiguchi, and K. Murakami, *Nano Lett.* **11**, 651 (2011).
- ¹¹M. V. Fernández-Serra, Ch. Adessi, and X. Blase, *Phys. Rev. Lett.* **96**, 166805 (2006).
- ¹²M. T. Björk, H. Schmid, J. Knoch, S. Riel, and W. Riess, *Nat. Nanotechnol.* **4**, 103 (2009).
- ¹³V. Schmidt, S. Senz, and U. Gösele, *Appl. Phys. A: Mater. Sci. Process.* **86**, 187 (2007).
- ¹⁴K. I. Seo, S. Sharma, A. A. Yasseri, D. R. Stewart, and T. I. Kamins, *Electrochem. Solid-State Lett.* **9**, G69 (2006).
- ¹⁵S. Ingole, P. Manandhar, B. Satishkumar, B. Chikkannanavar, E. A. Akhadov, and S. T. Picraux, *IEEE Trans. Electron Devices* **55**, 2931 (2008).
- ¹⁶M. Diarra, Y.-M. Niquet, C. Delerue, and G. Allan, *Phys. Rev. B* **75**, 045301 (2007).
- ¹⁷P. Eyben, W. Vandervorst, D. Alvarez, M. Xu, and M. Fouchier, *Scanning Probe Microscopy*, edited by S. Kalinin and A. Gruverman (Springer, New York, 2007), Chap. 1.2., p. 82.
- ¹⁸T. Hakkarainen, O. Douheret, S. Anand, L. Fu, H. H. Tan, and C. Jagadish, *Appl. Phys. Lett.* **97**, 041106 (2010).
- ¹⁹Z. P. Huang, N. Geyer, P. Werner, J. De Borr, and U. Gösele, *Adv. Mater. (Weinheim, Ger.)* **23**, 285 (2011).
- ²⁰J. F. Ziegler, J. P. Biersack, and U. Littmark, in *The Stopping and Ranges of Ions in Solids*, edited by J. F. Ziegler (Pergamon, New York, 1985), Vol. 1.
- ²¹X. Ou, P. D. Kanungo, R. Kögler, P. Werner, U. Gösele, W. Skorupa, and X. Wang, *Adv. Mater. (Weinheim, Ger.)* **22**, 4020 (2010).
- ²²X. Ou, R. Kögler, A. Mücklich, W. Skorupa, W. Möller, X. Wang, and L. Vines, *Appl. Phys. Lett.* **94**, 011903 (2009).
- ²³National Bureau of Standards Special Publication 400-64, 1981.
- ²⁴See supplementary material at <http://dx.doi.org/10.1063/1.3602924> for (1) Fabrication of SiNWs, (2) boron implantation steps, (3) extraction of radial R_S profiles, (4) calibration measurement, and (5) calculation of D_e/D_p ratio from the models.

Direct observation of antiferromagnetically oriented spin vortex states in magnetic multilayer elements

S. Wintz,^{1,a)} T. Strache,¹ M. Körner,¹ M. Fritzsche,¹ D. Markó,^{1,b)} I. Mönch,² R. Mattheis,³ J. Raabe,⁴ C. Quitmann,⁴ J. McCord,¹ A. Erbe,¹ and J. Fassbender¹

¹Helmholtz-Zentrum Dresden-Rossendorf, 01328 Dresden, Germany

²Institute for Integrative Nanosciences, IFW Dresden, 01069 Dresden, Germany

³Institut für Photonische Technologien, 07702 Jena, Germany

⁴SLS, Paul Scherrer Institut, 5232 Villigen, Switzerland

(Received 23 March 2011; accepted 15 May 2011; published online 9 June 2011)

We report on the coupling of spin vortices in magnetic multilayer elements. The magnetization distribution in thin film disks consisting of two ferromagnetic layers separated by a nonmagnetic spacer is imaged layer-resolved by using x-ray microscopy. We directly observe two fundamentally different vortex coupling states, namely antiferromagnetic and ferromagnetic orientation of the flux directions. It is found that these states are predetermined for systems that involve a sufficiently strong interlayer exchange coupling, whereas for the case of a purely dipolar interaction both states are transformable into each other. © 2011 American Institute of Physics. [doi:10.1063/1.3597297]

Micromagnetism has been a focus of fundamental and technological research over several decades. Within this field, spin vortices have attracted much attention due to their chiral nature and the variety of dynamic phenomena that they exhibit.^{1–4} As illustrated in Fig. 1(a), such a spin vortex consists of a planar magnetization curl circulating around a nanometer sized core region, in which the magnetization turns perpendicular to the plane.¹ They typically occur in ferromagnetic thin films, in particular as magnetic ground state of patterned micro- or nanostructures.⁵ In this kind of single layer structures, spin vortices have been observed directly—including their cores—using scanning probe⁶ and x-ray microscopy.⁷ Their magnetodynamic properties depend on static topological charges, namely the winding number n and the orientation of the core (polarity: p).² For a common vortex ($n=1$), the rotation sense of the gyrotropic core mode e.g., is fully determined by the p value.^{2,3}

When considering two or more vortices, interaction effects have to be taken into account. This holds true from the basic perspective, for instance the vortex-antivortex pair annihilation⁸ as well as for potential applications such as magnetoresistive memory devices⁹ or vortex-based spin-torque nano-oscillators.¹⁰ Of special interest in this technological context is the magnetic coupling between vertically stacked vortices, separated by a nonmagnetic spacer [cf. Fig. 1(b)]. Besides the dipolar interaction mediated by stray fields, interlayer exchange coupling (IEC)¹¹ can be present in such magnetic multilayer systems.

The product of the in-plane flux direction (circulation: c) and the polarity p defines the handedness $h=cp$ of a vortex. For a vortex pair this implies the existence of 2^2 nondegenerate configurations, which can be categorized according to the combination of their individual quantum numbers (p, h) or (c, p) .¹² In the following we use $c \in \{-1, 1\}$ and $p \in \{-1, 1\}$ to label the states as shown in Fig. 1(c). Equal vortex circulations (FM; $\Pi_i c_i=1$) in the two layers correspond to a ferromagnetic (fm) orientation of the in-plane magnetization components while opposite circulations

(AF; $\Pi_i c_i=-1$) correspond to an antiferromagnetic (afm) orientation. The core polarities p_i in the two layers can be aligned either parallel (P; $\Pi_i p_i=1$) or antiparallel (AP; $\Pi_i p_i=-1$). The four nondegenerate coupling states are expected to show different electrical resistances¹³ and qualitatively different dynamic responses to excitations by magnetic fields or spin-polarized currents.^{14–16} So far only stacked vortex pairs with FM configuration have been observed directly.^{17,18} AF configurations have been only inferred indirectly, by comparing micromagnetic simulations with the results of integral magneto-optical¹⁹ and magnetoresistance^{12,13} measurements, respectively. On this background we report on the direct observation of interlayer coupled spin vortices with both FM and AF configurations, which we find in the presence of IEC and even for a purely dipolar coupling.

We studied three different trilayers as potential candidates for the formation of interlayer coupled vortices. Each trilayer consists of two ferromagnetic layers, namely cobalt (Co) and nickel₈₁-iron₁₉ (NiFe), separated by a nonmagnetic spacer. Selecting different ferromagnetic elements allows the individual detection of the magnetic properties for each layer by element specific x-ray techniques.²⁰ The thicknesses (t) of the ferromagnetic layers are chosen so that for a micron sized lateral structure a magnetic vortex results as the ground state in each layer.²¹ A systematic variation of the interlayer cou-

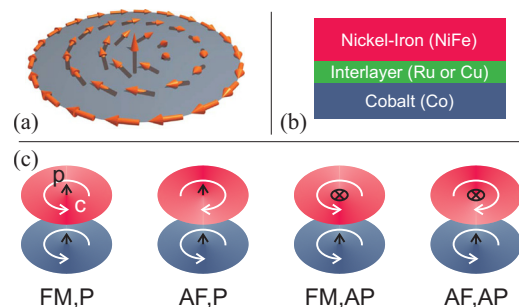


FIG. 1. (Color online) Illustration of magnetic disks and their micromagnetic structures. (a) Single layer disk with magnetization curl, indicated by arrows, and a vortex core in its center. (b) Multilayer stack, consisting of Co, a nonmagnetic interlayer, and NiFe. (c) Four fundamental configurations with respect to the individual in-plane circulations (c , white arrow) and core polarities (p , black arrow) possible in a stack of two magnetic vortices.

^{a)}Electronic mail: s.wintz@hzdr.de.

^{b)}Present address: Université Paris-Sud 11, 91405 Orsay, France.

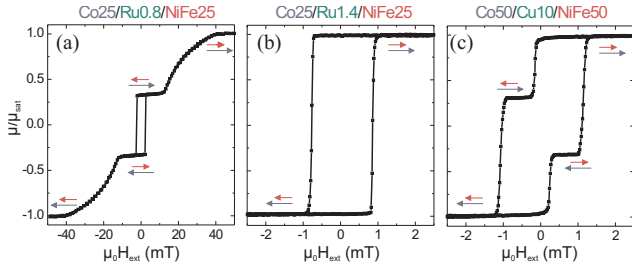


FIG. 2. (Color online) Magnetization reversal curves for three magnetic trilayer samples obtained by inductive magnetometry. (a) Co(23.9)/Ru(0.8)/NiFe(21.4) (nm) sample with afm IEC showing a gradual reorientation of the NiFe layer followed by an abrupt switching of the entire stack at 2 mT. (b) Co(23.9)/Ru(1.4)/NiFe(21.4) (nm) film with fm IEC and simultaneous switching at 1 mT. (c) Co(47.8)/Cu(10)/NiFe(42.8) (nm); dipolarly coupled layers showing independent switching of NiFe (0.25 mT) and Co (1 mT).

pling is achieved by using different thicknesses of ruthenium (Ru) and copper (Cu) as spacer layers.¹¹ A ten target UHV system was used for the dc magnetron sputter deposition of continuous polycrystalline films with the following thicknesses: Co(23.9)/Ru(0.8)/NiFe(21.4)/Al(5), Co(23.9)/Ru(1.4)/NiFe(21.4)/Al(5), and Co(47.8)/Cu(10)/NiFe(42.8)/Al(3) (nm) onto thermally oxidized silicon wafers. Here the aluminum (Al) cap layer has a protective purpose only. The Ru thicknesses approximately correspond to the first minimum ($t_{\text{Ru}}=0.8$ nm, afm IEC) and maximum ($t_{\text{Ru}}=1.4$ nm, fm IEC) of the t_{Ru} dependent IEC oscillation.¹¹ For the relatively thick Cu interlayer of $t_{\text{Cu}}=10$ nm, a purely dipolar coupling is expected. In order to experimentally verify these different coupling types, magnetization reversal curves of the trilayers have been measured by inductive magnetometry.

Figure 2(a) shows the magnetization reversal loop of the Co(23.9)/Ru(0.8)/NiFe(21.4) (nm) continuous film. The external field (H_{ext}) is applied along the easy axis and in saturation both films are aligned parallel. When reducing the applied field a continuous 180° reorientation of the NiFe layer to an antiparallel alignment occurs. This is supported by the relative magnetic moment $\mu/\mu_{\text{sat}}=0.33$ measured at remanence. Assuming standard material parameters²² for the saturation magnetization ($M_{\text{Co}}=1440$ kA/m, $M_{\text{NiFe}}=800$ kA/m) one would expect a ratio of $\mu/\mu_{\text{sat}}=(M_{\text{Co}}-M_{\text{NiFe}})/(M_{\text{Co}}+M_{\text{NiFe}})=0.34$. At $\mu_0 H_{\text{ext}} \approx -2$ mT the whole stack undergoes a 180° switching event. This is driven by the realignment of the stack's net-moment into the direction of the applied field while maintaining the antiparallel orientation of the layers. Beyond $\mu_0 H_{\text{ext}} \approx -10$ mT the NiFe layer starts to rotate into the direction of the applied field again, gradually overcoming the afm IEC. Saturation, i.e., a parallel alignment of both layers, is reached at $\mu_0 H_{\text{ext}} \approx -45$ mT $=\mu_0 H_{\text{sat}}$. From the saturation field (H_{sat}) we estimate the bilinear coupling constant to be $J \approx -0.5$ mJ/m² using $J = -\mu_0 H_{\text{sat}} M_{\text{Co}} t_{\text{Co}} M_{\text{NiFe}} t_{\text{NiFe}} / (M_{\text{Co}} t_{\text{Co}} + M_{\text{NiFe}} t_{\text{NiFe}})$.²³ This value confirms a strong afm IEC.

The film with an increased Ru thickness ($t_{\text{Ru}}=1.4$ nm) shows a simultaneous reversal of both layers at $\mu_0 H_{\text{ext}} \approx 1$ mT along the easy axis, thus indicating a fm IEC [cf. Fig. 2(b)]. The bilinear coupling strength cannot be derived from the shape of the hysteresis loop.²³ Ferromagnetic resonance investigations²⁴ however allow to determine an upper limit of 0.02 mJ/m² for J (not shown). For the case of the Cu interlayer ($t_{\text{Cu}}=10$ nm) we observe two switching fields during the magnetization reversal along the easy axis [cf. Fig.

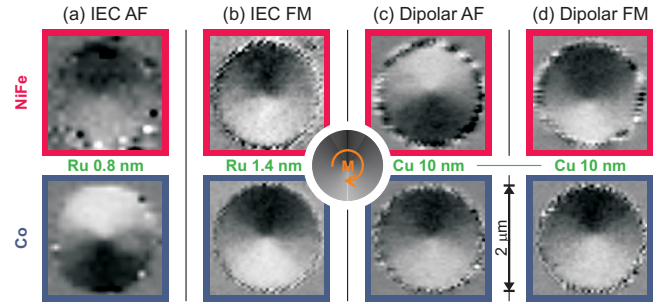


FIG. 3. (Color online) X-ray images showing the layer resolved magnetization for disks with 2 μm diameter and varied interlayer coupling. Left columns: IEC (a) afm IEC ($t_{\text{Ru}}=0.8$ nm) leading to AF configurations of the vortices, (b) fm IEC ($t_{\text{Ru}}=1.4$ nm) resulting in FM circulation states. Right columns showing two examples for dipolarly coupled vortices ($t_{\text{Cu}}=10$ nm) exhibiting both AF (c) and FM (d) configurations.

2(c)]. These events correspond to an initial switching of the relatively soft NiFe layer at $\mu_0 H_{\text{ext}} \approx 0.25$ mT and a subsequent switching of the more anisotropic Co layer at $\mu_0 H_{\text{ext}} \approx 1$ mT, respectively. This independent switching behavior verifies the predicted purely dipolar coupling.

In order to confine magnetic vortices into a vertical arrangement, trilayer disks with diameters of 0.25, 0.5, 1, and 2 μm were fabricated onto silicon-nitride membranes using electron beam lithography, sputter deposition, and subsequent lift-off processing. After demagnetization, the distribution of the magnetization orientation $\mathbf{e}_M(\mathbf{r}) := \mathbf{M}/M$ in the disks was imaged using scanning transmission x-ray microscopy (STXM), for details see Ref. 25. This method provides a lateral resolution of about 25 nm. A monochromatic x-ray beam is focused onto the sample by using a diffractive Fresnel zone plate. The sample itself is raster scanned through the beam while the transmitted intensity (I) is measured. The application of circularly polarized x-rays at the element specific L-absorption edges leads to a magnetic contrast due to x-ray magnetic circular dichroism.²⁰ Here the local difference in transmissivity is proportional to the projection of the sample's local magnetization orientation onto the photon propagation direction (\mathbf{e}_k); $I \sim \mathbf{e}_M \mathbf{e}_k$. We therefore tilt the sample's normal by 30° with respect to the beam axis in order to obtain information on the in-plane magnetization distribution. Layer selectivity is accomplished by imaging the sample with two different x-ray photon energies, corresponding to the Ni L₃-absorption edge (≈ 853 eV) and to the Co L₃-absorption edge (≈ 778 eV), respectively. This ensures that only the layer containing either of the elements contributes to the magnetic signal. The normalized difference of images taken with opposing circular light polarizations emphasizes the magnetic contrast while also removing topographic effects. As a reliable imaging of the relatively small vortex cores is at the detection limit of our setup in its present state, our investigation is focused on the vortex circulation configurations being AF or FM.

In the following we discuss the STXM results for interlayer coupled vortices in disks with a diameter of 2 μm . The magnetic contrast images of disks with different coupling are displayed in Fig. 3. From the continuous film measurements, afm IEC is expected for the disk containing a Ru spacer of $t_{\text{Ru}}=0.8$ nm. In this disk we observe a vortex pair with opposite circulations, as can be seen in Fig. 3(a). Clearly the white region in the Co layer is located below a black region in the NiFe layer and vice versa. This means an AF configu-

ration as sketched in Fig. 1(c) is realized. As this state is representative for most of the investigated structures of this trilayer type, we conclude that the afm IEC is sufficiently strong to deterministically induce the AF configuration. It is interesting to observe that the antiparallel magnetization orientation of both layers is strict on a local scale, which is a result of the relatively strong IEC. An increase of the Ru interlayer thickness to $t_{\text{Ru}}=1.4$ nm changes the IEC orientation to fm in the continuous film. A magnetic micrograph of a multilayer disk of this type is shown in Fig. 3(b). In contrast to Fig. 3(a), the same vortex circulation is exhibited in both layers, which corresponds to the FM configuration. For this structure we observe that the coupling is less strict; the position of the vortex core is slightly different in the two layers and the magnetization curl in the NiFe layer is not fully symmetric. Although the majority of the structures is in a micromagnetic state comparable to Fig. 3(b), we also observe a few FM vortex pairs whose cores are diametrically displaced from the center as well as nonvortex magnetization distributions in some rare cases. This situation can be partly attributed to the reduced strength of the IEC for larger Ru thicknesses.¹¹ For vortices interacting only by dipolar coupling, we observe both circulation configurations FM and AF. Figures 3(c) and 3(d) show such disks whose magnetic layers are separated by a Cu spacer of $t_{\text{Cu}}=10$ nm. While the magnetization distribution in Fig. 3(c) exhibits the AF configuration (opposite circulations), Fig. 3(d) shows a disk in the FM state (equal circulations). Here the configuration is not a fixed property of individual multilayer disks, e.g., induced by defects. Instead the configuration can be switched from FM to AF and back using demagnetization by an external field. However this switching is so far neither state selective nor deterministic. Again we also observe vortex pairs with diametrically off-centered core positions. At this point we cannot resolve if this is either due to pinning effects induced by sample imperfections or a consequence of lateral core repulsion that we anticipate for AP polarity configurations. States with P cores however, should favor centered and layer-congruent core positions assuming a lateral dipole-dipole attraction of the cores.¹⁴ Note that we have investigated disks with different sizes from 0.25 to 2 μm in diameter, though we find no qualitative changes with respect to lateral size for any of the three trilayers.

In summary we have investigated both patterned and continuous magnetic trilayer films. Hysteresis loops derived from inductive magnetometry provide information on the reversal process of continuous films and the type and strength of magnetic coupling involved. The local alignment of magnetization and the resulting vortex circulation configurations in multilayer disks are determined by layer-resolved x-ray microscopy. For IEC disks we directly observe and thereby prove the AF configuration, which had been predicted by others and we verify the FM configuration, already known to exist. These observations confirm the existence of fundamentally different vortex pair configurations in a vertical arrangement. For a thin Ru interlayer (strong afm IEC, AF states) the coupling is strict and local while for a thicker Ru interlayer (weak fm IEC, FM states) it is less strict. For disks with a purely dipolar coupling we observe both AF and FM con-

figurations and switching between the two is possible using external magnetic fields. In the future, a better spatial resolution should allow the detection of the core polarity p and the associated possible configurations. For disks with a purely dipolar coupling it should be possible to switch reliably between the FM and AF configuration using electrical currents or external fields, potentially leading to applications in data storage and spin-torque oscillators.

We thank A. Puzic, C. Bunce, and K. Lenz for their contribution to this work as well as V. Kühn, B. Eichler, B. Sarafimov, and K. Kirsch for technical support. The STXM experiments were performed using the X07DA (PoILux) beamline at the Swiss Light Source. Funding from BMBF (Contract Nos. 05 KS4WE1/6 and FKZ 13N10144) and EU (Grant No. 226716) is acknowledged.

- ¹E. Feldtkeller and H. Thomas, *Phys. Kondens. Mater.* **4**, 8 (1965).
- ²D. L. Huber, *J. Appl. Phys.* **53**, 1899 (1982).
- ³S. B. Choe, Y. Acremann, A. Scholl, A. Bauer, A. Doran, J. Stöhr, and H. A. Padmore, *Science* **304**, 420 (2004).
- ⁴B. Van Waeyenberge, A. Puzic, H. Stoll, K. W. Chou, T. Tylliszczak, R. Hertel, M. Fähnle, H. Brückl, K. Rott, G. Reiss, I. Neudecker, D. Weiss, C. H. Back, and G. Schütz, *Nature (London)* **444**, 461 (2006).
- ⁵R. P. Cowburn, D. K. Koltsov, A. O. Adeyeye, and M. E. Welland, *Phys. Rev. Lett.* **83**, 1042 (1999).
- ⁶T. Shinjo, T. Okuno, R. Hassdorf, K. Shigeto, and T. Ono, *Science* **289**, 930 (2000).
- ⁷K. W. Chou, A. Puzic, H. Stoll, G. Schütz, B. Van Waeyenberge, T. Tylliszczak, K. Rott, G. Reiss, H. Brückl, I. Neudecker, D. Weiss, and C. H. Back, *Appl. Phys. Lett.* **90**, 202505 (2007).
- ⁸R. Hertel and C. Schneider, *Phys. Rev. Lett.* **97**, 177202 (2006).
- ⁹N. Kikuchi, S. Okamoto, O. Kitakami, Y. Shimada, S. Kim, Y. Otani, and K. Fukamichi, *IEEE Trans. Magn.* **37**, 2082 (2001).
- ¹⁰A. Ruotolo, V. Cros, B. Georges, A. Dussaux, J. Grollier, C. Deranlot, R. Guillemet, K. Bouzehouane, S. Fusil, and A. Fert, *Nat. Nanotechnol.* **4**, 528 (2009).
- ¹¹S. S. P. Parkin, *Phys. Rev. Lett.* **67**, 3598 (1991).
- ¹²S. S. Cherepov, A. Konovalenko, V. Korenivski, and D. C. Worledge, *IEEE Trans. Magn.* **46**, 2124 (2010).
- ¹³N. Locatelli, V. V. Naletov, J. Grollier, G. de Loubens, V. Cros, C. Deranlot, C. Ulysse, G. Faini, O. Klein, and A. Fert, *Appl. Phys. Lett.* **98**, 062501 (2011).
- ¹⁴S.-H. Jun, J.-H. Shim, S.-K. Oh, S.-C. Yu, D.-H. Kim, B. Mesler, and P. Fischer, *Appl. Phys. Lett.* **95**, 142509 (2009).
- ¹⁵K. Y. Guslienko, K. S. Buchanan, S. D. Bader, and V. Novosad, *Appl. Phys. Lett.* **86**, 223112 (2005).
- ¹⁶A. V. Khvalkovskiy, J. Grollier, N. Locatelli, Y. V. Gorbunov, K. A. Zvezdin, and V. Cros, *Appl. Phys. Lett.* **96**, 212507 (2010).
- ¹⁷J. Wu, D. Carlton, E. Oelker, J. S. Park, E. Jin, E. Arenholz, A. Scholl, C. Hwang, J. Bokor, and Z. Q. Qiu, *J. Phys.: Condens. Matter* **22**, 342001 (2010).
- ¹⁸K. W. Chou, A. Puzic, H. Stoll, G. Schütz, B. Van Waeyenberge, T. Tylliszczak, K. Rott, G. Reiss, H. Brückl, I. Neudecker, D. Weiss, and C. H. Back, *J. Appl. Phys.* **99**, 08F305 (2006).
- ¹⁹K. Buchanan, K. Guslienko, A. Doran, A. Scholl, S. Bader, and V. Novosad, *Phys. Rev. B* **72**, 134415 (2005).
- ²⁰G. Schütz, W. Wagner, W. Wilhelm, P. Kienle, R. Zeller, R. Frahm, and G. Materlik, *Phys. Rev. Lett.* **58**, 737 (1987).
- ²¹H. Hoffmann and F. Steinbauer, *J. Appl. Phys.* **92**, 5463 (2002).
- ²²R. C. O'Handley, *Modern Magnetic Materials: Principles and Applications* (Wiley, New York, 2000) p. 99.
- ²³R. S. Beach, J. McCord, P. Webb, and D. Mauri, *Appl. Phys. Lett.* **80**, 4576 (2002).
- ²⁴J. Lindner and K. Baberschke, *J. Phys.: Condens. Matter* **15**, S465 (2003).
- ²⁵J. Raabe, G. Tzvetkov, U. Flechsig, M. Böge, A. Jaggi, B. Sarafimov, M. G. C. Vermoij, T. Huthwelker, H. Ade, D. Kilcoyne, T. Tylliszczak, R. H. Fink, and C. Quitmann, *Rev. Sci. Instrum.* **79**, 113704 (2008).

Erratum: “Direct observation of antiferromagnetically oriented spin vortex states in magnetic multilayer elements” [Appl. Phys. Lett. 98, 232511 (2011)]

S. Wintz,^{1,a)} T. Strache,¹ M. Körner,¹ M. Fritzsche,¹ D. Markó,¹ I. Mönch,² R. Mattheis,³ J. Raabe,⁴ C. Quitmann,⁴ J. McCord,¹ A. Erbe,¹ and J. Fassbender¹

¹Helmholtz-Zentrum Dresden-Rossendorf, 01328 Dresden, Germany

²Institute for Integrative Nanosciences, IFW Dresden, 01069 Dresden, Germany

³Institut für Photonische Technologien, 07702 Jena, Germany

⁴SLS, Paul Scherrer institute, 5232 Villigen, Switzerland

(Received 15 September 2011; accepted 15 September 2011; published online 3 October 2011)

[doi:10.1063/1.3646545]

The equation for the relative magnetic moment μ/μ_{sat} given on p. 2, 1. 25 suffers from a typographical error. The correct equation is $\mu/\mu_{\text{sat}} = (M_{\text{Co}}t_{\text{Co}} - M_{\text{NiFe}}t_{\text{NiFe}})/(M_{\text{Co}}t_{\text{Co}} + M_{\text{NiFe}}t_{\text{NiFe}}) = 0.34$. There are no implications for any of the

results presented, as the value given in the original article (0.34) has been calculated using the correct equation. The authors are grateful to Julia Osten for pointing out the error in the original article.

^{a)}Electronic mail: s.wintz@hzdr.de.

Reduced leakage current in BiFeO₃ thin films with rectifying contacts

Yao Shuai,^{1,a)} Shengqiang Zhou,^{1,2} Stephan Streit,¹ Helfried Reuther,¹ Danilo Bürger,¹ Stefan Slesazeck,³ Thomas Mikolajick,³ Manfred Helm,¹ and Heidemarie Schmidt¹

¹*Institute of Ion Beam Physics and Materials Research, Helmholtz-Zentrum Dresden-Rossendorf, P.O. Box 510119, Dresden 01314, Germany*

²*State Key Laboratory of Nuclear Physics and Technology, School of Physics, Peking University, Beijing 100871, People's Republic of China*

³*Namlab gGmbH, Nöthnitzer Strasse 64, 01187 Dresden, Germany*

(Received 22 March 2011; accepted 16 May 2011; published online 6 June 2011)

BiFeO₃ thin films were grown on Pt/c-sapphire substrates by pulsed laser deposition with different growth rates. With increasing growth rate the leakage current is decreased and the conduction mechanism changes from bulk-limited Poole–Frenkel emission to interface-limited Schottky emission. In the present letter, we show that only the growth rate of the BiFeO₃ films close to the metal contacts has to be increased in order to reduce the leakage current and to observe saturated polarization-electric field hysteresis loops. © 2011 American Institute of Physics. [doi:10.1063/1.3597794]

BiFeO₃ (BFO) is the most widely investigated single phase multiferroic material and has been the most promising candidate for multifunctional nonvolatile memory devices due to several advantages such as high Curie temperature (1123 K),¹ high Néel temperature (653 K),¹ and giant spontaneous polarization.² Nevertheless, its high leakage current density still remains a great challenge for practical applications, e.g., the ferroelectric random access memory.³ Particularly, the leakage behavior of BFO thin films at high electric fields is deteriorated and has received much attention, because high electric fields are usually needed to switch the polarization of a BFO thin film due to its high coercive electric fields.

There have been many approaches to decrease the large leakage current in BFO thin films. Atomic substitutions at cationic A-sites or B-sites can reduce the leakage current of BFO thin films by 1~3 orders of magnitude due to the formation of defect complexes or the suppression of oxygen vacancies.⁴⁻⁷ In addition, a solid solution approach where BFO and BaTiO₃ (Ref. 8) or BFO and PbTiO₃ (Refs. 9 and 10) are combined has also been reported to effectively decrease the leakage current. However, the ferroelectric properties of BFO are degraded if the doping or the solid solution approach was followed.

In the present letter, pure BFO thin films without any dopant or solid solution compound were grown using fixed temperature and oxygen pressure (thermodynamic conditions), but different growth rates which were controlled by the laser repetition rate. As the growth rate increases, the leakage current of correspondingly prepared Au/BFO/Pt stacks is considerably suppressed, and the conduction at high electric field has been changed from bulk-limited to interface-limited mechanism. This transition is related with the modification of the interface between the electrodes and the thin film. Due to the low leakage current, the BFO thin film which is grown at higher rate shows a saturated polarization electric (P-E) field hysteresis loop.

BFO thin films were deposited on Pt (100 nm)/sapphire substrates by pulsed laser deposition. The thermodynamic

parameters have been optimized to be 670 °C for the substrate temperature and 60 mTorr for the oxygen partial pressure. The laser fluence was kept at 2 J/cm² while the repetition rate was changed for different samples. The thickness of each film was measured by a step profilometer and the growth rate was calculated. The phase of the BFO thin films was detected by x-ray diffraction (XRD) using a Bruker D8 system with Cu K α radiation. The surface morphology is characterized by atomic force microscopy measurements. Auger electron spectroscopy (AES) has been used to determine the chemical composition of the stack. For electric property measurements, 0.3 mm² Au dots (top electrodes) were formed by magnetron sputtering. The leakage current was measured by a Keithley 2400. The sample labeling, growth condition, and properties are listed in Table I.

Figure 1 shows the XRD θ - 2θ patterns of the BFO thin film samples. Besides the substrate, only BFO has been identified in BFO-2 Hz [Fig. 1(a)]. However, as the growth rate increases, an impurity phase is present in BFO-10 Hz [Fig. 1(b)], which is believed to be Bi₂₅FeO₄₀ or Bi₂O₃. The same impurity phase has also been observed in BFO-10/2/10 Hz [Fig. 1(c)]. Therefore, a high growth rate can result in the formation of a Bi-rich phase.

The influence of the growth rate on the stoichiometry of the thin films has been examined by AES. As shown in Fig. 2(a), BFO-2 Hz exhibits a Bi-rich layer at the top interface between the Au electrode and the BFO thin film. By increasing the growth rate, the Bi content increases significantly in the Bi-rich layer [Fig. 2(b)], and the proportionate thickness of this Bi-rich is also extended. Furthermore, another Bi-rich layer at the bottom interface between the Pt electrode and the

TABLE I. Sample identification and description of growth parameters and conduction mechanisms.

Sample	Repetition rate (Hz)	Growth rate (nm/s)	Thickness (nm)	Conduction mechanism
BFO-2 Hz	2	0.04	312	PF
BFO-10/2/10 Hz	10/2/10	...	326	SE
BFO-10 Hz	10	0.21	358	SE

^{a)}Electronic mail: y.shuai@hzdr.de.

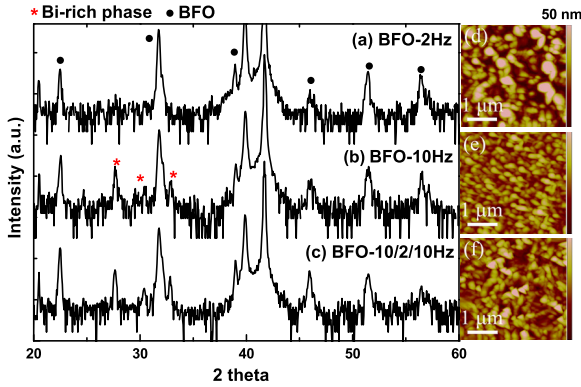


FIG. 1. (Color online) XRD pattern of (a) BFO-2 Hz, (b) BFO-10 Hz, and (c) BFO-10/2/10 Hz, and surface topography of (d) BFO-2 Hz, (e) BFO-10 Hz, and (f) BFO-10/2/10 Hz, respectively.

thin film is formed in BFO-10 Hz with increasing growth rate, which cannot be observed in BFO-2 Hz. The AES results indicate that a higher growth rate aggravates the segregation of Bi near the interface. It is likely due to the fact that with high growth rate the deposition is at a supersaturated state, which favors the formation of the Bi-rich phase.¹¹ The segregation of a Bi-rich phase at the interface has been reported in other literatures.^{12,13}

The leakage current, as shown in Fig. 3(a), has been suppressed by two orders of magnitude by simply increasing the growth rate. To get further insight into the electric properties, the conduction mechanism of the BFO thin films are investigated by plotting $\log J/E$ versus $E^{1/2}$ or $\log J$ versus $E^{1/2}$, corresponding to Poole-Frenkel (PF) emission or Schottky (SE) emission,¹⁴ respectively. PF emission is a bulk-limited while SE is an interface-limited conduction mechanism. The following formulas describe the J-E characteristics related with these two conduction mechanisms:

$$J = BE \exp - \left(\frac{E_I}{kT} - \frac{q}{kT} \sqrt{\frac{qE}{\pi\epsilon_0 K}} \right) \quad (1)$$

$$J = A^* T^2 \exp - \left(\frac{\varphi_b}{kT} - \frac{q}{kT} \sqrt{\frac{qE}{4\pi\epsilon_0 K}} \right). \quad (2)$$

The J-E curve of the BFO-2 Hz sample is well fitted to the log-linear form $\log J/E \sim E^{1/2}$ as illustrated in Fig. 3(b). The values of the optical dielectric constant K calculated from the slopes of the fitting using Eq. (1) are 5.68 and 6.51 for positive bias and negative bias, respectively. The reflection index n of pure BFO has been reported to be 2.5.¹⁵ Consequently an optical dielectric constant $K=n^2=6.25$ is

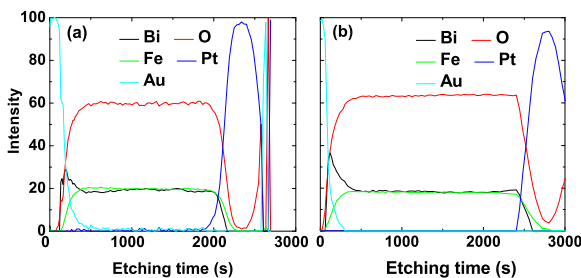


FIG. 2. (Color online) Depth profile of the (a) BFO-2 Hz and (b) BFO-10 Hz measured by AES.

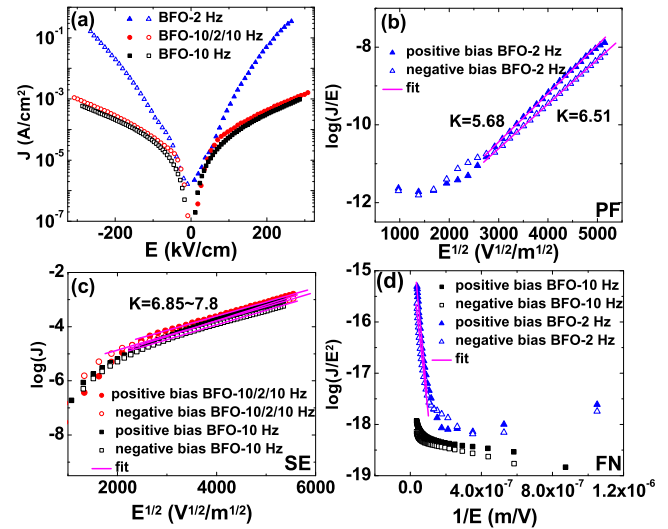


FIG. 3. (Color online) J-E curves of BFO thin films plotted on (a) $\log J \sim E$, (b) $\log J/E \sim E^{1/2}$, (c) $\log J \sim E^{1/2}$, and (d) $\log J/E^2 \sim 1/E$ scale.

expected, to which the calculated K values are very close. Therefore, PF is believed to dominate the conduction in BFO-2 Hz.

On the other hand, the fitting for BFO-10 Hz on a $\log J/E \sim E^{1/2}$ scale results in unreasonable optical dielectric constant K (not shown), which excludes the PF conduction mechanism. While the K values calculated using the fitting slopes in $\log J \sim E^{1/2}$ form and Eq. (2) amount to 6.3 and 7.3 for the two bias polarities, respectively [Fig. 3(c)]. These K values are in good agreement with the expected value of 6.25. With increasing growth rate, e.g., in the BFO-10 Hz sample, the SE conduction mechanism dominates.

It has been reported that the Bi-rich phase in BFO thin films has a high conductivity and can cause a large leakage current.^{16,17} Here we show that the BFO-10 Hz which contains a Bi-rich layer at the interface has a considerably reduced leakage current. Therefore, the interface between the electrode and the thin films, favoring the interface-limited SE conduction, plays a more important role than the presence of impurity phase. In order to confirm this conclusion, we prepared the third sample BFO-10/2/10 Hz. Although the leaky BFO-2 Hz layer constitutes ca. 80% of the BFO stack in BFO-10/2/10 Hz, the leakage current is still decreased by nearly two orders of magnitude as compared to BFO-2 Hz, and is only slightly higher than that in BFO-10 Hz [Fig. 2(a)]. As shown in Fig. 2(c), SE also dominates the high electric field region of BFO-10/2/10 Hz, which is similar to BFO-10 Hz. This is the direct evidence that the leakage current in the BFO-10 Hz sample is mainly controlled by the interface and not by the bulk thin film if a high Schottky barrier is formed.

The growth rate does play an important role in BFO thin film growth, it has however been neglected in recent years. Only a few groups have paid attention to this key parameter. For example, Shelke *et al.*¹⁸ grew epitaxial BFO thin films on (100)-SrTiO₃ substrates with various repetition rates and observed significantly reduced leakage current in high repetition grown thin film. Figures 1(d)–1(f) illustrates the topography of the BFO thin films. With increasing repetition rate the corresponding surface roughness decreases from 14.1 to 4.2 nm. The low surface roughness enables the formation of a Schottky barrier between the top electrode and

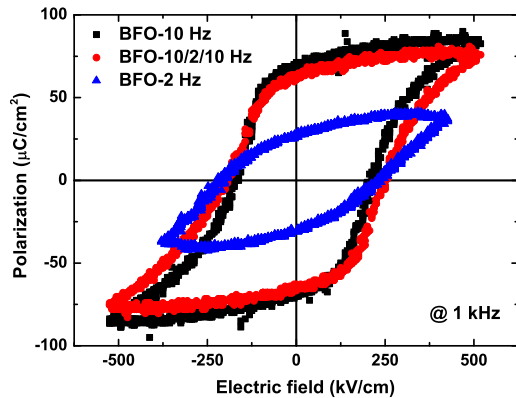


FIG. 4. (Color online) P-E field loops of BFO-10 Hz, BFO-10/2/10 Hz, and BFO-2 Hz.

the thin film. Furthermore, a high growth rate can reduce island size and increase the island density during the very beginning of the growth,¹⁹ leading to more compact thin films, which are also seen in Figs. 1(d)–1(f). Both smooth surface and compact thin film significantly decrease the concentration of defects and surface charges at the top and bottom electrode interfaces. It is known that both Pt and Au possess high work function. Therefore, in principle a Schottky contact should be formed when n-type BFO thin films are in contact either with Au or Pt. However, the rough surface and a large amount of defects cause a large number of charges in BFO-2 Hz and therefore considerably reduce the contact barrier.

Figure 4 shows the P-E loops of BFO-2 Hz, BFO-10 Hz, and BFO-10/2/10 Hz thin films. As expected, BFO-2 Hz exhibits an unsaturated P-E loop with a remanent polarization P_r of only $27 \mu\text{C}/\text{cm}^2$ due to the large leakage current. On the other hand, both BFO-10 Hz and BFO-10/2/10 Hz show well saturated P-E loops with nearly the same P_r of as large as $65 \mu\text{C}/\text{cm}^2$, which is comparable with epitaxial BFO thin films grown on single crystalline substrate.^{20,21}

In summary, BFO thin films show suppressed leakage currents as the growth rate increases. A high growth rate induces a higher Schottky barrier at the interface between the electrode and thin film and thus suppresses the leakage current particularly at high electric field and enables saturated P-E field hysteresis loop. Our letter can help to guide future work on ferroelectric memory devices where ferroelectric

thin films with high resistance and low leakage current have to be grown on a metal bottom.

Y.S. would like to thank the China Scholarship Council (Grant No. 2009607011). S.Z. acknowledges the funding by the Helmholtz-Gemeinschaft (Grant No. HGF-VH-NG-713). D.B., and H.S. thank the financial support from the Bundesministerium für Bildung und Forschung (BMBF) under (Grant No. 13N10144).

- ¹H. Naganuma and S. Okamura, *J. Appl. Phys.* **101**, 09M103 (2007).
- ²K. Y. Yun, D. Ricinchi, T. Kanashima, and M. Okuyama, *Appl. Phys. Lett.* **89**, 192902 (2006).
- ³C.-U. Pinnow and T. Mikojaick, *J. Electrochem. Soc.* **151**, K13 (2004).
- ⁴X. Qi, J. Dho, R. Tomov, M. G. Blamire, and J. L. MacManus-Driscoll, *Appl. Phys. Lett.* **86**, 062903 (2005).
- ⁵G. D. Hu, S. H. Fan, C. H. Yang, and W. B. Wu, *Appl. Phys. Lett.* **92**, 192905 (2008).
- ⁶S. K. Singh, K. Maruyama, and H. Ishiwara, *Appl. Phys. Lett.* **91**, 112913 (2007).
- ⁷G. D. Hu, X. Cheng, W. B. Wu, and C. H. Yang, *Appl. Phys. Lett.* **91**, 232909 (2007).
- ⁸S. O. Leontsev and R. E. Eitel, *J. Am. Ceram. Soc.* **92**, 2957 (2009).
- ⁹L. Chen, W. Ren, W. Zhu, Z.-G. Ye, P. Shi, X. Wu, and X. Yao, *Thin Solid Films* **518**, 1637 (2010).
- ¹⁰S. Gupta, A. Garg, D. C. Agrawal, S. Bhattacharjee, and D. Pandey, *J. Appl. Phys.* **105**, 014101 (2009).
- ¹¹X. Qi, P.-C. Tsai, Y.-C. Chen, Q.-R. Lin, J.-C.-A. Huang, W.-C. Chang, and I.-G. Chen, *Thin Solid Films* **517**, 5862 (2009).
- ¹²V. Fruth, M. Popa, J. M. Calderon-Moreno, E. M. Anghel, D. Berger, M. Gartner, M. Anastasescu, P. Osiceanu, and M. Zaharescu, *J. Eur. Ceram. Soc.* **27**, 4417 (2007).
- ¹³S. Yakovlev, J. Zekonyte, C.-H. Solterbeck, and M. Es-Souni, *Thin Solid Films* **493**, 24 (2005).
- ¹⁴X. H. Zhu, H. Béa, M. Bibes, S. Fusil, K. Bouzouhane, E. Jacquet, A. Barthélémy, D. Lebeugle, M. Viret, and D. Colson, *Appl. Phys. Lett.* **93**, 082902 (2008).
- ¹⁵S. Yakovlev, C.-H. Solterbeck, M. Kuhnke, and M. Es-Souni, *J. Appl. Phys.* **97**, 094901 (2005).
- ¹⁶L. You, N. T. Chua, K. Yao, L. Chen, and J. Wang, *Phys. Rev. B* **80**, 024105 (2009).
- ¹⁷H. Béa, M. Bibes, A. Barthélémy, K. Bouzouhane, E. Jacquet, A. Khodan, J.-P. Contour, S. Fusil, F. Wyczisk, A. Forget, D. Lebeugle, D. Colson, and M. Viret, *Appl. Phys. Lett.* **87**, 072508 (2005).
- ¹⁸V. Shelke, V. N. Harshan, S. Kotru, and A. Gupta, *J. Appl. Phys.* **106**, 104114 (2009).
- ¹⁹L. Guan, D. Zhang, X. Li, and Z. Li, *Nucl. Instrum. Methods Phys. Res. B* **266**, 57 (2008).
- ²⁰H. W. Jang, S. H. Baek, D. Ortiz, C. M. Folkman, R. R. Das, Y. H. Chu, P. Shafer, J. X. Zhang, S. Choudhury, V. Vaithyanathan, Y. B. Chen, D. A. Felker, M. D. Biegalski, M. S. Rzechowski, X. Q. Pan, D. G. Schlom, L. Q. Chen, R. Ramesh, and C. B. Eom, *Phys. Rev. Lett.* **101**, 107602 (2008).
- ²¹D. H. Kim, H. N. Lee, M. D. Biegalski, and H. M. Christen, *Appl. Phys. Lett.* **92**, 012911 (2008).

Rise and fall of defect induced ferromagnetism in SiC single crystals

Lin Li,^{1,2} S. Prucnal,² S. D. Yao,¹ K. Potzger,^{2,a)} W. Anwand,³ A. Wagner,³ and Shengqiang Zhou^{2,b)}

¹State Key Laboratory of Nuclear Physics and Technology, School of Physics, Peking University, Beijing 100871, China

²Institute of Ion Beam Physics and Materials Research, Helmholtz-Zentrum Dresden-Rossendorf, P.O. Box 51 01 19, 01314 Dresden, Germany

³Institute of Radiation Physics, Helmholtz-Zentrum Dresden-Rossendorf, P.O. Box 51 01 19, 01314 Dresden, Germany

(Received 4 April 2011; accepted 10 May 2011; published online 3 June 2011)

6H-SiC (silicon carbide) single crystals containing $V_{\text{Si}}-V_{\text{C}}$ divacancies are investigated with respect to magnetic and structural properties. We found that an initial increase in structural disorder leads to pronounced ferromagnetic properties at room temperature. Further introduction of disorder lowers the saturation magnetization and is accompanied with the onset of lattice amorphization. Close to the threshold of full amorphization, also divacancy clusters are formed and the saturation magnetization nearly drops to zero. © 2011 American Institute of Physics. [doi:10.1063/1.3597629]

Ferromagnetism in nominally diamagnetic materials such as H irradiated graphite,¹ Li doped ZnO,² defective TiO₂,³ or SiC (Ref. 4) recently entered the focus of research. Ferromagnetism related to intrinsic point defects^{3,4} can be achieved either by adjusting the growth/annealing conditions or by particle bombardment of the film. Spin-polarized charge carriers, magneto-optical effects, or manipulation of magnetism by external electric fields⁵ are application-relevant effects expected in those materials. Note that the microscopic origin of both the magnetic moments as well as the exchange interaction is not clear in most defective ferromagnetic materials. In contrast, in Ref. 1 it was shown that the magnetic order originates solely from the carbon π -electron system. In Ref. 4, on the other hand, it was shown that in neutron bombarded 6H-SiC single crystals, $V_{\text{Si}}-V_{\text{C}}$ divacancies form local magnetic moments arising from sp states which couple ferromagnetically due to the extended tails of the defect wave functions. While thermal neutron bombardment is a well-suited method for the creation of divacancies within the whole crystal, for applications a less expensive method to create a defined ferromagnetic film is required. Moreover, the location of ferromagnetic defects should be adjustable, as in the case of ion implantation with defined energy. In this letter we show that pronounced ferromagnetic properties of undoped 6H-SiC single crystals can be achieved by irradiation with energetic noble-gas ions serving as chemically neutral triggers for the defect. Moreover, it is shown that the ferromagnetic order breaks down with increasing lattice disorder due to increasing ion fluence.

Structural defects in ion irradiated 6H-SiC single crystals have been studied for long time. For example, in Ref. 6 it was found that 6H-SiC (0001) single crystals irradiated with 800 keV Ne⁺ ions exhibit a structural transition from the crystalline to the amorphous phase. The critical number of irradiation induced displacements per atom (dpa) for complete amorphization amounts to ~ 0.5 dpa at 300 K as was found by Rutherford backscattering and Raman spectroscopy. This value is similar to those obtained in the same

reference for irradiation with other chemically neutral ions such as Ar⁺ (1 MeV), Ar²⁺ (360 MeV), and Xe⁺ (1.5 MeV) which are in the range between 0.4 and 0.5 dpa which demonstrates the high reproducibility of the structural transition. At larger fluences, the thickness of the disordered layer increases. On the other hand, ion implantation generates point-like defects in the crystalline lattice. Using positron annihilation spectroscopy it was found that the $V_{\text{Si}}-V_{\text{C}}$ divacancy, as observed in Ref. 4, is a stable defect which appears under irradiation with different elements such as Ge (Ref. 7) or He.⁸ Defect agglomerations along with amorphization could be observed with increasing ion fluence.⁷

For the experiment, semi-insulating one-side polished 6H-SiC (0001) single crystals from the KMT Corporation (Hefei, China) have been implanted with Ne⁺ ions at an energy of 140 keV. The fluences implanted along with the induced maximum dpa calculated using SRIM-code⁹ are listed in Table I. The fluences have been chosen to not exceed the amorphization threshold of ~ 0.5 dpa specified in Ref. 6. All samples have been implanted at room temperature in order to avoid annealing of the ferromagnetically active defects. The implantation angle was 7° with respect to the surface normal in order to reduce the channeling effect. The projected range of the ions amounts to 185 nm with a straggling of 49 nm.⁹

Magnetometry was performed using a MPMS-XL magnetometer from Quantum Design. The inset of Fig. 1(a) shows the hysteresis loops measured at 5 K for all samples without subtraction of the diamagnetic background. The marginal ferromagnetic hysteresis of the virgin sample [Fig. 1(a),

TABLE I. Sample identifiers, ion energy, ion fluences, and maximum dpa of 6H-SiC single crystals implanted with Ne⁺ ions.

Sample identifier	Energy (keV)	Fluence (cm ⁻²)	Maximum dpa
Virgin			
5X13	140	5×10^{13}	0.024
1X14	140	1×10^{14}	0.048
5X14	140	5×10^{14}	0.24
1X15	140	1×10^{15}	0.48

^{a)}Electronic mail: k.potzger@hzdr.de.

^{b)}Electronic mail: s.zhou@hzdr.de.

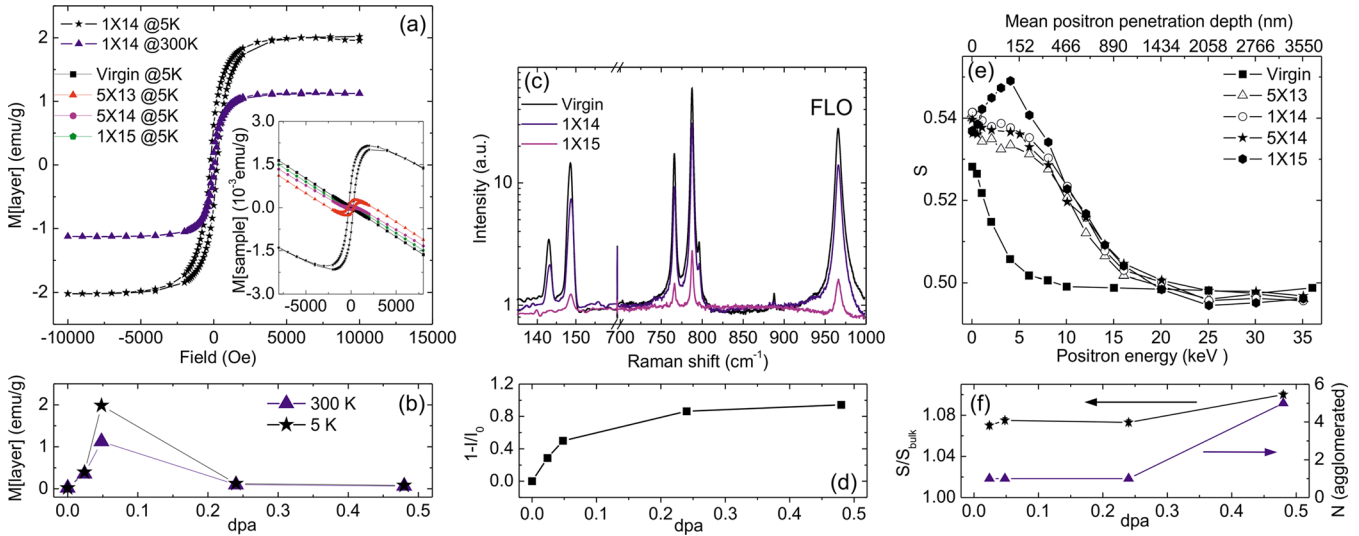


FIG. 1. (Color online) (a) Ferromagnetic hysteresis loops recorded at 5 or 300 K for sample 1X14. The magnetization M was related to a thin layer of 460 nm thickness. The 5 K as-measured loops without subtracting the diamagnetic background are shown in the inset. The magnetization M was related to the whole sample weight. (b) Evolution of the saturation magnetization with the dpa. (c) Raman spectra for virgin and Ne^+ implanted 6H-SiC single crystals. (d) shows the relative intensity variation in the FLO mode marked in (c) along with the dpa. (e) S -parameter depending on positron implantation energy and Ne^+ fluence implanted. Since the positron implantation profile corresponds to a broad Makhov-type distribution (Ref. 12), it probes defects also with the distribution tails, i.e., the mean positron implantation depth does not correspond directly to the geometric depth of the sample. (f) Dependence of the S -parameter (with respect to the bulk value S_{bulk}) as well as the estimated number N (agglomerated) of on the $V_{\text{Si}}-V_{\text{C}}$ divacancies in the cluster on the dpa.

inset] has not been subtracted for the implanted samples and the magnetization $M[\text{sample}]$ has been related to the mass of each sample. For comparison, Fig. 1(a) (main frame) exemplarily displays the ferromagnetic hysteresis loops for sample 1X14 with the largest saturation magnetization M_{S} at both 5 and 300 K. The diamagnetic background has been subtracted and $M[\text{layer}]$ was now related to the mass of a thin film of 460 nm thickness which represents the total thickness of the defective layer obtained from slow positron implantation spectroscopy (SPIS) explained below. The evolution of $M_{\text{S}}[\text{layer}]$ measured at both 5 and 300 K with increasing fluence is displayed in Fig. 1(b). There are several differences as compared to the magnetic data from Ref. 4. First of all, from the inset in Fig. 1(a) there is only a small increase in the slope of the linear background with increasing M_{S} in sharp contrast to Ref. 4. Consequently, the majority of the defect induced magnetic moments are involved in the ferromagnetic coupling. This hints toward a thin ferromagnetic layer defined by the implantation energy rather than a distribution of the moments over the whole sample volume. Second, the hysteresis loops measured at 5 K show larger coercive fields. Finally, after initial increase, M_{S} drops again with increasing fluence. The origin of this behavior is discussed along with structural investigations below.

For structural characterization, μ -Raman spectroscopy using a Nd:YAG laser with 532 nm wavelength recorded in the scattering geometry with a liquid nitrogen cooled charge-coupled device camera has been performed. Figure 1(c) exemplarily displays the Raman spectra for samples virgin, 1X14, and 1X15, respectively. With increasing fluence, the height of the SiC related peaks is reduced, as observed in Ref. 4. This behavior reflects the increasing disorder of the crystalline material with increasing fluence applied. As expected, the relative intensity variation in the folded longitudinal optical (FLO) mode given by $1-I/I_0$ [Fig. 1(d)] nearly reaches saturation for the largest Ne^+ fluence implanted (I_0 represents the maximum intensity for the virgin sample). The

saturation is associated with the threshold for complete amorphization at ~ 0.5 dpa as quantified in Ref. 6. This is in contrast to Ref. 4 where no saturation was observed.

For the investigation of the $V_{\text{Si}}-V_{\text{C}}$ divacancies, monoenergetic SPIS has been performed recording the S -parameter versus the incident positron energy. In brief, the momentum of the electron-positron pair prior to annihilation causes a Doppler broadening of the 511 keV annihilation line and can be characterized by the line-shape parameter S . The value of S is defined by the ratio of counts in the central region of the annihilation gamma peak to the total number of counts in the peak. The energy regions are selected to give $S=0.5$ for the virgin bulk material and then fixed for the irradiated samples. The S -parameter characterizes the positron annihilation with low momentum electrons while it increases with increasing size of the particular open volume defects (e.g., defect clustering). The variation in the incident positron energy enables the measurement of a depth dependence of S . For a more general discussion of SPIS we refer to Refs. 10 and 11. In Ref. 7 it was shown that the $V_{\text{Si}}-V_{\text{C}}$ divacancy in 6H-SiC can be identified by a value of the S -parameter of 0.5375. In Ref. 12, a relationship between the number of clustered divacancies and the S -parameter was established. Figure 1(e) displays the dependence of the S -parameter associated with the $V_{\text{Si}}-V_{\text{C}}$ divacancy on the implantation energy of the positrons and their mean penetration depth. It is evident that the defective region containing divacancies is a thin layer in the near surface region of the 6H-SiC single crystal. An estimation of the thickness d of the damaged layer containing $V_{\text{Si}}-V_{\text{C}}$ divacancies from the SPIS data resulted in $d=460 \pm 25$ nm. As depicted in Fig. 1(e), the S -parameter drastically increases between a fluence of 0.24 and 0.48 dpa reaching a maximum value of 0.55 ($=1.1 S_{\text{bulk}}$, where S_{bulk} represents the defect-free material) for sample 1X15 at a mean positron penetration depth of 120 nm. For comparison, Fig. 1(f) displays the evolution of the S -parameter with respect to S_{bulk} at a penetration depth of

PHYSICAL REVIEW B **84**, 140410(R) (2011)

Frequency dependence of spin relaxation in periodic systems

I. Barsukov,^{1,*} F. M. Römer,¹ R. Meckenstock,¹ K. Lenz,² J. Lindner,¹ S. Hemken to Krax,¹ A. Banholzer,² M. Körner,² J. Grebing,² J. Fassbender,² and M. Farle¹

¹Fakultät für Physik and Center for Nanointegration Duisburg-Essen (CeNIDE), Universität Duisburg-Essen, D-47048 Duisburg, Germany

²Institute of Ion Beam Physics and Materials Research, Helmholtz-Zentrum Dresden-Rossendorf,

P.O. Box 510119, D-01314 Dresden, Germany

(Received 10 October 2011; published 31 October 2011)

We show that in the presence of a periodic scattering potential the spin relaxation in ultrathin ferromagnets is not a monotonous function of the frequency, as has been usually assumed taking intrinsic Gilbert and extrinsic two-magnon processes into account. The spin relaxation rate is found to substantially increase at characteristic frequencies related to the periodicity of the magnon scattering potential. We propose a theoretical model which is experimentally confirmed in Ni₈₀Fe₂₀ thin films by artificially introducing different scattering periodicities. As a result, the current general approach for determining spin relaxation parameters in thin films has to be reconsidered.

DOI: 10.1103/PhysRevB.84.140410

PACS number(s): 76.60.Es, 75.70.Ak, 76.50.+g

Both intrinsic and extrinsic spin relaxation processes are crucial for understanding the magnetization dynamics.^{1–7} While the intrinsic ones, summarized as Gilbert damping, had been known and studied for decades,^{8–10} extrinsic relaxation processes have been analyzed by experimentalists and theoreticians^{1,11–14} in detail only more recently.

When classifying the extrinsic processes,¹⁵ the two-magnon scattering deserves to be paid particular attention. In thin films—probably the most often engineered system in applied magnetism today—the two-magnon scattering among the extrinsic processes is the dominating relaxation mechanism due to inevitable defects in the material. The two-magnon scattering is usually anisotropic in contrast to the Gilbert damping, which is isotropic for the majority of 3*d* metallic systems.^{2,16} Besides the two-magnon scattering's anisotropy and high intensity, its sensitive dependence on the symmetry of defects in the sample made it a matter of investigations into tailoring the spin relaxation.^{1,4,5,17} Also from a fundamental point of view, one must note that pure Gilbert damping is rather a theoretical construct and mostly encountered in combination with extrinsic relaxation processes in a real material. Only in simple systems such as unstructured permalloy thin films is pure Gilbert damping a valid approximation. This fact makes the separation of the intrinsic and extrinsic relaxation processes in the majority of thin-film systems necessary.

In the experiment the presence of extrinsic relaxation is identified by the frequency dependence of the linewidth (ΔB) of the resonant spin precession:^{2,12,18} The Gilbert damping exhibits a linear frequency dependence [Eq. (1)], whereas the two-magnon scattering follows a curved arcsin-like [Eq. (2)] behavior (Fig. 1), which was modeled by Arias and Mills.¹ Here, α denotes the intrinsic damping parameter, γ the spectroscopic splitting factor, $\omega/2\pi$ the precession frequency, and B_{\perp} the effective perpendicular field. Although nonmonotonous linewidth behavior had been considered for disordered polycrystalline systems previously,¹⁵ the monotonous behavior according to Eq. (2) has been used universally for years. Recently, possible deviations from the arcsin behavior of the linewidth came up for discussion,^{19–21} which, to the best of our knowledge, up to now had not been further investigated

due to the lack of an expanded theoretical model:

$$\Delta B_G \propto \frac{\alpha}{\gamma} \omega, \quad (1)$$

$$\Delta B_{2m} \propto \arcsin \sqrt{\frac{\sqrt{\omega^2 + (\gamma B_{\perp}/2)^2} - \gamma B_{\perp}/2}{\sqrt{\omega^2 + (\gamma B_{\perp}/2)^2} + \gamma B_{\perp}/2}}. \quad (2)$$

In this Rapid Communication we show that the frequency dependence of the linewidth may strongly differ from the standard arcsin expression and exhibits even periodic behavior. The two-magnon process depends on the properties of the scattering field determined by the defects. We calculate it for a system with a periodic uniaxial defect matrix, as can be found in nanopatterned or self-organized systems. We compare our theory with experimental results obtained on permalloy (Py = Ni₈₀Fe₂₀) thin films, in which periodic defect stripes have been patterned using ion implantation.

Ion implantation, in combination with lithographically defined masks, opens the possibility to create patterned hybrid magnetic materials.^{22,23} This in turn also allows to influence and tailor the magnetization *dynamics*, i.e., the magnetic damping properties, at the nanoscale.^{5,24,25} A periodic stripelike pattern of the ion-beam-modified Py will serve as the defect matrix introduced above. In a first step, 1×1 mm² square shaped 30-nm-thick Py films with a 3-nm Cr capping layer were grown by molecular beam epitaxy at a base pressure of 1×10^{-10} mbar. Due to the oxidized SiO₂/Si(001) substrate the films grow to be polycrystalline. Electron beam lithography was used to fabricate 1-mm long-stripes of width s_0 and spacing s_1 (i.e., with periodicity $l = s_0 + s_1$) into a 100-nm-thick polymethyl methacrylate (PMMA) resist covering the whole sample area (see Fig. 2). After resist development the samples were implanted with Cr⁺ ions with an energy of 5 keV and a fluence of 5×10^{15} ions/cm². The Cr⁺ ions either get absorbed in the PMMA resist or penetrate the Cr capping layer in between the PMMA stripes, thus reaching the Py layer as depicted in Fig. 2. TRIDYN²⁶ simulations of the depth profiles of the atomic concentrations after Cr⁺ implantation (not shown) reveal that a significant Cr concentration is

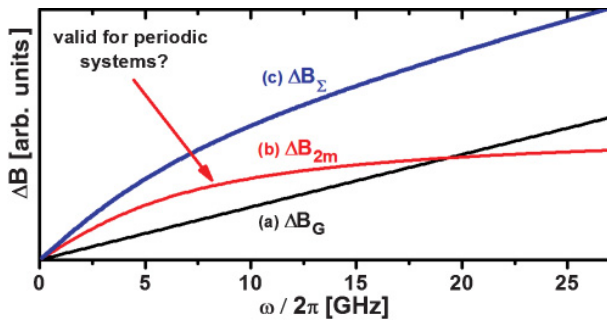
I. BARSUKOV *et al.*PHYSICAL REVIEW B **84**, 140410(R) (2011)

FIG. 1. (Color online) The linewidth as a function of the frequency. (a) The Gilbert contribution ΔB_G is linear. (b) The two-magnon contribution ΔB_{2m} exhibits the arcsin behavior. (c) The resulting linewidth ΔB_Σ is a sum of both contributions.

found in the topmost 7 nm of the sample. The concentration decreases with sample depth, starting with 50 at % Cr at the surface. Note that the ion beam also sputters the capping layer, removing up to 1.5 nm, which is less than the thickness of the capping layer. The Cr^+ dopants cause local variations of the saturation magnetization,^{25,27} whereas in Py no anisotropy is induced thereby. Therefore, we obtain samples in which the magnetization varies laterally, causing dipolar fields between the striplike defects.

Magnetic anisotropy and relaxation of such samples with different periodicities were studied by ferromagnetic resonance (FMR). Using a cylindrical microwave cavity at 9.8 GHz, in-plane angular-dependent FMR measurements have been performed. At room temperature, samples with periodic defect structures, as well as unmodified samples of $\text{Ni}_{80}\text{Fe}_{20}$ thin films, reveal a very small in-plane uniaxial anisotropy field $K_2/M < 0.02$ mT and an effective perpendicular field $B_\perp = \mu_0 M_{\text{eff}} = 0.81(1)$ T. The resonance fields of the samples with striplike modifications show, in addition, lateral confinement effects for external field orientations close to the stripes' normal, which were reported in detail in Ref. 28. The in-plane angular dependence of the linewidth of these samples exhibits uniaxial behavior with maxima for field directions perpendicular to the stripes and minima for directions parallel to the stripes. This uniaxial behavior is

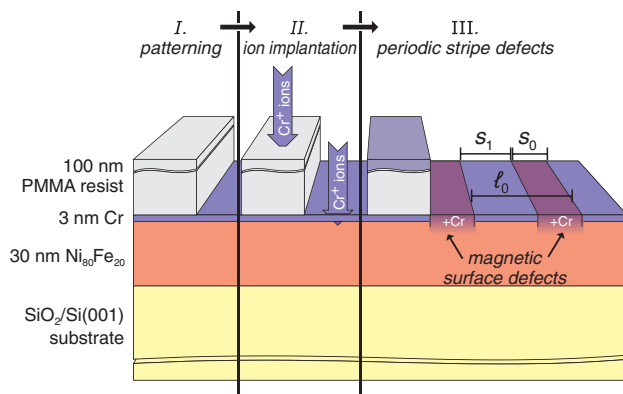


FIG. 2. (Color online) Sketch of the sample before and after ion implantation with Cr^+ . Ions are stopped either in the resist or in the $\text{Cr}/\text{Ni}_{80}\text{Fe}_{20}$ interface region, resulting in periodic stripe defects.

explained by the two-magnon scattering induced by dipolar interactions between the striplike defects in the sample, as described in Refs. 17 and 29. Samples with different stripe periodicities measured at 9.8 GHz showed variations of the two-magnon scattering strength perpendicular to the stripes. This observation motivated the study of the frequency dependence of the linewidth. A shorted coaxial microwave cable with a special end design was used to detect broadband FMR.³⁰ In-plane measurements in the *quasicontinuous* frequency range of 2–26 GHz were performed for directions parallel and perpendicular to the stripes.

In Fig. 3(a) the experimental frequency dependence of the linewidth for the magnetic field applied parallel to the stripes is shown. The general behavior of the linewidth frequency dependence is not affected by the direction of the external magnetic field in one single sample. The convex curvature is related to the high modulation field used to increase the signal-to-noise ratio. Additional measurements (not shown here) show no isotropic two-magnon relaxation channel due to, e.g., grain-grain effects³¹ in these polycrystalline samples. With the results shown in Fig. 3 we conduct comparative studies:

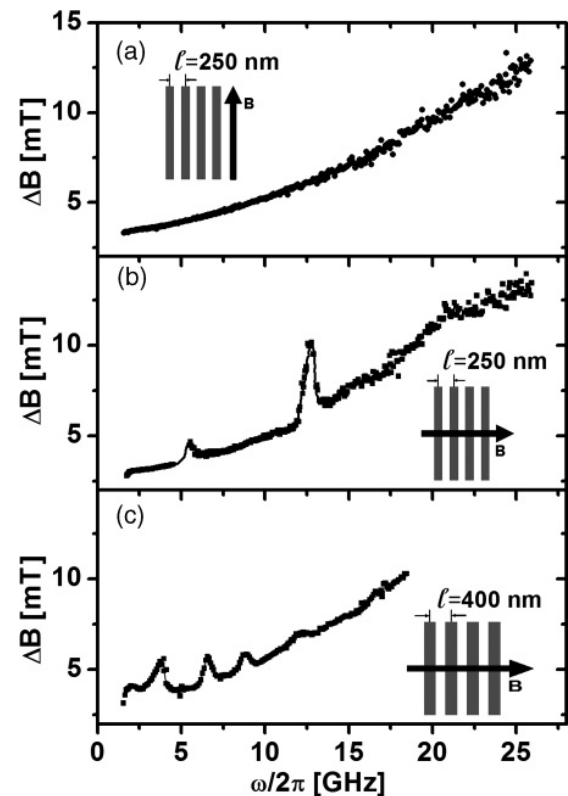


FIG. 3. Frequency dependence of the FMR linewidth of two samples structured with striplike defects. While the general behavior is the same within one single sample for B parallel to the stripes (a) and B perpendicular to the stripes (b), for the latter configuration additional peaks due to the two-magnon scattering occur. Increasing the defect's periodicity l from 250 to 400 nm in the second sample changes the position of the peaks and therefore the frequency dependence of the overall spin relaxation. Error bars are $\leq 15\%$. In (c) the frequency range is limited due to technical reasons. Solid lines are guides for the eye.

When the external magnetic field is applied perpendicular to the stripes, the behavior of the linewidth frequency dependence becomes nonmonotonous and is related to the two-magnon scattering process, which is known to be activated in such a configuration.^{17,29} One finds a large peak at ~ 12.7 GHz and two smaller ones at ~ 5.4 and ~ 21.2 GHz. These appear only for the direction perpendicular to the stripes. Yet the arcsin-like frequency dependence according to the Arias and Mills model¹ does not exhibit a nonmonotonous or even periodic behavior observed in experiment. In order to solve this problem, the mechanism of the two-magnon scattering is reconsidered in the following.

The dispersion relation of magnons parallel to the magnetization in a thin film is given by¹

$$\omega = \gamma \left[\left(B + \mu_0 M_s \left(1 - \frac{1 - e^{-kd}}{kd} \right) \sin^2 \phi_k + Dk^2 + B_{\text{MAE1}} \right) \times \left(B + B_{\perp} - \mu_0 M_s \left(1 - \frac{1 - e^{-kd}}{kd} \right) + Dk^2 + B_{\text{MAE2}} \right) \right]^{1/2}. \quad (3)$$

ω is a function not only of the wave vector k , but also of the external magnetic field B and sample parameters such as saturation magnetization M_s , effective perpendicular field B_{\perp} , spin-wave stiffness D , film thickness d , the spectroscopic splitting factor $\gamma = \mu_B g / \hbar$, and parameters B_{MAE1} and B_{MAE2} , which are functions of very small anisotropy fields. Here, ϕ_k describes the critical angle between the magnetization and the wave vector for which the scattering can occur. As explained in detail in Ref. 1, ϕ_k is very small, so that $\sin \phi_k \approx 0$. In a two-magnon process a uniform magnon with $k = 0$ is scattered into a nonuniform state with the same energy and different wave vector $k_S \neq 0$, as shown in Fig. 4. Due to the local nature of this scattering process the momentum conservation can be violated.¹⁵ In order to find the wave vector of such a final-state magnon one needs to solve the following equation:

$$\omega(k = 0) = \omega(k_S). \quad (4)$$

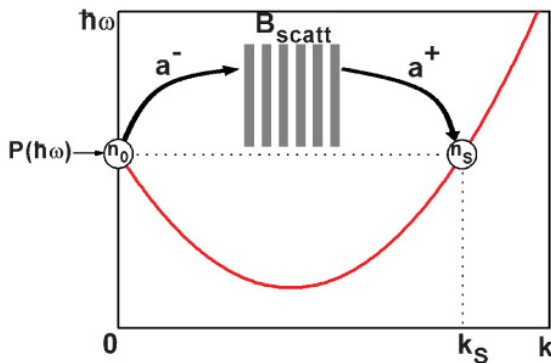


FIG. 4. (Color online) Dispersion relation of magnons in a thin film according to Eq. (3), which includes dipolar interaction, causing a minimum. In a two-magnon scattering process activated by the scattering field B_{scatt} , a uniform magnon $n_0 = |\hbar\omega, k = 0\rangle$, excited by a microwave field P , is annihilated (a^-) and a final state magnon $n_S = |\hbar\omega, k_S \neq 0\rangle$ is created (a^+).

By doing so, one finds that the frequency is eliminated as independent variable. However, the value of k_S still depends on the external field as it is linked to the frequency by the resonance condition of the uniform precession given by Eq. (3) for $k = 0$. Thus, the wave vector of the final-state magnons $k_S = k_S(\omega)$ is a monotonously increasing function of the frequency and can be calculated using the values of the effective perpendicular field, anisotropy fields, and g factor ($g = 2.11$) from the experiment and magnetization $M_S = 1.11 \times 10^6$ A/m and exchange stiffness $D = 1.847 \times 10^{-17}$ J/A of permalloy.³² The scattering process itself is enabled by the scattering field, which couples the uniform with the final-state magnons. The coupling strength and consequently the FMR linewidth scale with the square of the Fourier transform of the scattering field for $k = k_S$,^{33,34} being thus a function of frequency,

$$\Delta B_{2m}(\omega) \propto |\mathcal{F}\{B_{\text{scatt}}\}[k = k_S(\omega)]|^2. \quad (5)$$

Although the exact functional form of the material's scattering field is not known, it is also periodic. Due to the periodicity l of the defects, the Fourier transform of the scattering field can be assumed to have maxima for k values being a multiple of the periodicity $2\pi/l$ of the stripelike defects in the reciprocal space (see Fig. 2). This requirement can be accounted for phenomenologically by multiple Gauss profiles at these values according to

$$|\mathcal{F}\{B_{\text{scatt}}\}(k)|^2 \propto \sum_{n \in \mathbb{N}} \exp\left(-\frac{(n\frac{2\pi}{l} - k)^2}{2\sigma^2}\right). \quad (6)$$

The frequency dependence of the linewidth according to Eqs. (5) and (6) has been calculated numerically for different periodicities of the scattering field and is shown in Fig. 5. For

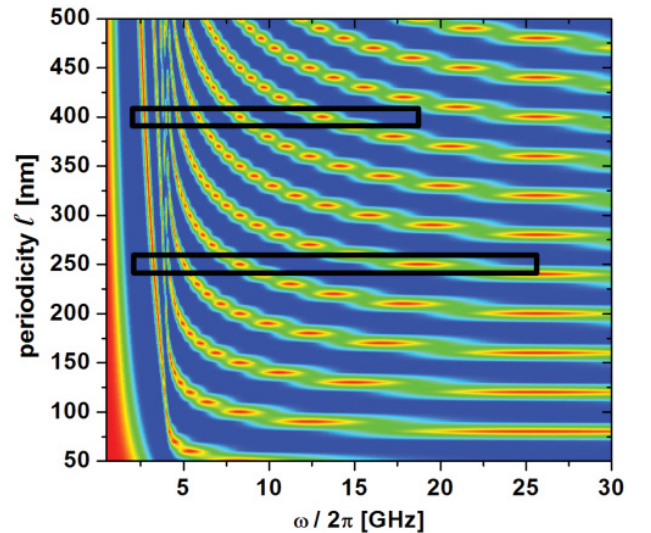


FIG. 5. (Color online) Color-coded normalized linewidth (scattering strength) according to Eqs. (5) and (6). The sections at $l = 250$ and 400 nm correspond to the frequency dependences of the linewidth shown in Figs. 3(b) and 3(c). The red (light gray) color means a larger linewidth than blue (dark gray). Elliptical structures appear due to limited numerical accuracy.

I. BARSUKOV *et al.*PHYSICAL REVIEW B **84**, 140410(R) (2011)

the experimental periodicities $l = 250$ and 400 nm (Fig. 3) the frequency dependence is represented by the horizontal line profile. A quantitative agreement depends very sensitively on the knowledge of the static magnetic parameters (e.g., local magnetization). The calculation confirms the experimental observation qualitatively very well. From Fig. 5 one directly recognizes which periodicity of defect structures must be patterned to enhance the spin relaxation rate in a ferromagnetic film. Based on the intrinsic relaxation of the material, additional enhancements by up to factor of 2 can be induced at chosen frequencies. The width of the peaks in Fig. 3(c) is determined not only by the angle between the line profile and the “structures” in Fig. 5, but also by the parameter σ in Eq. (6), representing the k -value selectivity of the scattering field. The exact form of the material’s scattering field would need to be known to calculate σ as well as the absolute scattering rate. Our theory is based on the general scattering field approach^{15,33,34} and could benefit from the Arias and Mills theory,¹ if it could be extended to a larger class of periodic defect structures.³⁵ Since the latter, which is beyond the scope of the present Rapid Communication, allows a transition to magnonic crystals, magnonic band gaps and the anomalous damping of the final-state magnons should also be taken into consideration.

In conclusion, we present a phenomenologic theory of the two-magnon scattering in periodically structured thin-film systems, which is confirmed by the experiment very well. Our results demonstrate that the frequency dependence of the overall spin relaxation in a large class of ferromagnetic systems is nonmonotonous and depends on the defect structure. Consequently, the usual practice of separation of intrinsic and extrinsic spin relaxation processes by means of their frequency dependence must be reconsidered. The exact structure of defects in a material, being periodic in the majority of ferromagnetic systems, needs to be ascertained first. Our findings are important for future developments, since they could explain the anomalous spin relaxation in magnonic crystals and help to tailor spin relaxation in spintronic devices by artificially inducing a defect structure to activate a desired spin relaxation channel in a specific frequency range.

We thank V. Kühn and I. Winkler for their help with the sample preparation and ion implantation. This work was supported by the DFG, SFB 491, Grants No. FA 314/6-1 and No. FA 314/3-2. I.B. thanks D. Mills and K. Baberschke for fruitful discussions.

*igor.barsukov@uni-due.de

¹R. Arias and D. L. Mills, *Phys. Rev. B* **60**, 7395 (1999).²K. Zakeri, J. Lindner, I. Barsukov, R. Meckenstock, M. Farle, U. von Hörsten, H. Wende, W. Keune, J. Rucker, and S. S. Kalarickal *et al.*, *Phys. Rev. B* **76**, 104416 (2007).³J. Lindner, K. Lenz, E. Kosubek, K. Baberschke, D. Spoddig, R. Meckenstock, J. Pelzl, Z. Frait, and D. L. Mills, *J. Magn. Magn. Mater.* **272-276**, E1653 (2004).⁴G. Woltersdorf and B. Heinrich, *Phys. Rev. B* **69**, 184417 (2004).⁵R. D. McMichael, D. J. Twisselmann, J. E. Bonevich, A. P. Chen, and W. F. Egelhoff Jr., *J. Appl. Phys.* **91**, 8647 (2002).⁶M. C. Hickey and J. S. Moodera, *Phys. Rev. Lett.* **102**, 137601 (2009).⁷V. Kamberský, *Phys. Rev. B* **76**, 134416 (2007).⁸T. L. Gilbert, *IEEE Trans. Magn.* **40**, 3443 (2004).⁹V. Kamberský, *Czech. J. Phys. B* **26**, 1366 (1976).¹⁰C. Scheck, L. Cheng, I. Barsukov, Z. Frait, and W. E. Bailey, *Phys. Rev. Lett.* **98**, 117601 (2007).¹¹P. Krivosik, N. Mo, S. Kalarickal, and C. E. Patton, *J. Appl. Phys.* **101**, 083901 (2007).¹²S. S. Kalarickal, P. Krivosik, M. Wu, C. E. Patton, M. L. Schneider, P. Kabos, T. J. Silva, and J. P. Nibarger, *J. Appl. Phys.* **99**, 093909 (2006).¹³M. C. Weber, H. Nembach, B. Hillebrands, M. J. Carey, and J. Fassbender, *J. Appl. Phys.* **99**, 08J308 (2006).¹⁴V. E. Demidov, O. Dzyapko, S. O. Demokritov, G. A. Melkov, and A. N. Slavin, *Phys. Rev. Lett.* **99**, 037205 (2007).¹⁵C. W. Haas and H. B. Callen, *Magnetism* (Academic, New York, 1963), Vol. I.¹⁶J. Seib, D. Steiauf, and M. Fähnle, *Phys. Rev. B* **79**, 092418 (2009).¹⁷I. Barsukov, R. Meckenstock, J. Lindner, M. Möller, C. Hassel, O. Posth, M. Farle, and H. Wende, *IEEE Trans. Magn.* **46**, 2252 (2010).¹⁸J. Lindner and K. Baberschke, *J. Phys.: Condens. Matter* **15**, S465 (2002).¹⁹K. Zakeri, J. Lindner, I. Barsukov, R. Meckenstock, M. Farle, U. von Hörsten, H. Wende, W. Keune, J. Rucker, and S. S. Kalarickal *et al.*, *Phys. Rev. B* **80**, 059901(E) (2009).²⁰J. Lindner, I. Barsukov, C. Raeder, C. Hassel, O. Posth, R. Meckenstock, P. Landeros, and D. L. Mills, *Phys. Rev. B* **80**, 224421 (2009).²¹K. Baberschke (private communication).²²L. Folks, R. E. Fontana, B. A. Gurney, J. R. Childress, S. Maat, J. A. Katine, J. E. E. Baglin, and A. J. Kellock, *J. Phys. D* **36**, 2601 (2003).²³J. Fassbender and J. McCord, *J. Magn. Magn. Mater.* **320**, 579 (2008).²⁴J. Fassbender and J. McCord, *Appl. Phys. Lett.* **88**, 252501 (2006).²⁵J. Fassbender, J. von Borany, A. Mücklich, K. Potzger, W. Möller, J. McCord, L. Schultz, and R. Mattheis, *Phys. Rev. B* **73**, 184410 (2006).²⁶W. Möller, W. Eckstein, and J. P. Biersack, *Comput. Phys. Commun.* **51**, 355 (1988).²⁷J. O. Rantschler, R. D. McMichael, A. Castillo, A. J. Shapiro, J. W. F. Egelhoff Jr., B. B. Maranville, D. Pulgurtha, A. P. Chen, and L. M. Connors, *J. Appl. Phys.* **101**, 033911 (2007).²⁸R. Meckenstock, I. Barsukov, C. Bircan, A. Remhof, D. Dietzel, and D. Spoddig, *J. Appl. Phys.* **99**, 08C706 (2006).²⁹I. Barsukov, P. Landeros, R. Meckenstock, J. Lindner, B. Krumme, H. Wende, D. L. Mills, and M. Farle (unpublished).³⁰N. Benatmane, S. P. Crane, F. Zavaliche, R. Ramesh, and T. W. Clinton, *Appl. Phys. Lett.* **96**, 082503 (2010).³¹S. S. Kalarickal, Nan Mo, P. Krivosik, and C. E. Patton, *Phys. Rev. B* **79**, 094427 (2009).³²Z. Frait, *Phys. Status Solidi B* **3**, K408 (1963).³³B. Heinrich and J. A. C. Bland, *Ultrathin Magnetic Structures* (Springer, Berlin, 1994), Vols. I–III.³⁴M. Sparks, *Ferromagnetic-Relaxation Theory* (McGraw-Hill, New York, 1964).³⁵P. Landeros and D. L. Mills (unpublished).

Spatial manipulation of magnetic damping in ferromagnetic-antiferromagnetic films by ion irradiation

Jeffrey McCord,^{1,*} Thomas Strache,¹ Ingolf Mönch,² Roland Mattheis,³ and Jürgen Fassbender¹

¹Helmholtz-Zentrum Dresden Rossendorf e.V., P.O. Box 510119, D-01314 Dresden, Germany

²Leibniz Institute for Solid State and Materials Research IFW Dresden, P.O. Box 270116, D-01171 Dresden, Germany

³IPHT Jena, Albert-Einstein-Straße 9, D-07745 Jena, Germany

(Received 22 February 2011; published 20 June 2011)

The spatial manipulation of the effective magnetic damping parameter in ferromagnetic-antiferromagnetic-ferromagnetic film systems is shown. By applying ultrathin antiferromagnetic layers in Ni₈₁Fe₁₉/IrMn/Ni₈₁Fe₁₉ sandwich structures in combination with low fluence Ni-ion irradiation, a lateral control of the effective magnetic damping parameter is achieved. With irradiation, an interfacial intermixing and roughening is introduced, by which the interfacial coupling mechanisms and the magnetic state of the interlayer are altered. We find an exponential decay of all relevant magnetic property parameters with irradiation. Local irradiation is then applied to generate a magnetic layer with spatially distributed regions of different values of damping. The resulting overall relaxation time of the mixed property film is a direct superposition of the individual relaxation contributions. Thereby, the ratio of the phases with individual damping parameter determines the resulting overall damping.

DOI: [10.1103/PhysRevB.83.224407](https://doi.org/10.1103/PhysRevB.83.224407)

PACS number(s): 75.70.-i

I. INTRODUCTION

The control of static and especially dynamic magnetic response of ferromagnetic (F) thin films is one of the biggest challenges in applied magnetism. Therefore, the adjustment of magnetic anisotropy and the connected resonance frequency, as well as the magnetic damping parameter, are of fundamental importance to ensure functionality in existing and envisioned spintronic applications.¹⁻³ One possibility to influence the magnetic properties of thin films is the modification of the bulk material's properties, such as changing the composition of the material.⁴ Recently, it has been shown that by introducing rare-earth or transition metals, the magnetic damping parameter in F films can be altered in the ferromagnetic parent material.⁵⁻⁸ Interfacial contributions in magnetic multilayers facilitate another path of spin engineering of magnetic thin-film properties. The most prominent example is the introduction of out-of-plane perpendicular anisotropy in magnetic multilayers.⁹ For such systems, it has been shown that the magnetic anisotropy can be converted from out-of-plane to in-plane in character by ion-irradiation-induced interfacial mixing, hence creating a magnetic property patterning.¹⁰ Moreover, a transition from antiferromagnetic to ferromagnetic coupling by local ion irradiation has been achieved in exchange-coupled sandwich structures.¹¹ Another relevant area of interface magnetism is the creation of a unidirectional anisotropy or exchange bias with the use of antiferromagnetic (AF) materials in thin-film multilayers,¹²⁻¹⁵ by which also a congruent increase of precessional frequency and magnetic damping is initiated.¹⁶⁻¹⁹ The origin of the AF layer-induced enhancement of damping is due to a combination of two-magnon scattering and additional interfacial magnetic dispersion effects.^{16,20} For very thin AF layer thickness, below or around the onset of exchange bias, a local spin fluctuation based contribution to damping from quasi-superparamagnetic AF grains is discussed.²¹ In this paper, we demonstrate the spatial and exclusive tailoring of magnetic damping effects in F-AF-F sandwich structures by ion irradiation. The modification is achieved with a minimal influence on other magnetic properties.

II. SAMPLE PREPARATION

A series of Si-SiO₂-Ta(4 nm)-Ni₈₁Fe₁₉ (15 nm)-Ir₂₃Mn₇₇-Ni₈₁Fe₁₉ (15 nm) sandwich structures with varying AF layer thickness $t_{\text{IrMn}} = 0-2.50$ nm were prepared by dc-magnetron sputtering in a multitarget ultrahigh-vacuum sputter system with a base pressure below 23×10^{-8} Torr at an Ar pressure of 53×10^{-3} Torr. To induce a uniaxial magnetic anisotropy, a magnetic field $H_{\text{dep}} = 100$ Oe was applied during film deposition. No protection layers were used to avoid secondary intermixing effects during ion irradiation. Therefore, for the given sandwich structure, only Ni₈₁Fe₁₉ to IrMn interfaces are relevant. No post-annealing steps, which potentially would induce additional mixing at the interface, were performed.

III. EXPERIMENTS AND DISCUSSION

The quasistatic reversal characteristics were deduced from inductive magnetometry. The exchange-bias field H_{eb} was obtained from the magnetization loop shift along the magnetically easy axis parallel to H_{dep} . The variation of coercivity H_c and field H_{eb} with t_{IrMn} is displayed in Fig. 1. For $t_{\text{IrMn}} \leq 2.50$ nm, no exchange bias is observed, only H_c increases sharply around $t_{\text{IrMn}} = 2.25$ nm. Below that thickness, only a minor increase of H_c with t_{IrMn} is found (see also the inset of Fig. 1). This behavior is in agreement with the results obtained from regular bilayer F/AF systems.^{17,22} Effects from different coupling strengths²³ from the top (F/AF) or bottom (AF/F) AF interface are not observed below the onset of exchange bias.

The corresponding dynamic magnetic properties of the films were characterized by pulsed inductive microwave magnetometry (PIMM),²⁴ whereby the precessional frequency f_{res} and the effective magnetic damping parameter α_{eff} and relaxation time τ_{rel} , respectively, were derived from analysis of the damped oscillation of the measurement signal.²⁵ All measurements were performed with an applied magnetic field H_{bias} to ensure a single magnetic domain state. Exemplary measurement data for different t_{IrMn} are shown in Fig. 2(a). Comparing Fig. 1(d) to Fig. 2(d), the AF-induced increase of

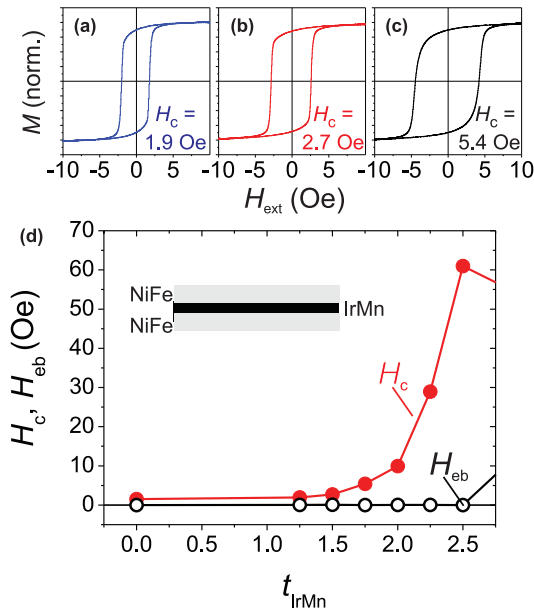


FIG. 1. (Color online) (a)–(c) Magnetization loops obtained from $Ni_{81}Fe_{19}$ (15 nm)-IrMn (t_{IrMn})- $Ni_{81}Fe_{19}$ (15 nm) trilayers with different AF layer thickness $t_{IrMn} = 1.25, 1.50,$ and 1.75 nm. The respective coercive fields H_c are indicated. (d) Change of H_c and exchange bias field H_{eb} with t_{IrMn} . The principal structure of the layer stack is indicated.

f_{res} starts at $t_{IrMn} = 1.75$ nm, which is well below the appearance of exchange bias. Moreover, α_{eff} sets in at even lower values of AF thickness, almost doubling at $t_{IrMn} = 1.50$ nm and then drastically increasing up to a value of $\alpha_{eff} = 0.055$ for $t_{IrMn} = 1.75$ nm. Overall, a major change of static and

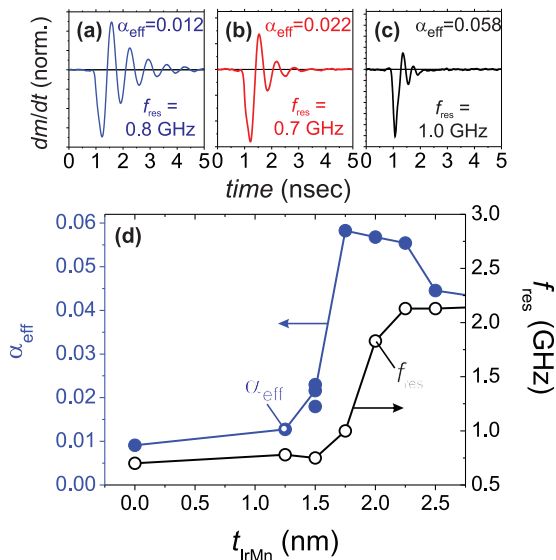


FIG. 2. (Color online) (a)–(c) Dynamic magnetic response dm/dt to a rf-magnetic pulse field²⁴ in $Ni_{81}Fe_{19}$ (15 nm)-IrMn- $Ni_{81}Fe_{19}$ (15 nm) structures for $t_{IrMn} = 1.25, 1.50,$ and 1.75 nm. A magnetic bias field $H_{bias} = 30$ Oe is applied during the measurements. The values of zero-field precessional frequency f_{res} and effective magnetic damping parameter α_{eff} are indicated. (d) Variation of f_{res} and α_{eff} with AF layer thickness t_{IrMn} .

dynamic magnetic properties is achieved by varying t_{IrMn} by only 1.0 nm. However, within this small range of AF layer thickness, the onset of magnetic property change is different for the individual magnetic property parameters. As will be shown next, the incremental onset of magnetic property alteration facilitates the almost exclusive adjustment of α_{eff} .

For that reason, a sandwich with $t_{IrMn} = 1.5$ nm was irradiated with Ni ions of different fluence. Ni as an element was chosen, as it is the main component of the F film in the sandwich structure and therefore only minor compositional changes in the F material are obtained with ion irradiation. The irradiation of the sandwich has two main effects: It introduces roughness at the F-AF interface and it also changes in the material composition around and within the AF layer. To distinguish between both effects, the process of ion irradiation was simulated using the TRIM code of the SRIM package.²⁶ The calculated depth distributions of damage, i.e., the number of target displacements, being the sum of generated vacancies and replacement collisions, of layer atoms per incoming ion is displayed in Fig. 3(a). An irradiation energy of 40 keV was chosen to ensure that the ion-induced damage distribution would be situated within the magnetic layers and would not reach the bottom F-substrate interface. From these results, the mean damage at the AF layer can be

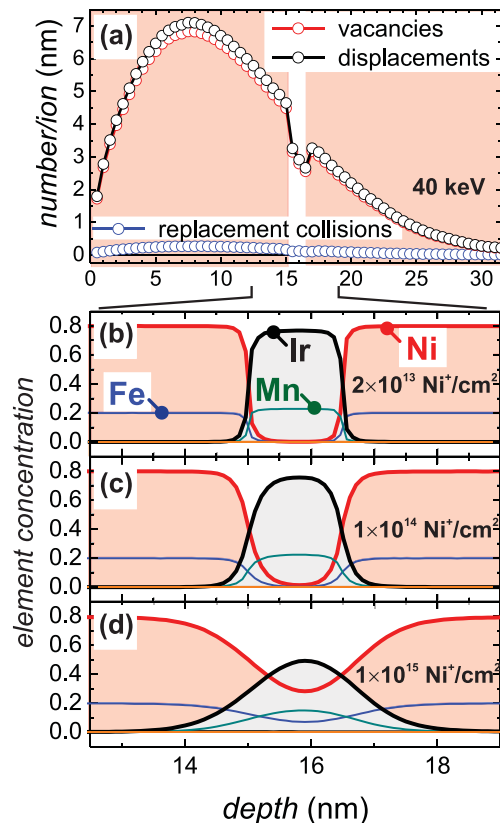


FIG. 3. (Color online) (a) TRIM simulation results of the ion-irradiation impact events per ion with Ni-ion irradiation at 40 keV in $Ni_{81}Fe_{19}$ (15 nm)/IrMn (1.50 nm)/ $Ni_{81}Fe_{19}$ (15 nm). The structure of the layer stack is indicated. (b)–(d) TRIDYN calculation results on interfacial mixing and alloying effects with different amounts of Ni-ion irradiation. The atomic concentrations are shown across the layer boundaries. The individual Ni-ion fluences are indicated.

estimated to approximately four displacements per target atom per 10^{15} cm² incident Ni⁺ ions. The compositional changes with increasing irradiation fluence were derived from Monte-Carlo-based binary collision computer simulations (TRIDYN²⁷) using the same parameters as for the SRIM modeling. The profiles of the atomic species distributions in the center of the Ni₈₁Fe₁₉-Ir₂₃Mn₇₇-Ni₈₁Fe₁₉ stack for different Ni-ion fluences are displayed in Figs. 3(b)–3(d). For low fluences, mainly the interface structure is altered due to interfacial intermixing. The interfaces become more rough. At larger fluences, alloying of the initially AF layer takes place, and a complete compositional alteration of the original IrMn composition is derived from the simulations. Even for the large Ni⁺ fluence of 10^{15} cm², the maximum calculated percentage change of Ni concentration in the original Ni₈₁Fe₁₉ film due to Ni implantation is 0.6%, and thereby no relevant modifications of magnetic properties other than from the intermixing effects are presumed to occur in the layer stack.

The effect of irradiation-induced intermixing at the F-AF interfaces on the static and dynamic magnetic properties is displayed in Fig. 4. The samples were irradiated at room temperature with Ni⁺ ions with different fluences $f(\text{Ni}^+)$. An almost immediate decay of coercivity and damping with fluence is found. This indicates a strong connection between the initial interfacial modifications and the change in magnetic properties. The results are in accordance with irradiation-induced interfacial changes obtained in exchange-bias samples with much thicker AF layers²⁸ as well as with exchange-coupled multilayer films.²⁹ In contrast, ion-induced changes of characteristic magnetic bulk properties occur linearly with irradiation fluence.^{30,31} As expected, no exchange-bias effect is initialized with irradiation. As demonstrated in Fig. 4(b), the

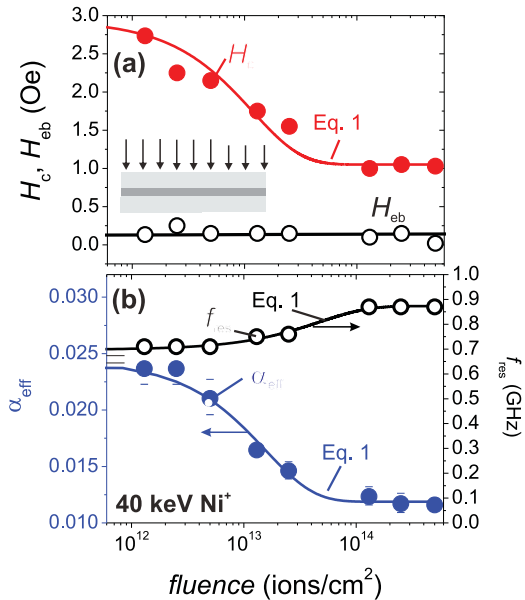


FIG. 4. (Color online) (a) Change of coercivity H_c and exchange bias field H_{cb} with fluence of Ni-ion irradiation in Ni₈₁Fe₁₉ (15 nm)/IrMn (1.50 nm)/Ni₈₁Fe₁₉ (15 nm). (b) Corresponding change of precessional frequency f_{res} and effective magnetic damping parameter α_{eff} . Both graphs are plotted on a semilogarithmic scale.

original precession frequency f_{res} in the sandwich structures increases only by a small amount, $\Delta f_{\text{res}} \approx 100$ MHz, with irradiation. Yet a strong decrease in α_{eff} with increasing fluence is found, approaching a value close to the bulk Ni₈₁Fe₁₉ damping parameter. For the given example, α_{eff} reduces from 0.024 down to 0.011. The change of magnetic properties follows nearly an exponential decay law. The exact origin of this dependency is not clear, but an irradiation-induced increase of interfacial intermixing or roughness is expected to result in a strong and exponential decrease of exchange coupling between the FM and AF layers.^{28,32} The lines in Fig. 4 are fits to the exponential dependency (Fig. (1)). Exemplarily, for $\alpha_{\text{eff}}^{\text{irr}}$ we obtain

$$\alpha_{\text{eff}}^{\text{irr}} = \alpha_{\text{eff}}^{\infty} - C e^{-\frac{f(\text{Ni}^+)}{f_0}}, \quad (1)$$

where $\alpha_{\text{eff}}^{\infty}$ is the saturation value of the damping parameter for strongly intermixed layers. The exponential decay rate f_0 for all magnetic parameters is in the order of $f_0 \approx 5 \times 10^{13}$ cm². The sharp reduction of damping with irradiation also indicates an interfacial origin of increased damping in the F-AF-F structures. Above $f(\text{Ni}^+) = 10^{14}$ cm², the saturation value of magnetic damping $\alpha_{\text{eff}}^{\infty}$ is nearly obtained.

The irradiation-induced change of damping now offers the opportunity to *laterally* change the effective damping parameter, as will be shown in the following. This is achieved by masking the film with a photolithographic mask and then selectively irradiating the magnetic layers, as sketched in Fig. 5(a). For the presented results, the film was masked with a wavelength of 10 μm . By laterally varying the duty cycle of the square

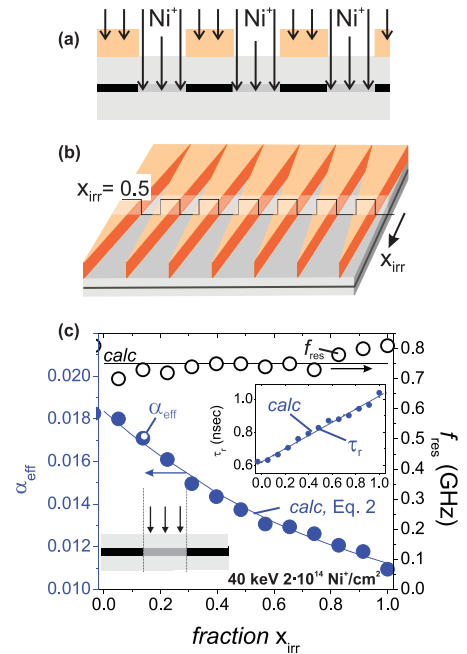


FIG. 5. (Color online) (a) Process of local irradiation through a stripelike photoresist mask. (b) Sample design for obtaining a sample with a gradient in the masked area. (c) Measured change of magnetic damping parameter α_{eff} and precessional frequency f_{res} in dependence on the fraction x_{irr} of the lower damped irradiated lateral phase. The calculated dependences of α_{eff} and τ_r are shown. The linear dependence of the relaxation time is shown in the inset of (c).

irradiation pattern, a linear change from 0 to 1 of irradiated fraction x_{irr} is obtained on a single sample [Fig. 5(b)]. Thereby, sample-to-sample variations are excluded. The dependency of α_{eff} and τ_r with material fraction after Ni irradiation with a fluence of 2×10^{14} is plotted in Fig. 5(c). In addition, the data are also compared to macrospin simulations of the magnetic response to a pulsed magnetic-field excitation, as in the experiments, by solving the Landau-Lifschitz-Gilbert equation.³³ The calculated results, assuming a superposition of both material fractions and analyzed analog to the experimental data, are added to Fig. 5(c). τ_r changes the fraction of the irradiated area linearly with x_{irr} . The overall value α_{eff} thereby varies with

$$\frac{1}{\alpha_{\text{eff}}^x} = \frac{1}{\alpha_{\text{eff}}^{\text{irr}}} x_{\text{irr}} + \frac{1}{\alpha_{\text{eff}}^{\text{nonirr}}} (1 - x_{\text{irr}}) \quad (2)$$

from the initial damping parameter value $\alpha_{\text{eff}}^{\text{nonirr}}$ to $\alpha_{\text{eff}}^{\text{irr}}$ with x_{irr} . In accordance with the results presented before (compare to Fig. 4), the precessional frequency increases slightly with x_{irr} .

IV. CONCLUSION

In conclusion, we demonstrate the use of ultrathin layers of AF materials to laterally manipulate and adjust the effective dynamic magnetic properties of F thin films over a wide

range. The controlled local modification is achieved by ion irradiation, due to ion-induced alterations of coupling across the F-AF interface structure. In the resulting mixed property film, the magnetic damping parameter is a result from a direct superposition of the individual relaxation-time contributions. Elementary dependencies to describe the effect of irradiation fluence and the hybrid magnetic properties are established. Due to the interfacial origin of the effect, the magnetic parameter changes will scale inversely proportional to the ferromagnetic thin-film thickness. Preparing layered F-AF films with mixed multiphase effective properties provides an alternative route for the tailoring of dynamic magnetic properties in soft-magnetic thin films. It should be extendable to other magnetic multilayer samples, exhibiting enhanced interfacial spin scattering.

ACKNOWLEDGMENTS

The authors thank K. Kirsch for help with the film deposition, I. Winkler for help with the ion irradiation, and M. Fritzsche for help with TEM investigations. J.M. and J.F. gratefully acknowledge the support of the Deutsche Forschungsgemeinschaft (DFG MC9/7 and FA314/3). A part of the initial research was performed at the IFW Dresden.

*j.mccord@hzdr.de

¹J. A. Katine, F. J. Albert, R. A. Buhrman, E. B. Myers, and D. C. Ralph, *Phys. Rev. Lett.* **84**, 3149 (2000).

²C. Chappert, A. Fert, and F. N. Van Dau, *Nat. Mater.* **6**, 813 (2007).

³S. Parkin, M. Hayashi, and L. Thomas, *Science* **320**, 190 (2008).

⁴R. O'Handley, *Modern Magnetic Materials: Principles and Applications* (Wiley, New York, 1998).

⁵S. G. Reidy, L. Cheng, and W. E. Bailey, *Appl. Phys. Lett.* **82**, 1254 (2004).

⁶A. Rebei and J. Hohlfield, *Phys. Rev. Lett.* **97**, 117601 (2006).

⁷J. O. Rantschler, R. D. McMichael, A. Castillo, A. J. Shapiro, W. F. Egelhoff, B. B. Maranville, D. Pulugutha, A. P. Chen, and L. M. Conners, *J. Appl. Phys.* **101**, 033911 (2007).

⁸G. Woltersdorf, M. Kiessling, G. Meyer, J.-U. Thiele, and C. H. Back, *Phys. Rev. Lett.* **102**, 257602 (2009).

⁹P. F. Carcia, A. D. Meinhardt, and A. Suna, *Appl. Phys. Lett.* **47**, 178 (1985).

¹⁰C. Chappert *et al.*, *Science* **280**, 1919 (1998).

¹¹S. Demokritov, C. Bayer, S. Poppe, M. Rickart, J. Fassbender, B. Hillebrands, D. Kholin, N. Kreines, and O. Liedke, *Phys. Rev. Lett.* **90**, 097201 (2003).

¹²W. H. Meiklejohn and C. P. Bean, *Phys. Rev.* **102**, 1413 (1956).

¹³J. Nogues and I. K. Schuller, *J. Magn. Magn. Mater.* **192**, 203 (1999).

¹⁴A. Berkowitz and K. Takano, *J. Magn. Magn. Mater.* **200**, 552 (1999).

¹⁵F. Radu and H. Zabel, in *Magnetic Heterostructures, Advances and Perspectives in Spinstructures and Spintransport*, edited by H. Zabel and S. D. Bader, Springer Tracts in Modern Physics Vol. 227 (Springer, Berlin, 2008), pp. 97–183.

¹⁶R. D. McMichael, M. D. Stiles, P. J. Chen, and W. F. Egelhoff, *J. Appl. Phys.* **83**, 7037 (1998).

¹⁷J. McCord, R. Mattheis, and D. Elefant, *Phys. Rev. B* **71**, 094420 (2005).

¹⁸J. McCord, R. Kaltofen, T. Gemming, R. Hühne, and L. Schultz, *Phys. Rev. B* **75**, 134418 (2007).

¹⁹J. McCord, R. Kaltofen, O. G. Schmidt, and L. Schultz, *Appl. Phys. Lett.* **92**, 162506 (2008).

²⁰B. K. Kuanr, R. E. Camley, and Z. Celinski, *J. Appl. Phys.* **93**, 7723 (2003).

²¹R. D. McMichael, C. G. Lee, J. E. Bonevich, P. J. Chen, W. Miller, and W. F. Egelhoff, *J. Appl. Phys.* **88**, 5296 (2000).

²²M. Ali, C. H. Marrows, M. Al-Jawad, B. J. Hickey, A. Misra, U. Nowak, and K. D. Usadel, *Phys. Rev. B* **68**, 214420 (2003).

²³G. Malinowski, M. Hehn, and P. Panissod, *J. Phys. Condens. Matter* **18**, 3385 (2006).

²⁴A. B. Kos, T. J. Silva, and P. Kabos, *Rev. Sci. Instrum.* **73**, 3563 (2002).

²⁵G. Sandler, H. Bertram, T. J. Silva, and T. Crawford, *J. Appl. Phys.* **85**, 5080 (1999).

²⁶J. Ziegler [<http://www.srim.org/>].

²⁷W. Möller and W. Eckstein, *Nucl. Instrum. Methods B* **2**, 814 (1984).

²⁸A. Mougín, T. Mewes, M. Jung, D. Engel, A. Ehresmann, H. Schmoranzler, J. Fassbender, and B. Hillebrands, *Phys. Rev. B* **63**, 060409 (2001).

²⁹S. O. Demokritov, C. Bayer, S. Poppe, M. Rickart, J. Fassbender, B. Hillebrands, D. I. Kholin, N. M. Kreines, and O. M. Liedke, *Phys. Rev. Lett.* **90**, 097201 (2003).

³⁰J. Fassbender and J. McCord, *Appl. Phys. Lett.* **88**, 252501 (2006).

³¹J. McCord, I. Mönch, J. Fassbender, A. Gerber, and E. Quandt, *J. Phys. D* **42**, 055006 (2009).

³²N. J. Gökemeijer, T. Ambrose, and C. L. Chien, *Phys. Rev. Lett.* **79**, 4270 (1997).

³³T. Gilbert, *IEEE Trans. Magn.* **40**, 3443 (2004).

Microstructure analysis at the interface of Er decorated Ge nanocrystals in SiO₂

A. Kanjilal,^{1,*} S. Gemming,¹ L. Rebohle,¹ A. Muecklich,¹ T. Gemming,² M. Voelskow,¹ W. Skorupa,¹ and M. Helm¹

¹Institute of Ion Beam Physics and Materials Research, Forschungszentrum Dresden-Rossendorf, PO Box 51 01 19, D-01314 Dresden, Germany

²Institute for Complex Materials, IFW Dresden, PO Box 27 01 16, D-01171 Dresden, Germany

(Received 16 December 2010; published 8 March 2011)

Using scanning transmission electron microscopy and aberration-corrected high-resolution transmission electron microscopy the existence of Er around Ge nanocrystals (NCs) is established. In fact, Ge NCs with Er-rich graded interfaces are proposed experimentally and validated by theoretical modeling using a *supercell* structure that consists of compounds determined by x-ray diffraction. The local electronic structure of the proposed interface geometry is found to be in accordance with the hypothesis behind the inverse energy transfer process from the Er³⁺ to Ge related oxygen-deficiency centers.

DOI: [10.1103/PhysRevB.83.113302](https://doi.org/10.1103/PhysRevB.83.113302)

PACS number(s): 78.67.Bf, 71.20.Eh, 79.20.Uv, 85.60.Jb

Energy saving light emitters (LEs), especially the production of economic white and bright light-emitting sources based on blue-violet devices enriched with yellow phosphors is a frontier field of research.¹ Successful fabrication of LEs according to Haitz's law¹ relies on the elaborate manufacturing techniques and complex design of LEs. Although semiconductor nanocrystals (NCs)² and/or rare-earth ions^{3,4} in a metal-oxide semiconductor (MOS) structure have shown their potential to develop efficient LEs, they have yet to reach the ultimate goal. In parallel, Si nanoparticles have been used as *sensitizers* in Er-doped SiO₂ for achieving an enhanced 1.53- μ m Er photoluminescence⁵⁻⁸ or electroluminescence (EL).⁹ Recently, alternatives based on Ge nanoparticles in Er-doped MOSLEs have also been demonstrated. Such MOSLEs provide an enhanced 400-nm EL at the expense of the 1.53- μ m Er emission¹⁰⁻¹² and has been explained in the framework of an *inverse energy-transfer* process from the Er³⁺ to the Ge related oxygen-deficiency centers (GeODCs).¹⁰ Note that the 400-nm EL is associated with the first-triplet to the ground-singlet ($T_1 \rightarrow S_0$) transition in GeODCs,¹⁰ whereas the intra- $4f^4 I_{13/2} \rightarrow 4f^4 I_{15/2}$ transition in Er³⁺ leads to the 1.53- μ m Er emission.¹³

Although the existence of Er³⁺ in the vicinity of Ge NCs has been accepted previously to explain the observed EL,¹⁰ detailed microstructure analysis at the NC/SiO₂ interface has not been reported yet. Here, we show the formation of an Er-rich graded interface at the NC-SiO₂ boundary using a combined experimental and theoretical approach. Initially, a theoretical modeling has been developed using a *supercell* structure that consists of compounds determined by x-ray diffraction.¹² In fact, the first principle calculation of the proposed interface geometry gives the local electronic structure, which is in agreement with the hypothesis behind the inverse energy-transfer process from the Er³⁺ to the GeODCs.¹⁰ The Er-rich graded interface model is also corroborated by x-ray structure determination,¹² scanning transmission electron microscopy (STEM),¹⁴ and aberration-corrected high-resolution transmission electron microscopy (HRTEM).¹⁵

The standard metal-oxide-semiconductor structures were fabricated by local-oxidation of Si (LOCOS) technology with a 200-nm-thick thermally grown SiO₂ layer on *n*-type Si(100) wafers. Initially, 130-keV Ge ions were implanted into the

SiO₂ layer, with a maximum concentration in the range of 3.5%–11.1% at $R_p \sim 112$ nm as derived from the SRIM-2006 calculations.¹⁶ The samples were annealed at 950 °C in a nitrogen atmosphere for 60 min. Subsequently, 250-keV Er ions were implanted with a maximum concentration lying in the range of 0.3%–1.4% at $R_p \sim 115$ nm, followed by annealing at 900 °C for 30 min in a nitrogen ambience. A 100-nm-thick Si-oxynitride (SiON) layer was deposited on top of the LOCOS structure, followed by the growth of semi-transparent indium-tin-oxide (ITO) and aluminum contacts on the front and rear surfaces, respectively. The ITO layer was patterned by optical lithography to prepare circular electrodes (diameter ~ 300 μ m). Depth profiles of the implanted elements were verified by performing Rutherford-backscattering spectrometry (RBS) using a 1.4-MeV He⁺ beam. High angle annular dark-field (HAADF)-STEM, HRTEM, energy-filtered TEM (EFTEM), energy-dispersive x-ray spectroscopy (EDS), and electron energy-loss spectroscopy (EELS) measurements were performed in cross-sectional geometry using a FEI-Titan 80-300 S/TEM instrument operating at 300 keV.

On the other hand, density-functional calculations (Fig. 1) were performed with the program package ABINIT,¹⁷ employing the generalized gradient approximation provided by the PBE exchange and correlation functions¹⁸ and the PAW package.¹⁹ An $8 \times 8 \times 4$ Monkhorst-Pack mesh, a plane-wave energy cutoff of 551 eV, and a parameter $U = 7.94$ eV (Ref. 20) for the localized states at the Er centers were applied; the density of states (DOS) curve in Fig. 1(d) is broadened with a Gaussian smearing of 0.125 eV, while the isodensity contours depicted in Fig. 1(c) correspond to 10% of the maximum density of the corresponding state.

Considering the importance of Er³⁺ around Ge NCs in Er-doped Ge-rich MOSLEs,¹⁰ a model structure at the NC/SiO₂ interface is proposed for evaluating the electronic properties. The presently employed supercell structure (Fig. 1) was derived from earlier x-ray structure investigations,¹² which revealed traces of Er-pyrogermanate (Er₂Ge₂O₇) as the secondary phase in Ge-rich SiO₂ when co-doped with 0.5% Er and annealed at 1100 °C for 30 min. The formation energies $H_f(\text{GeO}_x) \ll H_f(\text{SiO}_2) < H_f(\text{Er}_2\text{Ge}_2\text{O}_7)$ and $H_f(\text{Er}_2\text{Si}_2\text{O}_7) < H_f(\text{Er}_2\text{O}_3)$ suggest a thermodynamic driving force for the development of an Er-rich layer as a surfactant

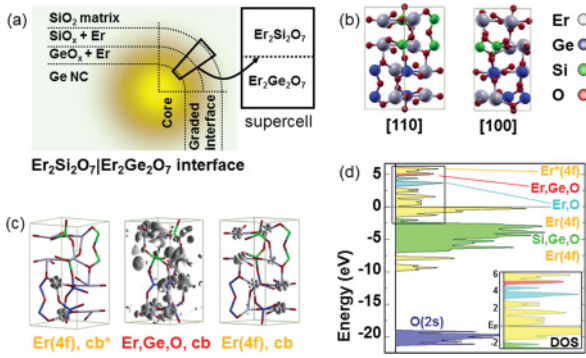


FIG. 1. (Color online) (a) Schematic view of the Er-rich graded interface between Ge NC core and surrounding SiO₂, showing the setup of the supercell for DFT calculation. (b) Model supercell structure consisting of Er₂Si₂O₇(001) and Er₂Ge₂O₇(001) layers. (c) Spatial extension of the conduction band (cb) states, representing high-lying Er(4f) cb* states localized at Er in the Ge-rich layer, occurrence of mixed (Er,Ge,O) cb states at lower energy and lower lying Er(4f) cb states. (d) Calculated DOS (E_F set to zero) for the supercell depicted in (b) giving the relative energy alignment of the Er-containing cb states and the occupied valence states; colors (different gray tones) denote the character of the peak obtained from a spatial decomposition of the DOS. The inset gives a magnified view of the DOS in the vicinity of E_F .

to lower the interfacial energy between Ge NCs and the surrounding SiO₂ matrix. Moreover, based on previous understanding of the observed EL behavior,^{10–12} a graded interface with Er-rich pyrogermanate and pyrosilicate layers at the NC-SiO₂ boundary is considered here [Fig. 1(a)], where the model structure is a mixture of Er₂Si₂O₇(001) and Er₂Ge₂O₇(001) layers as exhibited in Fig. 1(b). This choice reflects both the x-ray structure investigations and the decreasing formation energy of silicon, erbium, and germanium oxides. As the lattice parameters of the parent compounds differ by about 7%, optimization of the cell yields averaged supercell lattice parameters. The coordination numbers and the O arrangements around Er, Si, and Ge sites are, however, maintained during relaxation, and do not affect the crystal-field splitting.

To visualize the observed EL behavior,¹⁰ typical conduction-band states of the proposed structure [Fig. 1(b)] are depicted in Fig. 1(c) along with the corresponding DOS [see Fig. 1(d)]. A small band gap of ~ 0.22 eV [inset of Fig. 1(d)] separates the occupied and unoccupied Er 4f states around the Fermi level E_F (set to 0 eV). Further below, the valence band consists of Si-O and Ge-O bonding states, followed by Er 4f [between -7.5 and -10 eV, similar to ErAs (Ref. 20)] and O 2s states (around -20 eV). The Er 4f states at the conduction-band edge are followed by Er- and O-derived states

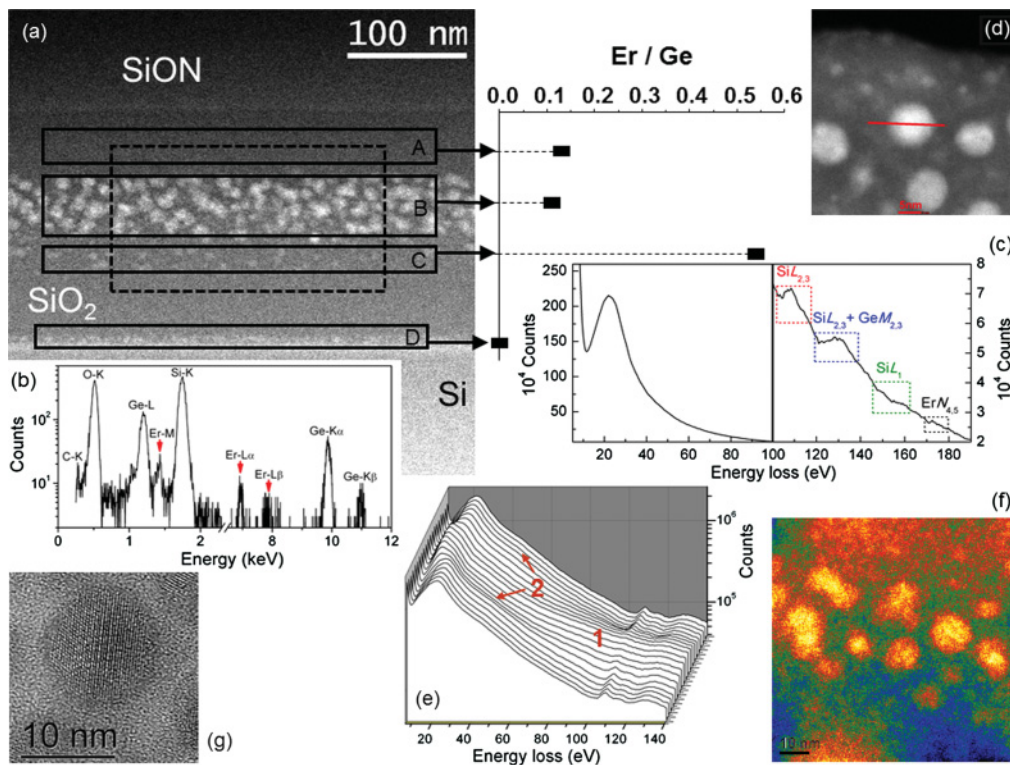


FIG. 2. (Color online) (a) Low magnification HAADF-STEM image, showing the distribution of Ge nanoparticles in SiO₂; the intensity ratio of the Er-L and Ge-K edges in regions of A, B, C, and D is shown in the adjacent plot. (b) and (c) display the EDS and EELS profiles, respectively, taken from the region indicated by a dashed rectangle in (a). (d) High-resolution HAADF-STEM image shows the formation of Ge nanoclusters with sizes in the range 7–10 nm (white contrast), while the small features below 2 nm are mostly Si nanoparticles. The trace [shown in (d)] represents the location along which a sequence of EELS profiles was recorded where a three-dimensional view of the recorded EELS profiles is exhibited in (e). Bands marked by “1” and “2” in (e) are associated with Ge and Er. (f) Bright region represents the high Ge content in the acquired EFTEM image at the Ge M_{4,5} edge. (g) HRTEM image confirms the formation of Ge NCs, while such a typical Ge NC is screened from the surrounding SiO₂ by a dark-gray patch. The scale bars in (d) and (f) are 5 and 10 nm, respectively.

and the delocalized (Er,Ge,O) states, which couple empty Ge p and d states with Er f states via O bridges. As shown by Pourovskii *et al.*,²⁰ a quantitative calculation of the Er multiplet structure is best achieved beyond the independent particle picture of the density-functional theory (DFT), but the qualitative DOS features are also reproduced well by the DFT. In fact, the occurrence of delocalized (Er,Ge,O) states within the localized unoccupied Er $4f$ manifold is in agreement with the hypothesis behind the inverse energy-transfer process from the Er³⁺ to the GeODCs, and so justifies the experimental evidence of the enhanced blue-violet EL.¹⁰

For detailed microstructural analysis, nanoparticles have been characterized by HRTEM, EFTEM, and HAADF-STEM in combination with EDS and EELS. A cross-sectional HAADF-STEM image of a sample containing 7.4% Ge and 0.8% Er is displayed in Fig. 2(a), showing an overall distribution of Ge nanoparticles (bright) in SiO₂. Note that no significant change is observed in Ge distribution after Er doping. A rectangular (dashed) box in Fig. 2(a) indicates the location from where the EDS and EELS profiles were recorded. The presence of elements such as Er and Ge along with Si and O is verified by EDS [Fig. 2(b)]. By taking the EDS in regions of A, B, C, and D, the intensity ratio of the Er- L and Ge- K edges was measured [Fig. 2(a)] to have the depth profile of the implanted species. On the other hand, the Ge $M_{4,5}$ edge at 28.7 eV (Refs. 21 and 22) and the Er $O_{2,3}$ edge at 29.4 eV (Refs. 21 and 23) are almost invisible in the recorded EELS profiles [Fig. 2(c)] due to the presence of the strong SiO₂ plasmon at ~ 22 eV (Ref. 21) in the lower energy window (5–100 eV). In addition, the presence of the extended Si $L_{2,3}$ edge of SiO₂ near the Ge $M_{2,3}$ edge at ~ 125 eV does not give a clear signature of the presence of Ge [right panel, Fig. 2(c)]. However, by measuring a sequence of EELS across a Ge nanoparticle [along the trace in Fig. 2(d)], one can find (i) a gradual transition from the plasmon of SiO₂ (22 eV) to Ge nanocluster (17 eV) (Ref. 24) and back to SiO₂, and (ii) the evolution of a broad tail (60–120 eV) of Ge (Ref. 25) from the cluster (marked by “1”) in Fig. 2(e). Although the bulk plasmons are dominant in Fig. 2(e), an additional broad peak (marked by “2”) in the range 30–45 eV can also be detected near the edges of the Ge nanoparticle. The origin of such a feature is possibly associated with the $5p \rightarrow 4d$ transitions in Er.²⁶ We were also able to map the Ge [Fig. 2(f)] using background subtracted EFTEM at the energy loss of Ge- $M_{4,5}$. Additionally, the HRTEM image shows the formation of Ge NCs where the lattice fringes are separated from the amorphous SiO₂ (light gray) matrix by an almost 1-nm-thick amorphous patch (dark gray) [see Fig. 2(g)]. As the atomic weight of Er is about 2.3 times higher than that of Ge, the dark-gray contrast across the crystalline Ge core can be tentatively attributed to the existence of an Er-rich zone, in agreement with the EELS measurements.

In HAADF-STEM imaging the intensity of an atom site depends on the atomic number Z as roughly $Z^{1.7}$ (Ref. 27). Judging from the ratio of the Z values, the contrast of Ge should be about 3.6 times weaker than that of Er in the ideal case. However, the relative intensity is certainly different in amorphous SiO₂ [see Figs. 2(a) and 2(d)], though EDS on an individual Ge nanoparticle reveals the existence of Er (not shown). In order to assess this effect, the Z -contrast

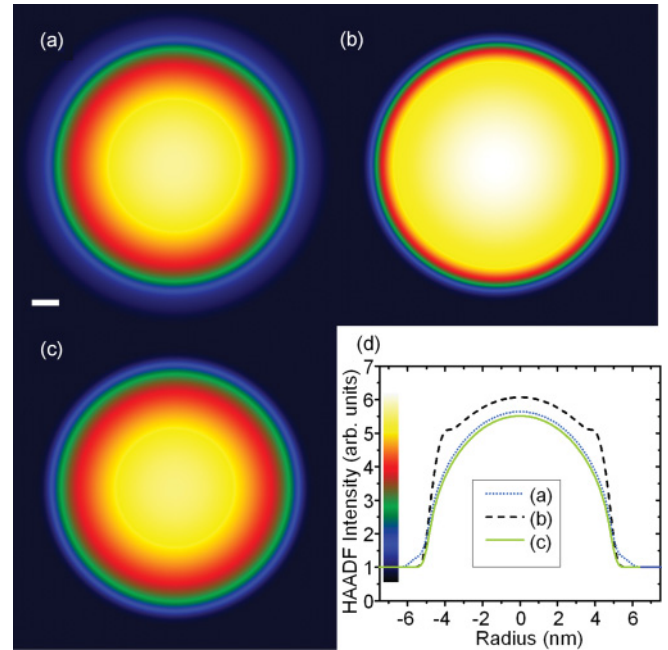


FIG. 3. (Color online) Z -contrast simulations were performed for (a) a Ge NC (10 nm diameter) with 1-nm-thick Er₂Ge₂O₇ interface layer, (b) a Ge NC (8 nm diameter) with 1-nm-thick Er covering, and (c) a pure Ge NC (10 nm diameter). (d) A quantitative comparison of the intensity profiles across the center of all three simulations shown in (a)–(c). In all cases the particles were embedded in a 30-nm-thick amorphous SiO₂ matrix and were imaged using a 0.5-nm electron probe. The color scale (grayscale) is embedded in panel (d) where the length of the scale bar in (a) is 1 nm.

intensity of the observed Ge nanoparticle was simulated by the weighted sum of the $Z^{1.7}$ of the atoms in a unit volume under the assumptions of (i) atomically unresolved imaging in amorphous SiO₂, and (ii) out of zone-axis conditions for the clusters. The Z -contrast simulations were carried out for Ge NCs embedded in a 30-nm-thick SiO₂ layer and a STEM beam size of 0.5 nm. Simulated HAADF images of a Ge NC (10 nm diameter) with a 1-nm-thick Er₂Ge₂O₇ interface layer, a Ge NC (8 nm diameter) with a 1-nm-thick Er shell, and a pure Ge NC (10 nm diameter) are shown in Figs. 3(a)–3(c). Figure 3(d) shows a quantitative comparison of the intensity profiles across the center of all three simulated images shown in Figs. 3(a)–3(c). All models lead to bright images, which are almost identical in size. While the pure Er is visible in the image as a bright ring, the Er₂Ge₂O₇ interface layer can hardly be detected when it is compared to Ge NC alone. However, close inspection reveals that the intensity reduces gradually across the cluster boundaries in the presence of the Er₂Ge₂O₇ interface layer. Comparison with experimental images [Figs. 2(a) and 2(d)] excludes the existence of a pure Er shell around Ge NCs as the experiments do not show a bright ring around the particles. In this scenario, the Er₂Ge₂O₇ interface layer is consistent with the experimental HAADF-STEM images. Considering the aforementioned experimental results and the Z -contrast simulations into account we argue that Ge NCs with Er-rich graded interfaces are formed in SiO₂, which is also in good agreement with our theoretical understanding.

BRIEF REPORTS

PHYSICAL REVIEW B **83**, 113302 (2011)

Using RBS,¹² we also found that the Er atoms are mainly situated in the regions B and C in Fig. 2(a). Assuming the formation of graded interface, the Er/Ge ratio of ~ 0.1 in region B implies that most of the Ge NCs with sizes in the range of 5–10 nm are partially covered by an Er-rich phase. On the other hand, the Er/Ge ratio has increased to ~ 0.5 in region C, indicating that the Er-rich phases are more pronounced in this region with Ge NCs below 5 nm in size and are possibly able to screen Ge NCs from the surrounding SiO₂.

In summary, we present the formation of an Er-rich graded interface at the Ge NC-SiO₂ boundary using a combined theoretical and experimental approach. Initially, a theoretical modeling is developed using a supercell structure at the NC/SiO₂ interface that consists of compounds determined by x-ray diffraction. The first-principles calculation of the proposed interface geometry gives the local

electronic structure where the results are in accordance with the hypothesis behind the inverse energy-transfer process from the Er³⁺ to the GeODCs. The existence of Er, especially the Er-rich graded interface at the NC-SiO₂ boundary, has been explored by investigating the HRTEM, EFTEM, and HAADF-STEM in combination with EDS and EELS in the microstructure level. Finally, the experimentally observed HAADF-STEM images have been assessed by the Z-contrast simulations, which confirm the presence of Er composites and the graded structure at the NC/SiO₂ interface.

We thank the Rossendorf Implantation Group for ion implantation and H. Felsmann, C. Neisser, and G. Schnabel for their careful semiconductor preparation work. This work was supported by the Alexander von Humboldt Foundation.

*akanjilal@purdue.edu

¹S. Pimputkar, J. S. Speck, S. P. DenBaars, and S. Nakamura, *Nature Photon.* **3**, 180 (2009).²R. J. Walters, G. I. Bourianoff, and H. A. Atwater, *Nature Mater.* **4**, 143 (2005).³A. Kanjilal, L. Rebohle, W. Skorupa, and M. Helm, *Appl. Phys. Lett.* **94**, 101916 (2009).⁴L. Rebohle, J. Lehmann, S. Prucnal, A. Kanjilal, A. Nazarov, I. Tyagulskii, W. Skorupa, and M. Helm, *Appl. Phys. Lett.* **93**, 071908 (2008).⁵D. Timmerman, I. Izeddin, P. Stallinga, I. N. Yassievich, and T. Gregorkiewicz, *Nature Photon.* **2**, 105 (2008).⁶B. Garrido, C. García, S.-Y. Seo, P. Pellegrino, D. Navarro-Urrios, N. Daldosso, L. Pavesi, F. Gourbilleau, and R. Rizk, *Phys. Rev. B* **76**, 245308 (2007).⁷K. Imakita, M. Fujii, and S. Hayashi, *Phys. Rev. B* **71**, 193301 (2005).⁸F. Priolo, C. D. Presti, G. Franzò, A. Irrera, I. Crupi, I. F. Iacona, G. Di Stefano, A. Piana, D. Sanfilippo, and P. G. Fallica, *Phys. Rev. B* **73**, 113302 (2006).⁹K. Sun, W. J. Xu, B. Zhang, L. P. You, G. Z. Ran, and G. G. Qin, *Nanotechnology* **19**, 105708 (2008).¹⁰A. Kanjilal, L. Rebohle, M. Voelskow, W. Skorupa, and M. Helm, *Appl. Phys. Lett.* **94**, 051903 (2009).¹¹A. Kanjilal, L. Rebohle, M. Voelskow, W. Skorupa, and M. Helm, *J. Appl. Phys.* **106**, 026104 (2009).¹²A. Kanjilal, L. Rebohle, N. K. Baddela, S. Zhou, M. Voelskow, W. Skorupa, and M. Helm, *Phys. Rev. B* **79**, 161302(R) (2009).¹³G. H. Dieke, *Spectra and Energy Levels of Rare Earth Ions in Crystals* (Interscience, New York, 1968), Chap. 13.¹⁴P. E. Batson, *Nature (London)* **366**, 727 (1993); U. Kaiser, D. A. Muller, J. L. Grazul, A. Chuvilin, and M. Kawasaki, *Nat. Mater.* **1**, 102 (2002).¹⁵K. W. Urban, *Science* **321**, 506 (2008).¹⁶J. F. Ziegler and J. P. Biersack, *SRIM-2006.02*, [<http://www.srim.org>].¹⁷X. Gonze, J.-M. Beuken, R. Caracas, F. Detraux, M. Fuchs, G.-M. Rignanese, L. Sindic, M. Verstraete, G. Zerah, F. Jollet, M. Torrent, A. Roy, M. Mikami, Ph. Ghosez, J.-Y. Raty, and D. C. Allan, *Comput. Mater. Sci.* **25**, 478 (2002); X. Gonze, G.-M. Rignanese, M. Verstraete, J.-M. Beuken, Y. Pouillon, R. Caracas, F. Jollet, M. Torrent, G. Zerah, M. Mikami, Ph. Ghosez, M. Veithen, J.-Y. Raty, V. Olevano, F. Bruneval, L. Reining, R. Godby, G. Onida, D. R. Hamann, and D. C. Allan, *Z. Kristallogr.* **220**, 558 (2005).¹⁸J. P. Perdew, K. Burke, and M. Ernzerhof, *Phys. Rev. Lett.* **77**, 3865 (1996).¹⁹M. Torrent, F. Jollet, F. Bottin, G. Zerah, and X. Gonze, *Comput. Mater. Sci.* **42**, 337 (2008).²⁰L. V. Pourovskii, K. Delaney, C. G. Van de Walle, N. A. Spaldin, and A. Georges, *Phys. Rev. Lett.* **102**, 096401 (2009).²¹P. Pellegrino, B. Garrido, J. Arbiol, C. Garcia, Y. Labour, and J. R. Morante, *Appl. Phys. Lett.* **88**, 121915 (2006).²²A. Ziegler, J. C. Idrobo, M. K. Cinibulk, C. Kisielowski, N. D. Browning, and R. O. Ritchie, *Science* **306**, 1768 (2004).²³C. C. Ahn and O. L. Krivanek, *EELS Atlas: A Reference Guide of Electron Energy Loss Spectra Covering All Stable Elements* (Gatan, Warrendale, 1983).²⁴S. Sato, S. Nozaki, and H. Morisaki, *Thin Solid Films* **343–344**, 481 (1999).²⁵R. Pantel, M. C. Cheynet, and F. D. Tichelaar, *Micron* **37**, 657 (2006).²⁶E. Bertel, F. P. Netzer, and J. A. D. Matthew, *Surf. Sci.* **103**, 1 (1981).²⁷R. F. Loane, E. J. Kirkland, and J. Silcox, *Acta Crystallogr. Sect. A* **44**, 912 (1988).



Statistics

Publications and patents

Books and chapters

1. Cavaleiro, A.; Czerwiec, T.; Helmersson, U.; van der Kolk, G.; Möller, W.; Oehr, C.; Tietema, R. (Editors)
Proceedings of the 12th international conference on plasma surface engineering
Garmisch-Partenkirchen, Germany, 13-17 September 2010 Amsterdam: Elsevier BV, 2011

Publications in journals

1. Abdulkadhim, A.; Takahashi, T.; Music, D.; Munnik, F.; Schneider, J. M.
MAX phase formation by intercalation upon annealing of TiC_x/Al (0.4 ≤ x ≤ 1) bilayer thin film
Acta Materialia **59**, 6168 (2011)
2. Al-Motasem, A. T.; Posselt, M.; Bergner, F.
Nanoclusters in bcc-Fe containing vacancies, copper and nickel: Structure and energetics
Journal of Nuclear Materials **418**, 215 (2011)
3. Al-Motasem, A. T.; Posselt, M.; Bergner, F.; Birkenheuer, U.
Structure, energetics and thermodynamics of copper-vacancy clusters in bcc-Fe: An atomistic study
Journal of Nuclear Materials **414**, 161 (2011)
4. Anwand, W.; Kanjilal, A.; Brauer, G.; Wagner, A.; Butterling, M.; Cowan, T. E.; Rebohle, L.; Skorupa, W.
Structural characterisation of Er implanted, Ge-rich SiO₂ layers using slow positron implantation spectroscopy
Materials Science Forum **666**, 41 (2011)
5. Aumayr, F.; Facsko, S.; El-Said, A. S.; Trautmann, C.; Schleberger, M.
Single-ion induced surface nanostructures - A comparison between slow highly-charged and swift heavy ions
Journal of Physics: Condensed Matter **23**, 393001 (2011)
6. Balocco, C.; Kasjoo, S. R.; Lu, X. F.; Zhang, L. Q.; Alimi, Y.; Winnerl, S.; Song, A. M.
Room-temperature operation of a unipolar nanodiode at terahertz frequencies
Applied Physics Letters **98**, 223501 (2011)
7. Banholzer, A.; Narkowicz, R.; Hassel, C.; Meckenstock, R.; Stienen, S.; Posth, O.; Suter, D.; Farle, M.; Lindner, J.
Visualization of spin dynamics in single nanosized magnetic elements
Nanotechnology **22**, 295713 (2011)
8. Barlak, M.; Piekoszewski, J.; Werner, Z.; Sartowska, B.; Pisarek, M.; Walis, L.; Starosta, W.; Kolitsch, A.; Grötzschel, R.; Bochenska, K.; Pochrybniak, C.
Modes of the use of high intensity plasma beams for ceramic surface modification
Surface & Coatings Technology **206**, 916 (2011)
9. Barsukov, I.; Römer, F. M.; Meckenstock, R.; Lenz, K.; Lindner, J.; Hemken to Krax, S.; Banholzer, A.; Körner, M.; Grebing, J.; Fassbender, J.; Farle, M.
Frequency dependence of spin relaxation in periodic systems
Physical Review B **84**, 140410(R) (2011)
10. Baumgart, C.; Müller, A.-D.; Müller, F.; Schmidt, H.
Kelvin probe force microscopy in the presence of intrinsic local electric fields
Physica Status Solidi (a) **208**, 777 (2011)
11. Bayer, B. C.; Sanjabi, S.; Baetz, C.; Wirth, C. T.; Esconjauregui, S.; Weatherup, R. S.; Barber, Z. H.; Robertson, S.; Hofmann J.

- Carbon nanotube forest growth on NiTi shape memory alloy thin films for thermal actuation**
Thin Solid Films **519**, 6126 (2011)
12. Bayer, B.; Hofmann, S.; Castellarin-Cudia, C.; Blume, R.; Baehtz, C.; Esconjauregui, S.; Wirth, C. T.; Oliver, R. A.; Ducati, C.; Knop-Gericke, A.; Schlogl, R.; Goldoni, A.; Cepek, C.; Robertson, J.
Support-catalyst-gas interactions during carbon nanotube growth on metallic Ta films
Journal of Physical Chemistry C **115**, 4359 (2011)
13. Bayer, B.; Zhang, C.; Blume, R.; Yan, F.; Fouquet, M.; Wirth, C.; Weatherup, R.; Lin, L.; Baehtz, C.; Oliver, R.; Knop-Gericke, A.; Schlogl, R.; Hofmann, S.; Robertson, J.
In-situ study of growth of carbon nanotube forests on conductive CoSi₂ support
Journal of Applied Physics **109**, 1143141 (2011)
14. Berndt, M.; Abrasonis, G.; Kovacs, Gy. J.; Krause, M.; Munnik, F.; Heller, R.; Kolitsch, A.; Möller, W.
Bulk diffusion induced structural modifications of carbon-transition metal nanocomposite films
Journal of Applied Physics **109**, 063503 (2011)
15. Bhattacharyya, J.; Wagner, M.; Zybell, S.; Winnerl, S.; Stehr, D.; Helm, M.; Schneider, H.
Simultaneous time and wavelength resolved spectroscopy under two-colour near infrared and terahertz excitation
Review of Scientific Instruments **82**, 103107 (2011)
16. Biermanns, A.; Hanisch, A.; Grenzer, J.; Metzger, T. H.; Pietsch, U.
Tuning the shape and damage in ion-beam induced ripples on silicon
Physica Status Solidi (a) **208**, 2608 (2011)
17. Bischoff, L.; Pilz, W.; Schmidt, B.
Amorphous solid foam structures on germanium by heavy ion irradiation
Applied Physics A **104**, 1153 (2011)
18. Böttger, R.; Bischoff, L.; Schmidt, B.; Krause, M.
Characterization of Si nanowires fabricated by Ga⁺ FIB implantation and subsequent selective wet etching
Journal of Micromechanics and Microengineering **21**, 095025 (2011)
19. Bracht, H.; Radek, M.; Kube, R.; Knebel, S.; Posselt, M.; Schmidt, B.; Haller, E.; Bougeard, D.
Ion-beam mixing in crystalline and amorphous germanium isotope multilayer structures
Journal of Applied Physics **110**, 093502 (2011)
20. Braucher, R.; Merchel, S.; Borgomano, J.; L. Boulès, D.
Production of cosmogenic radionuclides at great depth: a multi element approach
Earth and Planetary Science Letters **309**, 1 (2011)
21. Brauer, G.; Kuriplach, J.; Djuricic, C. C.; Ling, A. B.
Activities towards p-type doping of ZnO
Journal of Physics: Conference Series **265**, 012002 (2011)
22. Bruchhausen, A.; Gebbs, R.; Hudert, F.; Issenmann, D.; Klatt, G.; Bartels, A.; Schecker, O.; Waitz, R.; Erbe, A.; Scheer, E.; Huntzinger, J.; Mlayah, A.; Dekorsy, T.
Subharmonic resonant optical excitation of confined acoustic modes in a free-standing semiconductor membrane at GHz frequencies with a high-repetition-rate femtosecond laser
Physical Review Letters **106**, 077401 (2011)
23. Bugoi, R.; Poll, I.; Manucu-Adamesteanu, Gh.; Calligaro, T.; Pichon, L.; Neelmeijer, C.; Eder, F.
Ion beam analysis studies of ancient glass bracelets discovered in Bucharest
Romanian Reports in Physics (2011)
24. Cabral, A. R.; Beaudoin, G.; Munnik, F.
Lead in diagenetic pyrite: evidence for Pb-tolerant bacteria in a red-bed Cu deposit, Quebec Appalachians, Canada
Mineralogical Magazine **75**, 295 (2011)

25. Cabral, A. R.; Radtke, M.; Munnik, F.; Lehmann, B.; Reinholz, U.; Riesemeier, H.; Tupinambá, M.; Kwitko-Ribeiro, R.
Iodine in alluvial platinum–palladium nuggets
Chemical Geology **281**, 125 (2011)
26. Chen, C. L.; Richter, A.; Kögler, R.; Talut, G.
Dual beam irradiation of nanostructured FeCrAl oxide dispersion strengthened steel
Journal of Nuclear Materials **412**, 350 (2011)
27. Cherkouk, C.; Rebohle, L.; Skorupa, W.
Lysine adsorption on the silanized SiO₂-surface for immobilization of the estrogen receptor hER(alpha)
Applied Surface Science **257**, 3831 (2011)
28. Cherkouk, C.; Rebohle, L.; Skorupa, W.
Bioconjugation of the estrogen receptor hER(alpha) to a quantum dot dye for a controlled immobilization on the SiO₂ surface
Journal of Colloid and Interface Science **355**, 442 (2011)
29. Cormier, M.; Mougin, A.; Ferré, J.; Jamet, J.-P.; Weil, R.; Fassbender, J.; Baltz, V.; Rodmacq, B.
Fast propagation of weakly-pinned domain walls and current-assisted magnetization reversal in He⁺-irradiated Pt/Co/Pt nanotracks
Journal of Physics D: Applied Physics **44**, 215002 (2011)
30. Danesh, P.; Pantchev, B.; Wiezorek, J.; Schmidt, B.; Grambole, D.
Effect of hydrogen on hardness of amorphous silicon
Applied Physics A **102**, 131 (2011)
31. Das Kanungo, P.; Kögler, R.; Zhakarov, N.; Werner, P.; Scholz, R.; Skorupa, W.
Characterization of structural changes associated with doping silicon nanowires by ion implantation
Crystal Growth & Design **11**, 2690 (2011)
32. de Camargo, E. N.; Lobo, A. O.; Da Silva, M. M.; Ueda, M.; Garcia, E. E.; Pichon, L.; Reuther, H.; Otubo, J.
Determination of Ni release in NiTi SMA with surface modification by nitrogen plasma immersion ion implantation
Journal of Materials Engineering and Performance **20**, 798 (2011)
33. de Ro; Massoth, G. J.; Butterfield, D. A.; Christenson, B. W.; Ishibashi, J.; Ditchburn, R. G.; Hannington, M. D.; Brathwaite, R. L.; Lupton, J. E.; Kamenetsky, V. S.; Graham, I. J.; Zellmer, G. F.; Dziak, R. P.; Embley, R. W.; Dekov, V. M.; Munnik, F.; Lahr, J.; Evans, L. J.; Takai, K.
Submarine hydrothermal activity and gold-rich mineralization at Brothers Volcano, Kermadec Arc, New Zealand.
Mineralium Deposita **46**, 541 (2011)
34. Dev, B. N.; Roy, S.; Bera, S.; Tawara, Y.; Schell, N.; Grenzer, J.; von Borany, J.; Grötzschel, R.
Ion-irradiated laterally graded Ni/C multilayers: A combined X-ray standing wave and X-ray reflectivity analysis
Japanese Journal of Applied Physics **50**, 052501 (2011)
35. Donchev, A.; Koliutsch, A.; Schütze, M.; Yankov, R.
Combined Al- plus F-treatment of Ti-alloys for improved behaviour at elevated temperatures
Materials and Corrosion **62**, 695 (2011)
36. Drachenko, O.; Patané, A.; Kozlova, N. V.; Zhuang, Q. D.; Krier, A.; Eaves, L.; Helm, M.
Cyclotron resonance mass and Fermi energy pinning in the In(AsN) alloy
Applied Physics Letters **98**, 162109 (2011)
37. Drachenko, O.; Schneider, H.; Helm, M.; Kozlov, D.; Gavrilenko, V.; Wosnitza, J.; Leotin, J.
Modification to the central-cell correction of germanium acceptors
Physical Review B **84**, 245207 (2011)
38. Drachenko, O.; Winnerl, S.; Schneider, H.; Helm, M.; Wosnitza, J.; Leotin, J.
Compact magnetospectrometer for pulsed magnets based on infrared quantum cascade lasers
Review of Scientific Instruments **82**, 033108 (2011)

39. Ehrke, H.; Tobey, R. I.; Wall, S.; Cavill, S. A.; Först, M.; Khanna, V.; Garl, Th.; Stojanovic, N.; Prabhakaran, D.; Boothroyd, A. T.; Gensch, M.; Mirone, A.; Reutler, P.; Revcolevschi, A.; Dhesi, S. S.; Cavalleri, A.
Photoinduced melting of antiferromagnetic order in $\text{La}_{0.5}\text{Sr}_{1.5}\text{MnO}_4$ measured using ultrafast resonant soft X-ray diffraction
Physical Review Letters **106**, 217401 (2011)
40. El-Said, A. S.; Heller, R.; Facsko, S.
Nanostructuring of BaF_2 (1 1 1) surfaces by single slow highly charged ions
Nuclear Instruments and Methods in Physics Research B **269**, 901 (2011)
41. El-Said, A. S.; Wilhelm, R. A.; Heller, R.; Facsko, S.; Trautmann, C.; Aumayr, F.
Surface nanostructuring of SrTiO_3 single crystals by slow highly charged ions and swift heavy ions
Nuclear Instruments and Methods in Physics Research B **269**, 1234 (2011)
42. Elschner, C.; Levin, Alexandr A.; Wilde, L.; Grenzer, J.; Schroer, C.; Leo, K.; Riede, M.
Determining the C60 molecular arrangement in thin films by means of X-ray diffraction
Journal of Applied Crystallography **44**, 983 (2011)
43. Esconjauregui, S.; Bayer, B.; Fouquet, M.; Wirth, C.; Yan, F.; Xie, R.; Ducati, C.; Baehz, C.; Castellarin-Cudia, C.; Bhardwaj, S.; Cepek, C.; Hofmann, S.; Robertson, J.
Use of plasma treatment to grow carbon nanotube forests on TiN substrate
Journal of Applied Physics **109**, 1143121 (2011)
44. Faatz, B.; Baboi, N.; Ayvazyan, V.; Balandin, V.; Decking, W.; Duesterer, S.; Eckoldt, H.; Feldhaus, J.; Golubeva, N.; Honkavaara, K.; Koerfer, M.; Laarmann, T.; Leuschner, A.; Lilje, L.; Limberg, T.; Noelle, D.; Obier, F.; Petrov, A.; Ploenjes, E.; Rehlich, K.; Schlarb, H.; Schmidt, B.; Schmitz, M.; Schreiber, S.; Schulte-Schrepping, H.; Spengler, J.; Staack, M.; Tavella, F.; Tiedtke, K.; Tischer, M.; Treusch, R.; Vogt, M.; Willner, A.; Bahrtdt, J.; Follath, R.; Gensch, M.; Holldack, K.; Meseck, A.; Mitzner, R.; Drescher, M.; Miltchev, V.; Ronsch-Schulenburg, J. J.; Rossbach, J.
Flash II: Perspectives and challenges
Nuclear Instruments and Methods in Physics Research A **635**, S2 (2011)
45. Fan, J. C.; Zhu, C. Y.; Yang, B.; Fung, S.; Beling, C. D.; Brauer, G.; Anwand, W.; Grambole, D.; Skorupa, W.; Wong, K. S.; Zhong, Y. C.; Xie, Z.; Ling, C. C.
Comprehensive study of the p-type conductivity formation in radio frequency magnetron sputtered arsenic-doped ZnO film
Journal of Vacuum Science & Technology A **29**, 03A103 (2011)
46. Fernandes, B. B.; Ueda, M.; Mello, C. B.; Fernandes, P. B.; Reuther, H.; Ramos, A. S.
Modification of surface properties of Ti-16Si-4B powder alloy by plasma immersion ion implantation
Intermetallics **19**, 693 (2011)
47. Fiedler, J.; Heera, V.; Skrotzki, R.; Herrmannsdörfer, T.; Voelskow, M.; Mücklich, A.; Oswald, S.; Schmidt, B.; Skorupa, W.; Gobsch, G.; Wosnitza, J.; Helm, M.
Superconducting films fabricated by high fluence Ga implantation in Si
Physical Review B **83**, 214504 (2011)
48. Gago, R.; Redondo-Cubero, A.; Vinnichenko, M.; Vázquez, L.
Annealing of heterogeneous phase TiO_2 films: An X-ray absorption and morphological study
Chemical Physics Letters **511**, 367 (2011)
49. Giehler, M.; Wienold, M.; Schrottke, L.; Hey, R.; Grahn, H. T.; Pavlov, S. G.; Hübers, H.-W.; Winnerl, S.; Schneider, H.
Mid-infrared pump-related electric-field domains in GaAs/(Al,Ga)As quantum-cascade structures for terahertz lasing without population inversion
Journal of Applied Physics **110**, 103104 (2011)
50. Gruber, W.; Chakravarty, S.; Baehz, C.; Leitenberger, W.; Bruns, M.; Kobler, A.; Kübel, C.; Schmidt, H.
Strain relaxation and vacancy creation in thin platinum films
Physical Review Letters **107**, 265501 (2011)

51. Haidu, F.; Fronk, M.; Gordan, D. O.; Scarlet, C.; Salvan, G.; Zahn, R. T. D.
Dielectric function and magneto-optical Voigt constant of Cu₂O: A combined spectroscopic ellipsometry and polar magneto-optical Kerr spectroscopy study
Physical Review B **84**, 195203 (2011)
52. Hanzig, J.; Abendroth, B.; Hanzig, F.; Stöcker, H.; Strohmeyer, R.; Meyer, D. C.; Lindner, S.; Grobosch, M.; Knupfer, M.; Himcinschi, C.; Mühle, U.; Munnik, F.
Single crystal strontium titanate surface and bulk modifications due to vacuum annealing
Journal of Applied Physics **110**, 064107 (2011)
53. Ikonnikov, A.; Zholudev, M.; Spirin, K.; Lastovkin, A.; Maremyanin, K.; Aleshkin, V.; Gavrilenko, V.; Drachenko, O.; Helm, M.; Wosnitza, J.; Goiran, M.; Mikhailov, N.; Dvoretiskii, S.; Teppe, F.; Diakonova, N.; Consejo, C.; Chenaud, B.; Knap, W.
Cyclotron resonance and interband optical transitions in HgTe/CdTe (0 1 3) quantum well heterostructures
Semiconductor Science and Technology **26**, 125011 (2011)
54. Jagielski, J.; Grambole, D.; Jozwik, I.; Bielinski, D. M.; Ostaszewska, U.; Pieczynska, D.
Hydrogen loss from elastomers subjected to ion irradiation
Materials Chemistry and Physics **127**, 342 (2011)
55. Kalinichenka, S.; Röntzsch, L.; Baetz, C.; Weißgärber, T.; Kieback, B.
Hydrogen desorption properties of melt-spun and hydrogenated Mg-based alloys using in situ synchrotron X-ray diffraction and TGA
Journal of Alloys and Compounds **509**, S629 (2011)
56. Kanjilal, A.; Gemming, S.; Rebohle, L.; Muecklich, A.; Gemming, T.; Voelskow, M.; Skorupa, W.; Helm, M.
Microstructure analysis at the interface of Er decorated Ge nanocrystals in SiO₂
Physical Review B **83**, 113302 (2011)
57. Kehr, S. C.; Liu, Y. M.; Martin, L. W.; Yu, P.; Gajek, M.; Yang, S.-Y.; Yang, C.-H.; Wenzel, M. T.; Jacob, R.; von Ribbeck, H.-G.; Helm, M.; Zhang, X.; Eng, L. M.; Ramesh, R.
Near-field examination of perovskite-based superlenses and superlens-enhanced probe-object coupling
Nature Communications **2**, 249 (2011)
58. Kehr, S. C.; Yu, P.; Liu, Y. M.; Parzefall, M.; Khan, A. I.; Jacob, R.; Wenzel, M. T.; Ribbeck, H.-G.; Helm, M.; Zhang, X.; Eng, L. M.; Ramesh, R.
Microspectroscopy on perovskite-based superlenses
Optical Materials Express **1**, 1051 (2011)
59. Keller, A.; Fritzsche, M.; Ogaki, R.; Bald, I.; Facsko, S.; Dong, M. D.; Kingshott, P.; Besenbacher, F.
Tuning the hydrophobicity of mica surfaces by hyperthermal Ar ion irradiation
Journal of Chemical Physics **134**, 104705 (2011)
60. Keller, A.; Fritzsche, M.; Yu, Y.-P.; Liu, Q.; Li, Y.-M.; Dong, M.; Besenbacher, F.
Influence of hydrophobicity on the surface-catalyzed assembly of the islet amyloid polypeptide
ACS Nano **5**, 2770 (2011)
61. Keller, A.; Nicoli, M.; Facsko, S.; Cuerno, R.
Dynamic effects induced by renormalization in anisotropic pattern forming systems
Physical Review E **84**, 015202(R) (2011)
62. Keller, A.; Peverini, L.; Grenzer, J.; Mücklich, A.; Facsko, S.
Polycrystalline Ni thin films on nanopatterned Si substrates: from highly conformal isotropic to non-conformal anisotropic growth
Physical Review B **84**, 035423 (2011)
63. Kim, Y.; Pietsch, T.; Erbe, A.; Belzig, W.; Scheer, E.
Benzenedithiol: a broad-range single-channel molecular conductor
Nano Letters **11**, 3734 (2011)
64. Komissarova, T. A.; Jmerik, V. N.; Ivanov, S. V.; Drachenko, O.; Wang, X.; Yoshikawa, A.
Identification of the main contributions to the conductivity of epitaxial InN
Physical Review B **84**, 035205 (2011)

-
65. Kovacs, G.; Buerger, D.; Skorupa, I.; Schmidt, H.
Effect of the substrate on the insulator-metal transition of vanadium dioxide films
Journal of Applied Physics **109**, 063708 (2011)
66. Krause, J.; Wagner, M.; Winnerl, S.; Helm, M.; Stehr, D.
Tunable narrowband THz pulse generation in scalable large area photoconductive antennas
Optics Express **19**, 19114 (2011)
67. Krause, M.; Mücklich, A.; Zak, A.; Seifert, G.; Gemming, S.
High resolution TEM study of WS₂ nanotubes
Physica Status Solidi (b) **248**, 2716 (2011)
68. Krause, M.; Vinnichenko, M.; Shevchenko, N.; Mücklich, A.; Gemming, S.; Munnik, F.; Rogozin, A.; Kolitsch, A.; Möller, W.
Phase segregation and transformations in arsenic-implanted ZnO thin films
Journal of Physical Chemistry C **115**, 8798 (2011)
69. Kumar, H.; Ghosh, S.; Avasthi, D. K.; Kabiraj, D.; Mücklich, A.; Zhou, S.; Schmidt, H.; Stoquert, J. P.
Ion beam-induced shaping of Ni nanoparticles embedded in a silica matrix: from spherical to prolate shape
Nanoscale Research Letters **6**, 155 (2011)
70. Kumar, H.; Ghosh, S.; Bürger, D.; Li, L.; Zhou, S.; Kabiraj, D.; Avasthi, D. K.; Grötzschel, R.; Schmidt, H.
Role of Coulomb blockade and spin-flip scattering in tunneling magnetoresistance of FeCo-Si-O nanogranular films
Journal of Applied Physics **109**, 073914 (2011)
71. Kunze, T.; Gemming, S.; Posselt, M.; Seifert, G.
Tribological aspects of carbon-based nanocoatings - Theory and simulation
Zeitschrift für Physikalische Chemie **225**, 379 (2011)
72. Laufer, A.; Volbers, N.; Eisermann, S.; Potzger, K.; Geburt, S.; Ronning, C.; Meyer, B.
Determination of secondary ion mass spectrometry relative sensitivity factors for polar and non-polar ZnO
Journal of Applied Physics **110**, 094906 (2011)
73. Lehmann, J.; Shevchenko, N.; Mücklich, A.; von Borany, J.; Skorupa, W.; Schubert, J.; Lopes, J. M. J.; Mantl, S.
Millisecond flash-lamp annealing of LaLuO₃
Microelectronic Engineering **88**, 1346 (2011)
74. Li, L.; Prucnal, S.; Yao, S. D.; Potzger, K.; Anwand, W.; Wagner, A.; Zhou, S.
Rise and fall of defect induced ferromagnetism in SiC single crystals
Applied Physics Letters **98**, 222508 (2011)
75. Li, L.; Yao, S. D.; Roshchupkina, O.; Prucnal, S.; Akhmadaliev, S.; Champion, R. P.; Rushforth, A. W.; Fassbender, J.; Helm, M.; Gallagher, B. L.; Timm, C.; Schmidt, H.; Zhou, S.
Characterization and local magnetic modification of ion irradiated GaMnAs
Nuclear Instruments and Methods in Physics Research B **269**, 2469 (2011)
76. Li, L.; Zhou, S.; Buerger, D.; Roshchupkina, O.; Rushforth, A.; Champion, R. P.; Yao, S.; Grenzer, J.; Fassbender, J.; Helm, M.
Tailoring the magnetism of GaMnAs films by ion irradiation
Journal of Physics D: Applied Physics **44**, 045001 (2011)
77. Lushtinetz, R.; Gemming, S.; Seifert, G.
Anchoring functional molecules on TiO₂ surfaces: A comparison between the carboxylic and the phosphonic acid group
European Physical Journal Plus **126**, 98 (2011)
78. Macko, S.; Frost, F.; Engler, M.; Hirsch, D.; Hoche, T.; Grenzer, J.; Michely, T.
Phenomenology of iron-assisted ion beam pattern formation on Si(001)
New Journal of Physics **13**, 073017 (2011)

79. Marcham, M. K.; Keatley, P. S.; Neudert, A.; Hicken, R. J.; Cavill, S. A.; Shelford, L. R.; van der Laan, G.; Telling, N. D.; Childress, J. R.; Katine, J. A.; Shafer, P.; Arenholz, E.
Phase resolved X-ray ferromagnetic measurements in fluorescence yield
Journal of Applied Physics **109**, 07D353 (2011)
80. Martin, N.; Bigall, N. C.; Mönch, I.; Gemming, T.; Eychmüller, A.; Mattheis, R.; Schäfer, R.; Schultz, L.; McCord, J.
Enhanced nucleation of vortices in soft magnetic disks prepared by silica nanosphere lithography
Advanced Functional Materials **21**, 891 (2011)
81. Martin, N.; Mönch, I.; Schäfer, R.; Fassbender, J.; Schultz, L.; McCord, J.
Influence of dipolar energy on the magnetization reversal in magnetization-modulated thin film systems: Model and experiment
Physical Review B **83**, 174423 (2011)
82. Martinavičius, A.; Abrasonis, G.; Möller, W.
Influence of crystal orientation and ion bombardment on the nitrogen diffusivity in single-crystalline austenitic stainless steel
Journal of Applied Physics **110**, 074907 (2011)
83. McCord, J.; Strache, T.; Mönch, I.; Mattheis, R.; Fassbender, J.
Spatial manipulation of magnetic damping in ferromagnetic-antiferromagnetic films by ion irradiation
Physical Review B **83**, 224407 (2011)
84. Melikhova, O.; Cizek, J.; Kuriplach, J.; Prochazka, I.; Anwand, W.; Brauer, G.; Grambole, D.
Characterization of point defects in yttria stabilized zirconia single crystals
Journal of Physics: Conference Series **262**, 012038 (2011)
85. Merchel, S.; Bremser, W.; Alfimov, V.; Arnold, M.; Aumaître, G.; Benedetti, L.; Bourlès, D. L.; Caffee, M.; Fifield, L. K.; Finkel, R. C.; Freeman, S. P.; Martschini, M.; Matsushi, Y.; Rood, D. H.; Sasa, K.; Steier, P.; Takahashi, T.; Tamari, M.; Tims, S. G.; Tosaki, Y.; Wilcken, K. M.; Xu, S.
Ultra-trace analysis of ^{36}Cl by accelerator mass spectrometry: An interlaboratory study
Analytical and Bioanalytical Chemistry **400**, 3125 (2011)
86. Mitterer, C.; Fateh, N.; Munnik, F.
Microstructure-property relations of reactively magnetron sputtered VC_xN_y films
Surface & Coatings Technology **205**, 3805 (2011)
87. Mok, K. M.; Du, N.; Schmidt, H.
Vector-magneto-optical generalized ellipsometry
Review of Scientific Instruments **82**, 033112 (2011)
88. Mok, K. M.; Kovacs, G. J.; McCord, J.; Li, L.; Helm, M.; Schmidt, H.
Magneto-optical coupling of ferromagnetic thin films investigated by vector-magneto-optical generalized ellipsometry
Physical Review B **84**, 094413 (2011)
89. Mok, K. M.; Scarlat, C.; Kovacs, Gyorgy J.; Li, L.; Zviagin, V.; McCord, J.; Helm, M.; Schmidt, H.
Thickness independent magneto-optical coupling constant of nickel films in the visible spectral range
Journal of Applied Physics **110**, 123110 (2011)
90. Morris, C. M.; Stehr, D.; Kim, H. C.; Truong, T. A.; Pryor, C.; Petroff, P. M.; Sherwin, M. S.
Terahertz ionization of highly-charged quantum posts in a perforated electron gas
Nano Letters, DOI: 10.1021/nl1044154 (2011)
91. Müller, A.; Lorenz, M.; Brachwitz, K.; Lenzner, J.; Mittwoch, K.; Skorupa, W.; Grundmann, M.; Höche, T.
Fresnoite thin films grown by pulsed laser deposition: photoluminescence and laser crystallization
CrystEngComm **13**, 6377 (2011)
92. Nembach, H. T.; Livesey, K. L.; Kostylev, M. P.; Martin-Pimentel, P.; Hermsdoerfer, S. J.; Leven, B.; Fassbender, J.; Hillebrands, B.
Magneto-optical observation of four-wave scattering in a 15-nm $\text{Ni}_{81}\text{Fe}_{19}$ film during large-

- angle magnetization precession**
Physical Review B **84**, 184413 (2011)
93. Nomura, K.; Reuther, H.
Nano particles of iron oxides in SiO₂ glass prepared by ion implantation
Journal of Radioanalytical and Nuclear Chemistry **287**, 341 (2011)
94. Numazawa, S.; Ranjan, M.; Heinig, K.-H.; Facsko, S.; Smith, R.
Ordered Ag nanocluster structures by vapor deposition on pre-patterned SiO₂
Journal of Physics: Condensed Matter **23**, 222203 (2011)
95. Numazawa, S.; Smith, R.
A Markov chain model of classified atomistic transition states for discrete kinetic Monte-Carlo simulations
Physical Review E **84**, 046714 (2011)
96. Oates, T. W. H.; Ranjan, M.; Facsko, S.; Arwin, H.
Highly anisotropic effective dielectric functions of silver nanoparticle arrays
Optics Express **19**, 2014 (2011)
97. Oliveira, A. F.; Gemming, S.; Seifert, G.
Conformational analysis of aqueous BMP-2 using atomistic molecular-dynamics simulations
Journal of Physical Chemistry B **115**, 1122 (2011)
98. Ortolani, M.; Stehr, D.; Wagner, M.; Helm, M.; Pizzi, G.; Virgilio, M.; Grosso, G.; Capellini, G.; de Seta, M.
Long intersubband relaxation times in n-type germanium quantum wells
Applied Physics Letters **99**, 201101 (2011)
99. Ou, X.; Geyer, N.; Kögler, R.; Werner, P.; Skorupa, W.
Acceptor deactivation in individual silicon nanowires: From thick to ultrathin
Applied Physics Letters **98**, 253103 (2011)
100. Ou, X.; Kögler, R.; Wei, X.; Mücklich, A.; Wang, X.; Skorupa, W.; Facsko, S.
Fabrication of horizontal silicon nanowire arrays on insulator by ion irradiation
AIP Advances **1**, 042174 (2011)
101. Öztürk, O.; Okur, S.; Pichon, L.; Liedke, M. O.; Riviere, J. P.
Magnetic layer formation on plasma nitrided CoCrMo alloy
Surface & Coatings Technology **205**, S280 (2011)
102. Peplinski, B.; Adam, C.; Reuther, H.; Vogel, C.; Adamczyk, B.; Menzel, M.; Emmerling, F.; Simon, F.-G.
First identification of the tridymite form of AlPO₄ in a municipal sewage sludge ash
Zeitschrift für Kristallographie Proceedings **1**, 443 (2011)
103. Potzger, K.; Levin, A. A.; Shalimov, A.; Osten, J.; Meyer, D. C.
Defect-induced ferromagnetism in crystalline SrTiO₃
Journal of Magnetism and Magnetic Materials **323**, 1551 (2011)
104. Prochazka, I.; Cizek, J.; Anwand, W.; Brauer, G.; Grambole, D.; Schmidt, H.
Hydrogen-induced surface modifications of ZnO single crystals
Journal of Physics: Conference Series **262**, 012050 (2011)
105. Prucnal, S.; Facsko, S.; Baumgart, C.; Schmidt, H.; Liedke, M. O.; Rebohle, L.; Shalimov, A.; Reuther, H.; Kanjilal, A.; Mücklich, A.; Helm, M.; Zuk, J.; Skorupa, W.
n-InAs nanopyramids fully integrated into silicon
Nano Letters **11**, 2814 (2011)
106. Prucnal, S.; Rebohle, L.; Skorupa, W.
Electroluminescence from Er and Yb co-doped silicon dioxide layers: The excitation mechanism
Journal of Non-Crystalline Solids **357**, 915 (2011)
107. Prucnal, S.; Schumann, T.; Skorupa, W.; Abendroth, B.; Krockert, K.; Möller, H. J.
Solar cell emitters fabricated by flash lamp millisecond annealing
Acta Physica Polonica A **120**, 30 (2011)

108. Prucnal, S.; Turek, M.; Drozdziel, A.; Pyszniak, K.; Wójtowicz, A.; Zhou, S.-Q.; Kanjilal, A.; Shalimov, A.; Skorupa, W.; Zuk, J.
Optical and microstructural properties of self-assembled InAs quantum structures in silicon
Central European Journal of Physics **9**, 338 (2011)
109. Rafaja, D.; Wuestefeld, C.; Baehz, C.; Klemm, V.; Dopita, M.; Motylenko, M.; Michotte, C.; Kathrein, M.
Effect of internal interfaces on hardness and thermal stability of nanocrystalline Ti_{0.5}Al_{0.5}N coatings
Metallurgical and Materials Transactions A **42A**, 559 (2011)
110. Rawski, M.; Zuk, J.; Kulik, M.; Drozdziel, A.; Li, L.; Prucnal, S.; Pyszniak, K.; Turek, M.
Influence of hot implantation on residual radiation damage in silicon carbide
Acta Physica Polonica A **120**, 192 (2011)
111. Rebohle, L.; Kanjilal, A.; Skorupa, W.; Helm, M.
The inverse energy transfer between Ge nanocrystals and erbium in SiO₂ and its dependence on microstructure
Optical Materials **33**, 1075 (2011)
112. Rebohle, L.; Lehmann, J.; Prucnal, S.; Helm, M.; Skorupa, W.
The electrical and electroluminescence properties of rare earth implanted MOS light emitting devices in the near infrared
Journal of Luminescence, DOI: 10.1016/j.jlumin.2011.11.024 (2011)
113. Redondo-Cubero, A.; Vinnichenko, M.; Krause, M.; Mücklich, A.; Muñoz, E.; Kolitsch, A.; Gago, R.
Sublattice-specific ordering of ZnO layers during the heteroepitaxial growth at different temperatures
Journal of Applied Physics **110**, 113516 (2011)
114. Reichel, D.; Skorupa, W.; Lerch, W.; Gelpey, J. C.
Temperature measurement in rapid thermal processing with focus on the application to Flash Lamp Annealing
Critical Reviews in Solid State and Material Sciences **36**, 102 (2011)
115. Remskar, M.; Mrzel, A.; Virsek, M.; Godec, M.; Krause, M.; Kolitsch, A.; Singh, A.; Seabaugh, A.
The MoS₂ nanotubes with defect-controlled electric properties
Nanoscale Research Letters **6**, 26 (2011)
116. Ren, Y.; Jia, Y.; Chen, F.; Lu, Q.; Akhmaliev, Sh.; Zhou, S.
Second harmonic generation of swift carbon ion irradiated Nd:GdCOB waveguides
Optics Express **19**, 12490 (2011)
117. Richter, A.; Chen, C.-L.; Mücklich, A.; Kögler, R.
Irradiation damage in dual beam irradiated nanostructured FeCrAl oxide dispersion strengthened steel
Materials Research Society Symposium Proceedings **1298**, 141 (2011)
118. Sahle, C. J.; Zschintzsch, M.; Sternemann, C.; von Borany, J.; Nyrow, A.; Jeutter, N. M.; Wagner, R.; Frahm, R.; Tolan, M.
Influence of hydrogen on the thermally induced phase separation in GeO/SiO₂ multilayers
Nanotechnology **22**, 125709 (2011)
119. Saly, M. J.; Munnik, F.; Winter, C. H.
The atomic layer deposition of SrB₂O₄ films using the thermally stable precursor bis(tris(pyrazolyl)borate)strontium
Chemical Vapor Deposition **17**, 128 (2011)
120. Schmidt, M.; Brachwitz, K.; Schmidt, F.; Ellguth, M.; von Wenckstern, H.; Pickenhain, R.; Grundmann, M.; Brauer, G.; Skorupa, W.
Nickel-related defects in ZnO – A deep-level transient spectroscopy and photo-capacitance study
Physica Status Solidi (b) **248**, 1949 (2011)

121. Shuai, Y.; Zhou, S.; Bürger, D.; Helm, M.; Schmidt, H.
Nonvolatile bipolar resistive switching in Au/BiFeO₃/Pt
Journal of Applied Physics **109**, 124117 (2011)
122. Shuai, Y.; Zhou, S.; Bürger, D.; Reuther, H.; Skorupa, I.; John, V.; Helm, M.; Schmidt, H.
Decisive role of oxygen vacancy in ferroelectric versus ferromagnetic Mn-doped BaTiO₃ thin films
Journal of Applied Physics **109**, 084105 (2011)
123. Shuai, Y.; Zhou, S.; Streit, S.; Reuther, H.; Bürger, D.; Slesazeck, S.; Mikolajick, T.; Helm, M.; Schmidt, H.
Reduced leakage current in BiFeO₃ thin films with rectifying contacts
Applied Physics Letters **98**, 232901 (2011)
124. Shuai, Y.; Zhou, S.; Wu, C.; Zhang, W.; Bürger, D.; Slesazeck, S.; Mikolajick, T.; Helm, M.; Schmidt, H.
Control of rectifying and resistive switching behavior in BiFeO₃ thin films
Applied Physics Express **4**, 095802 (2011)
125. Sopik, B.; Lipavský, P.; Männel, M.; Morawetz, K.
Conserving T-matrix theory of superconductivity
Physical Review B **84**, 094529 (2011)
126. Steinhauser, G.; Merchel, S.; Knappik, R.
Nuclear analytical methods: We've got the hammer for your nail (Editorial)
Applied Radiation and Isotopes **69**, 1585 (2011)
127. Tang, F.; Frontzek, M.; Dshemuchadse, J.; Leisegang, T.; Zschornak, M.; Mietrach, R.; Hoffmann, J.-U.; Löser, W.; Gemming, S.; Meyer, D. C.; Loewenhaupt, M.
Crystallographic superstructure in R₂PdSi₃ compounds (R=heavy rare earth)
Physical Review B **84**, 104105 (2011)
128. Tavella, F.; Stojanovic, N.; Geloni, G.; Gensch, M.
Few-femtosecond timing at fourth-generation X-ray light sources
Nature Photonics **5**, 162 (2011)
129. Terentyev, D.; Malerba, L.; Bonny, G.; Al-Motasem, A. T.; Posselt, M.
Interaction of an edge dislocation with Cu–Ni-vacancy clusters in bcc iron
Journal of Nuclear Materials **419**, 134 (2011)
130. Ueda, M.; Silva Jr., A. R.; Mello, C. B.; Silva, G.; Reuther, H.; Oliveira, V. S.
Influence of the residual oxygen in the plasma immersion ion implantation (PI3) processing of materials
Nuclear Instruments and Methods in Physics Research B **269**, 3246 (2011)
131. Undisz, A.; Reuther, K.; Reuther, H.; Rettenmayr, M.
Occurrence and origin of non-martensitic acicular artifacts on NiTi
Acta Materialia **59**, 216 (2011)
132. Voelskow, M.; Stoimenos, I.; Reohle, L.; Skorupa, W.
The formation of near surface SiGe layers with combined high-dose ion implantation and flash-lamp annealing
Physica Status Solidi (c) **8**, 960 (2011)
133. Vogel, A.; Wintz, S.; Gerhardt, T.; Bocklage, L.; Strache, T.; Im, M.-Y.; Fischer, P.; Fassbender, J.; McCord, J.; Meier, G.
Field- and current-induced domain-wall motion in permalloy nanowires with magnetic soft spots
Applied Physics Letters **98**, 202501 (2011)
134. Wagner, M.; Helm, M.; Sherwin, M. S.; Stehr, D.
Coherent control of a THz intersubband polarization in a voltage controlled single quantum well
Applied Physics Letters **99**, 131109 (2011)
135. Wagner, S.; Uchida, H.; Burlaka, V.; Vlach, M.; Vlcek, M.; Lukac, F.; Cizek, J.; Baehtz, C.; Bell, A.; Pundt, A.

- Achieving coherent phase transition in palladium–hydrogen**
Scripta Materialia **64**, 978 (2011)
136. Weatherup, R. S.; Bayer, B. C.; Blume, R.; Ducati, C.; Baehtz, C.; Schlögl, R.; Hofmann, S.
In situ characterization of alloy catalysts for low-temperature graphene growth
Nano Letters **11**, 4154 (2011)
137. Weber, J. W.; Hinrichs, K.; Gensch, M.; van de Sanden, M. C. M.; Oates, T. W. H.
Microfocus infrared ellipsometry characterization of air-exposed graphene flakes
Applied Physics Letters **99**, 061909 (2011)
138. Werner, M.; Altstadt, E.; Jungmann, M.; Brauer, G.; Noack, K.; Rogov, A.; Krause-Rehberg, R.
Thermal analysis of EPOS components
Journal of Physics: Conference Series **265**, 012028 (2011)
139. Winnerl, S.; Orlita, M.; Plochocka, P.; Kossacki, P.; Potemski, M.; Winzer, T.; Malic, E.; Knorr, A.; Sprinkle, M.; Berger, C.; de Heer, W. A.; Schneider, H.; Helm, M.
Carrier relaxation in epitaxial graphene photoexcited near the Dirac point
Physical Review Letters **107**, 237401 (2011)
140. Winnerl, S.; Stehr, D.; Wagner, M.; Schneider, H.; Helm, M.; Seidel, W.; Michel, P.; Zibik, E. A.; Carpenter, B. A.; Porter, N. E.; Skolnick, M. S.; Wilson, L. R.; Grange, T.; Ferreira, R.; Bastard, G.; Orlita, M.; Plochocka, P.; Kossacki, P.; Potemski, M.; Sprinkle, M.; Berger, C.; de Heer, W. A.
Time resolved spectroscopy on quantum dots and graphene at the FELBE free-electron laser
Proceedings of SPIE **7937**, 793708 (2011)
141. Wintz, S.; Strache, T.; Körner, M.; Fritzsche, M.; Markó, D.; Mönch, I.; Mattheis, R.; Raabe, J.; Quitmann, C.; McCord, J.; Erbe, A.; Fassbender, J.
Direct observation of antiferromagnetically oriented spin vortex states in magnetic multilayer elements
Applied Physics Letters **98**, 232511 (2011)
Erratum *Applied Physics Letters* **99**, 149901 (2011)
142. Wojcik, H.; Merkel, U.; Jahn, A.; Richter, K.; Junige, M.; Klein, C.; Gluch, J.; Albert, M.; Munnik, F.; Wenzel, C.; Bartha, J. W.
Comparison of PVD, PECVD & PEALD Ru(-C) films as Cu diffusion barriers by means of bias temperature stress measurements
Microelectronic Engineering **88**, 641 (2011)
143. Wolf, M.; Patschureck, C.; Schafer, R.; Monch, I.; Schultz, L.; McCord, J.
Array anisotropy in structured thin film arrays: Influence on the magnetodynamics
Journal of Magnetism and Magnetic Materials **323**, 1703 (2011)
144. Wüstefeld, Ch.; Rafaja, D.; Dopita, M.; Motylenko, M.; Baehtz, C.; Michotte, C.; Kathrein, M.
Decomposition kinetics in $Ti_{1-x}Al_xN$ coatings as studied by in-situ X-ray diffraction during annealing
Surface & Coatings Technology **206**, 1727 (2011)
145. Xu, Q.; Zhou, S.; Wen, Z.; Wu, D.; Qiu, T.; Xu, M.; Potzger, K.; Schmidt, H.
Magnetic characterization of $Bi(Fe_{1-x}Mn_x)O_3$
Physics Letters A **375**, 1209 (2011)
146. Yang, J.; Zhang, C.; Chen, F.; Akhmadaliev, Sh.; Zhou, S.
Planar optical waveguides in $Bi_4Ge_3O_{12}$ crystal fabricated by swift heavy-ion irradiation
Applied Optics **50**, 6678 (2011)
147. Zaks, B.; Stehr, D.; Truong, T. A.; Petroff, P. M.; Hughes, S.; Sherwin, M. S.
THz-driven quantum wells: Coulomb interactions and Stark shifts in the ultrastrong coupling regime
New Journal of Physics **13**, 083009 (2011)
148. Zatsepin, D. A.; Mack, P.; Wright, A. E.; Schmidt, B.; Fitting, H.-J.
XPS analysis and valence band structure of a low-dimensional SiO_2/Si system after Si^+ ion implantation
Physica Status Solidi (a) **208**, 1658 (2011)

149. Zheng, C. C.; Xu, S. J.; Ning, J. Q.; Chen, Y. N.; Lu, X. H.; Ling, C.-C.; Che, C. M.; Gao, G. Y.; Hao, J. H.; Brauer, G.; Anwand, W.
Ion-implantation induced nano distortion layer and its influence on nonlinear optical properties of ZnO single crystals
Journal of Applied Physics **110**, 083102 (2011)
150. Zhou, J.; Facsko, S.; Lu, M.; Möller, W.
Nanopatterning of Si surfaces by normal incident ion erosion: Influence of iron incorporation on surface morphology evolution
Journal of Applied Physics **109**, 104315 (2011)
151. Zhou, S.; Bürger, D.; Li, L.; Skorupa, W.; Helm, M.; Oesterlin, P.; Schmidt, H.
Ferromagnetic Ge:Mn prepared by ion implantation and pulsed laser annealing
AIP Conference Proceedings **1399**, 699 (2011)
152. Zhou, S.; Shalimov, A.; Wang, Y.; Potzger, K.
Lattice damage and secondary phase formation in yttria stabilised zirconia implanted with Fe at different temperatures
Journal of Nuclear Materials **416**, 358 (2011)
153. Zimmermann, B.; Fietzke, F.; Möller, W.
Spatially resolved Langmuir probe measurements of a magnetically enhanced hollow cathode arc plasma
Surface & Coatings Technology **205**, S393 (2011)
154. Zotov, N.; Feydt, J.; Savan, A.; Ludwig, A.; von Borany, J.
Interdiffusion in Fe/Pt multilayers: In-situ high-temperature synchrotron radiation reflectivity study
Advanced Engineering Materials **13**, 475 (2011)
155. Zschintzsch, M.; Sahle, Ch. J.; von Borany, J.; Sternemann, C.; Mücklich, A.; Nyrow, A.; Schwamberger, A.; Tolan, M.
Ge-Si-O phase separation and Ge nanocrystals growth in Ge:SiO₂/SiO₂ multilayers – A new dc magnetron approach
Nanotechnology **22**, 485303 (2011)
156. Zschintzsch, M.; von Borany, J.; Jeutter, N. M.; Mücklich, A.
Stacked Ge nanocrystals with ultrathin SiO₂ separation layers
Nanotechnology **22**, 465302 (2011)
157. Zybell, S.; Schneider, H.; Winnerl, S.; Wagner, M.; Köhler, K.; Helm, M.
Photoluminescence dynamics in GaAs/AlGaAs quantum wells under pulsed intersubband excitation
Applied Physics Letters **99**, 041103 (2011)

Patents

1. Bischoff, L.; Akhamadakiev, Ch.
Flüssigmetall-Ionenquelle zur Erzeugung von Lithium-Ionenstrahlen
DE 10 2007 027 097 B4 - 30.12.2010 (granted)
2. Skorupa, W.; Prucnal, S.; Rebohle, L.; Helm, M.
Si-basierter Lichtemitter
DE 10 2007 019 209 B4 - 05.01.2011 (granted)
3. Voelskow, M.; Kanjilal, A.; Skorupa, W.
Verfahren zur Herstellung von SiC basierenden Dünnschicht-Solarzelle mit erhöhter Effizienz
DE 10 2009 055 215 A1 – 29.09.2011 (published)

Concluded scientific degrees

PhD theses

1. Jacob, R.
Scanning near-field infrared micro-spectroscopy on semiconductor structures
TU Dresden, 21.04.2011
2. Kosmata, M.
Elastic Recoil Detection of light elements with sub-nanometer depth resolution
TU Dresden, 21.12.2011
3. Liedke, B.
Ion beam processing of surfaces and interfaces – Modelling and atomistic simulation
TU Dresden, 23.09.2011
4. Martin, N.
Herstellung und Charakterisierung von magnetisch heterogenen Schichten und Elementen
TU Dresden, 07.06.2011
5. Martinavicius, A.
Structural and transport property changes in austenitic stainless steel induced by nitrogen incorporation
TU Dresden, 06.05.2011
6. Mukesh, R.
Metal nanoparticles / nanowires self-assembly on ripples patterned substrates
TU Dresden, 06.06.2011

Diploma theses

1. Baudisch, M.
Ultrabreitbandige THz-Spektroskopie an dotierten Halbleiter-Quantentöpfen
TU Dresden, 06.06.2011
2. Berger, S.
DFTB Investigation on various molecules
TU Dresden, 27.09.2011
3. Franke, C.
Zwei-Photonen-Übergänge und Intersubband-Dynamik in Halbleiterquantenfilmen
TU Dresden, 31.05.2011
4. Göttfert, F.
Relaxationsdynamik der Ladungsträger in Graphen
TU Dresden, 15.11.2011
5. Großmann, F.
Nanostrukturierung von Oberflächen durch Ionenbeschuss
TU Dresden, 19.12.2011
6. Haase, A.
Magnetische Eigenschaften von metallischen Grenzflächen und Strontiumtitanat
TU Dresden, 08.12.2011
7. Henschel, T.
Characterisation of nanomechanical resonators
TU Dresden, 23.09.2011
8. Mertzig, R.
Untersuchungen zur Physik von in hochdichten EBIS-Elektronenstrahlen gespeicherten

Eisenionen*TU Dresden, 09.05.2011*

9. Noack, H.
Untersuchung der elektrischen und magnetischen Eigenschaften von BiFeO₃-Filmen
Fernhochschule Darmstadt, 03.09.2011
10. Ronneberger, I.
DFT Simulation von Punktdefekten in Strontiumtitanat
TU Dresden, 31.10.2011
11. Steinbach, G.
DFT investigation of heteroepitaxial GaP on Si (001)
TU Chemnitz, 15.08.2011
12. Wenisch, R.
Theoretical and experimental investigations on Pd(II) dithiocarbamate compounds
TU Dresden, 25.02.2011

BSc theses

1. Günz, C.
Untersuchung seltenerd-dotierter SiO₂-Dünnschichten für Downconversion Anwendungen in der Photovoltaik
TU Ilmenau, 05.10.2011
2. Kuske, S.
Untersuchung der Ladungsträgermobilität in ZnO
FH Jena, 06.07.2011
3. Richter, H.
Entwicklung, Aufbau und Test eines mikrokontrollerbasierten Funktionsgenerators
FH Senftenberg, 05.07.2011
4. Schiwarth, M.
Calculation of the sterically accessible molecular surface in two dimensions
FH Zittau Görlitz, 31.03.2011

Appointments and honors

Appointments

1. **Prof. Dr. Jeffrey McCord.**
Head of the division “Nanomagnetism” accepted a W2-Heisenberg Professorship on “Nanoscale Magnetic Materials – Magnetic Domains” at the Faculty of Engineering of Kiel University, Kiel, Germany

Awards and honors

1. **David Ball**
PhD student in the junior research group “Magnetization Dynamics” of the division “Nanomagnetism” received a Student Travel Support Award of the IEEE International Magnetism Conference (InterMag) 2011, Taipei, Taiwan
2. **Dr. Ayman Sherif El-Said**
Postdoctoral Humboldt fellow in the group “Ion Induced Nanostructures” of the division “Nanostructures” received the Egypt State Incentive Award in Physics for the Year 2010, June 2011, Egypt
3. **Monika Fritzsche**
PhD student in the group “Ion Induced Nanostructures” of the division “Nanostructures” received the Best Poster Award at the workshop “Nanoscale Pattern Formation at Surfaces”, September 2011, El Escorial, Spain
4. **PD Dr. Sibylle Gemming**
Head of the division “Nanostructures” was appointed member of the Think Tank of the Helmholtz Association
5. **PD Dr. Sibylle Gemming**
Head of the division “Nanostructures” was nominated member of the AcademiaNet, the Expert Database of Outstanding Female Scientists and Scholars
6. **Sebastian Wintz**
PhD student in the junior research group “Transport in Nanostructures” of the division “Nanostructures” received a Student Travel Support Award of IEEE International Magnetism Conference (InterMag) 2011, Taipei, Taiwan

Participation in conferences and lectures / talks

Invited conference talks

1. Abrasonis, G.
Ion-assisted physical vapor deposition: principles and applications
13th International Conference - School on Advanced Materials and Technologies, 27.-31.08.2011, Palanga, Lithuania
2. Abrasonis, G.; Krause, M.; Oates, T. W. H.; Kovacs, Gy. J.; Mücklich, A.; Persson, P. O. A.; Heinig, K.-H. H.; Tucker, M. D.; Bilek, M. M. M.; Möller, W.
Ion-assisted growth of carbon-transition metal nanocomposite thin films: from self-organization to spin-dependent transport
2011 MRS Spring Meeting, 25.-29.04.2011, San Francisco, California, USA
3. Altstadt, E.; Bergner, F.; Hein, H.
Long term irradiation phenomena in RPV steels - the LONGLIFE project
25th Symposium on Effects of Radiation on Nuclear Materials, 15.-17.06.2011, Anaheim, USA
4. Cornelius, S.; Vinnichenko, M.; Munnik, F.; Heller, R.; Kolitsch, A.; Möller, W.
Structure and electrical properties of transparent conductive doped ZnO grown by reactive magnetron sputtering
IOP Workshop "Plasmas, Surfaces and Thin Films", 08.06.2011, London, England
5. Facsko, S.; Keller, A.; Liedke, B.; Heinig, K.-H.
Strength and limitations of continuum equations for sputter induced pattern formation
International Conference on Ion-Beam Induced Nanopatterning of Materials, 06.-10.02.2011, Bhubaneswar, India
6. Fassbender, J.
Seltene Metalle in der Hochtechnologie
1. Freiburger Ressourcen Technologie Symposium, 14.-15.02.2011, Freiberg, Germany
7. Gemming, S.
Density functional theory + transmission electron microscopy - Introduction to density functional theory & Transport through nanostructures
CECAM-Workshop DFTEM 2011, 24.-28.07.2011, Lausanne, Switzerland
8. Gemming, S.; Zschornak, M.; Weißbach, T.; Stöcker, H.; Meyer, D. C.; Gemming, T.; Lubk, A.; Spaldin, N. A.
Multifunctional oxides - Influence of defects on the ferroic properties
Workshop of the Collaborative Research Centre/Transregio TRR 80, 26.05.2011, Garching b. München, Germany
9. Gensch, M.
Photon diagnostics at X-ray FEL's
DIPAC 2011, 15.-19.05.2011, Hamburg, Germany
10. Grenzer, J.
In-situ X-ray scattering: A tool for investigation of nanostructure formation
8th Autumn School on X-ray Scattering from Surfaces and Thin Layers, 04.-07.10.2011, Smolenice Castle, Slovakia
11. Helm, M.
THz physics with a free-electron laser
THz Science and Technology - The Castle Meeting, 03.-06.07.2011, Schloss Rauschholzhausen, Germany
12. Helm, M.
THz spectroscopy of semiconductors at high electric and magnetic fields
4th Annual Meeting of the German Terahertz Center, 28.03.2011, Regensburg, Germany

13. Helm, M.
Terahertz nonlinear optics of exciton states
Workshop of the GDRI-CNRS: Semiconductors Sources and Detectors of THz Radiation, 29.03.-01.04.2011, Tignes, France
14. Helm, M.
Terahertz nonlinear and coherent effects in semiconductor nanostructures
International Symposium on Terahertz Nanoscience (TeraNano 2011), 24.-25.11.2011, Osaka, Japan
15. Helm, M.
The free-electron laser as a tool for time-resolved, nonlinear, and near-field spectroscopy
36th International Conference on Infrared, Millimeter, and Terahertz Waves (IRMMW-THz 2011), 02.-07.10.2011, Houston, TX, USA
16. McCord, J.; Hamann, C.; Strache, T.; Mönch, I.; Fassbender, J.
Magnetic properties of mixed property magnetic thin films prepared by selective ion irradiation
International Conference on Ion-Beam Induced Nanopatterning of Materials - IINM-2011, 06.-10.02.2011, Bhubaneswar, India
17. Merchel, S.; Akhmadaliev, S.; Rugel, G.
Beschleuniger zum Nachweis geringster Isotopenkonzentrationen
Fachgespräch Strahlungsmesstechnik und Software, 05.-07.10.2011, Gelsenkirchen, Germany
18. Merchel, S.; Munnik, F.; Andermann, C.; Bourlès, D.; Braucher, R.; Gloaguen, R.; Martschini, M.; Steier, P.
Setting-up an accelerator mass spectrometry (AMS) facility: The role of chemistry
75th Annual Meeting of the DPG and DPG Spring Meeting 2011, 13.-18.03.2011, Dresden, Germany
19. Michely, T.; Macko, S.; Engler, M.; Frost, F.; Müller, S.; Förster, D.; Höche, T.; Hirsch, D.; Fritzsche, M.; Mücklich, A.; Grenzer, J.
Phenomenology of pattern formation on Si(001) with and without impurities
Nanoscale Pattern Formation at Surfaces, 18.-22.09.2011, El Escorial, Spain
20. Neudert, A.; McCord, J.
Twin boundary motion and magnetic domain distribution investigated by optical polarization microscopy
International Conference on Ferromagnetic Shape Memory Alloys, 18.-22.07.2011, Dresden, Germany
21. Prucnal, S.; Facsko, S.; Baumgart, C.; Schmidt, H.; Liedke, M. O.; Mücklich, A.; Zhou, S.; Skorupa, W.
Liquid phase processing in the millisecond range for III-V heterostructures in silicon
30. Deutsches Nutzertreffen RTP und Heissprozesse, 23.-23.11.2011, Blaubeuren, Germany
22. Prucnal, S.; Facsko, S.; Baumgart, C.; Schmidt, H.; Liedke, M. O.; Mücklich, A.; Zhou, S.; Skorupa, W.
Ion beam synthesis of III-V nanocrystals in silicon
46. Deutsches Nutzertreffen Ionenimplantation, 24.11.2011, Blaubeuren, Germany
23. Scheinost, A. C.
The Rossendorf Beamline at ESRF: A multipurpose X-ray absorption spectroscopy and scattering beamline for environmental and materials sciences
SESAME User Meeting 2011, 12.11.2011, Amman, Jordan
24. Schmidt, B.; Heinig, K.-H.
Nanoparticle formation in solids
E-MRS 2011 Spring Meeting IUMRS ICAM 2011 & E-MRS/MRS Bilateral Conference on Energy, 09.-13.05.2011, Nice, France
25. Schmidt, B.; Philipp, P.; Zier, M.
Charge carrier depth profiling at ultra-shallow pn-junctions
Workshop "Moderne Methoden der Oberflächen- und Dünnschichtanalytik", 30.11.2011, Dresden, Germany

-
26. Schneider, H.
Infrared/terahertz applications in physical sciences
Free Electron Laser IR to THz Applications Workshop, 28.01.2011, Bangkok, Thailand
27. Schneider, H.
Nonlinear terahertz spectroscopy of semiconductor quantum structures
2. IR-ON Symposium: InfraRed Optical Nanostructures, 10.03.2011, Wien, Austria
28. Schneider, H.
Optical nonlinearities in quantum wells
Rosencher's Opto-Electronic Day, 24.05.2011, Palaiseau, France
29. Schneider, H.
Infrared photodetectors based on quantum wells
Workshop on Infrared Technology, 05.-09.12.2011, Rio de Janeiro, Brasil
30. Skorupa, W.
Advances in Si & Ge millisecond processing: From SOI to superconductivity and carrier-mediated ferromagnetism
219th Electrochemical Society Meeting, Symposium E1: Silicon compatible materials, processes and technologies for advanced integrated circuits and emerging applications, 01.-06.05.2011, Montreal, Canada
31. Skorupa, W.; Cherkouk, C.; Prucnal, D. Henke S.; Reuter, H.; Hahn, A.; Skorupa, K.; Jehmlich, R.; Werner, H.; Pfeiffer, D.; Eule, A.-C.
Plasma immersion implantation for the corrosion protection of lead in pipe organs
2. Internationale Konferenz des Instituts für Orgel und Orgelbau an der Hochschule für Künste Bremen, 17.-19.03.2011, Lemgo, Germany
32. Skorupa, W.; Rebohle, L.
Light-emission from rare-earth implanted amorphous silicon dioxide layers
EMRS Fall Meeting, Symposium B: Amorphous nanostructure materials, 19.-23.09.2011, Warsaw, Poland
33. Stehr, D.; Morris, C. M.; Talbayev, D.; Wagner, M.; Kim, H. C.; Taylor, A. J.; Schneider, H.; Petroff, P. M.; Sherwin, M. S.
Ultrafast carrier capture and THz resonances in InGaAs quantum posts
SPIE Photonics West 2011, 20.-27.01.2011, San Francisco, USA
34. Wagner, M.; Schneider, H.; Stehr, D.; Winnerl, S.; Teich, M.; Andrews, A. M.; Schartner, S.; Strasser, G.; Helm, M.
Terahertz nonlinear optics of intra-exciton transitions in quantum wells
EP2DS19/MSS15, 25.-29.07.2011, Tallahassee, USA
35. Wagner, M.; Schneider, H.; Stehr, D.; Winnerl, S.; Teich, M.; Helm, M.; Andrews, A. M.; Schartner, S.; Strasser, G.
Intraexciton terahertz nonlinear optics in quantum wells
75th Annual Meeting of the DPG and DPG Spring Meeting 2011, 13.-18.03.2011, Dresden, Germany
36. Winnerl, S.
Near-field spectroscopy on semiconductor micro- and nanostructures at FELBE
6th Workshop on Infrared Spectroscopy and Microscopy with Accelerator-Based Sources, 04.-08.09.2011, Trieste, Italy
37. Winnerl, S.; Schneider, H.; Helm, M.; Orlita, M.; Plochocka, P.; Kossacki, P.; Potemski, M.; Winzer, T.; Malic, E.; Knorr, A.; Sprinkle, M.; Berger, C.; de Heer, W. A.
Relaxation dynamics in graphene close to the Dirac point
International Symposium on THz nanoscience (TeraNano 2011), 24.-25.11.2011, Osaka, Japan
38. Winnerl, S.; Stehr, D.; Wagner, M.; Schneider, H.; Helm, M.; Seidel, W.; Michel, P.; Zibik, E. A.; Carpenter, B. A.; Porter, N. E.; Skolnick, M. S.; Wilson, L. R.; Grange, T.; Ferreira, R.; Bastard, G.; Orlita, M.; Plochocka, P.; Kossacki, P.; Potemski, M.; Sprinkle, M.; Berger, C.; de Heer, W. A.
Time resolved spectroscopy on quantum dots and graphene at the FELBE free-electron laser
SPIE Photonics West 2011, 22.-27.01.2011, San Francisco, USA

39. Zhou, S.
Ion implantation and short-time annealing for spintronics
Workshop „Ionen- und Positronenstrahlen“, 04.-05.07.2011, München, Germany
40. Zhou, S.; Potzger, K.; Yang, Z.; Helm, M.; Fassbender, J.
Ion irradiation as a controllable approach to study the defect-induced ferromagnetism
China-Germany Symposium on "Electronic structure calculations and their application in material science", 08.-11.11.2011, Chengdu, China

Conference talks

1. Abrasonis, G.; Krause, M.; Mücklich, A.; Heller, R.; Heinig, K. –H. H.; Gemming, S.; Möller, W.
Ion beam assisted deposition of C:Ni composites: Growth of regular nanostructures by surface-layer-limited phase separation
E-MRS 2011 Spring Meeting IUMRS ICAM 2011 & E-MRS/MRS Bilateral Conference on Energy, 09.-13.05.2011, Nice, France
2. Abrasonis, G.; Wintz, S.; Liedke, M. O.; Aksoy, F.; Liu, Z.; Kuepper, K.; Krause, M.; Gemming, S.
Environment controlled de-wetting kinetics of Rh-Pd bilayer thin films
75th Annual Meeting of the DPG and DPG Spring Meeting 2011, 13.-18.03.2011, Dresden, Germany
3. Akhmadaliev, Sh.; Heller, R.; Hanf, D.; Merchel, S.
First experiments at the new 6 MV-Tandetron at HZDR
75th Annual Meeting of the DPG and DPG Spring Meeting 2011, 14.-18.03.2011, Dresden, Germany
4. Al-Motasem, A. T.; Posselt, M.; Bergner, F.; Birkenheuer, U.
Structure and energetics of nanoclusters in bcc-Fe containing vacancies, Cu, and Ni.
E-MRS 2011 Spring Meeting IUMRS ICAM 2011 & E-MRS/MRS Bilateral Conference on Energy, 09.-13.05.2011, Nice, France
5. Al-Motasem, A. T.; Posselt, M.; Bergner, F.; Birkenheuer, U.
Structure and energetics of nanoclusters in bcc-Fe containing vacancies, Cu, and Ni
75th Annual Meeting of the DPG and DPG Spring Meeting 2011, 13.-18.03.2011, Dresden, Germany
6. Anwand, W.; Butterling, M.; Brauer, G.; Wagner, A.; Richter, A.; Chen, C.-L.; Kögler, R.
Ion implantation-induced defects in Oxide Dispersion Strengthened (ODS) steel probed by positron annihilation spectroscopy
Workshop "Ionen- und Positronenstrahlen", 04.-05.07.2011, München/Neubiberg, Germany
7. Baehz, Carsten; Wirth, Tobias C.; Bayer, Bernhard C.; Hofmann, S.; von Borany, J.
In-situ characterization of the carbon nanotube growth process by X-ray diffraction
XXII IUCr Congress, 22.-30.08.2011, Madrid, Spain
8. Balocco, C.; Kasjoo, S. R.; Lu, X. F.; Zhang, L. Q.; Alimi, Y.; Winnerl, S.; Song, A. M.
Novel unipolar nanodiodes for room-temperature THz detection
36th International Conference on Infrared, Millimeter, and Terahertz Waves (IRMMW-THz 2011), 02.-07.10.2011, Houston, USA
9. Barlak, M.; Piekoszewski, J.; Werner, Z.; Sartowska, B.; Pisarek, M.; Walis, L.; Starosta, W.; Kolitsch, A.; Gröetzchel, R.; Pochrybniak, K.; Bochenska, C.
Modes of the use of high intensity plasma beams for ceramic surface modification
SMMIB 2009, 13.-18.09.2009, Tokyo, Japan
10. Barlak, M.; Piekoszewski, J.; Werner, Z.; Sartowska, B.; Waliś, L.; Starosta, W.; Kierzek, J.; Bocheńska, K.; Heller, R.; Kolitsch, A.; Pochrybniak, C.; Kowalska, E.
Wettability of carbon and silicon ceramics induced by their alloying with Ti, Zr, and Cu elements using high intensity pulsed plasma beams
NUTECH-2011 International Conference on Development and Applications of Nuclear Technologies, 11.-14.09.2011, Krakow, Poland

11. Barlak, M.; Piekoszewski, J.; Werner, Z.; Sartowska, B.; Waliś, L.; Starosta, W.; Kierzek, J.; Bocheńska, K.; Heller, R.; Wilhelm, R.; Kolitsch, A.; Pochrybniak, C.; Kowalska, E.
High temperature oxidation resistance of stainless steel doped with Yttrium using ion implantation
NUTECH-2011 International Conference on Development and Applications of Nuclear Technologies, 11.-14.09.2011, Krakow, Poland
12. Baudisch, M.; Wagner, M.; Helm, M.; Stehr, D.
Interaction of intersubband transitions and ponderomotive response in doped GaAs/AlGaAs multiple quantum wells at the THz regime
75th Annual Meeting of the DPG and DPG Spring Meeting 2011, 13.-18.03.2011, Dresden, Germany
13. Baumgart, C.; Müller, A.-D.; Müller, F.; Helm, M.; Schmidt, H.
Kelvin probe force microscopy on doped semiconductor nanostructures with local, carrier-depleted space charge regions
75th Annual Meeting of the DPG and DPG Spring Meeting 2011, 13.-18.03.2011, Dresden, Germany
14. Beyer, R.; Burghardt, H.; von Borany, J.
Effect of the processing of embedded Ge nanocrystals upon the Si-SiO₂ interface state and border trap density
14th European Conference on Applications of Surface and Interface Analysis (ECASIA'11), 05.09.2011, Cardiff, Wales
15. Beyer, R.; von Borany, J.
Determination of size and density of embedded Ge nanocrystals in SiO₂ by scanning force microscopy using a tomographic approach
14th European Conference on Applications of Surface and Interface Analysis (ECASIA'11), 06.09.2011, Cardiff, Wales
16. Bhattacharyya, J.; Zybell, S.; Wagner, M.; Helm, M.; Hopkinson, M.; Wilson, L. R.; Schneider, H.
Time-resolved photoluminescence quenching measurements in InAs/GaAs quantum dots using terahertz laser pulses
International Workshop on Optical Terahertz Science and Technology (OTST 2011), 13.-17.03.2011, Santa Barbara, USA
17. Bhattacharyya, J.; Zybell, S.; Wagner, M.; Helm, M.; Hopkinson, M.; Wilson, L. R.; Schneider, H.
Time-resolved photoluminescence quenching measurements in InAs/GaAs quantum dots using terahertz laser pulses
75th Annual Meeting of the DPG and DPG Spring Meeting 2011, 13.-18.03.2011, Dresden, Germany
18. Bischoff, L.; Böttger, R.
Secondary electron emission from surfaces during focused ion beam irradiation
Nanoscale pattern formation at surfaces, 18.-22.09.2011, El Escorial, Spain
19. Böttger, R.; Bischoff, L.; Schmidt, B.; Krause, M.; Pilz, W.; Heinig, K.-H.; Facsko, S.
Novel Ge nanopattern by heavy Bi monomer irradiation
Nanoscale pattern formation at surfaces, 18.-22.09.2011, El Escorial, Spain
20. Bürger, D.
Elektrische Aktivierung von Dotanden durch Lasertempere oberhalb der Löslichkeitsgrenze
29. Treffen der Nutzergruppe Heißprozesse und RTP, 12.05.2011, Erlangen, Germany
21. Bürger, D.; Zhou, S.; Höwler, M.; Kovacs, G.; Reuther, H.; Skorupa, W.; Helm, M.; Schmidt, H.
Depth-resolved magnetotransport properties of ferromagnetic Ge:Mn
Subsecond Thermal Processing of Advanced Materials 2011 (subtherm-2011), 24.-27.10.2011, Dresden, Germany
22. Bürger, D.; Zhou, S.; Kovacs, György J.; Schmidt, H.
Spin-polarized hole transport in pulsed laser annealed Ge:Mn up to 30 K
75th Annual Meeting of the DPG and DPG Spring Meeting 2011, 13.-18.03.2011, Dresden, Germany

23. Butterling, M.; Anwand, W.; Wagner, A.; Skorupa, W.; Eule, A.-C.
Lead sheets for organ pipes - Positron Spectroscopy for cultural heritage
Positron Studies of Defects (PSD) 11 Delft, 28.08.-02.09.2011, Delft, Netherlands
24. Cherkouk, C.; Rebohle, L.; Gerlach, T.; Kunze, G.; Lenk, J.; Pietzsch, J.; Skorupa, W.
Immobilization strategies for the estrogen receptor hER α in optical biosensors using Si-based light emitters
E-MRS 2011 Spring Meeting IUMRS ICAM 2011 & E-MRS/MRS Bilateral Conference on Energy, 09.-13.05.2011, Nice, France
25. Cornelius, S.; Vinnichenko, M.; Munnik, F.; Heller, R.; Kolitsch, A.; Möller, W.
Aktivierung des Al Donators in reaktiv Magnetron-gesputterten ZnO Schichten
EFDS Workshop "Transparente leitfähige Oxide; Festkörperphysikalische Grundlagen, Materialien und Technologie", 16.05.2011, Dresden, Germany
26. Cornelius, S.; Vinnichenko, M.; Munnik, F.; Heller, R.; Kolitsch, A.; Möller, W.
Incorporation of Al in ZnO by reactive pulsed magnetron sputtering: electrical properties and dopant activation
MRS Spring Meeting 2011 (Symposium S: Plasma-assisted Materials Processing and Synthesis), 25.-29.04.2011, San Francisco, USA
27. Cornelius, S.; Vinnichenko, M.; Munnik, F.; Heller, R.; Kolitsch, A.; Möller, W.
Determination of the electrically active Al fraction in Al doped ZnO grown by pulsed reactive magnetron sputtering
75th Annual Meeting of the DPG and DPG Spring Meeting 2011, 13.-18.03.2011, Dresden, Germany
28. Donchev, A.; Schütze, M.; Kolitsch, A.; Yankov, R.
Enhancing the high temperature capability of Ti-alloys
European Congress and Exhibition on on Advanced Materials and Processes (EUROMAT 2011), 12.-15.09.2011, Montpellier, France
29. Donchev, A.; Schütze, M.; Kolitsch, A.; Yankov, R.
New developments concerning the fluorine effect for TiAl-alloys
European Congress and Exhibition on on Advanced Materials and Processes (EUROMAT 2011), 12.-15.09.2011, Montpellier, France
30. Ferhati, R.; Guilliard, N.; Weishaar, T.; Amirthapandian, S.; Fritzsche, M.; Bischoff, L.; Bolse, W.
Swift heavy ion beam shaping of sub-micron structures
75th Annual Meeting of the DPG and DPG Spring Meeting 2011, 13.-18.03.2011, Dresden, Germany
31. Fiedler, J.; Heera, V.; Skrotzki, R.; Herrmannsdörfer, T.; Voelskow, M.; Mücklich, A.; Posselt, M.; Heinig, K.-H.; Schmidt, B.; Skorupa, W.; Wosnitza, J.; Helm, M.
Superconducting states of flash-lamp annealed Ga implanted Ge
Subsecond Thermal Processing of Advanced Materials 2011 (subterm-2011), 25.-27.10.2011, Dresden, Germany
32. Fiedler, J.; Heera, V.; Skrotzki, R.; Herrmannsdörfer, T.; Voelskow, M.; Mücklich, A.; Schmidt, B.; Skorupa, W.; Gobsch, G.; Helm, M.; Wosnitza, J.
Structural characterization of buried superconducting Ga rich films in Si
75th Annual Meeting of the DPG and DPG Spring Meeting 2011, 13.-18.03.2011, Dresden, Germany
33. Fiedler, J.; Heera, V.; Skrotzki, R.; Herrmannsdörfer, T.; Voelskow, M.; Mücklich, A.; Skorupa, W.; Gobsch, G.; Helm, M.; Wosnitza, J.
Microstructure of superconducting films fabricated by high-fluence Ga implantation in Si
Workshop Ionen- und Positronenstrahlen, 04.-05.07.2011, Neubiberg, Germany
34. Fritzsche, M.; Facsko, S.; Mücklich, A.; Lenz, K.
Nanohole pattern formation on Ge by focused ion beam and broad beam
75th Annual Meeting of the DPG and DPG Spring Meeting 2011, 13.-18.03.2011, Dresden, Germany
35. Grenzer, J.; Roshchupkina, O.; Kögler, R.; Das Kanungo, P.; Werner, P.
Structural investigations of ion beam doped silicon nanowires

- 75th Annual Meeting of the DPG and DPG Spring Meeting 2011, 13.-18.03.2011, Dresden, Germany
36. Hauschild, D.; Vinnichenko, M.
Lasermodifikation von TCOs
5. Fachtagung Transparent leitfähige Schichten (TCO), 28.-30.11.2011, Neu-Ulm, Germany
37. Heera, V.; Fiedler, J.; Skrotzki, R.; Herrmannsdörfer, T.; Voelskow, M.; Mücklich, A.; Schmidt, B.; Skorupa, W.
Superconducting nanolayers in Ge and Si fabricated by Ga⁺ ion implantation and rapid thermal annealing
29. Treffen der Nutzergruppe Heißprozesse und RTP, 12.05.2011, Erlangen, Germany
38. Hippler, M.; Streit, S.; Lehmann, J.; Skorupa, W.; Schmidt, H.; Helm, M.; Lopes, J. M. J.; Schubert, J.; Huber, H.-P.; Kienberger, F.; Mantl, S.
Nanoanalysis of lanthanum scandate MOS capacitors addressing reliability after local current flow
IEEE Semiconductor Conference Dresden, 27.-28.09.2011, Dresden, Germany
39. Keller, A.; Andersen, O. Z.; Foss, M.; Facsko, S.; Kraft, D. C.; Besenbacher, F.
Response of human mesenchymal stem cells to nanopatterned surfaces
Nanoscale Pattern Formation at Surfaces, 18.-22.09.2011, El Escorial, Spain
40. Kogler, R.; Ou, X.; Geyer, N.; Das Kanungo, P.; Schwen, D.; Werner, P.; Skorupa, W.
Acceptor deactivation in silicon nanowires analyzed by scanning spreading resistance microscopy
Gettering and Defect Engineering in Semiconductor Technology XIV (GADEST 2011), 25.-30.09.2011, Loipersdorf, Austria
41. Kosmata, M.; Auerhammer, J.; Zier, M.; Schlaphof, F.; Schreiter, F.; von Borany, J.
Influence of proton elastic scattering on soft error generation of SRAMs
Conference on Radiation Effects on Components and Systems, 19.-23.09.2011, Sevilla, Spain
42. Kosmata, M.; Zier, M.; Munnik, F.
High-resolution RBS investigation of LaLuO₃ as candidate for a second-generation high-k material
6th International Workshop on High-Resolution Depth Profiling, 27.-30.06.2011, Paris, France
43. Krause, J.; Wagner, M.; Helm, M.; Stehr, D.
Tunable narrowband THz pulses from a large-area photoconductive emitter
International Workshop on Optical Terahertz Science and Technology (OTST 2011), 13.-17.03.2011, Santa Barbara, USA
44. Krause, J.; Wagner, M.; Winnerl, S.; Helm, M.; Stehr, D.
Generation of tuneable narrowband terahertz pulses using large-area photoconductive antennas
75th Annual Meeting of the DPG and DPG Spring Meeting 2011, 13.-18.03.2011, Dresden, Germany
45. Liedke, B.; Heinig, K.-H.; Facsko, S.; Möller, W.
Surface patterning by ion bombardment: predictions of largescale atomistic simulations
75th Annual Meeting of the DPG and DPG Spring Meeting 2011, 13.-18.03.2011, Dresden, Germany
46. Liedke, B.; Heinig, K.-H.; Facsko, S.; Möller, W.
The contributions of defect kinetics and sputtering to pattern formation
Nanoscale Pattern Formation at Surfaces Congress, 18.-22.09.2011, El Escorial, Madrid, Spain
47. Liedke, M. O.; Körner, M.; Lenz, K.; Shalimov, A.; Strache, T.; Ranjan, M.; Facsko, S.; McCord, J.; Fassbender, J.
Magnetic anisotropy modifications of single crystalline rippled Fe
The European Conference Physics of Magnetism 2011, 27.06.-01.07.2011, Poznan, Poland
48. Liedke, M. O.; Körner, M.; Lenz, K.; Strache, T.; McCord, J.; Ranjan, M.; Facsko, S.; Fassbender, J.
Magnetic anisotropy investigations in single crystalline Fe films on ripple MgO templates
75th Annual Meeting of the DPG and DPG Spring Meeting, 13.-18.03.2011, Dresden, Germany

49. Liedke, M. O.; Körner, M.; Lenz, K.; Strache, T.; Shalimov, A.; Ranjan, M.; Facsko, S.; Fassbender, J.; McCord, J.
Magnetic anisotropy engineering: single crystalline Fe films on ripple surfaces
IEEE International Magnetics Conference, Intermag 2011, 25.-29.04.2011, Tapei, Taiwan
50. Meier, G.; Vogel, A.; Wintz, S.; Gerhardt, T.; Bocklage, L.; Strache, T.; Im, M.-Y.; Fischer, P.; Fassbender, J.; McCord, J.
Field- and current-induced domain-wall motion in permalloy nanowires with magnetic soft spots
56th Annual Conference on Magnetism & Magnetic Materials, 30.10.-03.11.2011, Scottsdale, Arizona, USA
51. Merchel, S.; Akhmadaliev, S.; Rugel, G.
Bestimmung langlebiger Radionuklide mit Beschleunigermassenspektrometrie (AMS) mit DREAMS: Von Bergstürzen über Klimaforschung bis Rückbau
GDCh-Wissenschaftsforum Chemie 2011, 04.-07.09.2011, Bremen, Germany
52. Merchel, S.; Munnik, F.; Andermann, C.; Arnold, M.; Aumaître, G.; Benedetti, L.; Bourlès, Didier L.; Braucher, R.; Finkel, Robert C.; Fuchs, M.; Gloaguen, R.; Klemm, K.; Martschini, M.; Steier, P.; Wallner, A.
The role of chemistry in setting-up a new AMS facility
12th International Conference on Accelerator Mass Spectrometry (AMS-12), 20.-25.03.2011, Wellington, New Zealand
53. Mittendorff, M.; Winnerl, S.; Plochocka, P.; Kossacki, P.; Schneider, H.; Orlita, M.; Potemski, M.; Sprinkle, M.; Berger, C.; de Heer, Walter A.; Helm, M.
Relaxation dynamics of graphene in magnetic fields close to the Dirac point
75th Annual Meeting of the DPG and DPG Spring Meeting 2011, 13.-18.03.2011, Dresden, Germany
54. Mok, K.; Du, N.; Schmidt, H.
Vector-Magneto-Optical Generalized Ellipsometry applied to magnetically anisotropic multilayer and metamaterial samples
6th Workshop Ellipsometry, 21.-24.02.2011, Berlin, Germany
55. Mok, K. M.; Du, N.; Schmidt, H.
Magneto-optical dielectric tensor of Co, Fe, Ni, and of NiFe alloys under saturated magnetization conditions
75th Annual Meeting of the DPG and DPG Spring Meeting 2011, 13.03.2011, Dresden, Germany
56. Morris, C. M.; Stehr, D.; Kim, H. C.; Truong, T. A.; Pryor, C.; Petroff, P. M.; Sherwin, M. S.
Terahertz ionization of highly charged InGaAs quantum posts
International Workshop on Optical Terahertz Science and Technology (OTST) 2011, 13.-17.03.2011, Santa Barbara, USA
57. Ou, Xin; Geyer, N.; Kögler, R.; Schwen, D.; Werner, P.; Skorupa, W.
Doping of Si nanowires by ion implantation
Workshop "Ionen- und Positronenstrahlen", 04.07.2011, München, Germany
58. Philipp, P.; Bischoff, L.
Investigation of conductive nanostructures on ta-C films made by FIB lithography
E-MRS 2011 Spring Meeting, 09.-13.05.2011, Strassburg, France
59. Posselt, M.
Materials research at the Helmholtz-Beamline at European XFEL: Ideas for proposals
Workshop on Petawatt-Lasers at Hard X-Ray Light Sources Dresden-Rossendorf, 05.-09.09.2011, Dresden, Germany
60. Potzger, K.; Levin, A. A.; Shalimov, A.; Osten, J.; Meyer, D. C.
Defect-induced ferromagnetism in crystalline SrTiO₃
75th Annual Meeting of the DPG and DPG Spring Meeting 2011, 13.-18.03.2011, Dresden, Germany
61. Prucnal, S.
Doping of silicon by ion implantation and annealing
62th Freiburger Research Conference, 15.-17.06.2011, Freiberg, Germany

-
62. Prucnal, S.; Abendroth, B.; Krockert, K.; König, K.; Henke, D.; Kolitsch, A.; Möller, H. J.; Skorupa, W.
Millisecond annealing for advanced doping of dirty-silicon solar cells
Subsecond Thermal Processing of Advanced Materials 2011 (subtherm-2011), 25.-27.10.2011, Dresden, Germany
63. Prucnal, S.; Facsko, S.; Baumgart, C.; Schmidt, H.; Liedke, M. O.; Mücklich, A.; Zhou, S. Q.; Skorupa, W.
III-V/Si heterostructures fully integrated into silicon
Subsecond thermal processing of Advanced Materials 2011 (subtherm-2011), 25.-27.10.2011, Dresden, Germany
64. Prucnal, S.; Liedke, M. O.; Schmidt, H.-M.; Baumgart, Ch.; Shalimov, A.; Reuther, H.; Mücklich, A.; Helm, M.; Skorupa, W.
n-InAs/p-Si heterojunction with type-II band alignment
E-MRS 2011 Spring Meeting IUMRS ICAM 2011 & E-MRS/MRS Bilateral Conference on Energy, 09.-13.05.2011, Nice, France
65. Radek, M.; Bracht, H.; Posselt, M.; Schmidt, B.
Ion beam mixing in crystalline and amorphous germanium
48. Treffen des Arbeitskreises „Punktdefekte, 13.-14.10.2011, Dresden, Germany
66. Rebohle, L.; Lehmann, J.; Prucnal, S.; Helm, M.; Skorupa, W.
The electrical and electroluminescence properties of rare earth implanted MOS light emitting devices in the near infrared
EMRS Fall Meeting, 19.-23.09.2011, Warsaw, Poland
67. Reichel, D.; Skorupa, W.; Schumann, T.
Temperature measurement in ultra-short annealing processes
Subsecond Thermal Processing of Advanced Materials, 25.-27.10.2011, Dresden, Germany
68. Reichel, D.; Skorupa, W.; Schumann, T.
Aus alt mach neu – Ripple Pyrometrie für die Blitzlampenausheilung
Nutzertreffen Heißprozesse, 23.-24.11.2011, Blaubeuren, Germany
69. Reuther, H.; Talut, G.; Mücklich, A.; Stromberg, F.
Magnetism in Ge produced by implantation with Fe and Mn ions
7th Seeheim Workshop on Mössbauer Spectroscopy, 13.-17.06.2011, Frankfurt/Main, Germany
70. Roshchupkina, O. D.; Grenzer, J.; Strache, T.; McCord, J.; Fritzsche, M.; Muecklich, A.; Baetz, C.; Fassbender, J.
Structural modifications induced by FIB implantation in magnetic thin films
8th Autumn School on X-ray Scattering from Surfaces and Thin Layers, 04.-07.10.2011, Smolenice, Slovakia
71. Rugel, G.
Determination of the ⁶⁰Fe Half-Life – a successful Collaboration in ERAWAST
2nd Workshop on Exotic Radionuclides from Accelerator Waste for Science and Technology (ERAWAST II), 29.08.-02.09.2011, Villigen, Switzerland
72. Sahle, C. J.; Sternemann, C.; Nyrow, A.; Schwamberger, A.; Wieland, F.; Zschintzsch, M.; von Borany, J.; Hohl, A.; Tolan, M.
Phase separation and size controlled nanocrystal formation in GeO
75th Annual Meeting of the DPG and DPG Spring Meeting 2011, 13.-18.03.2011, Dresden, Germany
73. Scarlat, C.; Mok, K. M.; Zhou, S.; Lorenz, M.; Grundmann, M.; Helm, M.; Schubert, M.; Schmidt, H.
Voigt effect measurements on PLD grown nickel oxide thin films
75th Annual Meeting of the DPG and DPG Spring Meeting 2011, 13.-18.03.2011, Dresden, Germany
74. Schmidt, B.; Zier, M.; Philipp, P.; Potfajova, J.
Ultra-thin resistors for piezoresistive sensors
SENSOR+TEST Conference 2011, 7–9 June 2011, Nürnberg, Germany, 07.-09.06.2011, Nürnberg, BR Germany

75. Schmidt, K.; Akhmadaliev, C.; Anders, M.; Bemmerer, D.; Boretzky, K.; Caciolli, A.; Elekes, Z.; Fülöp, Z.; Gyürky, G.; Hannaske, R.; Junghans, A.; Marta, M.; Schwengner, R.; Szücs, T.; Wagner, A.; Zuber, K.
Resonanzstärken in der $^{40}\text{Ca}(\alpha,\gamma)^{44}\text{Ti}$ -Reaktion
DPG Spring Meeting 2011, 21.-25.03.2011, Münster, Germany
& *2nd workshop on Exotic Radionuclides from Accelerator Waste for Science and Technology (ERAWAST II), 02.09.2011, Paul Scherrer Institute, Switzerland*
76. Shuai, Y.; Wu, C.; Zhang, W.; Zhou, S.; Bürger, D.; Slesazeck, S.; Mikolajick, T.; Helm, M.; Schmidt, H.
Nonvolatile resistive switching in Au/BiFeO_3 rectifying junction
2011 MRS Fall Meeting & Exhibition, 28.11.2011, Boston, MA, USA
77. Shuai, Y.; Zhou, S.; Bürger, D.; Helm, M.; Schmidt, H.; Slesazeck, S.; Mikolajick, T.
Nonvolatile resistive switching in BiFeO_3 thin films
E-MRS 2011 Spring Meeting IUMRS ICAM 2011 & E-MRS/MRS Bilateral Conference on Energy, 09.-13.05.2011, Nice, France
& *ISPSA 2011, 05.07.2011, Jeju, Republic of Korea*
78. Talati, M.; Posselt, M.; Bonny, G.; Al-Motasem, A. T.; Bergner, F.
Vibrational effects on thermodynamics of copper-vacancy clusters in bcc-Fe
E-MRS 2011 Spring Meeting IUMRS ICAM 2011 & E-MRS/ MRS Bilateral Conference on Energy, 09.-13.05.2011, Nice, France
79. Teich, M.; Wagner, M.; Schneider, H.; Helm, M.; Stehr, D.
Terahertz induced intra-excitonic Autler-Townes effect in semiconductor quantum wells up to room temperature
5. THz-Frischlinge Treffen 2011, 06.-08.06.2011, Regensburg, Germany
80. Terentyev, D.; Malerba, L.; Bonny, G.; Al-Motasem, A. T.; Posselt, M.
Interaction of dislocations with Cu-Ni-vacancy clusters in Fe
16th Meeting of International Group on Radiation Damage Mechanisms in Pressure Vessel Steels (IGRDM-16), 04.-09.12.2011, Santa Barbara, USA
81. Ueda, M.; Fernandes, B. B.; Mello, C. B.; Lepienski, C. M.; Reuther, H.; Evangelista, S. H.
Improvement of CBERS-3/4 imaging camera pin-pull components by plasma immersion ion implantation
11th International Workshop on Plasma Based Ion Implantation & Deposition, PBII&D 2011, 08.-12.09.2011, Harbin, China
82. Viehrig, H.-W.; Houska, M.; Altstadt, E.; Kuechler, R.
Fracture mechanics characterisation of forged base metal ring of the decommissioned reactor pressure vessel of NPP Greifswald WWER-440 unit 4
25th Symposium on Effects of Radiation on Nuclear Materials, 15.-17.06.2011, Anaheim, USA
83. Vinnichenko, M.; Cornelius, S.; Krause, M.; Gago, R.; Munnik, F.; Kolitsch, A.; Moeller, W.
Al-doped ZnO films grown by reactive magnetron sputtering: properties evolution and secondary phase formation
MRS Spring Meeting 2011 (Symposium S: Plasma-assisted Materials Processing and Synthesis), 25.-29.04.2011, San Francisco, USA
84. Wagner, M.; Helm, M.; Sherwin, M. S.; Stehr, D.
Coherent switching of a THz intersubband polarization in a quantum well
11th International Conference on Intersubband Transitions in Quantum Wells (ITQW 2011), 11.-17.09.2011, Badesi, Italy
85. Wagner, M.; Stehr, D.; Schneider, H.; Winnerl, S.; Andrews, A. M.; Schartner, S.; Strasser, G.; Helm, M.
AC Stark effect of the intraexciton 1s-2p quantum well transition
International Workshop on Optical Terahertz Science and Technology (OTST 2011), 13.-17.03.2011, Santa Barbara, USA
86. Wilde, C.
Ionenenergieverteilung während der ZnO-Abscheidung durch Magnetronspütern: keramisches vs. metallisches Target
Transparente leitfähige Oxide - Festkörperphysikalische Grundlagen und Technologie, 16.-17.05.2011, Dresden, Germany

87. Wilhelm, R. A.; Heller, R.; Facsko, S.
Nanostructures induced by slow highly charged ions on KBr(001) surfaces
75th Annual Meeting of the DPG and DPG Spring Meeting 2011, 13.-18.03.2011, Dresden, Germany
88. Winnerl, S.; Orlita, M.; Plochocka, P.; Kossacki, P.; Potemski, M.; Winzer, T.; Malic, E.; Knorr, A.; Sprinkle, M.; Berger, C.; de Heer, W. A.; Schneider, H.; Helm, M.
Nonlinear transmission dynamics in graphene close to the Dirac point
36th International Conference on Infrared, Millimeter, and Terahertz Waves (IRMMW-THz 2011), 02.-07.10.2011, Houston, TX, USA
89. Wintz, S.; Puzic, A.; Strache, T.; Bunce, C.; Körner, M.; Liedke, M. O.; Banholzer, A.; Buhl, M.; Bernert, K.; Moench, I.; Mattheis, R.; McCord, J.; Raabe, J.; Quitmann, C.; Erbe, A.; Fassbender, J.
Interlayer coupled magnetic vortices
IEEE International Magnetics Conference, Intermag 2011, 25.-29.04.2011, Taipei, Taiwan
90. Yankov, R. A.; Kolitsch, A.; von Borany, J.; Munnik, F.; Mücklich, A.; Donchev, A.; Schütze, M.
Oxidation protection of TiAl alloys by plasma-based ion implantation of fluorine
4th International Workshop on Titanium Aluminides, 13.-16.09.2011, Nürnberg, Germany
91. Yankov, Rossen A.; Kolitsch, A.; von Borany, J.; Munnik, F.; Voelskow, M.; Schumann, T.; Skorupa, W.; Donchev, A.; Schütze, M.
Thin film intermetallic compound formation by flash-lamp annealing: an implication of ultra-fast alloying and metallurgy
Subsecond Thermal Processing of Advanced Materials 2011 (subtherm-2011), 25.-27.10.2011, Dresden, Germany
92. Zaks, B.; Stehr, D.; Truong, T. A.; Petroff, P. M.; Hughes, S.; Sherwin, M. S.
Anomalous Autler-Townes splitting in terahertz-driven quantum wells: interplay of Coulomb interactions, non-rotating wave effects and Stark shifts
International Workshop on Optical Terahertz Science and Technology (OTST 2011), 13.-17.03.2011, Santa Barbara, USA
93. Zybell, S.; Schneider, H.; Winnerl, S.; Helm, M.
Time-resolved photoluminescence from GaAs/AlGaAs multiquantum wells quenched by pulsed mid-infrared radiation
75th Annual Meeting of the DPG and DPG Spring Meeting 2011, 13.-18.03.2011, Dresden, Germany
94. Zybell, S.; Schneider, H.; Winnerl, S.; Köhler, K.; Helm, M.
Photoluminescence dynamics in GaAs/AlGaAs quantum wells under pulsed intersubband excitation
The 11th International Conference on Intersubband Transitions in Quantum Wells (ITQW 2011), 11.-17.09.2011, Sardinia, Italia

Posters

1. Abrasonis, G.; Krause, M.; Buljan, M.; Wintz, S.; Zschornak, M.; Grenzer, J.
Ion-assisted bottom-up nanostructuring of carbon-transition metal nanocomposite films: a GISAXS study
GISAXS 2011, 10.-12.10.2011, Hamburg, Germany
2. Andermann, C.; Gloaguen, R.; Bonnet, S.; Crave, A.; Merchel, S.
Erosion patterns in the Nepal Himalayas from river gauging, cosmogenic nuclides and precipitation data
European Geosciences Union (EGU) General Assembly 2011, 03.-08.04.2011, Wien, Austria
3. Arnold, M.; Boursès, Didier L.; Finkel, Robert C.; Nottoli, E.; Aumaître, G.; Keddadouche, K.; Benedetti, L.; Braucher, R.; Merchel, S.
Status of the French accelerator mass spectrometry facility ASTER after 4 years
12th International Conference on Accelerator Mass Spectrometry (AMS-12), 20.-25.03.2011, Wellington, New Zealand

4. Ball, D.; Günther, S.; Fritzsche, M.; Varvaro, G.; Makarov, D.; Lenz, K.; Fassbender, J.; Albrecht, M.
Granular CoCrPt:SiO₂ recording media on assemblies of GaSb nanocones
75th Annual Meeting of the DPG and DPG Spring Meeting 2011, 13.-18.03.2011, Dresden, Germany
5. Ball, D. K.; Günther, S.; Krone, P.; Fritzsche, M.; Varvaro, G.; Makarov, D.; Lenz, K.; Mücklich, A.; Facsko, S.; Fassbender, J.; Albrecht, M.
Magnetic properties of granular CoCrPt:SiO₂ recording media deposited on GaSb nanocones
IEEE International Magnetism Conference, Intermag 2011, 25.-29.04.2011, Taipei, Taiwan
6. Barsukov, I.; Rubacheva, A.; Melnichak, N.; Römer, F. M.; Meckenstock, R.; Lindner, J.; Wende, H.; Farle, M.; Lenz, K.; Banholzer, A.; Fassbender, J.; Mankovsky, S.; Ebert, H.; Landeros, P.; Mills, D. L.
Tailoring magnetization dynamics at the nanoscale
2nd international workshop on magnonics: From Fundamentals to Applications, 07.-10.08.2011, Recife, Brazil
7. Baumgart, C.; Habicht, S.; Feste, S.; Helm, M.; Schmidt, H.
Kelvin probe force microscopy imaging on locally doped silicon nanowires
Subsecond Thermal Processing of Advanced Materials 2011 (subtherm-2011), 25.-27.10.2011, Dresden, Germany
8. Böttger, R.; Bischoff, L.; Schmidt, B.; Krause, M.
Freestanding Si nanowires fabricated by Ga⁺ FIB implantation and subsequent anisotropic etching
75th Annual Meeting of the DPG and DPG Spring Meeting 2011, 13.-18.03.2011, Dresden, Germany
9. Bracht, H.; Schneider, S.; Klug, J. N.; Posselt, M.; Schmidt, B.
Concurrent annealing and irradiation of germanium to control dopant diffusion and activation
E-MRS 2011 Spring Meeting IUMRS ICAM 2011 & E-MRS/MRS Bilateral Conference on Energy, 09.-13.05.2011, Nice, France
10. Braucher, R.; Bourlès, Didier L.; Merchel, S.; Léanni, L.; Chauvet, F.; Arnold, M.; Aumaître, G.; Keddadouche, K.
Why are depth profiles promising?
12th International Conference on Accelerator Mass Spectrometry (AMS-12), 20.-25.03.2011, Wellington, New Zealand
11. Buhl, M.; Bernert, K.; Wintz, S.; Henschel, T.; Mattheis, R.; Raabe, J.; Grebing, J.; Potzger, K.; Erbe, A.; Fassbender, J.
Imaging of spin-torque induced magnetization dynamics in lateral spin injector configuration
75th Annual Meeting of the DPG and DPG Spring Meeting 2011, 14.-18.03.2011, Dresden, Germany
12. Bürger, D.; Seeger, M.; Zhou, S.; Skorupa, W.; Schmidt, H.
3d transition metal diffusion in diluted magnetic semiconductors prepared by pulsed laser processing
Subsecond Thermal Processing of Advanced Materials 2011 (subtherm-2011), 25.-27.10.2011, Dresden, Germany
13. Bürger, D.; Zhou, S.; Höwler, M.; Kovacs, G.; Reuther, H.; Skorupa, W.; Helm, M.; Schmidt, H.
Depth-resolved magnetotransport properties of ferromagnetic Ge:Mn
Subsecond Thermal Processing of Advanced Materials 2011 (subtherm-2011), 25.-27.10.2011, Dresden, Germany
14. Bürger, D.; Zhou, S.; Höwler, M.; Kovacs, G.; Reuther, H.; Skorupa, W.; Helm, M.; Schmidt, H.
Layer by layer investigation on the magneto-transport properties of ferromagnetic Ge:Mn prepared by pulsed laser
56th annual conference on magnetism and magnetic materials, 30.10.-03.11.2011, Scottsdale, Arizona, USA

15. Bürger, D.; Zhou, S.; Kovacs, György J.; Helm, M.; Schmidt, H.
Spin-polarized transport in pulsed-laser annealed Ge:Mn
Spintech VI, 01.-05.08.2011, Matsue, Japan
16. Cherkouk, C.; Rebohle, L.; Howitz, S.; Skorupa, W.
Microfluidic system for endocrine disrupting chemicals detection in waterish solution
Eurosensor XXV, 05.-8.9.2011, Athens, Greece
17. Cherkouk, C.; Rebohle, L.; Howitz, S.; Skorupa, W.
Mikrofluidisches System zum Nachweis von hormonaktiven Substanzen in wässrigen Lösungen
10. Dresdner Sensor-Symposium, 05.-07.12.2011, Dresden, Germany
18. Cormier, M.; Mougín, A.; Ferré, J.; Jamet, J.-P.; Weil, R.; Faßbender, J.; Baltz, V.; Rodmacq, B.
Fast propagation of weakly pinned domain walls and current-assisted magnetization reversal in He⁺-irradiated Pt/Co/Pt nanotracks
MORIS 2011, 22.06.2011, Nijmegen, The Netherlands
& *Magnetics and Optics Research International Symposium 2011, 21.-24.06.2011, Nijmegen, The Netherlands*
19. Denecke, Melissa A.; Merchel, S.; Eberhardt, K.
GDCh Working Group "Analytical methods using radionuclides and high-performance sources"
3rd ANKA / KNMF Joint Users Meeting, 13.-14.10.2011, Karlsruhe-Neureut, Germany
20. Derenko, S.; Grebing, J.; Härtling, T.
Gold nanoparticle arrays generated by modified Electron Beam Lithography and their applicability to plasmonic sensors
75th Annual Meeting of the DPG and DPG Spring Meeting 2011, 13.-18.03.2011, Dresden, Germany
21. Dubiel, S. M.; Reuther, H.; Cieślak, J.
Effect of He⁺ irradiation on SRO in Fe-Cr alloys
7th Seeheim Workshop on Mössbauer Spectroscopy, 13.-17.06.2011, Frankfurt/Main, Germany
22. Dubiel, S. M.; Reuther, H.; Cieslak, J.
Effect of He⁺ irradiation on a short-range order in Fe-Cr alloys
31st International Conference on the Applications of the Mössbauer Effect (ICAME2011), 25.-30.09.2011, Kobe, Japan
23. Eder, F.; Neelmeijer, C.; Pearce, Nick J. G.; Bichler, M.; Merchel, S.
Volcanic glass under fire - A comparison of three complementary analytical techniques
16. Tagung Festkörperanalytik, 04.-06.07.2011, Wien, Austria
24. Eder, F.; Neelmeijer, C.; Pearce, Nick J. G.; Bichler, M.; Merchel, S.
Improved fingerprinting of Melos obsidian using three complementary analytical techniques
3. Österreichischer Archäometrie-kongress, 13.-14.05.2011, Salzburg, Austria
25. Endler, R.; Voelskow, M.; Skorupa, W.
Grain alignment in poly-Si films by means of Plasma Immersion Ion Implantation (PIII) in combination with Flash Lamp Annealing (FLA)
Subsecond Thermal Processing of Advanced Materials 2011 (subtherm-2011), 25.-27.10.2011, Dresden, Germany
26. Endler, R.; Yankov, R. A.; Kolitsch, A.; Mücklich, A.; von Borany, J.; Munnik, F.; Voelskow, M.; Donchev, A.; Schütze, M.
Forming an oxidation protective coating on titanium and titanium-base alloys
11th International Workshop on Plasma-Based Ion Implantation and Deposition (PBII&D 2011), 08.-12.09.2011, Harbin, China
27. Fiedler, J.; Heera, V.; Skrotzki, R.; Herrmannsdörfer, T.; Voelskow, M.; Mücklich, A.; Posselt, M.; Heinig, K.-H.; Schmidt, B.; Skorupa, W.; Wosnitza, J.; Helm, M.
Superconducting states of flash-lamp annealed Ga implanted Ge
Subsecond Thermal Processing of Advanced Materials 2011 (subtherm-2011), 25.-27.10.2011, Dresden, Germany

28. Fiedler, J.; Heera, V.; Skrotzki, R.; Herrmannsdörfer, T.; Voelskow, M.; Mücklich, A.; Schmidt, B.; Skorupa, W.; Gobsch, G.; Helm, M.; Wosnitza, J.
Buried superconducting films in Si containing Ga-rich precipitates
E-MRS 2011 Spring Meeting IUMRS ICAM 2011 & E-MRS/MRS Bilateral Conference on Energy, 09.-13.05.2011, Nice, France
29. Fowley, C.; Sluka, V.; Bernert, K.; Deac, A.
Spin transfer oscillators with different geometries
Spin Master Voice, 13.-16.12.2011, Paris, France
30. Fritzsche, M.; Facsko, S.; Mücklich, A.
Comparison of pattern formation by focused ion beam and broad beam sputtering
Nanoscale Pattern Formation at Surfaces, 18.-22.09.2011, El Escorial, Spain
31. Gao, K.; Prucnal, S.; Skorupa, W.; Helm, M.; Yastrubchak, O.; Gluba, L.; Zhou, S.
Nitrogen implanted GaAs as a promising photovoltaic material
Next Generation Solar Energy, 12.-14.12.2011, Erlangen, Germany
32. Gemming, S.; Weissbach, T.; Zschornak, M.; Stöcker, H.; Meyer, D. C.; Leisegang, T.; Ronneberger, I.; Potzger, K.
Multifunctional oxides and the influence of defects on the ferroic properties
Joint Meeting of the DGK, DMG and ÖMG, 20.-24.09.2011, Salzburg, Austria
33. Germer, S.; Günz, C.; Lehmann, J.; Rebohle, L.; Helm, M.; Skorupa, W.
Investigation of rare earth implanted SiO₂ thin films for down-conversion applications in Photovoltaics
Subsecond Thermal Processing of Advanced Materials 2011 (subtherm-2011), 25.-27.10.2011, Dresden, Germany
34. Germer, S.; Rebohle, L.; Skorupa, W.; Helm, M.
Basic structures of photonic integrated circuits for smart biosensor applications
Doctoral Students Conference for the Discussion of Optical Concepts, 21.-25.03.2011, Naumburg, Germany
35. Grebing, J.; Faßbender, J.; Erbe, A.
Time efficient fabrication of ultra large scale nano dot arrays using electron beam lithography
37th International Conference on Micro and Nano Engineering, 20.-23.09.2011, Berlin, Germany
36. Grenzer, J.; Hanisch, A.; Facsko, S.; Mücklich, A.; Biermanns, A.; Pietsch, U.
Silicon ripple structures produced by Xe⁺ irradiation at medium energies
International Workshop on "Nanoscale Pattern Formation at Surfaces", 18.-22.09.2011, El Escorial, Spain
37. Grenzer, J.; Roshchupkina, O.; Fritzsche, M.; Mücklich, A.; Bischoff, L.
X-ray investigations on CoSi₂ nano wires manufactured by focused ion beam synthesis
E-MRS 2011 Spring Meeting IUMRS ICAM 2011 & E-MRS/MRS Bilateral Conference on Energy, 09.-13.05.2011, Nice, France
38. Hөwler, M.; Bernert, K.; McCord, J.; Potzger, K.; Fritzsche, M.; Mücklich, A.; Fassbender, J.; Kirsch, K.; Mattheis, R.; Slesazeck, S.
Preparation and characterization of magnetic tunnel junctions with spin transfer torque
75th Annual Meeting of the DPG and DPG Spring Meeting 2011, 13.-18.03.2011, Dresden, Germany
39. Ikeda-Ohno, A.; Weiss, S.; Bernhard, G.; Hennig, C.
Characterization of Ce(IV) hydrolytic species in aqueous solution by X-ray absorption spectroscopy, high energy solution X-ray scattering, and dynamic light scattering
Workshop on Analysis of Diffraction Data in Real Space (ADD2011), 12.-14.10.2011, ILL, Grenoble, France
40. Kimling, J.; Vogel, A.; Kobs, A.; Bocklage, L.; Wintz, S.; Strache, T.; Fassbender, J.; Im, M.-Y.; Fischer, P.; Merkt, U.; Oepen, H. P.; Meier, G.
Preparation of domain walls in Co/Pt multilayer wires
75th Annual Meeting of the DPG and DPG Spring Meeting 2011, 13.-18.03.2011, Dresden, Germany

41. Körner, M.; Liedke, M. O.; Lenz, K.; Ranjan, M.; Fritzsche, M.; Facsko, S.; Fassbender, J.; von Hörsten, U.; Krumme, B.; Wende, H.
Morphology induced magnetic anisotropy of thin films deposited on nanoscale ripple substrates
75th Annual Meeting of the DPG and DPG Spring Meeting 2011, 13.-18.03.2011, Dresden, Germany
42. Körner, M.; Liedke, M. O.; Lenz, K.; Ranjan, M.; Fritzsche, M.; Facsko, S.; Fassbender, J.; von Hörsten, U.; Krumme, B.; Wende, H.
Morphology induced magnetic anisotropy of thin films deposited on nanoscale ripple substrates
IEEE Magnetics Society Summer School, 22.-28.05.2011, New Orleans, USA
43. Krause, M.; Mücklich, A.; Viršek, M.; Remškar, M.; Zak, A.; Seifert, G.; Gemming, S.
Diameter dependent TEM and Raman study of WS₂ nanotubes
25th International Winterschool on: Electronic Properties of Novel Materials: "Molecular nanostructures", 26.02.-04.03.2011, Kirchberg, Austria
44. Lehmann, J.; Shevchenko, N.; Mücklich, A.; von Borany, J.; Skorupa, W.; Schubert, J.; Lopes, J. M. J.; Mantl, S.
Millisecond flash-lamp annealing of LaLuO₃
17th Conference on "Insulating Films on Semiconductors", 21.-24.06.2011, Grenoble, France
45. Lenz, K.; Körner, M.; Banholzer, A.; Liedke, M. O.; Grebing, J.; Fassbender, J.; Barsukov, I.; Römer, F. M.; Lindner, J.
Tailoring spin dynamics by magnetic nanopatterning using ion irradiation
2nd international workshop on magnonics: From Fundamentals to Applications, 07.-10.08.2011, Recife, Brasil
46. Martins, R. M. S.; Schell, N.; Mahesh, K. K.; Silva, R. J. C.; Braz Fernandes, F. M.
Synchrotron radiation-based X-ray diffraction during magnetron co-sputtering of Ni-Ti films
EUROMAT 2011 (Symposium A54: Shape Memory Alloys (SMA) - Materials and Devices), 14.-15.09.2011, Montpellier, France
47. Michalak, P. P.; Renno, A. D.; Merchel, S.; Munnik, F.; Wiedenbeck, M.
Natural analogs of synthetic reference materials: Assessing the limits of homogeneity testing at the picogram scale
Microscopy & Microanalysis 2011, 07.-11.08.2011, Nashville, USA
48. Michalak, P. P.; Renno, A. D.; Wiedenbeck, M.; Merchel, S.; Munnik, F.
A novel pilot program for homogeneity testing of natural analogs of synthetic mineral reference materials
89. Jahrestagung der Deutschen Mineralogischen Gesellschaft (DMG) in Kooperation mit der Deutschen Kristallographischen Gesellschaft (DGK) und der Österreichischen Mineralogischen Gesellschaft (ÖMG), 20.-24.09.2011, Salzburg, Austria
49. Mok, K.; Li, L.; Kovacs, G. J.; Helm, M.; Schmidt, H.
Magneto-optical properties of ferromagnetic thin films under saturated magnetization conditions
6th International School and Conference on Spintronics and Quantum Information Technology (SPINTECH6), 01.-05.08.2011, Matsue, Japan
50. Mücklich, A.; Fiedler, J.; Heera, V.
TEM investigation contributing to the comprehension of superconductivity in Ga-doped Si
MC2011, Microscopy Conference 2011, 28.08.-02.09.2011, Kiel, Germany
51. Neudert, A.; McCord, J.
Magnetic domain structure evolution in NiMnGa magnetic shape memory alloy
75th Annual Meeting of the DPG and DPG Spring Meeting 2011, 15.03.2011, Dresden, Germany
52. Ott, U.; Merchel, S.; Folco, L.; D'Orazio, M.
Cosmogenic noble gases of the Gebel Kamil iron meteorite
74th Annual Meeting of the Meteoritical Society, 08.-12.08.2011, London, UK

53. Pelic, B.; Bortolotto, L.; Goldberg, S.; Witschel, B.; Rafaja, D.; Masset, P. J.; Donchev, A.; Yankov, R.; Kolitsch, A.; Schütze, M.
Development and characterization of advanced coatings for TiAl alloys
European Congress and Exhibition on Advanced Materials and Processes (EUROMAT 2011), 12.-15.09.2011, Montpellier, France
54. Pezoldt, J.; Stauden, T.; Morales, F.; Polychroniadis, E. K.; Voelskow, M.; Skorupa, W.
SiC growth modification and stress reduction in FLASiC assisted liquid phase epitaxy
Subsecond Thermal Processing of Advanced Materials 2011 (subtherm-2011), 25.-27.10.2011, Dresden, Germany
55. Philipp, P.; Bischoff, L.
Investigation of conducting nanostructures on ta-C films made by FIB lithography
75th Annual Meeting of the DPG and DPG Spring Meeting 2011, 13.-18.03.2011, Dresden, Germany
56. Philipp, P.; Bischoff, L.
Investigations of nano structures on DLC films made by focused ion beam lithography
Diamond 2011 22nd European Conference on Diamond, Diamond-like Materials and Nitrides, 04.-08.09.2011, Garmisch-Partenkirchen, Germany
57. Prucnal, S.; Abendroth, B.; Krockert, K.; König, K.; Möller, H. J.; Skorupa, W.
Flash lamp annealing vs conventional annealing for mc-silicon solar cell
E-MRS 2011 Spring Meeting IUMRS ICAM 2011 & E-MRS / MRS Bilateral Conference on Energy, 09.-13.05.2011, Nice, France
58. Prucnal, S.; Endler, R.; Henke, D.; Kolitsch, A.; Abendroth, B.; Krockert, K.; König, K.; Möller, H. J.; Skorupa, W.
Solar cell emitters fabricated by PIII and flash lamp millisecond annealing
11th International Workshop on Plasma-Based Ion Implantation & Deposition, 08.-12.09.2011, Harbin, China
59. Roehringer, I.; Abramowski, U.; Zech, R.; Sosin, P.; Aldahan, A.; Merchel, S.; Kubik, P.; Zoeller, L.; Zech, W.
Timing and paleoclimate forcings of late quaternary glaciations in the Pamir Mountains: ¹⁰Be surface exposure dating of glacial landforms
European Geosciences Union (EGU) General Assembly 2011, 03.-08.04.2011, Vienna, Austria
60. Röhringer, I.; Zech, R.; Sosin, P.; Abramowski, U.; Aldahan, A.; Kubik, P.; Merchel, S.; Zöller, L.; Zech, W.
Glacial history of the Pamir Mountains during the last glacial cycle along a semi-humid to arid transect based on ¹⁰Be surface exposure dating
XXVIII INQUA (International Union for Quaternary Research) Congress, 20.-27.07.2011, Bern, Switzerland
61. Scarlat, C.; Xu, Q.; Mok, K.; Shalimov, A.; Fronk, M.; Salvan, G.; Zahn, D. R. T.; Helm, M.; Schmidt, H.; Iacomi, F.
Magnetic Mn-doped indium tin oxide films prepared by vacuum thermal evaporation
Next Generation Solar Energy From Fundamentals to Applications, 12.-14.12.2011, Erlangen, Germany
62. Scarlat, C.; Xu, Q.; Zhou, S.; Potzger, K.; Salvan, G.; Helm, M.; Schmidt, H.; Iacomi, F.
Annealed, stress-free, and ferromagnetic Mn-doped indium tin oxide films
Subsecond Thermal Processing of Advanced Materials 2011 (subtherm-2011), 25.-27.10.2011, Dresden, Germany
63. Scarlat, C.; Zhou, S.; Vinnichenko, M.; Kolitsch, A.; Helm, M.; Schmidt, H.
Optical and magnetic properties of Cr-implanted indium oxides thin films
75th Annual Meeting of the DPG and DPG Spring Meeting 2011, 13.-18.03.2011, Dresden, Germany
64. Shalimov, A.; Akhmadaliev, Sh.; Baetz, C.; Potzger, K.
Self-organized FePt nanoparticles in MgO synthesized by ion-implantation and high-temperature annealing
E-MRS 2011 Fall Meeting - Symposium A, 19.-23.09.2011, Warsaw, Poland

65. Shalimov, A.; Baehz, C.; Grenzer, J.; von Borany, J.
The Rossendorf beamline BM20 at the ESRF: overview and perspectives
IX Krajowe Sympozjum Użytkowników Promieniowania Synchrotronowego, KSUPS 2011, 26.-27.09.2011, Warsaw, Poland
66. Stehr, D.; Morris, C. M.; Schmidt, C.; Sherwin, M. S.
Fast scanning terahertz spectrometer based on synchronized fiber lasers
International Workshop on Optical Terahertz Science and Technology (OTST 2011), 13.-17.03.2011, Santa Barbara, USA
67. Sterba, J. H.; Munnik, F.; Pearce, N. J. G.
Raising the temper - μ -spot analysis of temper inclusions in experimental ceramics
13th International Conference on Modern Trends in Activation Analysis, 13.-18.03.2011, Texas, USA
68. Talati, M.; Posselt, M.; Bonny, G.; Al-Motasem, A. T.; Bergner, F.
Investigations of structure, energetics, thermodynamics and kinetics of copper-vacancy clusters in bcc-Fe
European Nuclear Young Generation Forum (ENYGF), 17.-22.05.2011, Prague, Czech Republic
69. Talati, M.; Posselt, M.; Bonny, G.; Al-Motasem, A. T.; Bergner, F.
Phonon contribution to the thermodynamics of pure and mixed clusters in bcc-Fe
75th Annual Meeting of the DPG and DPG Spring Meeting 2011, 13.-18.03.2011, Dresden, Germany
70. Vinnichenko, M.; Cornelius, S.; Kolitsch, A.
Effects of secondary phase formation on dielectric function of Al-doped ZnO thin films
6th Workshop Ellipsometry, 21.02.-24.03.2011, Berlin, Germany
71. Vinnichenko, M.; Hauschild, D.; Lissotschenko, V.; Cornelius, S.; Krause, M.; Gago, R.; Mücklich, A.; Kolitsch, A.
Effects of very rapid thermal processing on the properties and bonding structure of Al-doped ZnO thin films
Subsecond Thermal Processing of Advanced Materials 2011 (subtherm-2011), 25.-27.10.2011, Dresden, Germany
72. Vogel, A.; Wintz, S.; Gerhardt, T.; Bocklage, L.; Strache, T.; Im, M.-Y.; Fischer, P.; Fassbender, J.; McCord, J.; Meier, G.
Domain-wall motion in permalloy nanowires with magnetic soft spots
IEEE International Magnetism Conference, Intermag 2011, 25.-29.04.2011, Taipei, Taiwan
73. Wagner, M.; Helm, M.; Sherwin, M. S.; Stehr, D.
Coherent control of a THz-intersubband polarization in a quantum well
EP2DS19/MSS15, 25.-29.07.2011, Tallahassee, USA
74. Wallner, A.; Melber, K.; Merchel, S.; Ott, U.; Forstner, O.; Golser, R.; Kutschera, W.; Priller, A.; Steier, P.
Stable isotope measurements in presolar grains
12th International Conference on Accelerator Mass Spectrometry (AMS-12), 20.-25.03.2011, Wellington, New Zealand
75. Wieser, M.; Liu, S.-P.; Weisbrod, S.; Tang, Z.; Marx, A.; Scheer, E.; Erbe, A.
Electrical characterization of short DNA fragments
75th Annual Meeting of the DPG and DPG Spring Meeting 2011, 13.-18.03.2011, Dresden, Germany
76. Wilhelm, R. A.; Heller, R.; Facsko, S.
Surface modification on KBr(001) with slow highly charged ions in high fluence and high potential energy regime
XXVII International Conference on Photonic, Electronic and Atomic Collisions, 27.07.-02.08.2011, Belfast, United Kingdom
77. Winnerl, S.; Orlita, M.; Plochocka, P.; Schneider, H.; Helm, M.; Potemski, M.; Sprinkle, M.; Berger, C.; de Heer, W. A.
Relaxation dynamics in graphene excited in the mid and far infrared
Graphene Week 2011, 24.04.-29.09.2011, Obergurgl, Austria

78. Wintz, S.; Bunce, C.; Körner, M.; Strache, T.; Raabe, J.; Quitmann, C.; McCord, J.; Erbe, A.; Fassbender, J.
Dynamics of interlayer coupled magnetic vortex pairs
56th Annual Conference on Magnetism & Magnetic Materials, 30.10.-03.11.2011, Scottsdale, Arizona, USA
79. Wintz, S.; Puzic, A.; Strache, T.; Bunce, C.; Körner, M.; Schönherr, T.; Neudert, A.; McCord, J.; Moench, I.; Mattheis, R.; Raabe, J.; Quitmann, C.; Erbe, A.; Fassbender, J.
Vortex coupling in magnetic multilayer elements
75th Annual Meeting of the DPG and DPG Spring Meeting 2011, 13.-18.03.2011, Dresden, Germany
80. Yankov, R. A.; Kolitsch, A.; von Borany, J.; Mücklich, A.; Munnik, F.; Steinert, M.; Frenzel, C.; Donchev, A.; Schütze, M.
Surface engineering of Ti and low-Al content Ti-base alloys for high-temperature environmental protection
Dresdner Werkstoffsymposium "Werkstoffe für die Mobilität", 08.-09.12.2011, Dresden, Germany
81. Yankov, R. A.; von Borany, J.; Mücklich, A.; Munnik, F.; Kolitsch, A.; Donchev, A.; Schütze, M.
Surface protection of titanium against degradation in high-temperature oxidizing environments
E-MRS 2011 Spring Meeting IUMRS ICAM 2011 & E-MRS/MRS Bilateral Conference on Energy, 09.-13.05.2011, Nice, France
82. Yildirim, C.; Schildgen, Taylor F.; Ehtler, Helmut P.; Strecker, Manfred R.; Melnick, D.; Niedermann, S.; Merchel, S.; Martschini, M.; Steier, P.
Late Quaternary rock uplift rate at the northern margin of the Central Anatolian Plateau: inferences from pediment surfaces and multiple cosmogenic nuclides
7th TOPO-EUROPE Workshop - A forum investigating the cause and creation of the topography of Europe, 06.-09.10.2011, Davos, Switzerland
83. Zhou, S.; Li, L.; Chen, L.; Rushforth, A. W.; Fassbender, J.; Helm, M.; Zhao, J.; Campion, R. P.; Gallagher, B. L.; Schmidt, H.
Tailoring the magnetism of GaMnAs via defect engineering by energetic ions
6th International School and Conference on Spintronics and Quantum Information Technology (SPINTECH6), 01.-05.08.2011, Matsue, Japan
84. Zhou, S.; Potzger, K.; Yang, Z.; Helm, M.; Fassbender, J.
Ion irradiation as a controllable approach to study the defect-induced ferromagnetism
The 56th Magnetism and Magnetic Materials Conference, 30.10.-03.11.2011, Phoenix / Scottsdale, USA
85. Zier, M.; Kosmata, M.; Munnik, F.
Depth profiling of ultra-shallow boron implants by high depth resolution ERD
20th International Conference on Ion Beam Analysis, 10.-15.04.2011, Itapema, Brazil
86. Zier, M.; Reinholz, U.; Riesemeier, H.; Radtke, M.; Munnik, F.
Accurate stopping power determination of ¹⁵N ions for hydrogen depth profiling by a unique combination of ion beams and synchrotron radiation
20th International Conference on Ion Beam Analysis, 10.-15.04.2011, Itapema, Brazil

Lectures / talks

1. Borany, J. von
Die Nutzung der Hochenergie-Ionenimplantation für die Verbesserung des Schaltverhaltens von Leistungshalbleiter- Bauelementen
2. Mitteldeutscher Innovationstag, 14.04.2011, Dresden, Germany
2. Drachenko, O.
High-field cyclotron resonance spectroscopy of novel semiconductor structures
Lectures at the University of Kiev, 07.06.2011, Kiev, Ukraine
3. Facsko, S.
Applications of ion beams in nanotechnology
Dies academicus timisoarensis, 26.-27.05.2011, Timisoara, Romania

4. Fiedler, J.
Warum Ge und Si durch Ionenimplantation zu Supraleitern werden
Institutsseminar SS 2011, Institut für Physik, TU Ilmenau, 18.05.2011, Ilmenau, Germany
5. Fritzsche, M.
Herstellung und Untersuchung von (selbstorganisierten) Nanostrukturen – Das NVision 40 am HZDR
Invited talk, CrossBeam® Workshop, 03.-04.05.2011, Jena, Germany
6. Gemming, S.; Facsko, S.; Erbe, A.
Nanostructures – Small and beautiful
Kristallographisches Oberseminar, 27.05.2011, München, Germany
7. Gemming, S.
Structure and properties of molybdenum sulfide nanostructures
Workshop Electronic Structure of Novel Materials, 23.06.2011, Meissen, Germany
8. Gensch, M.
The coherent THz facility at ELBE: Enroute to naturally synchronized THz pump THz probe experiments beyond the 100 J pulse energy limit and single shot electron bunch diagnostics
Kolloquium PTB, 16.08.2011, Berlin, Germany
9. Gensch, M.
4th Generation THz-light sources in Dresden: Potential for characterisation of organic materials
IPF Colloquium, 17.03.2011, IPF Dresden, Germany
10. Gensch, M.
An approach for few femtosecond timing of fourth generation X-ray lightsources and single shot electron bunch diagnostics
X-FEL Seminar, 25.03.2011, Hamburg, Germany
11. Gensch, M.
The coherent THz facility at ELBE: Enroute to naturally synchronized THz pump THz probe experiments beyond the 100 J pulse energy limit and single shot electron bunch diagnostics
Invited seminar at the Ultrafast Meeting of the Brookhaven National Lab, 07.10.2011, New York, USA
12. Grenzer, J.
Material science towards the fs range: What we can do?
Workshop on Petawatt-Lasers at Hard X-Ray Light Sources, 05.-09.09.2011, Helmholtz-Zentrum Dresden-Rossendorf, Germany
13. Grenzer, J.; Baehtz, C.; von Borany, J.
The ROBL Upgrade: in-situ investigations for material science
DGM Fachausschusssitzung, BAM Berlin, 27.05.2011, Berlin, Germany
14. Helm, M.
Intersubband transitions and quantum cascade lasers
TeraNano PIRE Kickoff meeting, 07.-08.10.2011, Houston, USA
15. Helm, M.
THz science in semiconductor quantum structures
Nano-Carbon Terahertz Science, 22.11.2011, Osaka University, Japan
16. Kolitsch, A.
Ionenimplantation und Unterstützung von PVD Prozessen mit energetischen Ionen als innovativer Technologiefortschritt
Oberflächenmodifikation von Werkstoffen, 13.05.2011, Zittau, Germany
17. Kranz, A.; Heinig, K.-H.; Liedke, B.
Atomistische Simulation der Selbstorganisation bei der Ionenstrahlerosion
Spring meeting of the DFG FOR 845 "Selbstorganisierte Nanostrukturen durch niederenergetische Ionenstrahlerosion", 01.-02.02.2011, Siegen, Germany

18. McCord, J.
Aspects of magnetic heterostructures - statics, dynamics, and magnetic domains
Seminar des Sonderforschungsbereichs SFB 668, 01.02.2011, Hamburg, Germany
19. Merchel, S.; Akhmedaliev, S.; Pavetich, S.; Rugel, G.
Dreams for DREAMS - The DREsden Accelerator Mass Spectrometry facility
Graduiertenkollegseminar des Graduiertenkolleg "Elementspeziation", 16.-18.10.2011, Bad Münster am Stein, Germany
20. Merchel, S.
Terrestrial cosmogenic radionuclides for geomorphology applications
Seminar, School of Geography, Politics and Sociology, 02.11.2011, Newcastle upon Tyne, UK
21. Mok, K. M.; Schmidt, H.
3D vector magneto-optical ellipsometry investigations on magnetic thin film samples at room temperature
Halbleiterphysik-Seminar (AG Zahn), TU Chemnitz, 21.01.2011, Chemnitz, Germany
22. Posselt, M.
Kinetics and thermodynamics of defects and nanostructures
Seminar, Materials Science Laboratory, Los Alamos National Laboratory, 27.10.2011, Los Alamos, USA
23. Posselt, M.
Kinetics and thermodynamics of defects and nanostructures
Seminar, Condensed Matter and Materials Division, Lawrence Livermore National Laboratory, 24.10.2011, Livermore, USA
24. Posselt, M.
Structure, energetics and thermodynamics of embedded nanoclusters
Seminar, Department of Mathematical Sciences, Loughborough University, 20.10.2011, Loughborough, UK
25. Schneider, H.
Strong-field terahertz spectroscopy of semiconductor quantum structures
Physics Colloquium, Shanghai Jiao Tong University, 07.09.2011, Shanghai, China
26. Schneider, H.
Terahertz investigations on semiconductor quantum structures
Seminar, Jet Propulsion Laboratory, Pasadena CA (USA), 10.02.2011, Pasadena, CA, USA
27. Schneider, H.
High-field terahertz spectroscopy of semiconductor quantum structures
Seminar, Université Paris VII, 12.05.2011, Paris, France
28. Schneider, H.
High-field terahertz investigations on semiconductor quantum structures
Seminar, Hebrew University of Jerusalem, 09.11.2011, Jerusalem, Israel
29. Zhou, S.
Ion implantation and short-time annealing for spintronics
Seminar at University of Jena, 30.06.2011, Jena, Germany
30. Zhou, S.; Potzger, K.; Yang, Z.; Helm, M.; Fassbender, J.
Ion irradiation as a controllable approach to study the defect-induced ferromagnetism
Invited seminar at the Institute of Solid State Physics, Chinese Academy of Sciences, 13.10.2011, Hefei, China

Workshops, colloquia and seminars

Organization of workshops

1. Schmidt, H., and Skorupa, W.
International topical workshop on „Subsecond thermal processing of advanced materials 2011”
25.-27.10.2011, Dresden, Germany

Colloquia

1. Beschoten, Bernd
Physikalisches Institut, RWTH Aachen, Germany
Time-resolved transport of electron spins in nanostructures
27.01.2011
2. Bilek, Marcela
Applied and Plasma Physics, School of Physics, University of Sydney, NSW, Australia
A radical way of hardness nature's nanomachines
22.06.2011
3. Bonnani, Alberto
Institut für Halbleiter- und Festkörperphysik, Johannes Kepler University, Linz, Austria
Making nitrides magnetic: From nanoscale characterization to the understanding of macroscopic properties
14.07.2011
4. Bratschitsch, Rudolf
Institut für Physik, TU Chemnitz, Germany
Ultrafast quantum optics, plasmonics, and spintronics with solid-state nanosystems
24.03.2011
5. Fischer, Peter
IEEE Distinguished Lecturer Program, Lawrence Berkeley National Laboratory, USA
Magnetic soft X-ray microscopy: A path towards imaging magnetism down to fundamental length and time scales
06.07.2011
6. Hahn, Horst
Karlsruhe Institute of Technology (KIT), Institute for Nanotechnology and Joint Research Laboratory Nanomaterials (KIT-TUD), Technische Universität Darmstadt, Germany
Tailored and tuneable properties of nanostructures
27.10.2011
7. Hellwig, Olav
San Jose Research Center, Hitachi Global Storage Technologies, San Jose, CA, USA
Advanced magnetic nanostructures for recording media: Applications in hard disk drives
28.09.2011
8. Hoffmann, Axel
Material Science Division Argonne National Laboratory, Argonne, USA
Pure spin currents: Discharging spintronics
08.03.2011
9. Holy, Vaclav
Department of Condensed Matter Physics, Faculty of Mathematics and Physics, Charles University Prague, Czech Republic
X-ray diffraction study of defects in epitaxial layers
11.11.2011

10. Lemme, Max
KTH Royal Institute of Technology, Sweden
Graphene – In your laptop tomorrow?
04.11.2011
11. Lindner, Jürgen
AG Struktur und Magnetismus nanoskaliger Systeme, Universität Duisburg-Essen, Germany
Spinwave excitations in nanostructures: New experimental approaches for single structure investigations
22.09.2011
12. Mantl, Siegfried
Institut für Bio- und Nanosysteme (IBN1-IT), Forschungszentrum Jülich, Germany
Materials and concepts for low power transistors
16.06.2011
13. Mougin, Alexandra
Laboratoire de Physique des Solides, Université Paris-Sud, France
Coupling with a multiferroic BiFeO₃: Control under electric field
10.02.2011
14. Raab, Michael
GLOBALFOUNDRIES Dresden Module One LLC & Co. KG, Germany
Globalfoundries - Company overview and technology update
04.03.2011
15. Radu, Ilie
Institute of Molecules and Materials, Radboud University Nijmegen, NL
Ultrafast magnetism: From X-rays to THz excitations
10.03.2011

Seminar series

**Understanding advanced materials and processes on the atomic level:
Materials research with ultrashort, intense and coherent X-ray pulses and high-power lasers**

1. Posselt, M.
Ultrafast X-ray diffraction / spectroscopy
18.08.2011
2. Posselt, M.
Using the coherence of the intense and ultrashort X-rays pulses at XFEL
02.09.2011
3. Grenzer, J.
Material science toward the fs range: Experimental challenges using an XFEL
04.11.2011

Seminars

1. Abou-Ras, D.
Institut für Technologie, Helmholtz-Zentrum Berlin für Materialien und Energie, Berlin, Germany
Solving open questions in materials science by means of TEM: Using the example of thin-film solar cells
01.07.2011
2. Altpeter, I.
Fraunhofer-Institut für Zerstörungsfreie Prüfverfahren (IZFP), Saarbrücken, Germany
Magnetische und mikromagnetische Prüfverfahren und Prüfgeräte zur integralen und ortsaufösenden Werkstoffcharakterisierung
05.07.2011
3. Assmann, W.
Beschleunigerlabor, Fakultät für Physik, TU München, Germany

Nanocrystal ejection in electronic sputtering

10.02.2011

4. Bali, R.
Max-Planck- Institute of Microstructure Physics, Halle, Germany
Magnetic properties of Fe-Co alloy films on Ir(001)
07.03.2011
5. Bird, J.
University at Buffalo, NY, USA
Hybrid ferromagnetic/semiconductor devices: a route for gating graphene?
17.06.2011
6. Börrnert, F.
Institut für Festkörperforschung, IFW Dresden, Germany
sp²-carbon-electron interactions studied by low-voltage TEM
30.06.2011
7. Borschel, C.
Institute for Solid State Physics, University of Jena, Germany
Ion beam irradiation of nanostructures – Monte Carlo simulations with 3D targets
07.06.2011
8. Bradley, M.
Department of Physics, Colorado State University, USA
Spontaneous nanoscale pattern formation induced by ion bombardment of solid surfaces
23.06.2011
9. Buljan, M.
Material Physics Division, Rudjer Bosovic Institute, Zagreb, Croatia
Preparation and characterization of self-assembled quantum dots in amorphous matrices
15.07.2011
10. Bulutay, C.
Department of Physics, Bilkent University, Ankara, Turkey (presently at ETH Zürich, Switzerland)
An atomistic computational insight to linear, nonlinear and quantum optics of Si and Ge nanocrystals
12.07.2011
11. Chen, F.
School of Physics, Shandong University, China
Optical waveguides and photonic structures produced by energetic ion beams in optical crystals: The research at Shandong University
08.06.2011
12. Deac, A.
Institute of Condensed Matter Physics, Ecole Polytechnique Fédérale de Lausanne, Lausanne, Switzerland
Spin-transfer dynamics in spin-valves with in-plane polarizer and perpendicular free layer
24.06.2011
13. Dhagat, P.
Associate Professor in the School of Electrical Engineering and Computer Science (EECS) at Oregon State University, USA
Investigating magnetoacoustic interactions and applications
09.12.2011
14. Ellmer, K.
Abteilung Solare Brennstoffe, Helmholtz-Zentrum Berlin für Materialien und Energie, Berlin, Germany
Reactive magnetron sputtering of oxides and sulfides for thin film solar cells
01.06.2011
15. Gao, K.
Fudan University, Shanghai, China
Structural and Optical Properties of ZnO Nanocrystalline Thin Films Synthesized by ECR-

- PLD**
09.12.2011
16. Gierak, J.
Laboratory for Photonics and Nanostructures/CNRS Marcoussis, France
Exploration of the ultimate patterning capabilities of focused ion beams
23.02.2011
 17. Gradhand, M.
Theoretical Physics, University Bristol, UK
Materials design for an application of the spin Hall effect
28.09.2011
 18. Gunapala, S.
NASA - Jet Propulsion Laboratory, Pasadena, USA
III-V quantum structures for infrared detection
20.05.2011
 19. Guziewicz, E., and Stonert, A.
Physics Institute, Polish Academy of Sciences, Warsaw, Poland
Soltan Institute of Nuclear Studies, Swierk and Warsaw, Poland
RBS/channeling analysis of zinc oxide films obtained in low temperature ALD process
20.01.2011
 20. Haßdenteufel, A.
Institut für Physik, TU Chemnitz, Germany
All-optical switching - Current state and perspectives
29.09.2011
 21. Hauet, T.
Département Physique de la Matière et des Matériaux, Université Nancy, France
Some ways to understand and tune switching field and switching field distribution of bit pattern media
01.06.2011
 22. Heidarian, A.
Institute of Physical Chemistry, Polish Academy of Sciences, Warsaw, Poland
Structural, magnetic and electrical properties of Mg doped $\text{La}_{0.75}\text{Sr}_{0.25}\text{MnO}_3$ manganite
22.06.2011
 23. Hirori, H.
Institute for Integrated Cell-Material Sciences and Department of Physics, Kyoto University, Japan
Nonlinear THz spectroscopy on semiconductors with intense terahertz pulses
05.12.2011
 24. Höfer, B.
Experimental Physics II, University of Bayreuth, Germany
Excited state complexes for OLED applications
04.07.2011
 25. Jansen, R.
National Institute of Advanced Industrial Science and Technology (AIST) Tsukuba, Japan
Electrical and thermal spintronics in silicon
24.10.2011
 26. Kalchmair, S.
Center for Micro- and Nanostructures, TU Wien, Austria
Photonic crystal resonators in quantum well photodetectors
25.08.2011
 27. Katsaros, G.
Institut für Integrative Nanowissenschaften, IFW Dresden & CEA Grenoble
Spin orbit effects in SiGe self-assembled quantum dots
15.12.2011
 28. Keller, A.
Interdisciplinary Nanoscience Center (iNANO), Aarhus University, Denmark

-
- Biological response to ion-beam modified surfaces: from peptides to stem cells**
27.04.2011
29. Krause, B.
Karlsruhe Institute of Technology (KIT); Institute for synchrotron radiation (IIS)
In situ X-ray study of vanadium carbide
14.12.2011
30. Lorenz, K.
Instituto Tecnológico e Nuclear, Sacavém, Portugal
Rare earth doping of III-nitride semiconductors: from thin films to nanostructures
30.11.2011
31. Lu, G.-H.
Department of Physics, Beihang University, Beijing 100191, China
Towards understanding hydrogen behaviors in tungsten via multiscale modelling
07.11.2011
32. Mackova, A.
Laboratory of Nuclear Analytical Methods, Nuclear Physics Institute of Academy of Science of the Czech Republic
Structural study of thin layers prepared by ion implantation in crystalline materials (LiNbO₃ a ZnO) using ion beam analytical methods
10.11.2011
33. Marinova-Atanassova, M.
Department for New Energies Technologies and Nanomaterials, LITEN, CEA, Grenoble, France
Defects in cubic silicon carbide
30.06.2011
34. McGilp, J.
School of Physics, Trinity College, Dublin, Ireland
Epioptics: The optics of surfaces and interfaces
22.03.2011
35. McKenzie, D.
School of Physics, University of Sydney, Australia
Advances in the simulation of materials
20.06.2011
36. Norris, S. A.
Methodist University, Dallas, TX, USA
Towards a quantitative continuum model for irradiation-induced morphology evolution
21.07.2011
37. Paul, A.
Institute Complex Magnetic Materials, Helmholtz-Zentrum Berlin, Germany
Polarized neutron scattering in nano-layered systems
13.01.2011
38. Pavetich, S.
Isotope Research, Faculty of Physics, University Vienna, Austria
AMS-measurement of the reaction $^{35}\text{Cl}(n,g)^{36}\text{Cl}$ and its relevance to astrophysics and nuclear technology
18.05.2011
39. Riedl, T.
Technische Universität Dresden, Germany
TEM/STEM studies of perovskite thin films and bulk nanocrystalline alloys
30.06.2011
40. Ristow, O.
Universität Konstanz, Germany
All optical investigations of high frequency mechanical modes in semiconductor nanostructures
09.12.2011

41. Roehringer, I.
Universität Bayreuth, Germany
Klima- und Vergletscherungsgeschichte des Pamir: Rekonstruktion mittels Be-10 Expositionsdatierung
20.01.2011
42. Sendler, T.
Naturwissenschaftliche Fakultät II (Physik), Universität Regensburg, Germany
Spin injection into GaAs
14.06.2011
43. Sluka, V.
Peter-Grünberg-Institut (PGI-6), Forschungszentrum Jülich, Germany
Spin-transfer torque-induced dynamics of magnetic vortices in nanopillars
23.09.2011
44. Tonouchi, M.
University of Osaka, Japan
Terahertz spectroscopy of ferroelectric thin films: BiFeO₃ and strained SrTiO₃
11.07.2011
45. Uilson, S.
Institute of Education, Science and Technology Sul-Rio-Grandense - Campus Pelotas Centro, Pelotas, Brazil
Structural and luminescence properties of nanoparticles produced by hot ion implantation
02.09.2011
46. Varvaro, G.
Team of the Institute for Structure of Matter (ISM-CNR), Rome, Italy
Nanostructured magnetic materials
17.10.2011
47. Wang, X.H.
University of Hong Kong, China
Optical investigations of FIB patterned InGaN/GaN MQW nanopillar array
24.05.2011
48. Weber, W.
NaMLab Dresden, Germany
Silicide device nanowire structures and their electrical applications
13.07.2011
49. Werner, Z.
Andrzej Soltan Institute for Nuclear Studies, Otwock University, Poland
Lattice location of manganese atoms implanted into silicon after plasma pulse annealing
27.01.2011
50. Wiedenbeck, M.
Helmholtz-Zentrum Potsdam, Deutsches GeoForschungsZentrum, Germany
The Potsdam SIMS Lab: What we are doing and where we are headed
28.01.2011
51. Wolf, D.
Triebenberg TEM Lab, Institut für Strukturphysik, TU Dresden, Germany
2D and 3D imaging in the Transmission-Electron-Microscope from nanometer to atomic resolution
30.07.2011
52. Yi, J.
Department of Physics, National University of Singapore, Singapore
Unusual ferromagnetism in ZnO
17.06.2011

Exchange of researchers

SPIRIT visitors

1. Barlak, M.
Soltan Institute for Nuclear Studies, Otwock, Poland; 24.-29.01.2011
2. Beleni, V.
Nuclear Physics Institute of ASCR, Rez, Czechia; 18.-22.07.2011
3. Corso, A.J.
Institute for Photonics and Nanotechnology CNR-IFN Padova, Italy; 16.-20.01.2011
4. Geetanjali, D.
INSP, UMPC, Ilday, France; 12.-15.12.2011
5. Guziewicz, E.
IEMT Warschau, Poland; 15.-22.2011, 02-09.04.2011
6. Ilday, S.
METU Ankara, Turkey; 20.-24.09.2011
7. Jozwik, P.
IEMT Warschau, Poland; 03.-05.10.2011
8. Laird, A.
University of York, UK; 03.-25.03.2011
9. Langegger, R.
Technische Universität Wien, Austria; 26.-30.09.2011
10. Lenz, Ch.
Technische Universität Wien, Austria; 10.-15.07.2011
11. Macías, M.
Instituto de Ciencia de Materiales de Sevilla, Spain; 13.-24.03.2011
12. Mackova, A.
Nuclear Physics Institute of ASCR, Rez, Czechia; 09.-10.11.2011
13. Magnfält, D.
Linköpings University, Sweden; 16.-21.10.2011
14. Malinsky, P.
Nuclear Physics Institute of ASCR, Rez, Czechia; 18.-22.07.2011, 07.-11.11.2011
15. Martin, E.
University of York, UK; 03.-25.03.2011
16. Meissl, W.
Technische Universität Wien, Austria; 11.-16.12.2011
17. Nasdala, L.
Technische Universität Wien, Austria; 10.-12.07.2011
18. Paulitsch, J.
Montanuniversität Leoben, Austria; 05.-06.12.2011
19. Pelezzo, M.
Institute for Photonics and Nanotechnology CNR-IFN Padova, Italy; 16.-20.01.2011
20. Pochrybniak, C.
Soltan Institute for Nuclear Studies, Otwock, Poland; 13.-22.06.2011
21. Ratajczak, R.
IEMT Warschau, Poland; 22.-28.10.2011, 16.-19.11.2011

22. Ritter, R.
Technische Universität Wien, Austria; 23.-27.05.2011, 11.-16.09.2011, 11.-16.12.2011
23. Stonert, A.
IEMT Warschau, Poland; 15.-22.01.2011, 02-09.04.2011
24. Tamuleviciene, A.
Institute of Materials Science of KTU, Kaunas, Lithuania; 06.-15.11.2011
25. Tansel, T.
Technical University Ankara, Turkey; 03.-07.01.2011
26. Terriza, A.
Instituto de Ciencia de Materiales de Sevilla, Spain; 13.-24.03.2011
27. Tsvetkova, T.
University of Exeter, UK; 04.-11.06.2011
28. Werner, Z.
Soltan Institute for Nuclear Studies, Otwock, Poland; 24.-29.01.2011
29. Zeiner, C.
Technische Universität Wien, Austria; 25.-27.10.2011
30. Zupella, P.
Institute for Photonics and Nanotechnology CNR-IFN Padova, Italy; 16.-20.01.2011

FEL visitors

1. Beck, M.
Universität Konstanz, Germany; 03.-11.03.2011, 15.-19.04.2011, 20.-27.10.2011
2. Bossini, D.
Radboud University Nijmegen, The Netherlands; 06.-12.12.2011
3. Chatterjee, S.
Philipps-Universität Marburg, Germany; 17.-24.10.2011, 28.11.-31.12.2011
4. Cilento, F.
University of Trieste, Italy; 25.-27.10.2011
5. dal Conte, S.
Eindhoven University of Technology, The Netherlands; 25.10.-01.11.2011
6. Demsar, J.
Universität Konstanz, Germany; 03.-06.03.2011
7. Deßmann, N.
Aerospace Center DLR, Berlin, Germany; 23.-28.10.2011
8. Dienst, A.
University of Oxford, UK; 12.-15.04.2011
9. Ewers, B.
Philipps-Universität Marburg, Germany; 17.-24.10.2011, 28.11.-31.12.2011
10. Fausti, D.
University of Trieste, Italy; 12.-22.04.2011, 25.10.-01.11.2011
11. Fromherz, T.
Universität Linz, Austria; 22.-30.05.2011
12. Ghosh, A.
Fritz-Haber Institute Berlin, Germany; 26.-30.05.2011
13. Gianetti, C.
University of Brescia, Italy; 25.10.-01.11.2011

14. Heigold, M.
Max-Planck-Institut für Quantenoptik Garching and Ludwig-Maximilians-Universität München, Germany; 01.-11.12.2011
15. Kampfrath, T.
Fritz-Haber Institute Berlin, Germany; 26.-30.05.2011
16. Karsch, S.
Max-Planck-Institut für Quantenoptik Garching and Ludwig-Maximilians-Universität München, Germany; 08.-09.12.2011
17. Khrennikov, K.
Max-Planck-Institut für Quantenoptik Garching and Ludwig-Maximilians-Universität München, Germany; 04.-06.12.2011
18. Kimel, A.
Radboud University Nijmegen, The Netherlands; 26.-30.05.2011
19. Kirchschrager, R.
Universität Linz, Austria; 22.-30.05.2011
20. Klammer, M.
Universität Konstanz, Germany; 15.-19.04.2011
21. Mährlein, S.
Fritz-Haber Institute Berlin, Germany; 06.-12.12.2011
22. Malik, D.
Radboud University Nijmegen, The Netherlands; 26.-30.05.2011
23. Malnasi-Csizmadia, A.
Eotvos University, Budapest, Hungary; 25.-30.11.2011
24. Montagnese, M.
University of Groningen, The Netherlands; 12.-22.04.2011
25. Moroziv, S.
Institute for Physics of Microstructures of the Russian Academy of Sciences, Nizhny Novgorod, Russia; 22.-29.05.2011
26. Morris, C.
University of California, Santa Barbara, USA; 27.06.-04.07.2011
27. Novelli, F.
University of Trieste, Italy; 15.-22.04.2011.
28. Ortolani, M.
CNR-IFN, Institute for Photonics and Nanotechnology, Rome, Italy; 24.-29.06.2011
29. Pavlov, S.
Aerospace Center DLR, Berlin, Germany; 23.-28.10.2011
30. Radu, I.
Radboud University Nijmegen, The Netherlands; 26.-30.05.2011, 06.-12.12.2011
31. Rousseau, I.
Universität Konstanz, Germany; 06.-11.03.2011, 15.-19.04.2011, 20.-27.10.2011
32. Shastin, V.
Institute for Physics of Microstructures of the Russian Academy of Sciences, Nizhny Novgorod, Russia; 23.-28.10.2011
33. Wenz, J.
Max-Planck-Institut für Quantenoptik Garching and Ludwig-Maximilians-Universität München, Germany; 01.-03.12.2011
34. Zhukavin, R.
Institute for Physics of Microstructures of the Russian Academy of Sciences, Nizhny Novgorod, Russia; 23.-28.10.2011

ROBL-MRH visitors

1. Bayer B.C.
Department of Engineering, University of Cambridge, United Kingdom; 29.06.-05.07.2011
2. Brauns M.
Fraunhofer Institut IFAM, Germany; 09.03.2011, 16.03.2011
3. Buljan M.
Dept of Condensed Matter Physics, Charles University, Praha, Czech Republic; 07.-14.06.2011
4. Canevet E.
CEA – CENG Grenoble, France; 23.-27.04.2011
5. Colin J.-F.
LITEN/DEHT/LBA, CEA Grenoble, France; 23.-27.04.2011
6. Endrino J.
CSIC – ICMM, Instituto de Ciencia de Materiales de Madrid, Spain; 13.-16.04.2011
7. Gruber W.
Institute of Metallurgy, TU Clausthal, Germany; 18.-22.02.2011
8. Hofmann S.
Department of Engineering, University of Cambridge, United Kingdom, 29.06.-05.07.2011
9. Kalinichenka S.
Fraunhofer Institut IFAM, Germany; 09.-16.03.2011
10. Kanak J.
Department of Electronics, University of Science and Technology; Poland; 06.-12.07.2011
11. Kidambi P. R.
Department of Engineering, University of Cambridge, United Kingdom; 29.06.-05.07.2011
12. Leibenguth P.
Chair of Functional Materials, Saarland University, Germany; 16.-19.04.2011
13. Lukac F.
Department of Low Temperature Physics, Charles University, Praha, Czech Republic; 02.-08.03.2011
14. Martin J. F.
LITEN/DEHT/LBA, CEA Grenoble, France; 23.-27.04.2011
15. Mougin A.
Laboratoire de Physique des Solides, CNRS UMR 8602 - Universite Paris-Sud 11, France; 06.-12.07.2011
16. Pundt A.
Institut für Materialphysik, Georg-August-Universität Göttingen, Germany; 02.-08.03.2011
17. Röntzsch L.
Fraunhofer Institut IFAM, Germany; 09.-16.03.2011
18. Schmidt A.
Fraunhofer Institut IFAM, Germany; 09.-16.03.2011
19. Schmidt H.
Institute of Metallurgy, TU Clausthal, Germany; 18.-22.02.2011
20. Schubert J.
Peter Grünberg Institute 9 (PGI-9), Forschungszentrum Jülich, Germany; 17.-21.06.2011
21. Simonin L.
LITEN/DEHT/LBA, CEA Grenoble, France; 23.-27.04.2011
22. Sveklo I.
Laboratory of Magnetism, University of Bialystok, Poland; 06.-12.07.2011

23. Uchida H. T.
Institut für Materialphysik, Georg-August-Universität Göttingen, Germany; 02.-08.03.2011
24. Vlcek M.
Department of Low Temperature Physics, Charles University, Praha, Czech Republic; 02.-08.03.2011
25. Wagner S.
Institut für Materialphysik, Georg-August-Universität Göttingen, Germany; 02.-08.03.2011
26. Weatherup R.
Department of Engineering, University of Cambridge, United Kingdom; 29.06.-05.07.2011
27. Wirth C. T.
Department of Engineering, University of Cambridge, United Kingdom; 29.06.-05.07.2011
28. Woll K.
Chair of Functional Materials, Saarland University, Germany; 16.-19.04.2011
29. Zschornak M.
Institut Kristallographie und Festkörperphysik, TU Dresden, Germany; 13.-16.04.2011

Other guests

1. Bilek, M.
School of Physics, University of Sydney, Australia; 19.-24.06.2011
2. Bradley, M.
Colorado State University, Fort Collins, USA; 15.-27.06.2011
3. Buljan, M.
Ruder Boskovic Institute, Zagreb, Croatia; 19.06.-31.07.2011
4. Bulutay, C.
Department of Physics, Bilkent University, Ankara, Turkey; 12.-15.07.2011
5. Chang, C.-H.
Hsinchu, Taiwan, 01.05.-31.10.2011
6. Gaiduk, P.
Belarusian State University, Minsk, Belarus; 21.-30.10.2011
7. Gordienko, S.
Institute of Semiconductor Physics, Kiev, Ukraine; 14.11.-11.12.2011
8. Keles, U.
Department of Physics, Bilkent University, Ankara, Turkey; 08.11.-08.12.2011
9. Khanbabaee, B.
Institut für Festkörperphysik, Siegen, Germany; 01.-11.11.2011
10. Lu, G.-H.
Department of Physics, Beihang University, Beijing, China; 05.-09.11.2011
11. Luo, W.
Chengdu, China; 01.-31.12.2011
12. Ming, X.
Applied Physics Department, Xi'an University of Technology, Shaanxi, China; 01.-31.12.2011
13. Morris, C.
Institute for Terahertz Science and Technology, University of California, Santa Barbara, USA; 27.06.-04.07.2011
14. Norris, S.
SM University, Dallas, USA; 19.-30.07.2011
15. Ranjan, M.
Institute for Plasma Research, Gandhinagar, India; 19.04.-11.06.2011

16. Shevchenko, E.
North-Caucasus State Technical University, Russia; 01.10.-31.12.2011
17. Sias, U.
Universidade Federal do Rio Grande do Sul, Brazil; 28.08.-04.09.2011
18. Zhou, H.-B.
Department of Physics, Beihang University, Beijing, China; 05.11.-31.12.2011

Laboratory visits

1. Abrasonis, G.
ESRF Grenoble, France; 12.-16.04.2011
DESY Hamburg, Germany; 15.-21.12.2011
2. Akhmadaliev, C.
Frascati, Italy; 06.-11.03.2011
3. Banholzer, A.
Swiss Light Source, PSI Villigen, Switzerland; 31.03.-10.04.2011; 26.06.-04.07.2011; 05.-12.10.2011.; 01.-09.12.2011
4. Borany, J. von
ESRF Grenoble, France; 16.-21.06.2011; 26.-29.11.2011
5. Buhl, M.
Swiss Light Source, PSI Villigen, Switzerland; 31.03.-10.04.2011; 23.06.-04.07.2011; 05.-12.10.2011; 01.12.-09.12.2011
6. Drachenko, O.
LNCMP Toulouse, France; 10.-18.03.2011; 27.08.-04.09.2011
Institute for Microstructures, Nizhny Novgorod, Russia; 25.04.-02.05.2011
Kurchatov Institute, Moscow, Russia; 03.-07.05.2011
7. Erbe, A.
Swiss Light Source, PSI Villigen, Switzerland; 24.-29.06.2011
8. Fowley, C.
Dublin University, Ireland; 25.11.-03.12.2011; 16.-23.12.2011
9. Friedrich, D.
Bilkent University, METU, Ankara, Turkey; 27.10.-24.11.2011
10. Grebing, J.
Universität Konstanz, Germany; 23.-27.2011.; 27.03.-04.04.2011
Swiss Light Source, PSI Villigen, Switzerland; 05.-12.10.2011
11. Grenzer, J.
ESRF Grenoble, France; 15.-18.01.2011; 28.03.-01.04.2011; 07.-17.06.2011; 25.11.-02.12.2011
12. Heinig, K.-H.
Bilkent University, METU, Ankara, Turkey; 04.-07.10.2011
13. Henschel, T.
Universität Konstanz, Germany; 20.03.-01.04.2011
14. Kosmata, M.
University of Uppsala, Sweden; 14.-21.05.2011
ESRF Grenoble, France; 16.-21.06.2011
15. Kühn, V.
Universität Konstanz, Germany; 09.-13.05.2011
16. Lehmann, J.
University of Porto Alegre, Brazil; 28.11.-19.12.2011
17. Liedke, B.
Bilkent University, METU, Ankara, Turkey; 04.-19.10.2011

18. Liedke, M.O.
ESRF Grenoble, France; 05.-12.07.2011
19. Martinavicius, A.
Universität Rouen, France; 17.-29.01.2011
20. Merchel, S.
CEREGE, Aix-en-Provence, France; 23.-27.05.2011; 20.-25.11.2011; 12.-16.12.2011
BESSY Berlin, Germany; 26.-29.09.2011
University of Newcastle, UK; 31.10.-07.11.2011
21. Munnik, F.
BESSY Berlin, Germany; 26.-29.09.2011
22. Osten, J.
Swiss Light Source, PSI Villigen, Switzerland; 31.03.-10.04.2011; 01.-09.12.2011
Glasgow University, U.K.; 17.-22.04.2011
23. Pavetich, S.
CEREGE, Aix-en-Provence, France; 21.-25.11.2011
24. Reuther, H.
ESRF Grenoble, France; 13.-17.06.2011
25. Roshchupkina, O.
ESRF Grenoble, France; 10.-17.06.2011; 25.11.-02.12.2011
26. Rugel, G.
CEREGE, Aix-en-Provence, France; 23.-27.05.2011; 20.11.-25.11.2011
TU München, Germany; 04.-16.05.2011; 02.-11.07.2011; 22.-29.08.2011; 10.-15.11.2011
27. Schmidt, B.
Frascati, Italy; 06.-11.03.2011
28. Schneider, H.
ThEP Center, Chiang Mai, Thailand; 25.01.-29.01.2011
Jet Propulsion Lab, Pasadena, USA; 06.-12.02.2011
Jiao Tong University, Shanghai, China; 01.-25.04.2011; 27.08.-04.09.2011
Université Paris Diderot, Paris, France; 09.-28.05.2011
Universität Freiburg, Germany; 13.-18.06.2011
Hebrew University, Al-Quds University, Jerusalem, Israel; 04.11.-10.11.2011
29. Schönherr, T.
Universität Konstanz, Germany; 24.01.-04.02.2011; 02.-13.05.2011
30. Shuai, Y.
Shanghai, China; 09.-21.07.2011
31. Steinbach, G.
Swiss Light Source, PSI Villigen, Switzerland; 01.-09.12.2011
32. Strache, T.
Glasgow University, U.K.; 17.-22.04.2011
33. Vinnichenko, M.
BESSY Berlin, Germany; 01.-06.03.2011; 06.-12.06.2011
34. Weidauer, R.
ESRF Grenoble, France; 17.-28.10.2011
35. Wenisch, R.
DESY Hamburg, Germany; 15.-21.12.2011
36. Wintz, S.
Advanced Light Source, Berkeley, USA; 24.-31.03.2011; 17.10.-20.12.2011
Swiss Light Source, PSI Villigen, Switzerland; 01.-10.04.2011; 26.06.-01.07.2011; 18.-
21.09.2011; 05.-12.10.2011
ESRF Grenoble, France; 12.-16.04.2011
BESSY Berlin, Germany; 26.07.-01.08.2011

37. Zhou, S.
ESRF Grenoble, France; 19.-22.04.2011
Chinesisch-Deutsches Zentrum für Wissenschaftsförderung Hefei, China; 08.-21.10.2011
38. Zschornak, M.
ESRF Grenoble, France; 12.-16.04.2011

Projects

The projects are listed by funding institution and project starting date. In addition, the institute has several bilateral service collaborations with industrial partners and research institutions. These activities are not included in the following overview.

European Projects

1. 03/2009 – 02/2013 European Union EU
SPIRIT – Support of Public and Industrial Research using Ion Beam Technology
Prof. W. Möller Phone: 0351 260 2245 w.moeller@hzdr.de
2. 03/2009 – 08/2011 European Union EU
ELISA – European Light Sources Activities: Synchrotrons and Free Electron Lasers
Prof. M. Helm Phone: 0351 260 2260 m.helm@hzdr.de

Helmholtz Association Projects

1. 03/2011 – 02/2016 Helmholtz-Gemeinschaft HGF
Functional Materials - Helmholtz Young Investigators' Group
Dr. Shengqiang Zhou Phone: 0351 260 2484 s.zhou@hzdr.de
2. 07/2011 – 06/2012 Helmholtz-Gemeinschaft HGF
NANONET - Helmholtzkolleg
Dr. A. Erbe Phone: 0351 260 2366 a.erbe@hzdr.de
3. 08/2011 – 07/2012 Helmholtz-Gemeinschaft HGF
HEF-ALION - spinoff funding
Prof. A. Kolitsch Phone: 0351 260 3348 a.kolitsch@hzdr.de
4. 10/2011 – 09/2016 Helmholtz-Gemeinschaft HGF
MEMRIOX - Virtual Institute
Dr. S. Gemming Phone: 0351 260 2470 s.gemming@hzdr.de

German Science Foundation Projects

1. 07/2007 - 01/2013 Deutsche Forschungsgemeinschaft DFG
Hybride magnetische Materialien
Prof. J. Fassbender Phone: 0351 260 3096 j.fassbender@hzdr.de
2. 08/2007 - 10/2013 Deutsche Forschungsgemeinschaft DFG
Atomistische Simulation der Selbstorganisation bei der Ionenstrahlerosion
Dr. K.-H. Heinig Phone: 0351 260 3288 k.h.heinig@hzdr.de
3. 09/2007 - 09/2011 Deutsche Forschungsgemeinschaft DFG
A Infrared scattering near-field optical microscopy near dielectric (polaritonic) resonances using a free-electron laser
Prof. M. Helm Phone: 0351 260 2260 m.helm@hzdr.de
4. 07/2008 - 06/2012 Deutsche Forschungsgemeinschaft DFG
Morphologie-induzierte magnetische Anisotropie- und Dämpfungspänomene
Prof. J. Fassbender Phone: 0351 260 3096 j.fassbender@hzdr.de

-
5. 02/2009 – 11/2011 Deutsche Forschungsgemeinschaft DFG
Electric-field control of magnetoresistance (Ferromagnetism II)
Dr. H. Schmidt Phone: 0351 260 2724 heidemarie.schmidt@hzdr.de
 6. 02/2009 – 09/2012 Deutsche Forschungsgemeinschaft DFG
Magnetismus von nanoskaligen CoCrPt-SiO₂-Filmen in templatbedingt geometrisch eingeschränkten Dimensionen (MAGTEMPLAT)
Prof. J. Fassbender Phone: 0351 260 3096 j.fassbender@hzdr.de
 7. 09/2009 – 08/2012 Deutsche Forschungsgemeinschaft DFG
Bestimmung der elektronischen Struktur von Punktdefekten mittels DAFS
Dr. S. Gemming Phone: 0351 260 2470 s.gemming@hzdr.de
 8. 11/2009 – 03/2013 Deutsche Forschungsgemeinschaft DFG
Electric field control of magnetoresistance (TCOMR)
Dr. H. Schmidt Phone: 0351 260 2724 heidemarie.schmidt@hzdr.de
 9. 04/2010 – 10/2011 Deutsche Forschungsgemeinschaft DFG
Oxidkristalle II
Dr. S. Gemming Phone: 0351 260 2470 s.gemming@hzdr.de
 10. 04/2010 – 03/2013 Deutsche Forschungsgemeinschaft DFG
Strukturbildende Prozesse in amorphen Kohlenstoffschichten
Dr. L. Bischoff Phone: 0351 260 2963 l.bischoff@hzdr.de
 11. 05/2010 – 03/2011 Deutsche Forschungsgemeinschaft DFG
Dynamic metallographic and magneto-optical polarization microscopy of magnetic shape memory systems (MSMA)
Dr. J. McCord Phone: 0351 260 3709 j.mccord@hzdr.de
 12. 05/2010 – 06/2011 Deutsche Forschungsgemeinschaft DFG
Hybride magnetische Materialien
Dr. J. McCord Phone: 0351 260 3709 j.mccord@hzdr.de
 13. 08/2010 – 09/2013 Deutsche Forschungsgemeinschaft DFG
Supraleitung in hochdotierten Gruppe IV Halbleitern (SuSi)
Dr. V. Heera Phone: 0351 260 3343 v.heera@hzdr.de
 14. 09/2010 – 08/2013 Deutsche Forschungsgemeinschaft DFG
Terahertz non-linear detection and quantum optical studies by resonant two-photon transitions in semiconductor quantum wells (TERATOP)
Dr. H. Schneider Phone: 0351 260 2880 h.schneider@hzdr.de
 15. 11/2010 – 10/2013 Deutsche Forschungsgemeinschaft DFG
Relaxation dynamics in graphene investigated in the mid- and far-infrared spectral range
Dr. S. Winnerl Phone: 0351 260 3522 s.winnerl@hzdr.de
 16. 01/2011 - 12/2013 Deutsche Forschungsgemeinschaft DFG
Wechselwirkung langsamer hochgeladener Ionen mit der Oberfläche von Ionenkristallen und Isolatoren
Dr. S. Facsko Phone: 0351 260 2987 s.facsko@hzdr.de
 17. 01/2011 – 12/2013 Deutsche Forschungsgemeinschaft DFG
Selbstorganisierte Oberflächenmuster auf Germanium durch schwere Clusterionen
Dr. L. Bischoff Phone: 0351 260 2963 l.bischoff@hzdr.de
 18. 03/2011 – 02/2014 Deutsche Forschungsgemeinschaft DFG
High-field studies of the band dispersion in novel semiconductor materials: Dilute nitride semiconductors and Ge/SiGe quantum wells
Dr. O. Drachenko Phone: 0351 260 3593 o.drachenko@hzdr.de
 19. 04/2011 – 03/2014 Deutsche Forschungsgemeinschaft DFG
Nukleation von Spinordnung in niederdimensionalen kolloidalen Partikelsystemen
Dr. A. Erbe Phone: 0351 260 2366 a.erbe@hzdr.de

20. 04/2011 – 03/2013 Deutsche Forschungsgemeinschaft DFG
Modification of DNA towards high conductance
 Dr. A. Erbe Phone: 0351 260 2366 a.erbe@hzdr.de
21. 08/2011 - 07/2014 Deutsche Forschungsgemeinschaft DFG
Nanostrukturierung von Oberflächen mit direkter Extraktion der Ionen aus Plasmaquellen
 Dr. S. Facsko Phone: 0351 260 2987 s.facsko@hzdr.de
22. 09/2011 - 08/2012 Deutsche Forschungsgemeinschaft DFG
Terahertz dynamics in carbon based nanostructures
 Prof. M. Helm Phone: 0351 260 2260 m.helm@hzdr.de

Federally Funded Projects

1. 07/2008 - 08/2011 Bundesministerium für Bildung und Forschung BMBF
Multifunktionale Speicherkonzepte
 Prof. J. Fassbender Phone: 0351 260 3096 j.fassbender@hzdr.de
2. 05/2009 – 04/2011 Bundesministerium für Bau, Verkehr und Stadtentwicklung BMBVS
FZD- Applikationslabor Ionentechnologie
 Prof. A. Kolitsch Phone: 0351 260 3348 a.kolitsch@hzdr.de
3. 06/2009 – 05/2012 Bundesministerium für Bildung und Forschung BMBF
Rezeptor-selektive Anreicherung und Bio-LED-Sensorik zur Detektion von (anti-) östrogen- und (anti-) androgenwirkenden Substanzen (BIO-LED-Sensorik)
 Dr. L. Rebohle Phone: 0351 260 3368 l.rebohle@hzdr.de
4. 06/2009 – 05/2011 AG Industrieller Forschungsvereinigungen (AiF) BMWi
Unterdrückung der Sauerstoffversprödung von Titanlegierungen (II)
 Prof. A. Kolitsch Phone: 0351 260 3348 a.kolitsch@hzdr.de
5. 01/2010 – 03/2012 AG Industrieller Forschungseinrichtungen (AiF) BMWi
Advanced coatings to suppress environmental embrittlement of TiAl alloys (ACETAL)
 Prof. A. Kolitsch Phone: 0351 260 3348 a.kolitsch@hzdr.de
6. 03/2010 – 04/2011 Bundesministerium für Wirtschaft BMWi
Exist – Gründerstipendium SAXRAY
 Dr. S. Gemming Phone: 0351 260 2470 s.gemming@hzdr.de
7. 04/2010 – 03/2013 Bundesministerium für Bildung und Forschung BMBF
RainbowEnergy
 Dr. K.-H. Heinig Phone: 0351 260 3288 k.h.heinig@hzdr.de
8. 05/2010 – 07/2013 AG Industrieller Forschungseinrichtungen (AiF) BMWi
TCO Grenzflächenoptimierung
 Prof. A. Kolitsch Phone: 0351 260 3348 a.kolitsch@hzdr.de
9. 07/2010 – 06/2013 Gesellschaft für Chemische Technik und Biotechnologie DECHEMA
Ionenimplantation von TiAl-Proben
 Prof. A. Kolitsch Phone: 0351 260 3348 a.kolitsch@hzdr.de
10. 10/2010 – 09/2013 Bundesministerium für Bildung und Forschung BMBF
Photoinitiated dynamics studied in the fs to ns time and the THz to PHz frequency domain: Picosecond beamline at FELBE (PIDID)
 Dr. H. Schneider Phone: 0351 260 2880 h.schneider@hzdr.de
11. 12/2010 – 12/2011 Gesellschaft für Chemische Technik und Biotechnologie DECHEMA
CI-Ionenimplantation von Proben Nickelbasislegierungen
 Prof. A. Kolitsch Phone: 0351 260 3348 a.kolitsch@hzdr.de

- | | | | |
|-----|-------------------|---|---------|
| 12. | 05/2011 – 09/2013 | Gesellschaft für Chemische Technik und Biotechnologie
Ionenimplantation für Hochtemperatur-Oxidationsschutz
<i>Prof. A. Kolitsch</i> <i>Phone: 0351 260 3348</i> <i>a.kolitsch@hzdr.de</i> | DECHEMA |
| 13. | 10/2011 – 10/2013 | Bundesministerium für Bildung und Forschung
WTZ Indien: Plasmonische Strukturen
<i>Dr. S. Facsko</i> <i>Phone: 0351 260 2987</i> <i>s.facsko@hzdr.de</i> | BMBF |
| 14. | 10/2011 – 09/2012 | Swiss National Science Foundation
Spin-dependent transport in superlattice nanostructures
<i>Dr. A. Deac</i> <i>Phone: 0351 260 3709</i> <i>a.deac@hzdr.de</i> | SNF |

Saxony State Funded Projects

- | | | | |
|----|-------------------|---|-----|
| 1. | 07/2009 – 06/2012 | Sächsische Aufbaubank
High-k Gate Dielektrika 2. Generation (KZWEI)
<i>Dr. W. Skorupa</i> <i>Phone: 0351 260 3612</i> <i>w.skorupa@hzdr.de</i> | SAB |
| 2. | 12/2010 – 05/2013 | Sächsische Aufbaubank
Kelvin-Kraft-Mikroskopie
<i>Dr. H. Schmidt</i> <i>Phone: 0351 260 2724</i> <i>heidemarie.schmidt@hzdr.de</i> | SAB |

Personnel Exchange Projects

- | | | | |
|----|-------------------|--|------|
| 1. | 05/2009 – 04/2011 | Alexander-von-Humboldt-Stiftung
Gastaufenthalt Dr. J. Bhattacharyya (Tata Institute of Fundamental Research, India)
<i>Dr. H. Schneider</i> <i>Phone: 0351 260 2880</i> <i>h.schneider@hzdr.de</i> | AvH |
| 2. | 07/2009 – 06/2011 | Deutscher Akademischer Austauschdienst
Projektbezogener Personenaustausch mit Großbritannien (University of Glasgow)
<i>Prof. J. Fassbender</i> <i>Phone: 0351 260 3096</i> <i>j.fassbender@hzdr.de</i> | DAAD |
| 3. | 09/2009 – 08/2012 | Alexander-von-Humboldt-Stiftung
Gastaufenthalt Dr. El-Said (Mansoura University, Egypt)
<i>Dr. S. Facsko</i> <i>Phone: 0351 260 2987</i> <i>s.facsko@hzdr.de</i> | AvH |
| 4. | 01/2010 – 12/2011 | Deutscher Akademischer Austauschdienst
Projektbezogener Personenaustausch mit Frankreich (CEREGE Aix-en-Provence)
<i>Dr. S. Merchel</i> <i>Phone: 0351 260 2802</i> <i>s.merchel@hzdr.de</i> | DAAD |
| 5. | 01/2010 – 12/2011 | Deutscher Akademischer Austauschdienst
Projektbezogener Personenaustausch mit Brasilien (University Porto Alegre)
<i>Dr. L. Rebohle</i> <i>Phone: 0351 260 3368</i> <i>l.rebohle@hzdr.de</i> | DAAD |
| 6. | 01/2011 – 12/2012 | Deutscher Akademischer Austauschdienst
Projektbezogener Personenaustausch mit Spanien (Universidad Politécnica de Madrid)
<i>Dr. F. Munnik</i> <i>Phone: 0351 260 2174</i> <i>f.munnik@hzdr.de</i> | DAAD |
| 7. | 01/2011 – 06/2011 | Deutscher Akademischer Austauschdienst
Projektbezogener Personenaustausch mit Frankreich (University Nancy)
<i>Dr. J. McCord</i> <i>Phone: 0351 260 3709</i> <i>j.mccord@hzdr.de</i> | DAAD |
| 8. | 11/2011 – 10/2012 | Alexander-von-Humboldt-Stiftung
Rückkehrstipendium Dr. A. Keller
<i>Prof. J. Fassbender</i> <i>Phone: 0351 260 3096</i> <i>j.fassbender@hzdr.de</i> | AvH |

Bilateral Projects

1. 05/2008 - 04/2012 FHR Anlagenbau Ottendorf-Okrilla/IHP Frankfurt/O. Industry
Blitztemperung 200
Dr. W. Skorupa Phone: 0351 260 3612 w.skorupa@hzdr.de
2. 09/2008 - 06/2011 TU Dresden TUD
Modellieren der Bedeckung keramischer Oberflächen mit Wachstumsproteinen (BIOMIN)
Dr. S. Gemming Phone: 0351 260 2470 s.gemming@hzdr.de
3. 07/2009 – 06/2011 TU Bergakademie Freiberg TU-BA
Eigenschaften nano- und mikrokristalliner Si-Dünnschichten
Dr. W. Skorupa Phone: 0351 260 3612 w.skorupa@hzdr.de
4. 04/2010 – 03/2012 FHR Anlagenbau / Centrotherm Industry
Entwicklung industrietauglicher Temperaturmessung
Dr. W. Skorupa Phone: 0351 260 3612 w.skorupa@hzdr.de
5. 05/2010 – 06/2011 Brehm Präzisionstechnik Ulm GmbH Industry
Osteofit 2030
Prof. A. Kolitsch Phone: 0351 260 3348 a.kolitsch@hzdr.de
6. 10/2010 – 09/2013 DTF Technology Dresden Industry
DTF- Industriedoktoranden
Prof. A. Kolitsch Phone: 0351 260 3348 a.kolitsch@hzdr.de
7. 12/2010 – 06/2011 EagleBurgmann Germany Industry
Abscheidung von Hartstoffschichten
Prof. A. Kolitsch Phone: 0351 260 3348 a.kolitsch@hzdr.de
8. 04/2011 – 12/2011 VAAT Industry
Hall Effekt Messungen und Analysen
Prof. A. Kolitsch Phone: 0351 260 3348 a.kolitsch@hzdr.de

Experimental equipment

Accelerators, ion implanters and ion-assisted-deposition

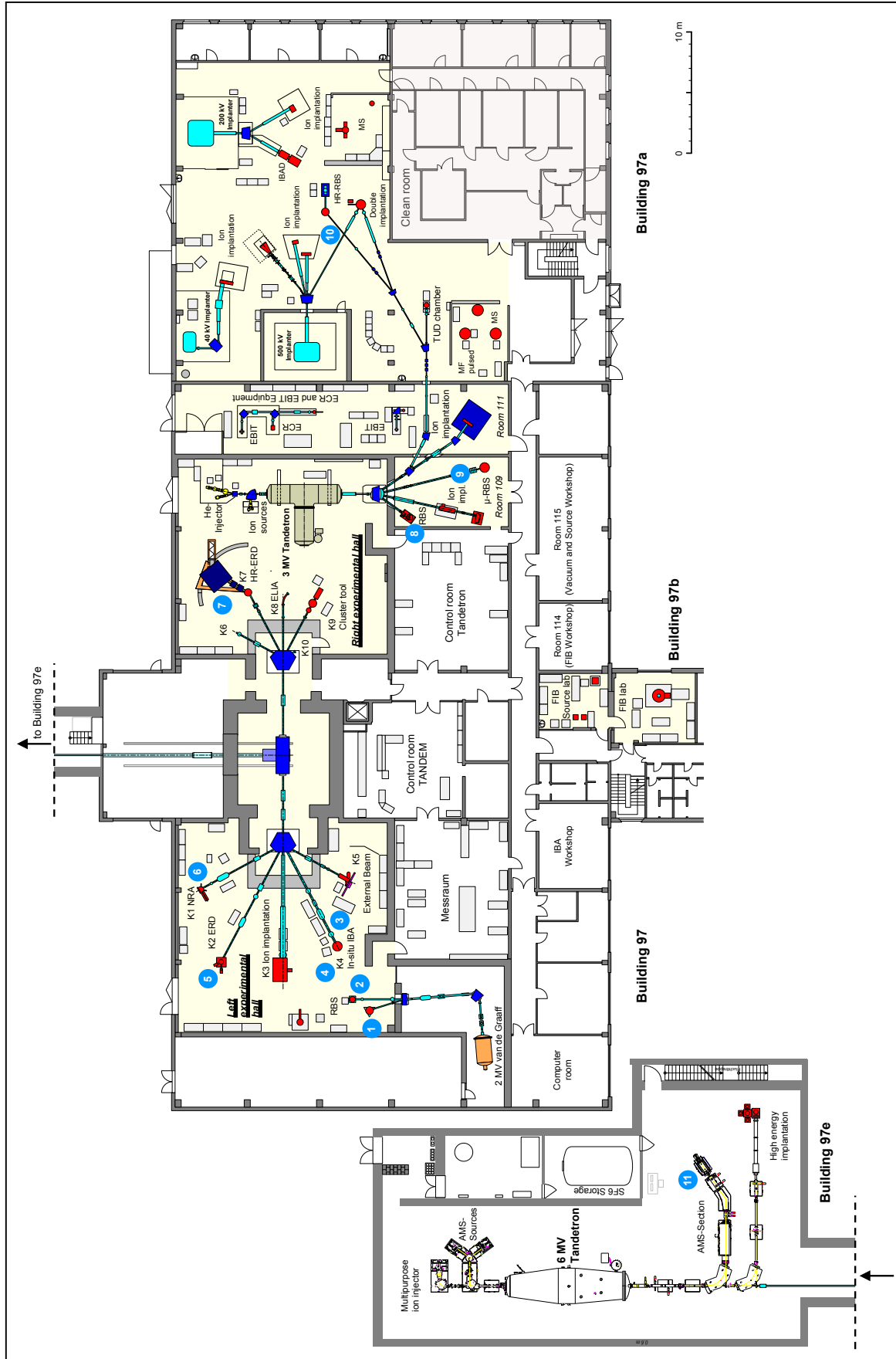
Van de Graaff Accelerator (VdG)	1.8 MV	TuR Dresden, DE
Tandetron Accelerator (T1)	3 MV	HVEE, NL
Tandetron Accelerator (T2)	6 MV	HVEE, NL
Low-Energy Ion Implanter	0.5 - 50 kV	Danfysik, DK
High-Current Ion Implanter	20 - 200 kV	Danfysik, DK
High-Energy Ion Implanter	40 - 500 kV	HVEE, NL
Plasma Immersion Ion Implantation	5 - 60 keV	GBR, DE / Home-built
Focused Ion Beam (15 nm, variable ions)	30 keV, 10 A/cm ²	Orsay Physics, FR
Highly-Charged Ion Facility	25 eV – 25 keV × Q Q = 1...40 (Xe)	Home-built
Dual-Beam Magnetron Sputter Deposition		Roth & Rau, DE
Ion-Beam-Assisted Deposition		Danfysik, DK
Ion-Beam Sputtering	200 - 2000 V	Home-built
UHV Ion Irradiation (Ar, He, etc.)	0 - 5 keV Scan 10×10 mm ²	VG, USA

Ion Beam Analysis (IBA)

A wide variety of advanced IBA techniques are available at the MeV accelerators (see figure).

RBS	Rutherford Backscattering	(1), (2), (3), (8)	VdG, T1, T2
RBS/C	RBS + Channelling	(1), (2), (3), (8)	VdG, T1, T2
	High-Resolution RBS/C	(7), (10)	T1
ERDA	Elastic Recoil Detection Analysis	(2), (4), (5)	VdG, T2
	High-resolution ERDA	(7)	T2
PIXE	Proton-Induced x-ray Emission	(3)	T2
PIGE	Proton-Induced γ Emission	(3)	T2
NRA	Nuclear Reaction Analysis	(4)	T2
NRRA	Nuclear Resonance Reaction Analysis	(6)	T2
N μ P	Nuclear Microprobe	(9)	T1
AMS	Accelerator Mass Spectrometry	(11)	T1
	(focused to cosmogenic radionuclides: ¹⁰ Be, ²⁶ Al, ³⁶ Cl, ⁴¹ Ca, ¹²⁹ J)		

Some stations are equipped with additional process facilities enabling *in-situ* IBA investigations during ion irradiation, sputtering, deposition, annealing etc..



Ion Beam Centre: Schematic Overview of Installations.

Other particle-based analytical techniques

SEM	Scanning Electron Microscope	1 - 30 keV + EDX	Hitachi, JP
TEM	Transmission Electron Microscope (Titan 80-300 with Image Corrector)	80 - 300 keV + EDX, +GIF	FEI, NL
FIB/SEM	Focused Ion / Electron Cross Beam (NVision 40 with Elphy Plus Litho)	0.5 – 30 keV + IL, + EDX	Zeiss-NTS, DE Raith, Bruker, DE
AES	Auger Electron Spectroscopy	+ XPS	Fisions, UK
CEMS	Mössbauer Spectroscopy	⁵⁷ Fe source	Home-built
PAS	Positron Annihilation Spectroscopy	²² Na source 30 V - 36 kV	Home-built

Photon- based analytical techniques

XRD/XRR	X-Ray Diffraction and Reflection	Cu-K α	Bruker AXS, DE
HR-XRD	High-Resolution XRD	Cu-K α	GE Inspection, DE
TFA	Thin Film Analysis, including Grazing Incidence Small Angle Scattering (GISAXS)	Cu-K α	PANalytical, NL
XRD/XRR	with Synchrotron Radiation	5 – 35 keV	ROBL at ESRF, FR
SE	Spectroscopic Ellipsometry	250 - 1700 nm	Woollam, US
FTIR	Fourier-Transform Infrared Spectr.	600 - 7000 cm ⁻¹	Nicolet, US
FTIR	Fourier-Transform Infrared Spectr	50 - 15000 cm ⁻¹	Bruker, DE
	Ti:Sapphire Femtosecond Laser	78 MHz	Spectra Physics, US
	Femtosecond Optical Parametric Osci.		APE, DE
	Ti:Sapphire Femtosecond Amplifier	1 kHz	Femtolasers, AT
	Ti:Sapphire Femtosecond Amplifier	250 kHz	Coherent, US
	Femtosecond Optical Parametric Amplifier		Light Conversion, LI
THz-TDS	Terahertz Time-Domain Spectroscopy	0.1 - 4 THz	Home-built
Raman	Raman Spectroscopy	> 45 cm ⁻¹ shift	Jobin-Yvon-Horiba, FR
PL	Photoluminescence	300 - 1500 nm	Jobin-Yvon-Horiba, FR
TRPL	Time-Resolved PL	$\tau = 3$ ps - 2 ns $\tau > 5$ ns	Hamamatsu Phot., JP Stanford Research, US
EL	Electroluminescence (10-300 K)	300 - 1500 nm	Jobin-Yvon-Horiba, FR
	Optical Split-Coil Supercond. Magnet	7 T	Oxford Instrum., UK
PR	Photomodulated Reflectivity	300 - 1500 nm	Jobin-Yvon-Horiba, FR
PLE	Photoluminescence Excitation	300 - 1500 nm	Jobin-Yvon-Horiba, FR
OES	Optical Emission Spectroscopy	250 – 800 nm	Jobin-Yvon-Horiba, FR

Magnetic thin film deposition and analysis

MBE	Molecular Beam Epitaxy with in-situ FIB		<i>CreaTec, DE</i>
MBE	Molecular Beam Epitaxy		<i>Home-built</i>
PLD	Pulsed Laser Deposition		<i>SURFACE, DE</i>
MFM	Magnetic Force Microscope	~ 50 nm resol	<i>VEECO / DI, US</i>
SQUID	Supercond. Quantum Interf. Device	± 7 T	<i>Quantum Design, US</i>
MOKE	Magneto-Optic Kerr Effect (in-plane)	± 0.35 T	<i>Home-built</i>
MOKE	Magneto-Optic Kerr Effect (perpend.)	± 2 T	<i>Home-built</i>
SKM	Scanning Kerr Microscope		<i>Home-built</i>
	Kerr Microscope		<i>Evico Magnetics, DE</i>
TR-MOKE	Time-Resolved MOKE (Pump-Probe)		<i>Home-built</i>
VNA-FMR	Vector Network Analyzer Ferromagnetic Resonance		<i>Agilent / Home-built</i>
ME	Magnetoellipsometer		<i>LOT, DE; AMAC, US</i>

Other analytical and measuring techniques

STM	Scanning Tunneling Microscope (with AFM-Option)		<i>DME, DK</i>
STM	<i>In-situ</i> Scanning Tunneling Microscope (T variable)		<i>Omicron, DE</i>
AFM	Atomic Force Microscope (Tapping Mode)		<i>SIS, DE</i>
AFM	Atomic Force Microscope (with c-AFM, SCM-Module)		<i>Veeco Instruments, UK</i>
KFM	Kelvin Probe Force Microscopy		<i>Anfatec, DE</i>
	Dektak Surface Profilometer		<i>Veeco, US</i>
	Micro Indenter / Scratch Tester		<i>Shimatsu, JP</i>
MS	Mass Spectrometers (EQP-300, HPR-30)		<i>HIDEN, DE & US</i>
	Wear Tester (pin-on disc)		<i>Home-built</i>
LP	Automated Langmuir Probe		<i>Impedans, IE</i>
HE	Hall Effect Equipment	2 - 400 K, ≤ 9 T	<i>LakeShore, US</i>
RS	Sheet-Rho-Scanner		<i>AIT, South Korea</i>
DLTS	Deep Level Transient Spectroscopy	(+ I-U / C-V) (10 - 300 K, 1 MHz)	<i>PhysTech, DE</i>
IV / CV	Photocapacitance (+I-V/G-V)	(250 - 2500 nm)	<i>Home-built</i>
IV / CV	I-V and C-V Analyzer		<i>Keithley, US</i>
IV / CV	I-V and C-V Semi-Automatic Prober	(-60 – 300°C)	<i>Süss, DE; Keithley, US</i>
IV	I-V Prober	(4.2 – 600 K)	<i>LakeShore, Agilent, US</i>

Processing and preparation techniques

Physical Deposition	Sputtering DC / RF, Evaporation	<i>Nordiko, UK</i>
	Electron Beam Evaporation System	<i>Leybold Optics, DE</i>
	Thermal Evaporation	<i>Bal-Tec, LI</i>
Chemical Deposition	Plasma Enhanced CVD (for a-Si, SiO ₂ , SiON, Si ₃ N ₄)	<i>Oxford Instruments, UK</i>
Dry Etching	Plasma and RIE Mode	<i>Sentech, DE</i>
Reactive Ion Beam Etching	Ø 6", Ar, CF ₄	<i>Roth & Rau, DE</i>
Etching / Cleaning	incl. Anisotropic Selective KOH Etching	
Photolithography	Mask-Aligner, 2 µm-level	<i>Süss, DE</i>
Electron Beam Lithography	Raith 150-TWO: Ø 6", 10 nm res.	<i>Raith, DE</i>
Thermal Treatment	Room Temperature - 2000°C	
	• Furnace	<i>InnoTherm, DE</i>
	• Rapid Thermal Annealing	<i>ADDAX, FR</i>
	• Flash-Lamp Units (0.5 – 20 ms)	<i>Home-built; FHR, DE</i>
	• RF Heating (Vacuum)	<i>JIP.ELEC, FR</i>
	• Laser annealing (CW, 808 nm, 450 W)	<i>LIMO, DE</i>
Bonding Techniques	Ultrasonic Wire Bonding	<i>Kulicke & Soffa, US</i>
Cutting, Grinding, Polishing		<i>Bühler, DE</i>
TEM Sample Preparation	Plan View and Cross Section incl. Ion Milling Equipment	<i>Gatan, US</i>

SPIRIT

The Institute of Ion Beam Physics and Materials Research is coordinating the Integrated Infrastructure SPIRIT under the FP7 Capacities Programme of the European Union. The duration of the project is from March 2009 to February 2013, the total funding is 6.991.000 €.

SUPPORT OF PUBLIC AND INDUSTRIAL RESEARCH USING ION BEAM TECHNOLOGY

Integrated Activity, EU Project No. 227012
www.spirit-ion.eu



SPIRIT integrates 11 leading ion beam facilities from 6 European Member States and 2 Associated States. Nine of the partners provide Transnational Access to European researchers and industry at their infrastructures. Ion beams in an energy range from ~10 keV to ~100 MeV are supplied for modification and analysis of solid surfaces, interfaces, thin films and nanostructured systems, being mainly applied in research related to materials, biomedicine, environment, and cultural heritage. SPIRIT aims at increasing user access and the quality of research by sharing best practice, balancing supply and demand, harmonizing procedures and extending the services into new emerging fields and to new users especially from the New European Member States and industry. The project comprises a management section (4% of the total funding) and three interlinked activities of Transnational Access (45%), Networking (19%) and Joint Research (32%).

Potential users from public or industrial research are invited for free use of the ion beam facilities at the SPIRIT partners laboratories, either by conducting experiments personally or by sending samples in case of standard ion implantation or ion beam materials analysis. Regularly, access is given on a transnational basis, i.e. the user has to be employed in a European Member or Associate State in which the specific infrastructure is not situated.

Proposals may be turned in continuously through the SPIRIT website and will be evaluated promptly by an international User Selection Panel. Any successful proposer will be granted free access to the infrastructure, with the associated travel costs and daily expenses being covered by the European Commission.

In 2011, Transnational Access has been extended from originally seven to now nine SPIRIT laboratories, enabling also the use of the facilities at the University Pierre et Marie Curie in Paris and at the Ruder Boskovic Institute in Zagreb.

During the Mid-Term Meeting of the project in March-2011, SPIRIT was officially evaluated by the European Commission. The evaluation report documents an excellent performance of the project in all its activities.



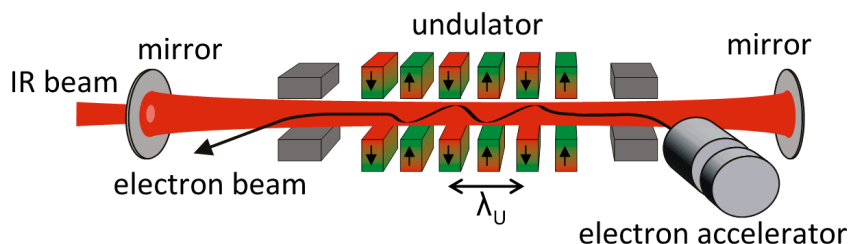
The SPIRIT Consortium

The top nine partners provide Transnational Access.

Helmholtz-Zentrum Dresden-Rossendorf	Germany
CNRS – CENBG Bordeaux	France
Katholieke Universiteit Leuven	Belgium
Jozef Stefan Institut Ljubljana	Slovenia
Universität der Bundeswehr München	Germany
CEA – JANNUS Saclay and CIMAP Caen	France
University of Surrey	U.K.
University de Pierre et Marie Curie Paris	France
Ruder Boskovic Institute Zagreb	Croatia
Institute Tecnologico e Nuclear Lisboa	Portugal
Swiss Federal Institute of Technology Zurich	Switzerland

Free Electron Laser FELBE

ELBE is an acronym for the free-electron laser (FEL) at the Electron Linear accelerator with high Brilliance and Low Emittance (ELBE) located at the Helmholtz-Zentrum Dresden-Rossendorf, Germany. The heart of ELBE is a superconducting linear accelerator operating in cw mode with a pulse repetition rate of 13 MHz. The electron beam (40 MeV, 1 mA max.) is guided to several laboratories where secondary beams (particle and electromagnetic) are generated. Two free-electron lasers (U27-FEL and U100-FEL) produce intense, coherent electromagnetic radiation in the mid and far infrared, which is tunable over a wide wavelength range (4 – 250 μm) by changing the electron energy or the undulator magnetic field. Main parameters of the infrared radiation produced by FELBE are as follows:



Wavelength λ	4 – 22 μm 18 – 250 μm	FEL with undulator U27 FEL with undulator U100
Pulse energy	0.01 – 2 μJ	depends on wavelength
Pulse length	1 – 25 ps	depends on wavelength
Repetition rate	13 MHz	3 modes: <ul style="list-style-type: none"> • cw • macropulsed (> 100 μs, < 25 Hz) • single pulsed (Hz...kHz)

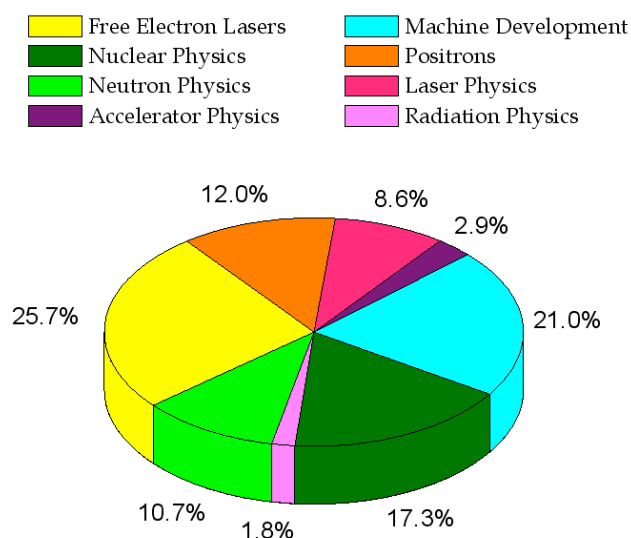
The free electron laser is a user facility. Applications for beam time can be submitted twice a year, typically by April 15 and October 15. Users from EU countries received support through the FP7 Integrated Infrastructure Initiative (I3) ELISA (**E**uropean **L**ight **S**ources **A**ctivities). Typical applications are picosecond pump-probe spectroscopy (also in combination with several other femtosecond lasers, which are synchronized to the FEL), near-field microscopy and nonlinear optics. The FELBE facility also serves as a far-infrared source for experiments at the High-Field Laboratory Dresden (HLD) involving pulsed magnetic fields up to 70 Tesla.

The statistics shows that the FEL used 1287 hours beamtime of the ELBE accelerator. This corresponds to 25.7% of total beamtime, which is again distributed among internal and external users.

For further information please contact Prof. Manfred Helm (m.helm@hzdr.de) or visit the FELBE webpage www.hzdr.de/FELBE.



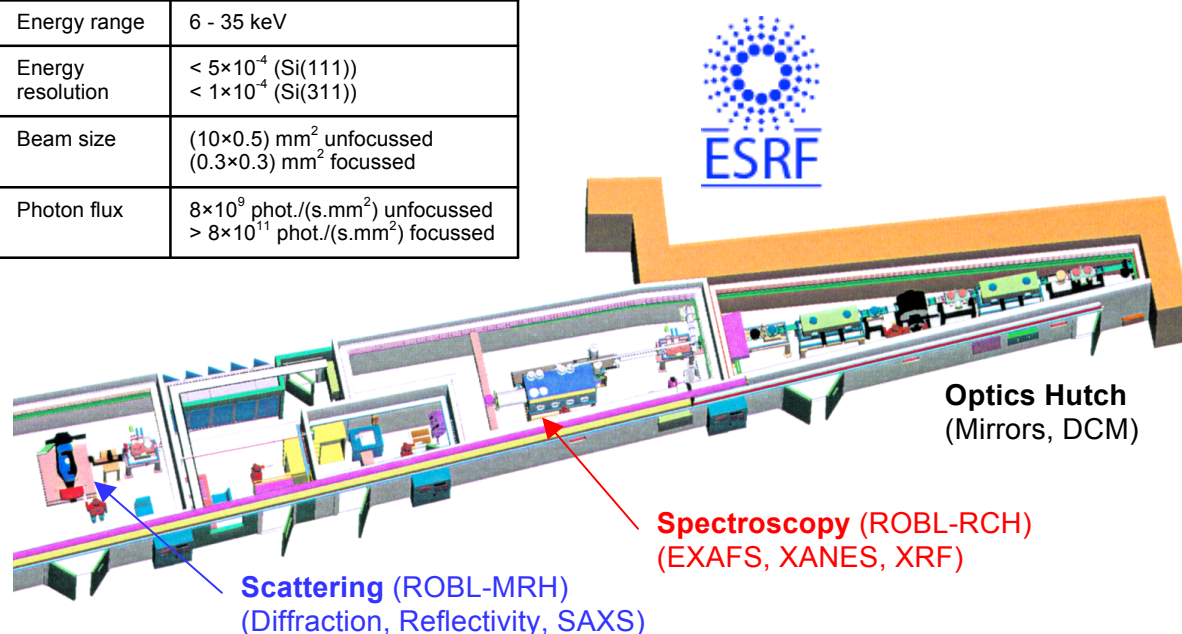
Beamtime Distribution at ELBE 2011



ROBL

The **RO**ssendorf **B**eamLine (ROBL), operated by the HZDR since 1998, is a bending magnet synchrotron beam line located at the European Synchrotron Radiation Facility (ESRF) in Genoble, France. In Summer 2011 the complete beamline optics was renewed. Beside conventional Silicon single crystals for monochromatisation also a multilayer optics is now available increasing the flux by two orders of magnitude by reduced energy resolution. Additionally, the beam can be focused by toroidal shape mirrors and the beam stability was enhanced by improved beam diagnostic devices. The set-up and main parameters are sketched as follows:

Energy range	6 - 35 keV
Energy resolution	$< 5 \times 10^{-4}$ (Si(111)) $< 1 \times 10^{-4}$ (Si(311))
Beam size	$(10 \times 0.5) \text{ mm}^2$ unfocussed $(0.3 \times 0.3) \text{ mm}^2$ focussed
Photon flux	$8 \times 10^9 \text{ phot.}/(\text{s} \cdot \text{mm}^2)$ unfocussed $> 8 \times 10^{11} \text{ phot.}/(\text{s} \cdot \text{mm}^2)$ focussed



The attraction of ROBL is based upon the high specialization of its two end-stations for Radiochemistry (RCH) and Materials Research (MRH). ROBL-RCH is one of only two stations in Europe dedicated to X-ray absorption spectroscopy of actinides and other radionuclides. The core competence of ROBL-MRH is the analysis of thin films, multilayers and (ion-beam-synthesized) nanostructures using X-ray scattering techniques. Main aspects are the analysis of phase formation or transformations, nanostructure evolution, surface and interface characterization or strain/stress investigations at thin films. An increasing number of experiments are performed as *in-situ* X-ray studies using process chambers for magnetron sputter deposition or annealing under vacuum or various also reactive atmospheres. All scattering experiments can be complemented by spectroscopic investigations.

ROBL has the status of user facility. Applications for ROBL beam time can be submitted twice a year, typically by March, 1 and September, 1 via the official ESRF proposal submission portal. Successfully reviewed proposals will be financially supported by the ESRF by covering travel and accommodation costs. In addition, there is also the possibility to use in-house research beam time for collaborative experiments between external users and HZDR scientists for studies of common interest.

For further information please contact

Dr. A. Scheinost (ROBL-RCH): scheinost@esrf.fr

Dr. C. Bähtz (ROBL-MRH): baehtz@esrf.fr

or visit the ROBL webpage www.hzdr.de/ROBL

Services

Main areas of competence

- Ion implantation in a broad range of ion energy (~ 200 eV to ~ 50 MeV) and substrate temperature
- Advanced ion beam technologies (high energy ion implantation, plasma immersion ion implantation, focused ion beam) for (micro)electronic applications
- Deposition of functional coatings using ion-assisted physical vapor deposition
- Advanced annealing technologies with flash lamps and lasers in the subsecond range
- Development and fabrication of sensors and detectors for charged particle spectroscopy
- High energy ion implantation service for power devices and laser structures
- Surface analysis of solid materials with high energy ion beams
- Computer simulation of ion beam interaction with materials
- Optical characterization of materials (luminescence, FTIR, Raman)

Offers

- Consultation and problem evaluation for ion beam applications
- Process development for ion beam processing of metals, ceramics, semiconductors, thin films
- Preparation and treatment of material samples, tools or complex parts of devices
- Ion implantation and ion beam analysis services
- Fabrication of silicon radiation sensors under clean room conditions
- Structural diagnostics of materials surfaces including e-beam (SEM, TEM, AES) and X-ray techniques (XRD, XRR with both Cu-K and Synchrotron (5-35 keV) radiation).

Contact

Please direct your inquiries about the application of ion beams for modification and analysis of materials to one of the following experts:

Field of application	Responsible	Phone / Fax*	E-mail
Ion implantation and high-energy ion beam analysis	Dr. Johannes von Borany	3378 / 3438	j.v.borany@hzdr.de
Ion technologies for surface modification and doping	Prof. Andreas Kolitsch	3348 / 2703	a.kolitsch@hzdr.de
Advanced surface annealing	Dr. Wolfgang Skorupa	3612 / 3411	w.skorupa@hzdr.de
Semiconductor preparation Detector / Sensor fabrication	Dr. Bernd Schmidt	2726 / 3285	bernd.schmidt@hzdr.de
Focused ion beams	Dr. Lothar Bischoff	2963 / 3285	l.bischoff@hzdr.de
Structural diagnostics	Dr. Johannes von Borany	3378 / 3438	j.v.borany@hzdr.de
Materials research with Synchrotron radiation at ROBL (ESRF)	Dr. Carsten Bähtz	2367	baehtz@esrf.fr
Optical materials characterization	Dr. Harald Schneider	2880 / 3285	h.schneider@hzdr.de

*For all phone/ fax-numbers choose the country / local code: +49 351 260 - xxxx (for HZDR)
+33 47 688 - xxxx (for ROBL)

The institute also recommends the homepages of its spin-off companies

- | | | |
|------------------------|--------------------------|--|
| • HZDR Innovation GmbH | | www.hzdr-innovation.de |
| • GeSiM mbH | Si-Microsystems | www.gesim.de |
| • APT Dresden | Applied Pulse Technology | www.apd-dresden.de |
| • DTF GmbH | Thin Film Technology | www.dtf-technology.de |

**Helmholtz-Zentrum
Dresden-Rossendorf e.V.**
**Institute of Ion Beam Physics
and Materials Research (IIM)**

P.O. Box 51 01 19
01314 Dresden
Phone: +49 351 260 2345
Fax: + 49 351 260 3285
<http://www.hzdr.de/FWI>

DIRECTORS

Prof. Dr. Manfred Helm (- 2260) / Prof. Dr. Jürgen Fassbender (- 3096)
Prof. Dr. Wolfhard Möller (- 2245) (retired)

DIVISIONS

<p>SEMICONDUCTOR MATERIALS FWIM Dr. Wolfgang Skorupa (- 3612)</p> <ul style="list-style-type: none"> ◆ Semiconductor Nanostructures ◆ Nanophotonics ◆ Subsecond Thermal Processing ◆ Magnetic Semiconductors 	<p>ION BEAM ANALYSIS FWIA Dr. Silke Merchel (- 2802)</p> <ul style="list-style-type: none"> ◆ MeV Accelerator Operation ◆ High-Energy Ion Beam Analysis ◆ Accelerator Mass Spectrometry ◆ Non-destructive Analysis of Art Objects
<p>SEMICONDUCTOR SPECTROSCOPY FWIH Dr. Harald Schneider (- 2880)</p> <ul style="list-style-type: none"> ◆ Semiconductor Quantum Structures ◆ Terahertz Spectroscopy ◆ Femtosecond Spectroscopy ◆ Free Electron Laser at ELBE ◆ Optical Characterization (PL, FTIR, Raman) 	<p>ION TECHNOLOGY FWII Prof. Dr. Andreas Kolitsch (- 3326)</p> <ul style="list-style-type: none"> ◆ Ion Implanter / PIII operation ◆ Ion Beam and Plasma Assisted Deposition ◆ Transparent Conductive Oxides ◆ Biotechnological Materials ◆ Industrial Services and Projects
<p>STRUCTURAL DIAGNOSTICS FWIS Dr. Johannes von Borany (- 3378)</p> <ul style="list-style-type: none"> ◆ Electron Microscopy (TEM, SEM) ◆ Electron Spectroscopy (AES, XPS) ◆ SEM / FIB Cross Beam Techniques ◆ X-ray Analysis / Mössbauer Spectroscopy ◆ Materials Research with Synchr. Radiation 	<p>NANOMAGNETISM FWIN Prof. Dr. Jürgen Fassbender (- 3096)</p> <ul style="list-style-type: none"> ◆ Modification of Magnetic Materials ◆ Nano-Spintronics ◆ Magnetization Dynamics ◆ Magnetism at Interfaces ◆ High Anisotropy Nanoparticles
<p>THEORY FWIT Dr. Matthias Posselt (- 3279)</p> <ul style="list-style-type: none"> ◆ Atomistic Computer Simulations ◆ Defects, Impurities, Nanostructures, Surfaces and Interfaces ◆ Formation, Evolution and Self-Organization ◆ Energetics and Kinetics 	<p>NANOSTRUCTURES FWIO Dr. Sibylle Gemming (- 2470)</p> <ul style="list-style-type: none"> ◆ Ion Induced Nanostructure Formation ◆ Slow Highly-Charged Ions ◆ Transport Phenomena in Nanostructures ◆ DFT Modelling of Nanostructured Matter ◆ Nanocomposite Materials
<p>PROCESS TECHNOLOGY FWIP Dr. Bernd Schmidt (- 2726)</p> <ul style="list-style-type: none"> ◆ Clean Room Operation ◆ Semiconductor Technology and Processing ◆ Focused Ion Beam Technology ◆ Si Detector and Sensor Development ◆ Electrical Device Characterization 	

List of personnel 2011

DIRECTORS		OFFICE	
Prof. Dr. M. Helm, Prof. Dr. J. Fassbender		S. Gebel, S. Kirch	
SCIENTIFIC STAFF			
Permanent staff		Non-permanent	
Dr. G. Abrasonis	Dr. H. Reuther	Dr. J. Auerhammer (P)	Dr. K. Lenz
Dr. C. Akhmadaliev	Dr. B. Schmidt	Dr. J. Bhattacharyya (P)	Dr. B. Liedke (P)
Dr. C. Bächtz	Dr. H. Schneider	Dr. C. Bunce (P)	Dr. M. O. Liedke (P)
Dr. L. Bischoff	Dr. W. Skorupa	Dr. C. Cherkouk (P)	Prof. W. Möller (P)
Dr. J. von Borany	Dr. M. Voelskow	Dr. A. Cordeiro (P)	Dr. A. Neudert
Dr. S. Facsko	Dr. S. Winnerl	Dr. A. Deac	Dr. X. Ou (P)
Dr. S. Gemming		Dr. O. Drachenko (P)	Dr. W. Pilz (P)
Dr. J. Grenzer		Dr. A. S. El-Said (P)	Dr. S. Prucnal (P)
Dr. V. Heera		Dr. A. Erbe	Dr. A. Rogozin (P)
Dr. K.-H. Heinig		Dr. C. Fowley	Dr. G. Rugel
Dr. R. Kögler		Dr. M. Friedrich	K. Saravanan (P)
Prof. A. Kolitsch		Dr. J. Grebing	Dr. A. Shalimov
Dr. J. McCord		Dr. R. Heller	Dr. H. Schmidt
Dr. S. Merchel		D. Henke (P)	Dr. V. Sluka
Dr. A. Mücklich		M. Herrmann (P)	Dr. D. Stehr
Dr. F. Munnik		Dr. A. Keller (P)	Dr. M. Vinnichenko (P)
Dr. C. Neelmeijer		Dr. G. Kovacs	Dr. M. Wagner
Dr. M. Posselt		G. Krahl (P)	Dr. R. Yankov (P)
Dr. K. Potzger		Dr. M. Krause (P)	Dr. S. Zhou (P)
Dr. L. Rebohle		Dr. T. Leisegang (P)	Dr. M. Zier (P)
TECHNICAL STAFF			
Permanent staff		Non-permanent	
Rb. Aniol	H. Lange	M. Steinert	C. Frenzel (P)
Ry. Aniol	U. Lucchesi	U. Strauch	M. Kretzschmar
E. Christalle	F. Ludewig	K. Thiemig	V. Kühn (P)
S. Eisenwinder	R. Mester	A. Vetter	T. Putzke (P)
B. Gebauer	M. Mißbach	J. Wagner	T. Schönherr
D. Hanf	C. Neisser	R. Weidauer	I. Skorupa (P)
J. Haufe	A. Reichel	A. Weise	A. Weißig (P)
A. Henschke	B. Scheumann	J. Winkelmann	
H. Hilliges	G. Schnabel	G. Winkler	
S. Klare	A. Schneider	I. Winkler	
J. Kreher	A. Scholz	L. Zimmermann	
A. Kunz	T. Schumann	J. Zscharschuch	

(P) Projects

PhD STUDENTS

A. Banholzer	A. Heidarian	M. Neubert	A. Thorn
C. Baumgart	M. Höwler	S. Numazawa	Y. Wang
K. Bernert	R. Jacob	J. Osten	R. Wensch
M. Buhl	Z. Jiang	S. Pavetich	U. Wiesenhütter
D. Bürger	T. Kaspar	P. Philipp	M. Wieser
S. Cornelius	M. Körner	D. Reichel	C. Wilde
R. Endler	M. Kosmata	O. Roshchupkina	R. Wilhelm
M. Fehrenbacher	A. Kranz	C. Scarlat	S. Wintz
J. Fiedler	J. Lehmann	Y. Shuai	M. Zschintzsch
C. Franke	L. Li	T. Sandler	M. Zschornak
D. Friedrich	N. Martin	G. Steinbach	S. Zybell
M. Fritzsche	A. Martinavicius	D. Stephan	
K. Gao	M. Mittendorff	T. Strache	
S. Germer	K. M. Mok	M. Teich	

STUDENTS (diploma / MSc / BSc)

M. Baudisch	C. Günz	M. Langer	H. Sasse
S. Berger	A. Haase	R. Mertzig	M. Schiwarth
S. Dießner	T. Henschel	H. Noack	J. Schmidt
F. Göttfert	J. Kelling	H. Richter	S. Streit
F. Großmann	S. Kuske	I. Ronneberger	